ISDM 2015

Proceedings

International Students Day of Metallurgy 2015 - Aachen

Impressum

Dieser Konferenzband wird von der Fachschaft Materialwissenschaft und Werkstofftechnik gemeinsam mit der Fachgruppe für Materialwissenschaft und Werkstofftechnik herausgegeben.

Herausgeber

Fachschaft Materialwissenschaft und Werkstofftechnik
Intzestr. 1
52072 Aachen

fachschaft@fsmuw.rwth-aachen.de
www.fsmuw.rwth-aachen.de

Fachgruppe für Materialwissenschaft und Werkstofftechnik
Intzestr. 1
52062 Aachen

ReferentMuW@rwth-aachen.de
www.muw.rwth-aachen.de

Redaktion

Nadine Loose (Cover)
Markus Scheller

Coverfotos

Bild rechts: Linde AG
Rest: L. Wels

Auflage: 300
Erschienen: Mai 2015

Dear participants of the 22nd international student's day of metallurgy,

on behalf of the students and members of the RWTH Aachen we would like to welcome all our guests here in Aachen. You are part of Europe's present and future of metallurgy and materials science and we are honoured by your presence at our conference.

Since its very beginning the ISDM has stood for the connection of international students of metallurgy and the exchange of knowledge between them. Therefore we are proud to welcome students from fifteen cities located in six different countries in and outside of Europe.

Furthermore, we would like to welcome and thank our sponsors from the European metallurgy, materials science and plant manufacturing business. This conference would not have been realizable without their contribution. Their support shows the strong bonds that have been established over the years between the students, the universities and the companies in our field of knowledge.

It is our foremost objective that you enjoy your stay in Aachen – that you are alighted by the technical presentations, establish some great contacts on our contact fair, get an insight into local companies during one of the provided excursions and have a great time on the evening events.

We hope that the connections, which are represented by this convention, will further develop and improve as the ISDM carries on upholding its tradition.

Good luck! szczęść Boże! Zdar boh! Zdařbůh! GLÜCK AUF!

Contents

Macrostructure and microstructure of small sized Mg-Cf composite casts obtained by die casting

Hanna Myalska, Łukasz Kociuba, Anita Olszówka-Myalska
Silesian University of Technology
Institute of Materials Science, 40-019 Katowice, ul. Krasińskiego 8, Poland
E-Mail: hanna.myalska@polsl.pl

Abstract

Small sized casts of composite with AZ31 magnesium alloy matrix and short carbon fibers were investigated. For manufacturing of composite casts a pressure die casting of Mg-Cf suspension was applied. Shape and surface of obtained small sized cast elements were correct and any macrostructural defects were not found. Observation of composite microstructure using scanning electron microscope (SEM) and light microscope (LM) showed that fibers does not obstruct a suspension flow in thin sections of composite cast and only a minor orientation of short carbon fibers on longitudinal section in element of diameter ϕ=5mm was visible.

1 Introduction

Carbon fibers (Cf) because of them excellent mechanical properties seem to be a good component improving properties of magnesium alloys [1]. However, commercial products fabricated from Mg-Cf composite are not available because many technological problems with manufacturing elements of satisfied properties, different shape and size. Pressure infiltration of carbon fabrics by liquid magnesium as a technology for Mg-Cf system was proposed by some authors [2]. Stir casting technology but with applying of short carbon fibers was suggested by researchers from Silesian University of Technology [3, 4]. They used high pressure casting for fabrication of Mg-Cf casts.

The aim of the presented paper was to examine if application of short carbon fibers can create problems with a suspension flow and may cause defects as pores at a composite cast surface and inside. This issue is particularly important in the case of small thin-walled casts. In experiments the macrostructure of Mg-Cf small-sized casts surface was observed and the microstructure was examined for characterization of Cf distribution in chosen region of cast element.

2 Experimental procedure and results

Magnesium composite reinforced with carbon fibers (7 vol.%) was obtained by die casting method. As a matrix commercially available magnesium alloy AZ31 was used. A chemical composition of AZ31 is shown in Table 1.

Table 1: Chemical composition of AZ31 magnesium alloy.

Al	**Zn**	**Mn**	**Cu**	**Ca**	**Mg**
2.5-3.55 %	0.7-1.3%	0.2-1.0%	0.5 %	0.4%	Rest

As a reinforcement carbon roving STS 5631 1600 tex was applied but carbon fibers were chopped and prepared in the form of 3D granules of separated short fibers with a length up to 300 µm with different orientation (Figure 1, Figure 2.).

Figure 1: 3D granules of short carbon fibers applied in experiment.

Then a suspension of commercial AZ31 magnesium alloy with carbon fibers (Cf) was prepared by mechanical stirring in a protective atmosphere of a CO_2 and SF_6 gas mixture. In the next step the suspension of a temperature of 680 °C was poured with a ladle into a cold chamber pressure die casting machine. Two types of casts were obtained - samples for mechanical examinations (130 mm length, l_o=30 mm and φ=6 mm), and finished composite products of a complex shape (mass 14 g). Their macrographs are visible in Figure 3 and Figure 4 respectively.

The surface of all fabricated casts after removing from casting machine was smooth and without macroscopic defects. Then the heads were removed from these and obtained final composite elements are presented in Figure 5 and Figure 6a. To obtain a final composite product of complex shape (Figure 5) a trimming procedure on a press completed with a trimming tool was carried out.

Microstructure observations by conventional light microscopy (LM) (Nikon Eclipse MA 200) were carried on the composite samples obtained for tensile strength examination. Two types of polished specimen without any additional etching were prepared from a central region of sample where ϕ was 6 mm. They were perpendicularly or paralely oriented

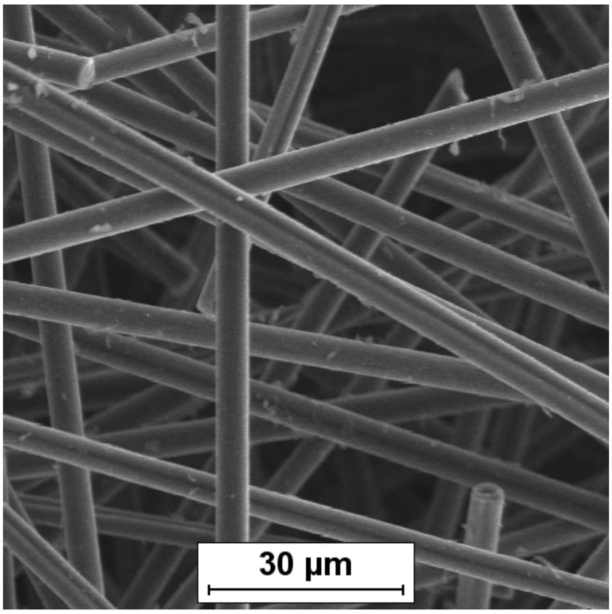

Figure 2: SEM micrograph of Cf distribution in 3D granule.

Figure 3: Macrograph of Mg-Cf composite cast with samples for mechanical properties examination.

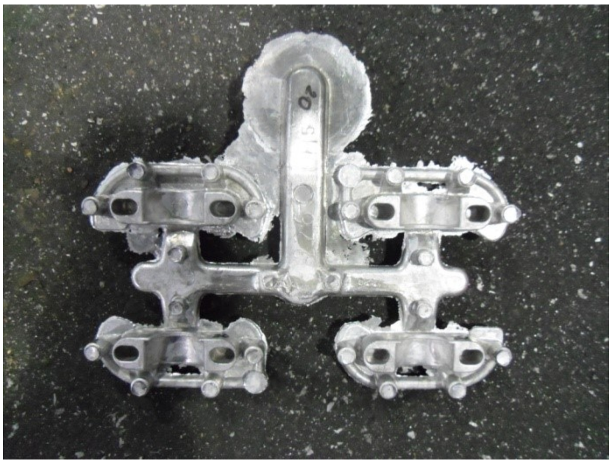

Figure 4: Macrograph of Mg-Cf composite cast with four complex shape final products.

Figure 5: Macrograph of Mg-Cf cast composite product after trimming.

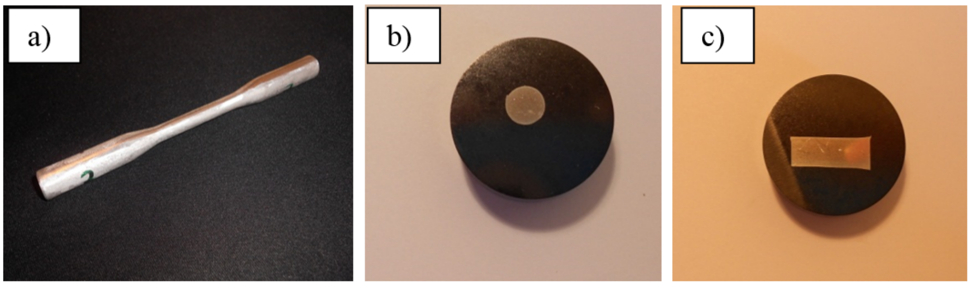

Figure 6: Macrograph of Mg-Cf cast composite – sample for tensile strength examination (a) and polished samples perpendicularly (b) and parallel (c) oriented to the suspension flow orientation prepared for microstruture examination.

to the orientation of a suspension flow during pressure die casting procedure. Obtained results are presented in Figure 7, Figure 8. For perpendiculary cross-sections (Figure 7) the uniform distribution of fibers in a matrix was observed and the fibers evidently oriented perpenidiculary to the suspension flow were almost absent. That character of orientation was observed incidentaly only, where an intial configuraton of fibers in 3D granule was saved (Figure 7c,d). But in that case a full penetration of metal matrix into carbon granules was still ensured and any pores were not detected. In case of polished speciman oriented pararelel to a suspension flow (Figure 8) some short fibers exhibited a tendency for orientation but effect of them agglomeration was not visible.

In Figure 9 the surface of sample fractured in mechanical tests examination was presented. The observations were carried out by scanning electron microscopy (Hitachi S-4200). There are visible fibers with different orientation, surrounded and good bonded with a matrix. The decohesion of short fibers was occurred in planes oriented different to them principal axis and that suggests strong bonding between components.

3 Conclusions

Some results of for magnesium matrix composite with short carbon fibers manufactured by pressure die casting technology were presented. They were focused on examination of short carbon behaviour in thin walled parts of small sized cast. The general conclusions

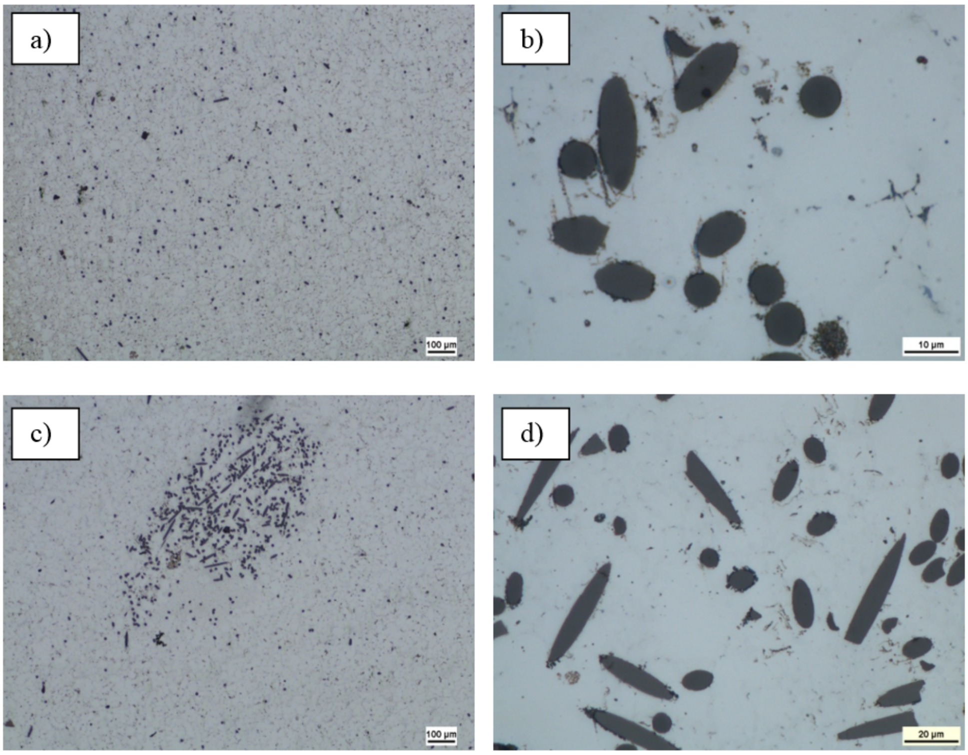

Figure 7: LM micrograph of Mg-Cf cast composite cross-sectioned perpendicularly to a suspension flow.

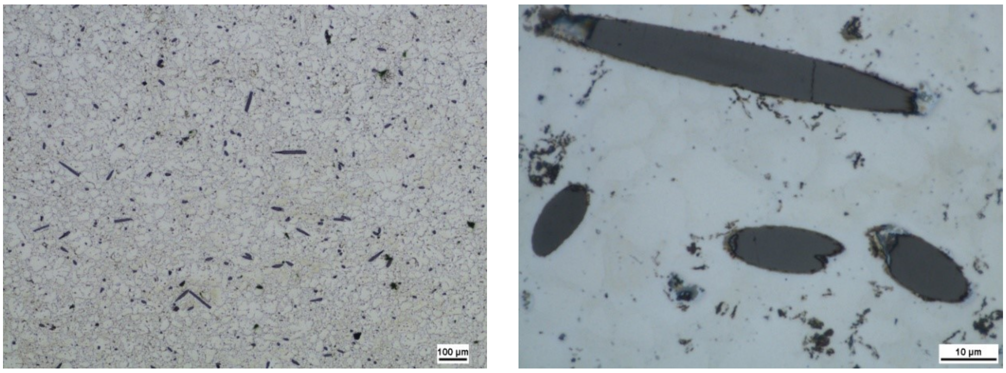

Figure 8: LM micrograph of Mg-Cf cast composite cross-sectioned parallel to a suspension flow.

that can be formed are as follows:

- Obtained casts reproduced the surface of the applied steel dies properly and their surface was smooth and without macroscopic defects.
- The carbon fibers were completely wetted with AZ31 alloy and micropores on the interface were not observed.
- In a thin sections of the sample some of carbon fibers were located almost parallel to a suspension flow direction and no perpendicular fibers were observed.
- Presented results suggest that applied short carbon fibers as a component of magnesium alloy suspension does not obstruct it lamellar movement in a thin walled dies used to pressure casting.

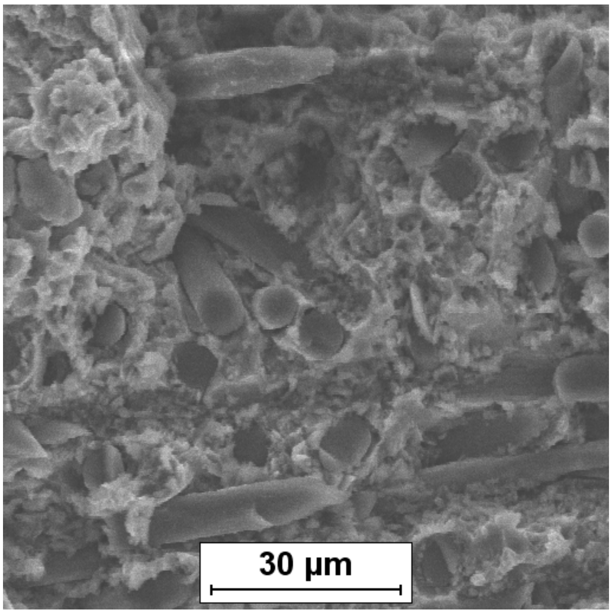

Figure 9: SEM micrograph of Mg-Cf cast composite surface fractured in tensile strength test.

4 Aknowledgement

In experiments were used materials obtained in project NR15-0077-10/2010 financed by Ministry of Science and Higher Education of Poland

References

[1] Gupta, M. and Sharon, N.: *Magnesium, Magnesium Alloys, Magnesium Composites.* John Wiley & Sons, 2011.

[2] Hufenbach, W. et al.: “Fabrication technology and material characterization of carbon fibre reinforced magnesium”. In: *Journal of Materials Processing and Technology* 175 (2006), pages 218–224.

[3] Olszówka-Myalska, A. and Myalski, J.: “Applying stir casting method for Mg alloy- short carbon fiber composite processing”. In: *Composites Theory and Parctice* 14: 2 (2014), pages 81–85.

[4] Olszówka-Myalska, A. and Myalski, J.: “Magnesium alloy AZ31 - short carbon fiber composite obtained by pressure die casting”. In: *Solid State Phenomena* 229 (2015), pages 115–122.

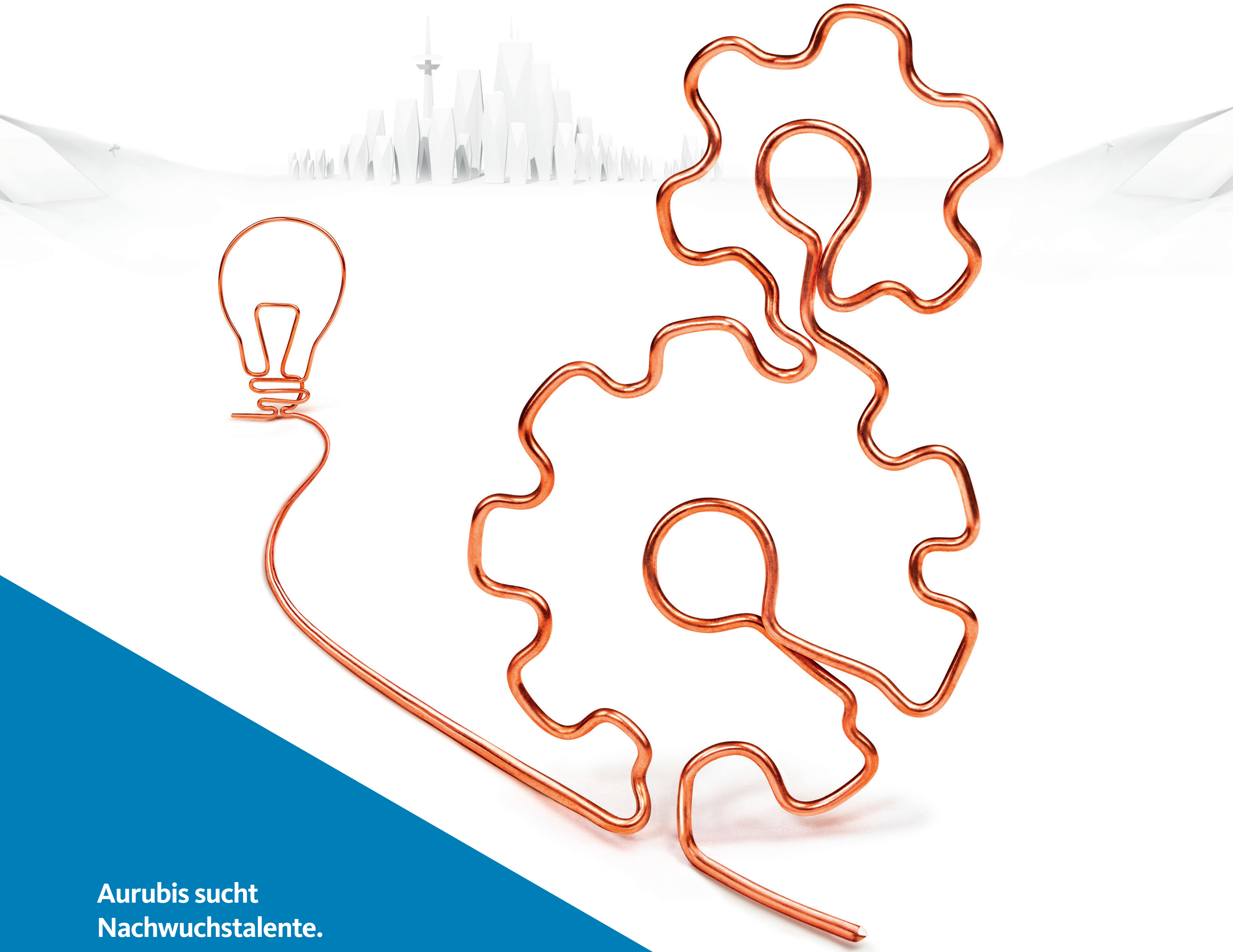

Preparation and properties of ZNO nanoparticles

Ladislav Svoboda, Petr Praus
VŠB – Technical University of Ostrava
17. listopadu 15, 708 / 33, Ostrava-Poruba
E-Mail: ladislav.svoboda@vsb.cz

Abstract

This work deals with the preparation and properties of zinc oxide nanoparticles. Semiconductor ZnO nanoparticles were prepared by thermal annealing at different temperatures and by precipitation reactions including an irradiation induced method of preparation. In the second case zinc acetate was mixed with NaOH under different conditions. Prepared samples were analyzed and characterized by X-ray diffraction, UV-Vis spectroscopy, luminescence, transmission and scanning electron microscopy. The crystallite sizes, structure and shape of prepared ZnO nanoparticles were specified.

Keywords: Nanoparticles, zinc oxide, X-ray diffraction, thermal annealing

1 Introduction

Zinc oxide is a wide-band gap n-type semiconductor due to oxygen vacancies and zinc interstitials. This semiconductor has several favourable properties, including good transparency, high electron mobility and strong room-temperature luminescence [1, 2]. Nanostructures of ZnO can be synthesized into a variety of morphologies, including nanowires, nanorods, tetrapods, nanobelts, nanoflowers, nanoparticles etc. Many methods have been described for the production of ZnO nanomaterials such as laser ablation [3], hydrothermal methods [4], electrochemical depositions [5], thermal annealing [6] and sol-gel methods [7].

One of the most important factors related to ZnO nanoparticles is dependence of their properties on size. The decrease of a semiconductor particle size leads to the increase of its specific surface area and gap energy, which is known as the quantum size effect or quantum confinement. The large surface of nanoparticles results in their high adsorption capacity and catalytic activity.

The aim of this work was to prepare ZnO nanoparticles by different methods and investigate their properties. For this purpose, prepared ZnO powders were characterized by X-ray diffraction, luminescence and transmission electron microscopy. The crystallite sizes, structure and shape of prepared ZnO nanoparticles were specified.

2 Experimental

2.1 Material and chemicals

The used chemicals were of analytical reagent grade: zinc acetate dihydrate and sodium hydroxide, (all from Lachema, Czech Republic). Water deionized by reverse osmosis (Aqua Osmotic, Czech Republic) was used for the preparation of all samples.

2.2 Thermogravimetry

Termogravimetry (TG) analysis was performed on Thermal Analyzer SETSYS-1750 (SETARAM Instrumentation, France) in inert atmosphere of Argon, the heating rate was $10\,°\mathrm{C\,min^{-1}}$ and the weight of the sample was 33.26 mg.

2.3 X-ray powder diffraction analysis

X-ray powder diffraction (XRPD) patterns were recorded under CoK_α irradiation ($\lambda = 0.1789\,\mathrm{nm}$) using the Bruker D8 Advance diffractometer (Bruker AXS) equipped with a fast position sensitive detector VÅNTEC Measurements were carried out in the reflection mode. Powder samples were pressed in a rotational holder. Phase composition was evaluated using database PDF 2 Release 2004 (International Centre for Diffraction Data).

2.4 Transmission electron microscopy

Transmission electron microscopy (TEM) with high resolution images of ZnO nanoparticles were examined by a JEM 220FS microscope (Jeol, Japan) operating at 200 kV. The nanoparticles were dispersed in ethanol and with ultrasonic sprayer deposited on a TEM grid with carbon holey support film.

2.5 Photoluminescence spectra measurements

Photoluminescence (PL) spectra were measured by a spectrometer FLS920 (Edinburgh Instrument Ltd, UK). The spectrometer was equipped with a 450 W Xenon lamp (Xe900). The excitation wavelength was 365 nm. A width of excitation and emission slits was 3 nm.

2.6 Preparation of nanoparticles

Zinc oxide nanoparticles were prepared by a) thermal annealing of zinc acetate and b) by precipitation reaction of zinc acetate with sodium hydroxide. In the second case zinc acetate was mixed with NaOH under UV irradiation with the maximum emission at 254 nm and the final ratios of Zn : OH were set at 1 : 3. Preparation method of each sample is briefly described in Table 1.

Table 1: Overview of prepared ZnO samples.

Number of sample	Method	Temperature/time (°C h^{-1})	Precursors
1	thermal annealing	350/1	zinc acetate dihydrate
2		350/2	
3		350/3	
4		400/1	
5		400/2	
6		400/3	
7		700/3	
8	precipitation reaction + thermal annealing	350/2	zinc acetate dehydrate + sodium hydroxide
9	precipitation reaction + UV irradiation + thermal annealing	350/2	zinc acetate dehydrate + sodium hydroxide

3 Results and discussion

3.1 Preparation of nanoparticles

In thermal annealing method 2 g of powdered zinc acetate was annealed at different temperatures for 1-3 hours. After calcination the samples were crushed in a mortar. In the second case ZnO was prepared by the precipitation reaction followed by thermal annealing. Into the stirred solution of 60 ml 3.3 mmol l^{-1} zinc acetate was added by drop-wise 40 ml 15 mmol l^{-1} (flow rate was about 0.67 ml min^{-1}). For the preparation of powder sample, the solution was filtered and the filter cake was subsequently annealed at 350 °C for 2 hours. The third sample was prepared by similar method with the difference that solution was continuously irradiated by an UV lamp.

3.2 Thermal annealing

A sample of zinc acetate dihydrate was analyzed at a heating rate of 10 °C min^{-1} in an air atmosphere. Measurement was carried out in the temperature range of 50-700 °C. The resulting TGA curve is shown in Figure 1. The initial weight loss of 5.4 mg, which is about 20 % of total weight at 150 °C was due to dehydration thereby obtaining anhydrous zinc acetate. Subsequent weight loss is due to the formation of zinc oxide. The total weight loss of 26.8 mg (80 %) was finished at the temperature 350 °C.

3.3 X-ray powder diffraction analysis

The X-ray powder diffraction was performed (see Figure 2) and subsequently was found the average crystallite size of ZnO. Measured data of the samples are listed in the following Table 2. All the diffraction peaks (see Figure 2) can be indexed to the hexagonal structure with lattice constants of a = 0.325 nm and c = 0.521 nm from JCPDS card No. 01-70-2551

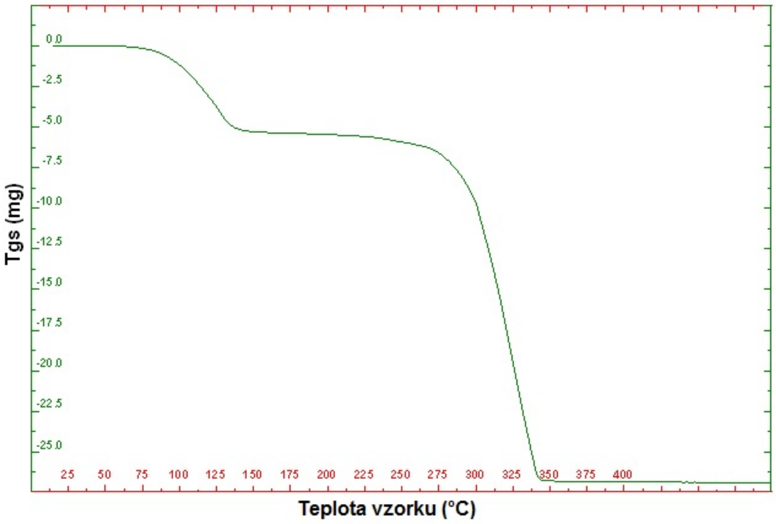

Figure 1: Thermogravity curve of annealing of zinc acetate dihydrate.

Table 2: Calculated average crystallite sizes of ZnO by XRPD.

Number of sample	Temperature/time (,C/h)	Average crystallite size (nm)
1	350/1	35.47
2	350/2	35.87
3	350/3	38.62
4	400/1	32.10
5	400/2	37.22
6	400/3	38.33
7	700/3	88.79
8	350/2	38.41
9	350/2	14.76

and no other peaks (impurities) were observed, S.G. = P63mc. From measured data it is obvious that with increasing temperature and time of annealing the average size was increasing. As a result of annealing time the crystallite sized increased up to 20 % which was also observed by other authors [8, 9]. It is also interesting that the smallest crystallite size of 14.74 nm was obtained by the precipitation under UV irradiation. This effect is still unclear and will be further studied.

3.4 Transmission electron microscopy

Statistical analysis from TEM images (see Figure 3) confirmed results of the XRPD analysis and showed that thermal annealing created larger ZnO particles compared to ZnO particles prepared by the precipitation reactions. The mean crystallite size of ZnO nanoparticles prepared by annealing of zinc acetate was about 40 nm and their distribution was very large from 20 nm to 120 nm. On the other hand, the mean size of ZnO crystallites prepared by precipitation with UV irradiation was about 15 nm.

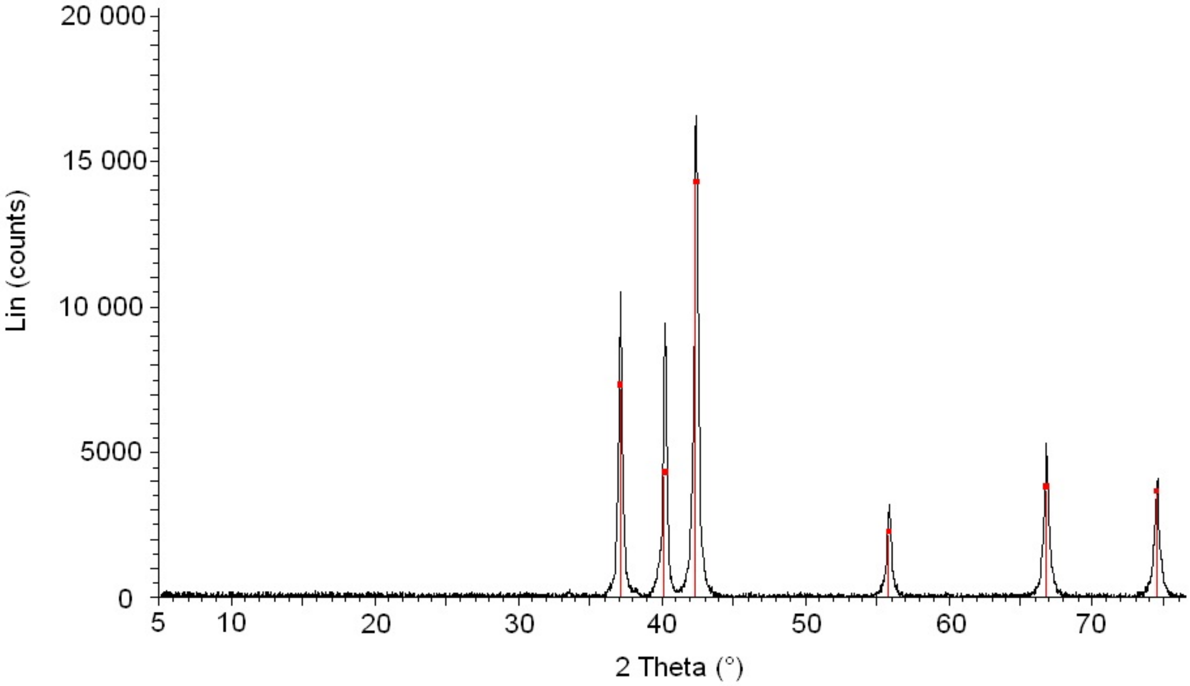

Figure 2: XRPD pattern of ZnO powder prepared at temperature of 350 °C for 1 h.

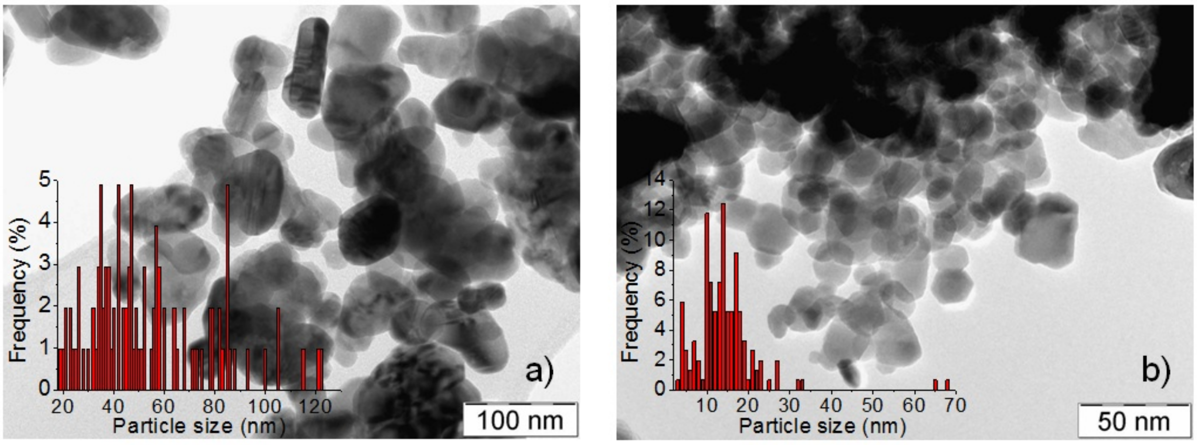

Figure 3: TEM images of ZnO a) prepared by thermal annealing, b) prepared by precipitation reaction under UV light. Size distribution histograms of ZnO size were placed as insets.

3.5 Optical properties

Figure 4 shows the UV-vis spectra of ZnO(1), ZnO(2) and ZnO(3) nanoparticles. The absorption peak of ZnO are shifted to lower energy (red shift) in order ZnO(3), ZnO(2) and ZnO(1). The obtained spectra were transformed to the depencies of $(F(R) \cdot h\nu)^2$ on $h\nu$ (Fig. 4-inset) in order to obtain the vlaues of the energy of absorption edge. The band gap energy of ZnO nanoparticles was 3.23 eV for ZnO(1), 3.24 eV for ZnO(2) and 3.26 eV for ZnO(3). The band gap energy is shifted to lower energy with increased concentration of defects in ZnO nanoparticles.

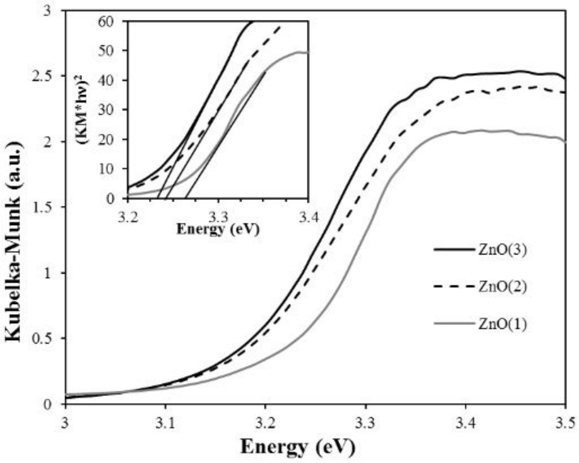

Figure 4: UV-Vis diffuse reflectance spectra with estimated transition energies, Inset - Determination of absorption edges of investigated photocatalysts.

3.6 Photoluminescence spectra measurements

Figure 5 shows the PL spectra of ZnO nanoparticles measured at room temperature using Xe lamp as the excitation source. The quantum yield of the PL spectra from ZnO nanoparticles prepared by the thermal annealing was small and the maximum emission was around 520 nm (green emission). ZnO prepared by the precipitation reaction under UV irradiation showed the much higher quantum yield with the maximum emission at 650 nm (orange-red emission). These broad visible emissions are explained to be caused by defects (interstitial Zn, O vacancies) in ZnO structures (green emission) and boundary of ZnO grains [10, 11]. Therefore we can suppose that these defects were concentrated on surface of small ZnO grains agglomerated into the larger nanoparticles originated by the precipitation.

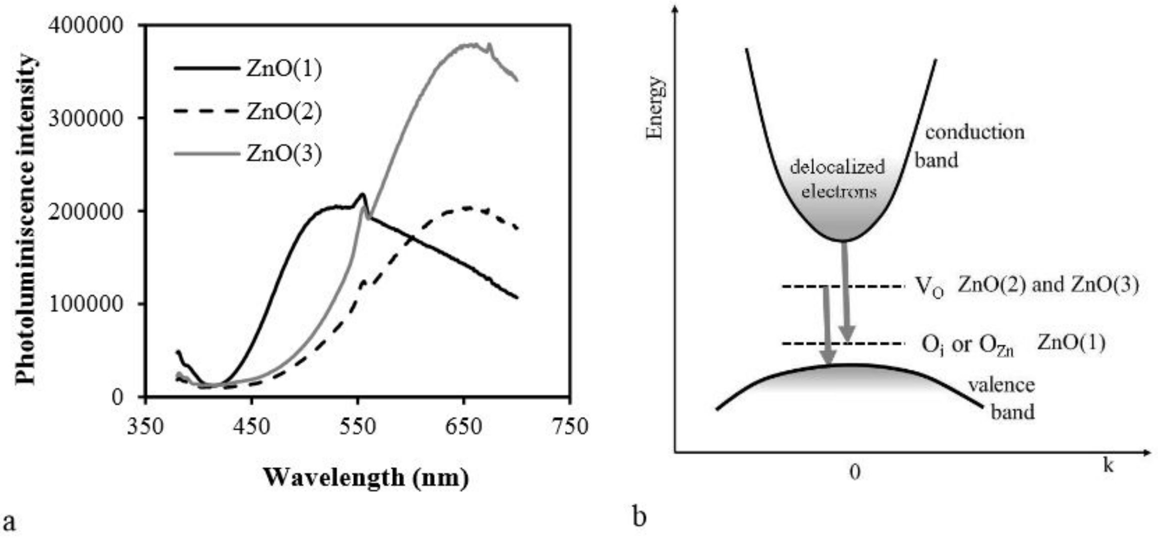

Figure 5: (a) Photoluminescence spectra of ZnO nanoparticles, (b) Scheme of suggested most probable electron transitions responsible for measured PL maxima.

4 Conclusion

ZnO nanoparticles were synthesized by 2 different methods: a) thermal annealing of zinc acetate dihydrate and b) precipitation of zinc ions in aqueous solution with sodium hydroxide. The thermal annealing method gave ZnO nanoparticles larger than the preparation method. This was confirmed by XRPD and TEM images. Also the intensity and positions of broad visible emissions were very different likely as a result of different amounts of oxygen present in both nanostructures. In our research it was observed that temperature and time of annealing had influence on the final particle size: with increasing time and temperature the particles size of ZnO was increasing. The effect of UV irradiation during the precipitation on the ZnO nanoparticles size stayed still unclear and will be studied in near future.

5 Acknowledgements

This work was supported by the Czech Science Foundation (P107/11/1918), by the Ministry of Education, Youth and Sports of the Czech Republic in the “National Feasibility Program I”, project LO1208 “TEWEP”and by VŠB-Technical University of Ostrava (SP 2014/55). and by the Project No. CV6005531 „Support and development of international relationship and mutual foreign activities of students and staff on FMMI“, funded by VŠB – Technical University of Ostrava, Czech Republic.

References

[1] Wagner, P and Helbig, R: “Halleffekt und anisotropie der beweglichkeit der elektronen in ZnO”. In: *Journal of Physics and Chemistry of Solids* 35.3 (1974), pages 327–335.

[2] Ryu, Y., Lee, T., and White, H.: “Properties of arsenic-doped p-type ZnO grown by hybrid beam deposition”. In: *Applied Physics Letters* 83.1 (2003), pages 87–89.

[3] Kumar, S. S. et al.: “Synthesis, characterization and optical properties of zinc oxide nanoparticles”. In: *International Nano Letters* 3.1 (2013), pages 1–6.

[4] Ni, Y.-h. et al.: “Hydrothermal preparation and optical properties of ZnO nanorods”. In: *Materials Science and Engineering: B* 121.1 (2005), pages 42–47.

[5] Chang, S.-S. et al.: “Luminescence properties of Zn nanowires prepared by electrochemical etching”. In: *Materials Letters* 53.6 (2002), pages 432–436.

[6] Wang, R.-C. and Tsai, C.-C.: “Efficient synthesis of ZnO nanoparticles, nanowalls, and nanowires by thermal decomposition of zinc acetate at a low temperature”. In: *Applied Physics A* 94.2 (2009), pages 241–245.

[7] Risti´c, M. et al.: “Sol–gel synthesis and characterization of nanocrystalline ZnO powders”. In: *Journal of Alloys and Compounds* 397.1 (2005), pages L1–L4.

[8] Audebrand, N., Auffrédic, J.-P., and Louër, D.: “X-ray diffraction study of the early stages of the growth of nanoscale zinc oxide crystallites obtained from thermal decomposition of four precursors. General concepts on precursor-dependent microstructural properties”. In: *Chemistry of materials* 10.9 (1998), pages 2450–2461.

[9] Maensiri, S., Laokul, P., and Promarak, V.: “Synthesis and optical properties of nanocrystalline ZnO powders by a simple method using zinc acetate dihydrate and poly (vinyl pyrrolidone)”. In: *Journal of crystal growth* 289.1 (2006), pages 102–106.

[10] Cai, J. et al.: “Red luminescence in ZnO films prepared by a glycol-based Pechini method”. In: *Physics Letters A* 372.22 (2008), pages 4104–4108.

[11] Dejene, F. B. et al.: “Optical properties of ZnO nanoparticles synthesized by varying the sodium hydroxide to zinc acetate molar ratios using a Sol-Gel process”. In: *Central European Journal of Physics* 9.5 (2011), pages 1321–1326.

Scanning electron microscopy investigations of WC-Co coatings modified by TiC and Cr_3C_2 deposited with HVAF method

Hanna Myalska, Grzegorz Moskal
Silesian University of Technology
Institute of Materials Science, 40-019 Katowice, ul. Krasińskiego 8, Poland
E-Mail: hanna.myalska@polsl.pl

Abstract

Tungsten carbide coatings deposited with high velocity air fuel technique (HVAF) were examined. Standard WC-Co 83-17 powder was mixed with either TiC or Cr_3C_2 sub-microcrystalline powder and deposited on a steel substrate. Observation of the coatings microstructure using scanning electron microscope (SEM) revealed good homogeneity of deposited coatings.

1 Introduction

Wear is an unavoidable effect in mechanical components of power generation units construction equipment, chemical processing equipment, aircraft mobiles and automobiles. The solution for that problem is application of wear resistant alloys or suitable wear resistant coatings [1, 2].

Thermal sprayed carbide coatings are widely applied for surface modification because of their unique properties [3]. In these coatings, good bonding between the hard phases such as WC, Cr_3C_2 or TiC and a ductile metal matrix such as Co or NiCr is ensured [3, 4]. The mixture of WC-Co powders is primarily used as a hard facing coating with good wear and shock resistance up to 425 °C. At higher temperatures, WC decomposes [5], which leads to the decrease of wear resistance.

The reduction of WC grain size, to the nanometer range, has resulted in increased hardness, fracture toughness and resistance to abrasive and sliding wear of sintered WC–Co composites. The improvement of such properties is explained by the fact that as the carbide grain size decreases, the mean free path of Co matrix is reduced, which results in increased hardness according to the Hall–Petch relationship and increased fracture toughness due to a greater amount of plastic deformation with cracking [6–9].

In this paper, the influence of sub-microcrystalline additions on microstructure of WC-Co coatings deposited with thermal spraying were examined. For the HVAF method, standard WC-Co powder was used as base component. Sub-microcrystalline Cr_3C_2 and TiC powders were then added to the standard WC-Co. The aim of this study is to examine the possibility of microstructure uniformity improvement of fabricated coatings.

2 Experiment

In order to deposit WC-Co coatings with different sub-microcrystalline additions, a high velocity air fuel technique was applied. In the experiment, the standard Amperit 526.074 WC-Co powder with a composition of 83-17 and the same powder with addition of Cr_3C_2 and TiC were used respectively. The sub-microcrystalline powders were applied to modify the microstructure of standard WC-Co coating.

The WC-Co standard powder with a sub-microcrystalline carbides application, was blended in a weight ratio 95-5 before HVAF deposition. Then microstructure characterization of the obtained coatings was carried out with a HITACHI S-4200 scanning electron microscope with a 1500 and 5000 magnification. The surface distribution of elements was performed using HITACHI S-4200 equipped with energy dispersed X-ray spectroscopy (EDS, Thermo NORAN (System Seven)), with 3000 magnification.

3 Results

The microstructure characterization of the obtained coatings was conducted using scanning electron microscope and the results of observations are shown in Figure 1, Figure 2 and Figure 3.

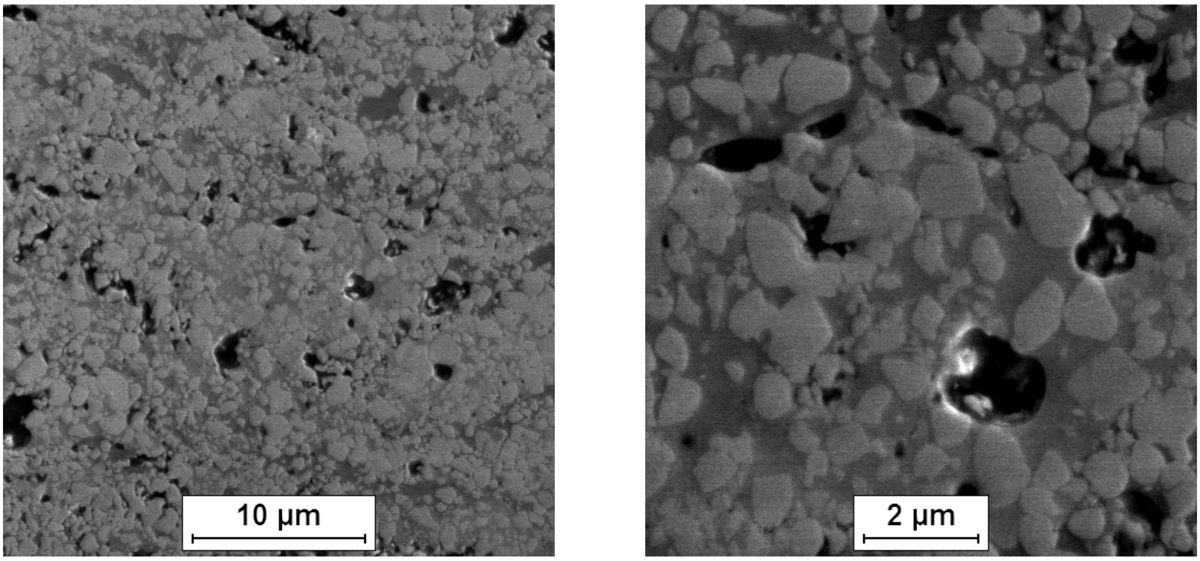

Figure 1: Microstructure of the coating deposited from WC-Co standard powder, SEM.

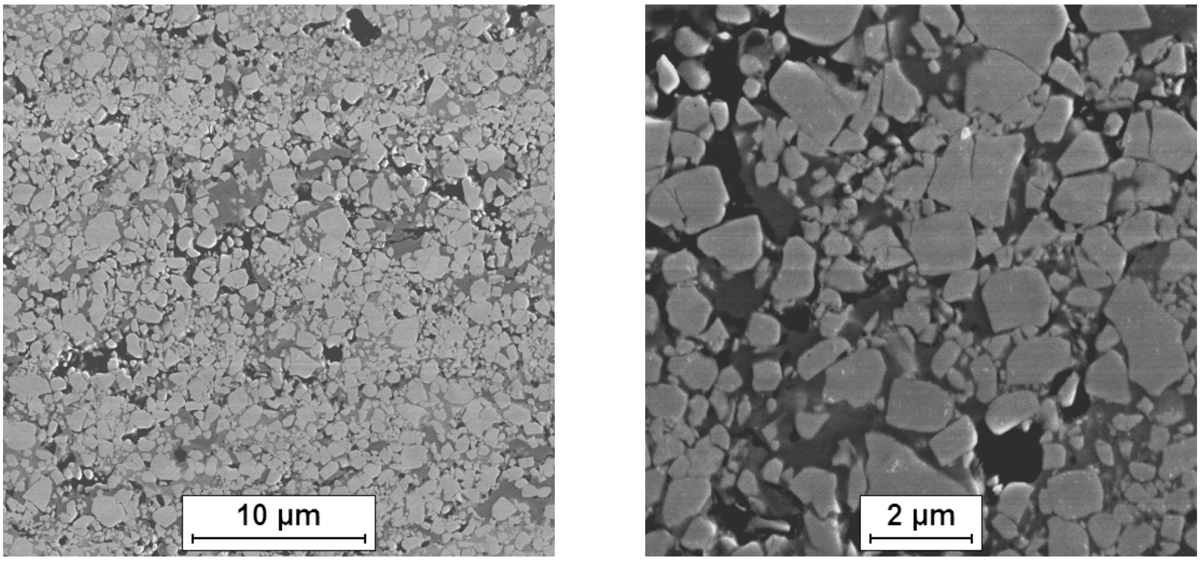

Figure 2: Microstructure of the coating deposited from a mixture of WC-Co standard powder and Cr_3C_2 powder, SEM.

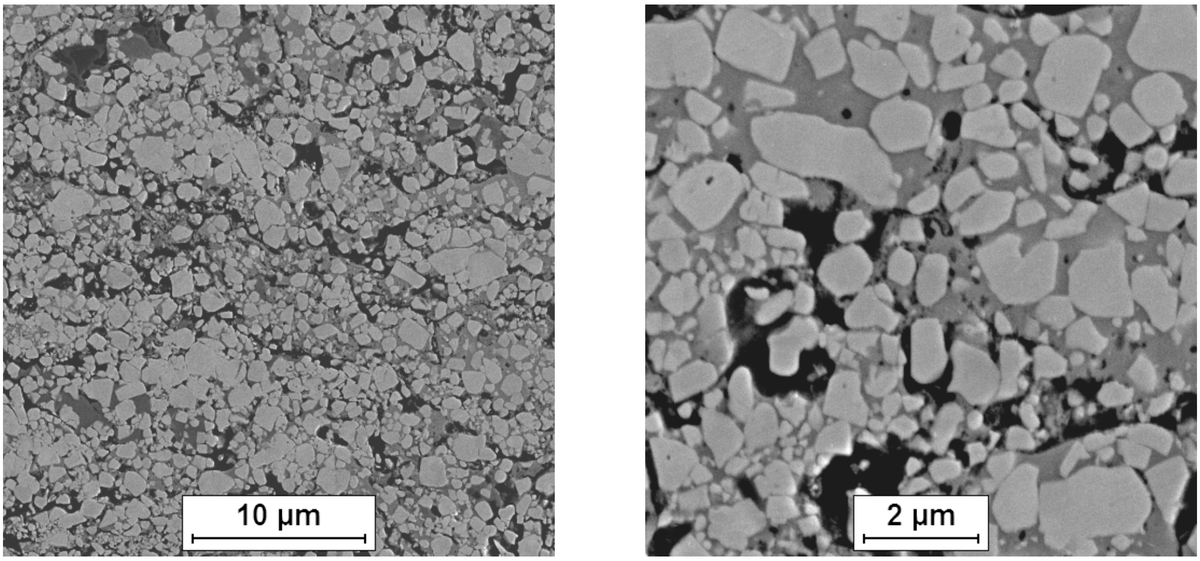

Figure 3: Microstructure of the coating deposited from a mixture of WC-Co standard powder and TiC powder, SEM.

In a coating formed from standard WC-Co powder, the diameter of cross-sectioned WC grains was less than 1.5 µm. In the case of the coating obtained from WC-Co superfine powder, the WC grains were uniformly distributed in a cobalt matrix but their boundaries were not sharp at the same magnification. In the applied magnification, using a secondary electron mode (SE), no distinct differences in microstructure of coatings deposited from mixtures of standard WC-Co powder with sub-microcrystalline additions were revealed.

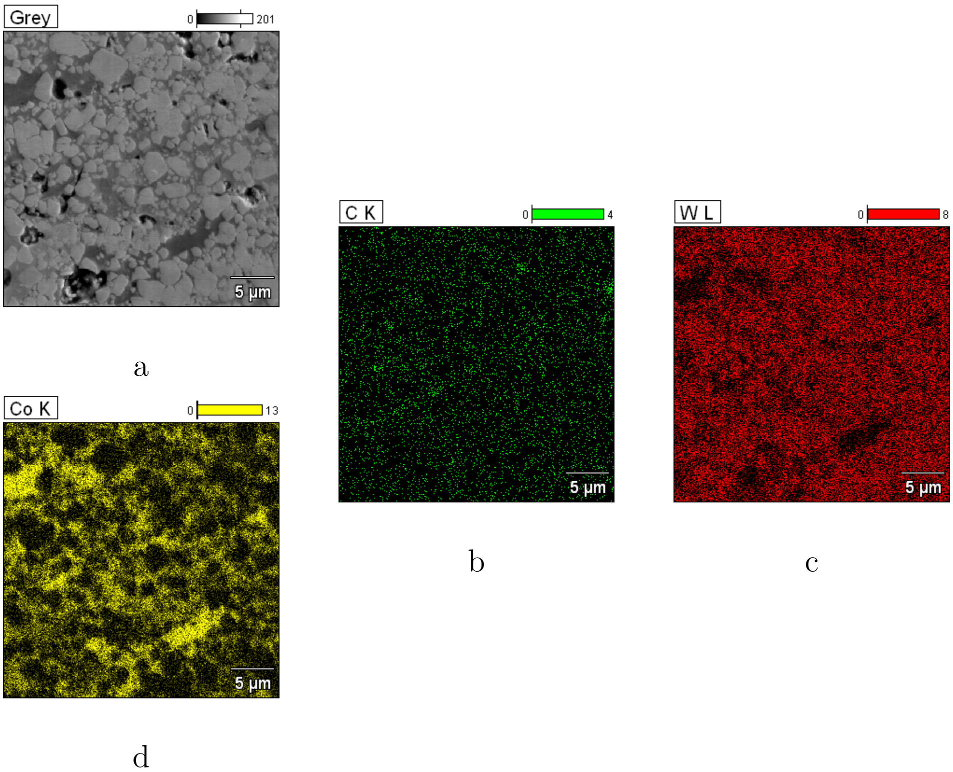

a

b

c

d

Figure 4: Mapping of (b) carbon, (c) tungsten and (d) cobalt of the coating deposited from a WC-Co standard powder, SEM, EDS.

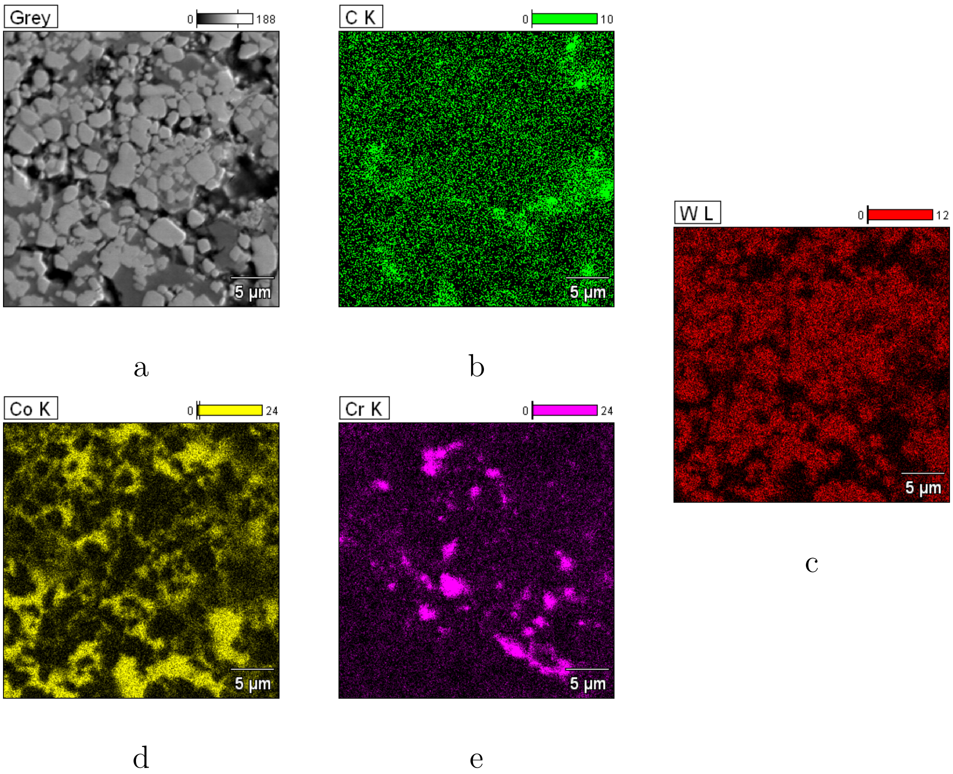

a

b

c

d

e

Figure 5: Mapping of b) carbon, c) tungsten, d) cobalt and e) chromium of the coating deposited from a mixture of WC-Co standard powder and Cr_3C_2 powder, SEM, EDS.

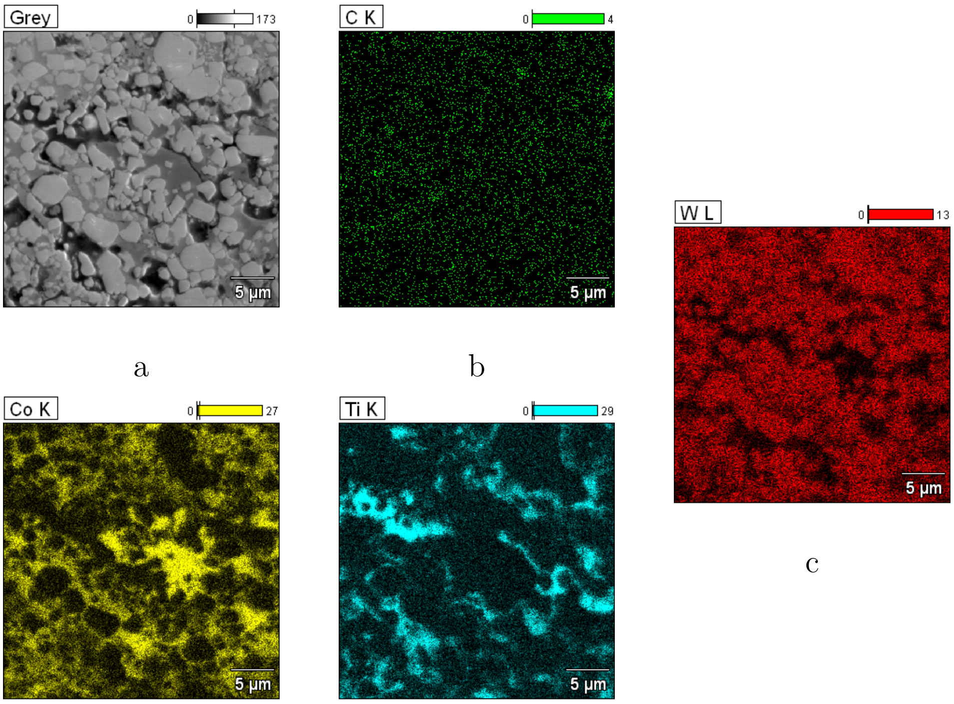

a b c d e

Figure 6: Mapping of c) carbon, c) tungsten, d) cobalt and e) titanium of the coating deposited from a mixture of WC-Co standard powder and TiC powder, SEM, EDS.

The results of selected elements mapping using EDS technique are shown in Figure 4, Figure 5 and Figure 6. Uniform distribution of carbon for all deposited coatings was revealed. Also uniform distribution of tungsten was observed for coatings deposited from standard WC-Co powder, superfine WC-Co and from the mixture of WC-Co and WC. Cobalt was present mostly in the matrix (darker grey areas). The mapping of elements revealed a presence of chromium and titanium in the coatings deposited from the mixtures of WC-Co with Cr_3C_2 and WC-Co with TiC. During the investigation the darkest areas in the SEM images shown in Figure 5 and Figure 6 occurred zones enriched with chromium or titanium. The enriched zones of titanium and chromium probably indicate diffusion of those elements into cobalt matrix. Thus, there is a high probability of a reaction, which occurred between matrix and sub-microcrystalline powders. The influence of TiC sub-microcrystalline powder on coating phase composition was confirmed in previous investigation [9].

4 Conclusions

Some results of investigations obtained for tungsten carbide coatings with sub-microcrystalline additions deposited with high velocity air fuel technique were presented. The characterization of the coatings was focused on sub-microcrystalline carbides distribution in a cobalt matrix. The general conclusions can be formed as follows:

- Carbides in WC-Co coatings deposited with high velocity air fuel technique are distributed in cobalt matrix uniformly.

- The sub-microcrystalline additions TiC and Cr_3C_2 applied in WC-Co coatings fabricated with the same technique are also located uniformly in cobalt matrix.
- EDS examinations results suggest a diffusion of titanium and chromium from sub-microcrystalline carbides into cobalt matrix and that as an additional effect may also influence on coatings properties.

References

[1] Barbezat, G.: “Advanced thermal spray technology and coating for lightweight engine blocks for the automotive industry”. In: *Surf. Coat. Technol.* 200 (2005), 1990—1993.

[2] Thakur, L. et al.: “An investigation on erosion behavior of HVOF sprayed WC–CoCr coatings”. In: *Applied Surface Science* 258 (2011), 1225—1234.

[3] Economou, S. et al.: “Processing and structure and tribological behaviour of TiC-reinforced plasma sprayed coatings”. In: *Wear* 220 (1998), pages 34–50.

[4] Fochl, J., Weissenberg, T., and Wiedermeyer, J.: “General aspects for tribological applications of hard particles coatings”. In: *Wear* 130 (1989), pages 275–288.

[5] Basa, S. N. and Sarin, V. K.: “Oxidation behaviour of WC-Co”. In: *Materials Science and Engineering* A 209 (1996), pages 206–212.

[6] Exner, H. E.: “Physical and chemical nature of cemented carbides”. In: *Int. Met. Rev.* 4 (1979), pages 149–173.

[7] Jianhong, H. et al. In: *Metall. Mater. Trans.* A 31 (2000), 541—553.

[8] Jia, K. and Fischer, T. In: *Wear* 203–204 (1997), 310—318.

[9] H.Myalska, Moskal, G., and Szymański, K.: “Microstructure and properties of WC-Co coatings and modified by sub-microcrystalline carbides and obtained by different methods of high velocity spray process”. In: *Surf. Coat. Technol.* 7 (2014). DOI: 10.1016/j.surfcoat.2014.07.097.

Process chain for new steel grades – from semifinished product precision steel tube to hydroforming: Potentials for automotive light weight construction for chassis and car body

Freytag, P.[1]; Bartschat, P.[1]; Otto, M. [2]; Kessler, N.[3]; Maiwald, T.[4]; Wiebe, J.[5]
[1]Salzgitter Hydroforming GmbH & Co. KG, [2,5] Salzgitter Mannesmann Forschung GmbH, [3] Salzgitter Mannesmann Precision GmbH, [4] Salzgitter Flachstahl GmbH
[1]Gewerbering 26a, 08451 Crimmitschau, Germany; [2] Eisenhuettenstrasse 99, 38239 Salzgitter, Germany; [3] Wiesenstrasse 36, 45473 Mülheim/Ruhr, Germany; [4] Eisenhuettenstrasse 99, 38239 Salzgitter, Germany; [5] Ehinger Strasse 200, 47259 Duisburg

Keywords: HSD®-steel, TWIP, density reduced, HFI-tube

1 Introduction

High manganese austenitic steel grades, e.g. HSD®-steel from Salzgitter AG, are the consequent solution for new light weight steels in the automotive industry. The combination of high strength and high elongation is the major motivation for new developments in all kinds of automobile applications. The full light-weight potential of these steels can be achieved due to the consistent combination of improved design, high performance manufacturing methods, the usage of well known techniques combining improved mechanical properties and enhanced part geometries with high sophisticated forming methods to achieve the optimum in weight, performance, and pricing. One of these feasible production methods is the manufacturing method of hydroforming, which integrates the possible aims of design freedom, the accuracy and stiffness of precision tubes with the high strength of HSD®-steel, which is strong enough to replace even press hardened body parts when using the hydroforming process. This article will give an overview regarding the first fundamental results on a hydroformed HSD®-steel tube, which was produced for the first time. Furthermore, additional up- and downstream processes in the production of light-weight components made of these steels will be considered. The results show the full potential of the combination of HSD®-steel with the optimal manufacturing method for an example of a redesigned test component with characteristics of chassis and body structures, with specific challenges to the achievable geometry based on hydroforming and HSD®-steel. In addition the article will give prospects for future fields of research and development, as well as, possible series application of hydroformed precision tubes made of HSD®-steel.

2 HSD®-steel

The HSD®-steel is characterized by its high strength and high formability (Table 1), this combination ranks the material well above the properties achieved by those of carbon steels. The higher levels of Si and Al ensure optimum mechanical and technological properties and reduces the material's density, where a typical level for HSD®-steel is $7.4\,\mathrm{g\,cm^{-3}}$ at room temperature.

Table 1: Mechanical properties of the strip, overview.

	HSD®-steel
Yield strength [MPa]	620
Tensile strength [MPa]	1000
Total elongation A_{80} [%]	50
Youngs-modulus [GPa]	180
n-value [-]	0.36
r-value [-]	1.0
ρ [g/cm^3]	7.4

A stress-strain curve (Figure 1) of the HSD®-steel is compared with a cold-rolled high strength dual phase steel HCT780XD and a micro alloyed HC340LAD. Within an HSD®-steel the high strength level of a dual phase steel can be combined with a high elongation, which is comparable to a soft deep drawing steel.

Due to the TWIP effect, which combines high strain hardening and high elongation, the strength of the material can easily be increased by an additional cold-rolling step, achieving a material that combines yield strength of 900 MPa with a tensile strength of 1150 MPa and a total elongation of > 30 %. Customer requirements can, therefore, be easily accommodated with HSD®-steels with a suitable combination of heat treatment and cold rolling during the steel manufacturing process.

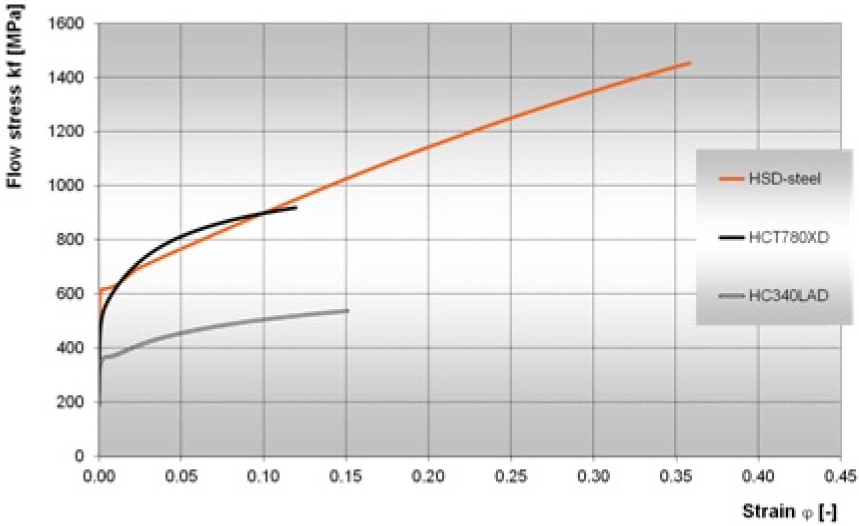

Figure 1: Stress-strain curves of HSD®-steels compared to conventional steel grades.

3 Precision steel tube manufacturing for HSD®-steels

The production of precision seamless and welded steel tubes is the core competence of Salzgitter Mannesmann Precision GmbH (SMP) established over more than 100 years according to international standards in particular of EN 10305. This comprises seamless cold-drawn tubes (EN 10305-1), welded cold-drawn tubes (EN 10305-2), and welded cold-sized tubes (EN 10305-3) [1–3].

HSD®-steel precision tubes are produced using the process route for welded cold-drawn tubes: coils of steel strips are continuously roll-formed to an open tube and subsequently passed through a ring inductor which induces high-frequency current in the open tube. The induced current completes its path around the formed strip by flowing along the edges and crowding around the apex of the gap between them. This heats up the open tube rapidly, raising the strip edges to welding temperature as they arrive at the apex. Pressure rolls force the heated edges together, completing the weld. (Figure 2). The welding bead which is formed on the inside and outside of the tube during the upsetting process are subsequently removed by planing. The high frequency induction (HFI) welding process is characterized by its high productivity and profitability compared to other welding processes.

A further core process in manufacturing of a precision steel tube is the cold-drawing process. Cold-drawing is forming under a combination of tensile and compressive conditions according to DIN 8584 [5]. Here the precision tubes are formed by means of a drawing mandrel and drawing die. These precision steel tubes fulfill higher requirements concerning the homogeneity of the microstructure, manufacturing tolerances, and size accuracy compared to welded cold-sized tubes. Furthermore, with the help of a cold-drawing process it is also possible to enhance the mechanical properties within a material-depending range. Figure 3 shows the manufacturing process for welded precision tubes as a short overview in order to highlight the core processes.

Welded cold-drawn precision steel tubes made of HSD®-steel were produced for the first time within an internal research and development project. The goals were to evaluate the

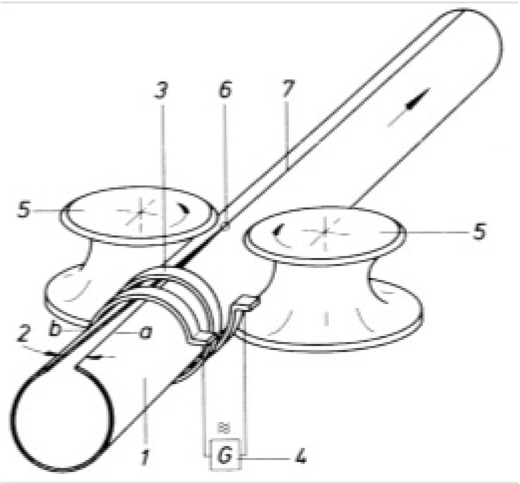

Figure 2: Inductive HFI welding [4]. 1: Open tube; 2: Convergence angle; 3: Ring inductor; 4: Welding generator; 5: Pressure rolls; 6: Weld point; 7: Longitudinal weld.

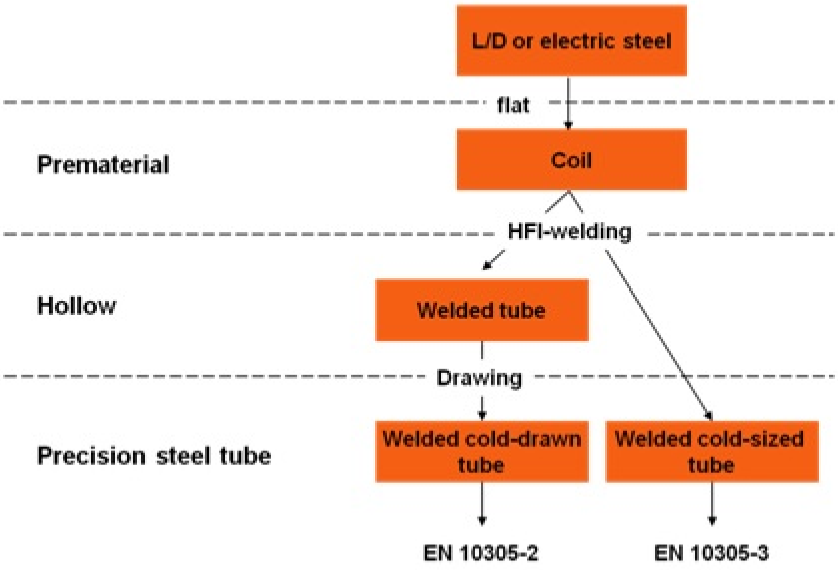

Figure 3: Simplified manufacturing stages for welded precision steel tubes.

HFI weldability and the producibilty of such tubes having an austenitic microstructure, during all manufacturing stages. Figure 4 points out the reached mechanical properties after the production route (welding, cold-drawing and heat-treatment). In the diagram the most tube-depending mechanical properties are presented after tensile testing (at room temperature according to ISO 6892-1 [6]). The achieved mechanical properties of this precision tube are promising for applications, which need high strength combined with a high ductility. First results from the initial tubes show values of the tensile strength of about 950 MPa with a very high total elongation of $A_5 = 60$ % for the base material.

Furthermore, additional tests were needed to estimate the whole tube potential. Therefore, tests such as drift-expanding tests and flattening tests, according to ISO 8493 and ISO 8492 were carried out for tube characterization [7, 8]. The values of the drift-expanding test show that the maximum expanding of the outside diameter is between Du/Da = 25.5 - 33.6 %. For comparison the value of a normalized tube made of E 355 is

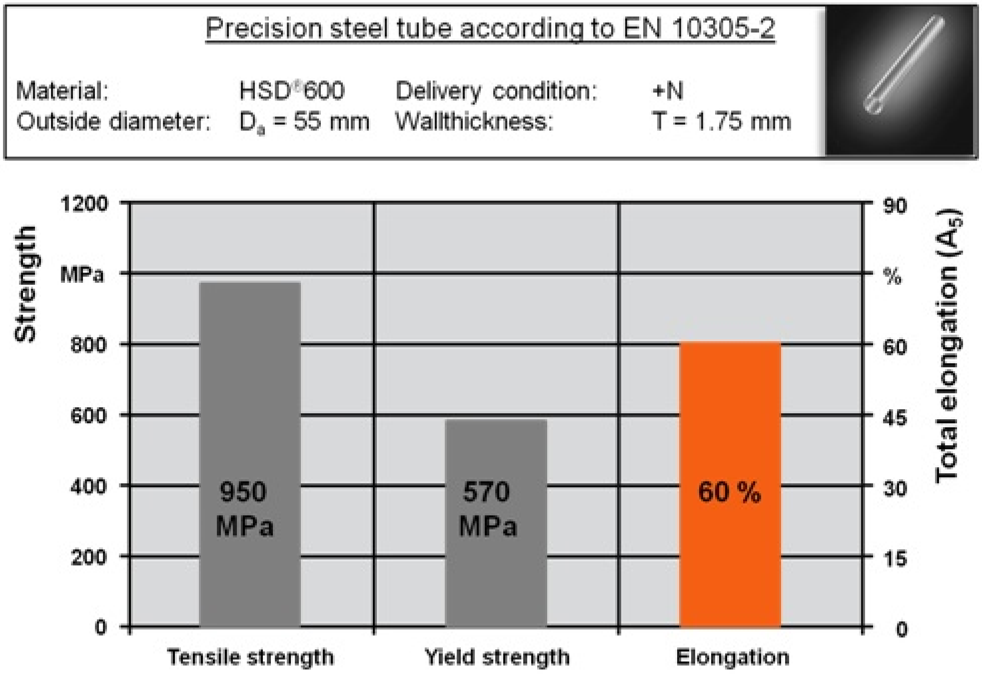

Figure 4: Mechanical properties of a welded cold-drawn HSD®600 precision tube.

Du/Da = 15 % according to standards [2]. The flattening test was also carried out on a tube. The longitudinal weld was tested in 12 and 3 o´clock position [8]. The results are shown in Figure 5. In 12 o´clock position the tube was completely flattened without any cracks. However, in 3 o´clock position, first crack initiations occurred during complete flattening. The properties of the weld seam are different compared to the base material. Hence, current investigations are focused on the improvement of these properties.

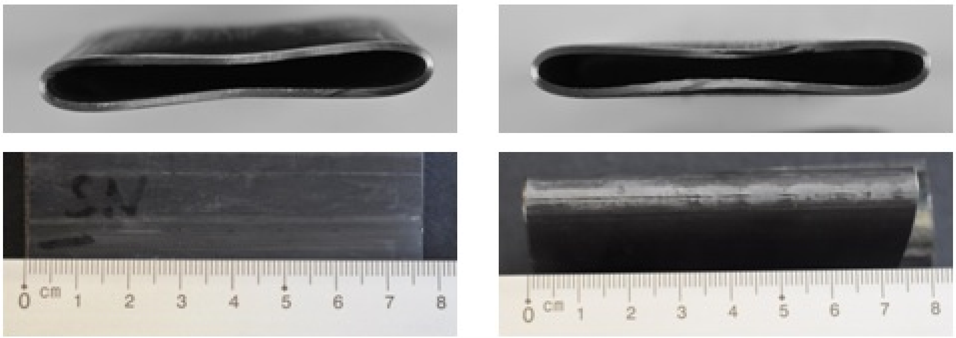
Weld in 12 o´clock position

Weld in 3 o´clock position

Figure 5: Photographs of a welded cold-drawn HSD®600 precision tube after flattening.

4 HSD®-tube – application hydroforming

During the past years, hydroforming has not only established itself as an outstanding and irreplaceable forming method in many industrial markets but has constantly evolved into its most important field of application – the automotive industry.

Considering fluid or gas conducting components, there are plenty applications in exhaust and EGR cooler systems. Due to decreasing available space in the engine compartment and other locations in the car, the complex shapes of hydroforming parts; in addition to their mono-shell design are highly appreciated for exhaust systems. Other advantages are their high accuracy, very good fatigue behavior even under high temperatures, and low weight.

For climate and heat system applications, the parts contribute with their ability of function integration – hence increased efficiency, as well as, extraordinary narrow bending radii.

The focus of this article, however, is another important application for hydroformed parts. Discussing properties, such as, stiffness and high strength in connection with variable cross-sections, it becomes obvious that hydroformed parts are optimally suitable for designing structural components. Whether, they are used for chassis components or car body parts (Figure 6), the advantages are numerous. Compared to conventionally formed parts they stand out with their high accuracy – facilitating joining operations – and with the high stiffness due to the closed cross-section. Even aluminum multi-chamber profiles are hydroformed for this reason.

Nevertheless, the biggest share of hydroformed parts is made from steel, whereas, the use of this material offers even higher potentials. The work-hardening effect created by hydroforming is outstanding in its dimension and wholly applied all over the component. Using this potential increases crash performance and reduces weight significantly. What could be more obvious than combining this effect with new innovative materials to further exceed all properties of this kind of components known today?

Inlet cones catalytic Cross-beams – chassis A-pillar – convertible car

Figure 6: Series components (from left: exhaust components, chassis parts, car body part).

The potential of HSD®-steel reaching a noteworthy degree of widening >50 % offers the chance for variable cross-sections and the integration of complex forms and connecting elements into the part. At the same time, the trials aim for reaching strength of more than 1200 MPa. Even more, this property could be reached by cold forming without including any heat treatment or annealing process. Even though, these goals have been proofed to be reachable in theory and in a few first attempts, there are still some challenges to overcome. The welding seam, for example, turned out to be a weak point since it has different properties than the base material. However, by optimal positioning of the welding seam this is a solvable task, which is already handled within hydroforming operations today.

It becomes clear that in terms of light-weight design this group of HSD®-steel grades has excellent potential for a new generation of structural components. Making the advantages even more concrete, the Salzgitter Group has developed a demonstrator component which gives an insight into the possibilities with hydroformed HSD®-tubes.

This demonstrator combines different metal forming challenges such as a square shape with small edge radii, at one tube end, and an extraordinary high expansion at the other tube end. Furthermore, it includes two different form elements that require an especially high degree of partial material stretching. For the first time, by-form elements can be produced with such a distinctive shape that offers ideal conditions for slipping over connecting parts, positioning them and enables optimal preparation for welding.

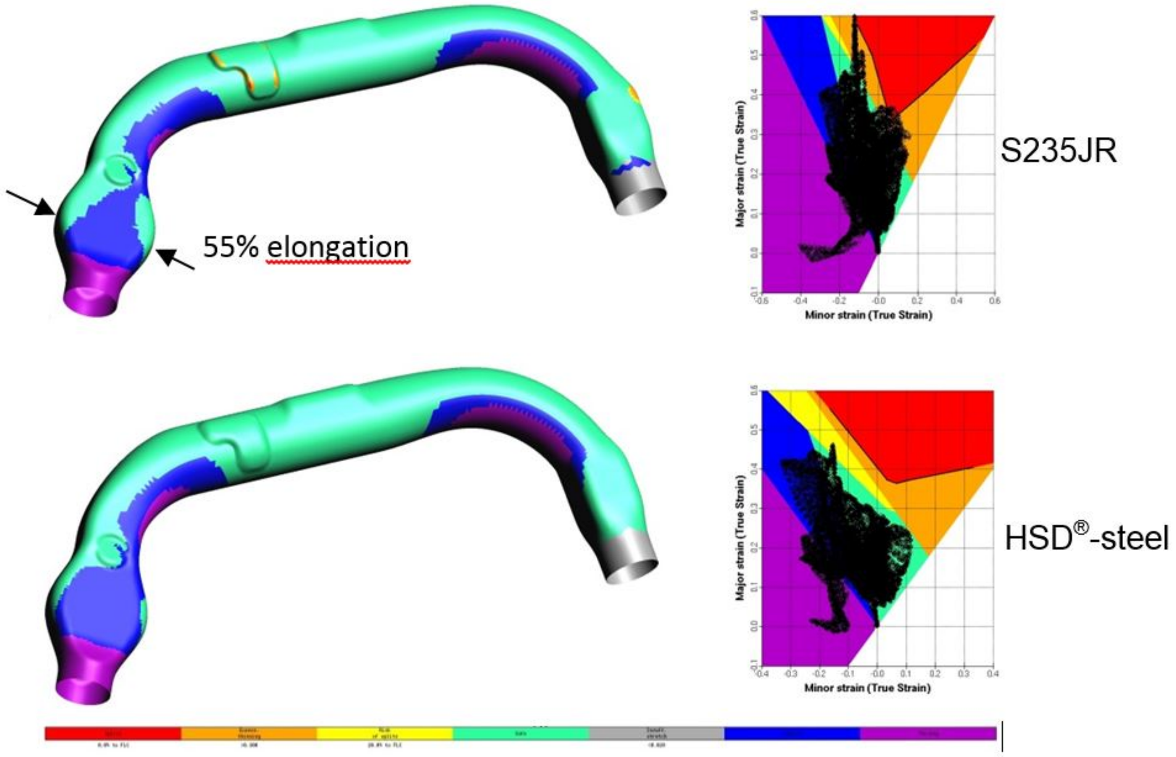

Figure 7: Forming behavior of a hydroformed HSD®-component compared to mild steel.

The cross-section analysis shows a maximum elongation of 55 %, Figure 7. The work-hardening effect has its maximum, of course, in the same area. The forming simulation shows a strength of up to 1400 MPa locally. In most areas of the part (that receive a sufficient amount of stretching) the strength hardly drops below 1000 MPa.

For a better understanding of the real HSD®-steel benefits, a direct comparison with conventional mild steel is helpful. Choosing a very good formable mild steel grade, e.g. S235JR, the FEM simulation shows that even its forming behavior is worse compared with the HSD®-steel, Figure 7.

At the same time the HSD®-steel reaches a strength exceeding the mild steel's by nearly a factor 3, Figure 8.

Taking into account that these figures are valid for a closed profile, which has a stiffness and (torsion) resistance many times higher than an open profile and considering that no

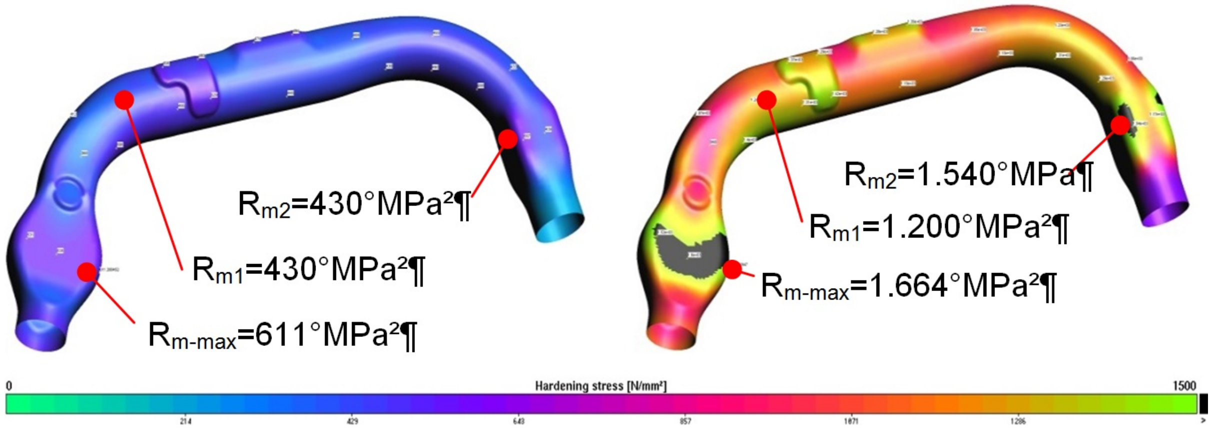

Figure 8: Work hardening by hydroforming (left: S235JR, right: HSD®600).

heat-treatment is needed, the full potential of this combination becomes obvious.

5 Conclusions

Within the Salzgitter Group a possible application of a new Fe-Mn-Al-Si-steel was evaluated in a cooperation of the R&D-department, the steel production, the tube manufacturing and the hydroforming experts.

As shown in this article the good mechanical-technological properties of the HSD®-steel could be transferred to an HFI-welded HSD®-tube with tensile strength values of approx. TS (R_m) of 950 MPa and a total elongation TE (A_5) of 60 %. Using such a semi-finished product, for the hydroforming process, enables the engineers in the automotive industry to increase component performance. As an example of the possibilities of the component performance, the reachable component strength was evaluated within a finite element analysis of a demonstrator component. As shown in this analysis component strength of over 1500 MPa is reachable with sufficient ductility remaining. Detailed results on real parts are planned for the oral presentation.

References

[1] *DIN EN 10305-1: Steel tubes for precision applications – Technical delivery conditions. Part 1: Seamless cold drawn tubes.* Beuth Verlag, Berlin. 2010.

[2] *DIN EN 10305-2: Steel tubes for precision applications – Technical delivery conditions. Part 2: Welded cold drawn tubes.* Beuth Verlag, Berlin. 2010.

[3] *DIN EN 10305-3: Steel tubes for precision applications – Technical delivery conditions. Part 3: Welded cold sized tubes.* Beuth Verlag, Berlin. 2010.

[4] Brensing, K.-H. and Sommer, B.: "Herstellverfahren für Rohre". In: *Broschüre der Mannesmann Röhrenwerke* ().

[5] *DIN 8584: Fertigungsverfahren Zugdruckumformen.* Beuth Verlag, Berlin. 1971.

[6] *DIN EN ISO 6892-1: Metallic materials – tensile testing – Part 1: Method of a test at room temperature.* Beuth Verlag, Berlin. 2009.

[7] *DIN EN ISO 8493: Metallic materials – tube – drift expanding test.* Beuth Verlag, Berlin. 2004.

[8] *DIN EN ISO 8492: Metallic materials – tube – flattening test.* Beuth Verlag, Berlin. 2004.

The modeling of composite materials reinforced with glassy carbon or silicon carbide wear mechanisms based on fem methods

Krzysztof Windyś, Bartosz Hekner
Silesian University of Technology
Faculty of Materials Engineering and Metallurgy, Krasińskiego 8 STR, 40-019 Katowice, Poland
Windys.krzysztof@gmail.com, bartosz.hekner@polsl.pl

This article would bring near results of testing composites which matrix is aluminum alloy and reinforcement particles are glassy carbon and silicon carbide including different shapes of them. Program Solidworks was used to create simplified composite compound of cuboid matrix and cubic or spherical reinforcement particles. Further analysis were made using Algorframe program by which friction characteristics were tested. In future it is planned to create more specified models where reinforcement particles would be closer to real structure of materials and models including more particles simulating whole material.

Keywords: Composites, FEM, glassy carbon, wear, friction, aluminum matrix

1 Introduction

Nowadays of quick development of computer science it is possible to use compute methods to reduce costs of manufacturing new elements and materials. Application of FEM (Finite element method) allows to research innovative materials without need to create them by making virtual models which reflects their actual working conditions and wear mechanisms. Models presented in this article would be tested on friction resistance. It is going to be proved that silicon carbide particles in flexible aluminum matrix would be snatched from matrix and that glassy carbon particles would be sheared. [1]

2 Assumptions

To all analyzed models were set strength in value of 10 MPa affecting straight to top surface and tangent strength in value of 4 MPa affecting with 'Y' axis. As it was mentioned in introduction matrix of tested composite was aluminum alloy which characteristics appear in Figure 1 and reinforcement particles were made of silicon carbide and glassy carbon which characteristics figure below in Figure 2 and Figure 3. Data of materials has been taken from Algorframe program database however data of glassy carbon has been taken from literature [2]. Size and spacing of particles in analyzed models is described on Figure 4 and Figure 5 dimensions have been given in millimeters.

Stresses appeared after simulation has been described by the Huber- von Mises's scale.

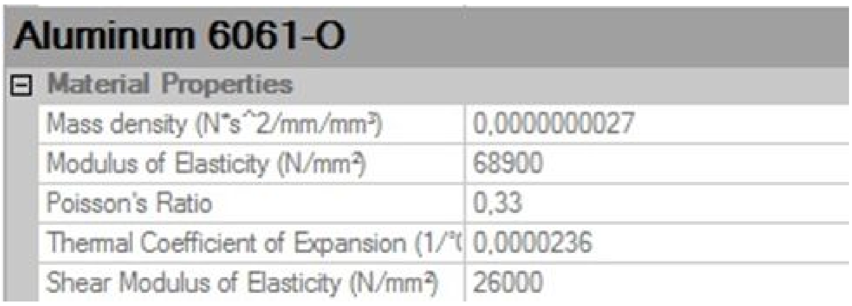

Aluminum 6061-O

⊟ **Material Properties**

Mass density (N*s^2/mm/mm^3)	0,0000000027
Modulus of Elasticity (N/mm^2)	68900
Poisson's Ratio	0,33
Thermal Coefficient of Expansion (1/°	0,0000236
Shear Modulus of Elasticity (N/mm^2)	26000

Figure 1: Characteristics of Aluminum alloy used as matrix.

Glassy Carbon

⊟ **Material Properties**

Mass density (N*s^2/mm/mm^3)	0,0000000011
Modulus of Elasticity (N/mm^2)	30000
Poisson's Ratio	0,2
Thermal Coefficient of Expansion (1/°	0
Shear Modulus of Elasticity (N/mm^2)	0

Figure 2: Characteristics of Glassy Carbon used as reinforcement particle.

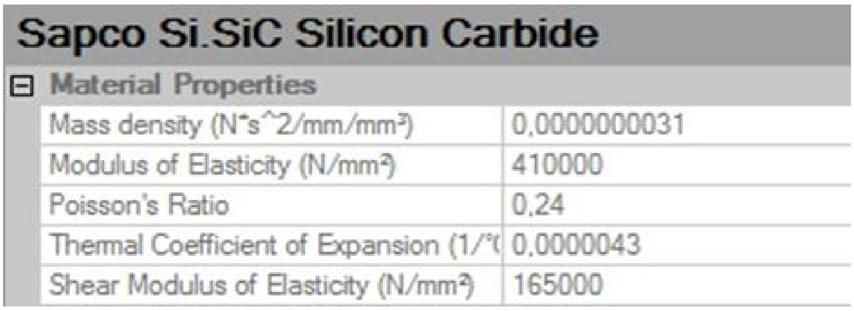

Sapco Si.SiC Silicon Carbide

⊟ **Material Properties**

Mass density (N*s^2/mm/mm^3)	0,0000000031
Modulus of Elasticity (N/mm^2)	410000
Poisson's Ratio	0,24
Thermal Coefficient of Expansion (1/°	0,0000043
Shear Modulus of Elasticity (N/mm^2)	165000

Figure 3: Characteristics of Silicon Carbide used as reinforcement particle.

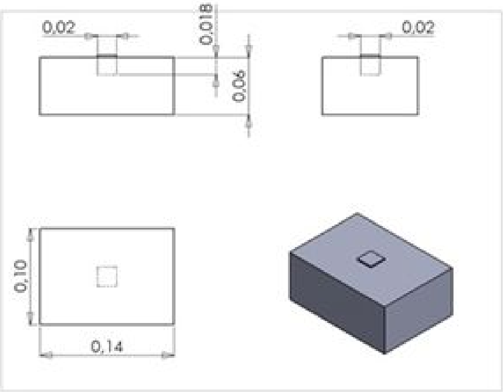

Figure 4: Dimension of the model with cubic particle.

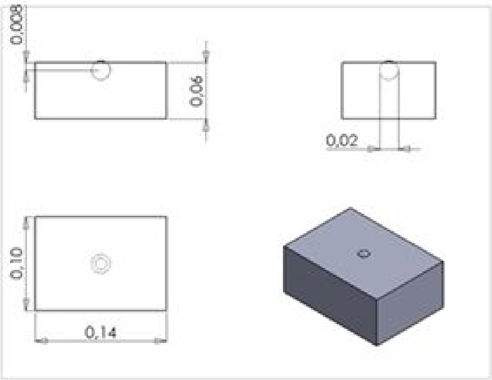

Figure 5: Dimension of model with spherical particle.

3 Analysis

After exporting models from Solidworks to Algorframe it was needed to generate net on models to perform simulations. Net creates benchmarks which allows to calculate stress and deformation. Figure 6 and Figure 7 shows models before and after procedure of generating net.

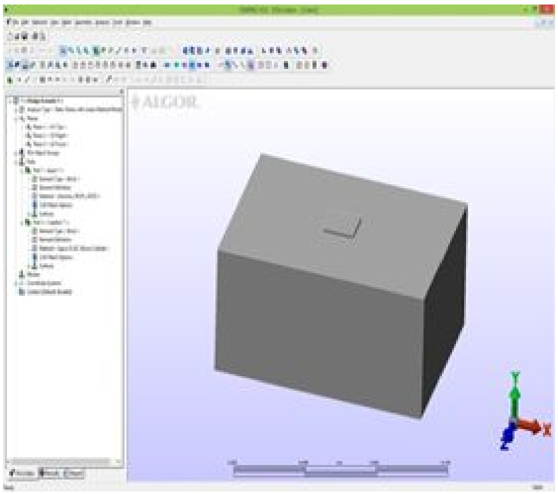

Figure 6: Model without generated net.

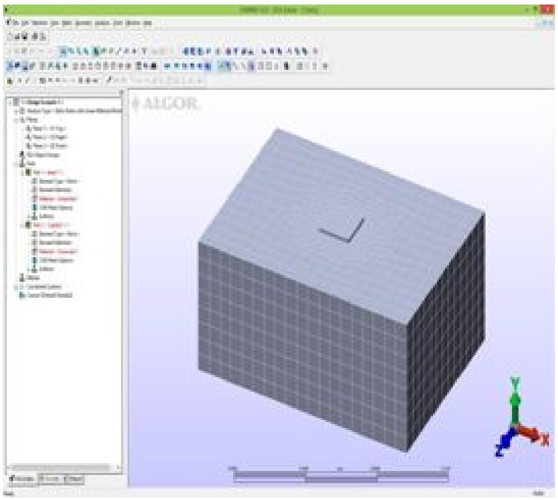

Figure 7: Model with generated net.

Model was fixed at bottom surface in ‘X’ and ‘Y’ axis and at front surface in ‘Z’ axis. It is important because material would not deform itself.

Analysis of created models in relation to shear strength:

3.1 Stress analysis at model with aluminum matrix and cubic silicon carbide particle

Model has been charged with forces which resultant show vectors at the Figure 8.

By increasing transparency of matrix it is possible to state that the biggest stress appear in the bottom part of reinforcement particle after impact of forces (Figure 9).

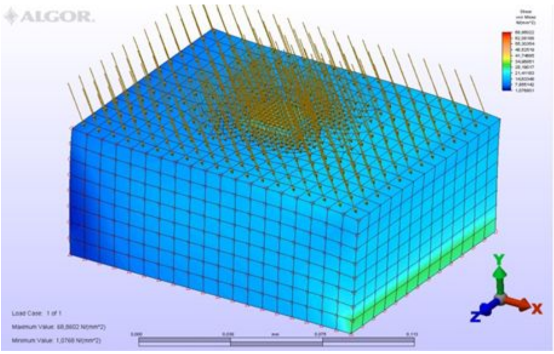

Figure 8: The impact of forces resultant.

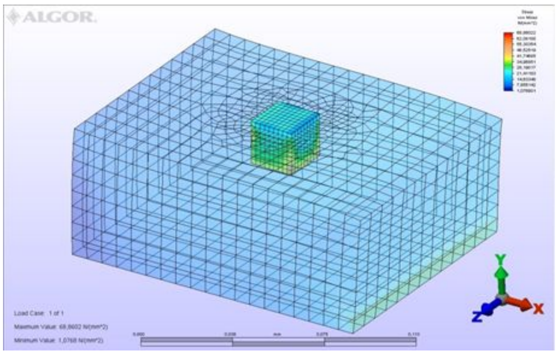

Figure 9: Stress appearing in the reinforcement particle inside transparent matrix.

In cubic reinforcement particle of silicon carbide maximal stress in this scheme is 68,9 MPa and minimal 7,6 MPa. Change of color palette in Figure 10 describe stress deployment.

In this model reinforcement particle takes the charges instead of matrix and also inside of it is the biggest stress (Figure 11). It is possible that the composite is going to be destroy as a result of snatching particle from the matrix.

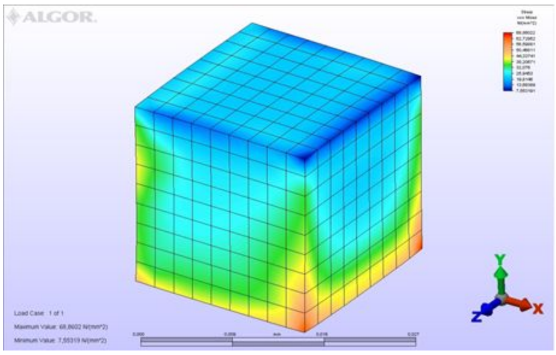

Figure 10: Stress deployment in particle.

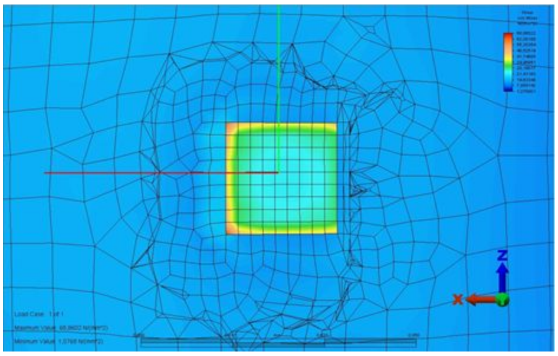

Figure 11: Stress in model from the 'XZ' surface view.

3.2 Stress analysis at model with aluminum matrix and cubic glassy carbon particle

Model has been charged with forces which resultant show vectors at the Figure 12.

By increasing transparency of matrix it is possible to state that after impact of forces the biggest stress appear in the part of reinforcement particle protruding over matrix (Figure 13).

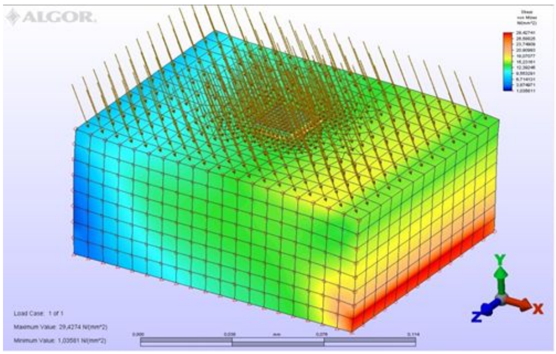

Figure 12: The impact of forces resultant.

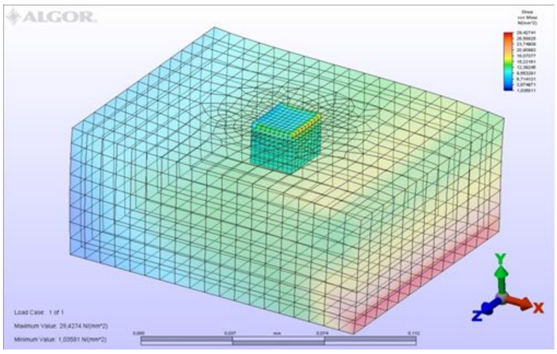

Figure 13: Stress appearing in the reinforcement particle inside transparent matrix.

In cubic reinforcement particle of glassy carbon maximal stress in this scheme is 19,1 MPa and minimal 5,1MPa. Change of color palette in Figure 14 describe stress deployment.

In this model charges are mainly take by matrix. Analyzing deployment of stress in this scheme particle would probably shear. Because of that maximal model stress value do not exceed 29,4 MPa (Figure 14).

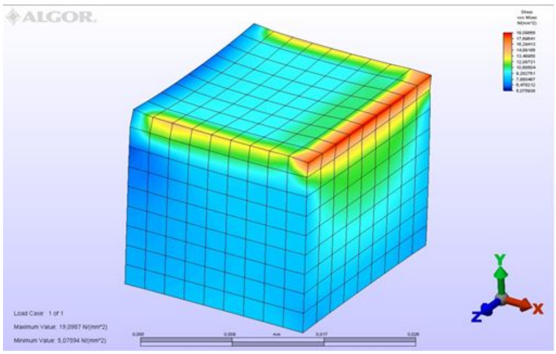

Figure 14: Stress deployment in particle.

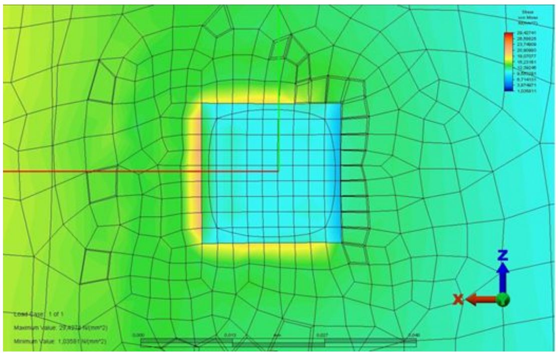

Figure 15: Stress in model from the 'XZ' surface view.

3.3 Stress analysis at model with aluminum matrix and spherical silicon carbide particle

Model has been charged with forces which resultant show vectors at the Figure 16.

By increasing transparency of matrix it is possible to state that the biggest stress appear in circumference of reinforcement particle after impact of forces (Figure 17).

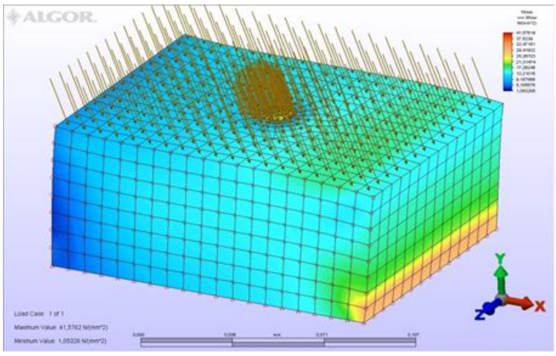

Figure 16: The impact of forces resultant.

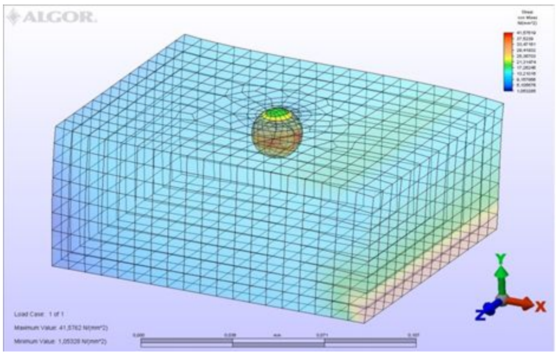

Figure 17: Stress appearing in the reinforcement particle inside transparent matrix.

In spherical reinforcement particle of silicon carbide maximal stress in this scheme is 41,6 MPa and minimal 17,4 MPa. Change of color palette in Figure 18 describe stress deployment.

In this model reinforcement particle takes the charges instead of matrix and also inside of it is the biggest stress (Figure 19). It is possible that the composite is going to be destroy as a result of snatching particle from the matrix.

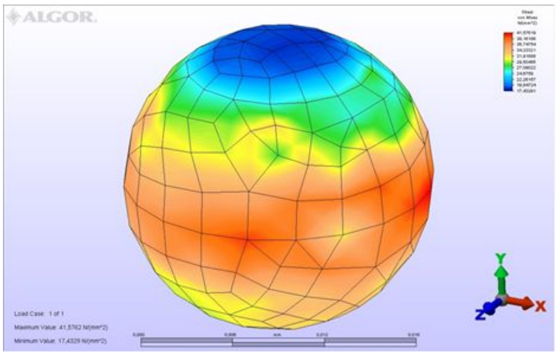

Figure 18: Stress deployment in particle.

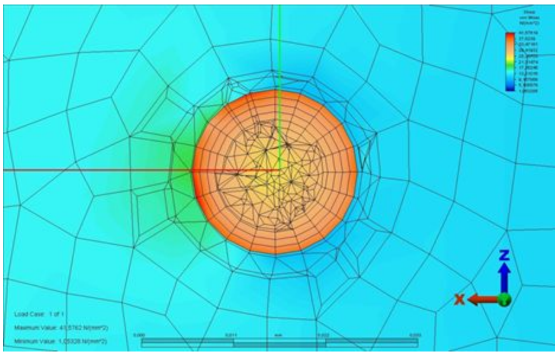

Figure 19: Stress in model from the 'XZ' surface view.

3.4 Stress analysis at model with aluminum matrix and spherical glassy carbon particle

Model has been charged with forces which resultant show vectors at the Figure 20.

By increasing transparency of matrix it is possible to state that after impact of forces the biggest stress appear in the part of reinforcement particle protruding over matrix (Figure 21).

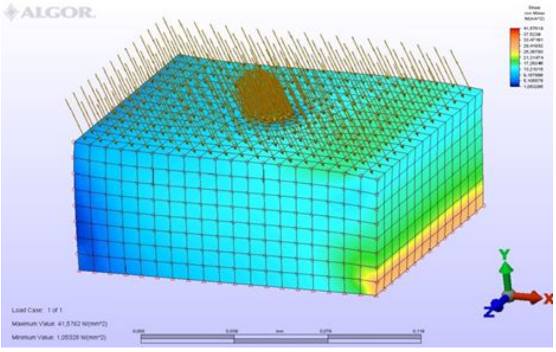

Figure 20: The impact of forces resultant.

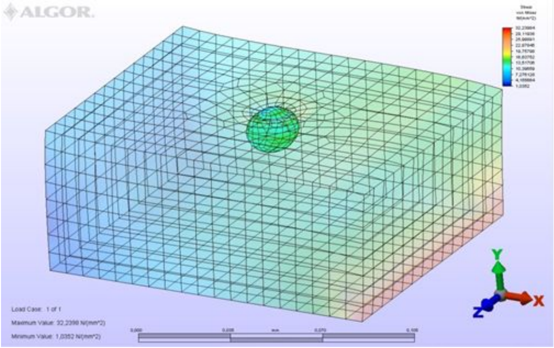

Figure 21: Stress appearing in the reinforcement particle inside transparent matrix.

In spherical reinforcement particle of glassy carbon maximal stress in this scheme is 16,9 MPa and minimal 6,7 MPa. Change of color palette in Figure 22 describe stress deployment.

In this model charges are mainly take by matrix. Analyzing deployment of stress in this scheme particle would probably shear. Because of that maximal model stress value do not exceed 32,2 MPa (Figure 23).

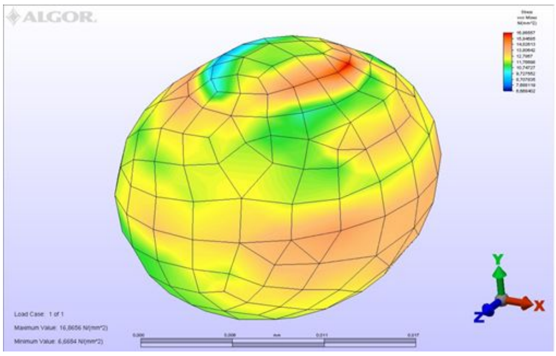

Figure 22: Stress deployment in particle.

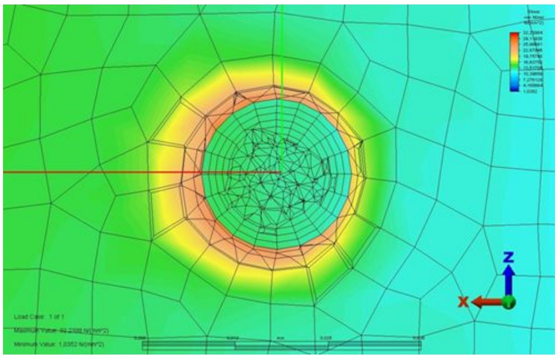

Figure 23: Stress in model from the 'XZ' surface view.

4 Conclusions

Analysis of results of simulation brings to conclusions that:

- Reinforcement particles made of silicon carbide take charges and would be destroyed by snatching through the matrix,
- Reinforcement particles made of glassy carbon reduce stress in matrix and are getting destroyed in top layers by shear,
- Usage of spherical reinforcement particle made of silicon carbide reduce stress in matrix in compare to cubic particle made of same material,
- Usage of spherical reinforcement particle made of glassy carbon increase stress in matrix in compare to silicon carbide particle
- The highest stress appears in scheme reinforced with cubic silicon carbide particles at value 68,9 MPa
- The lowest stress appears in scheme reinforced with cubic glassy carbon particles at value 29,4 MPa, however they are found in edge part of matrix what leads to suggestion that for this scheme the lowest stress appear in particle in value 19,1 MPa

Analysis was simplified because models did not include interphase boundary. In it is planned to expire simulations by modeling particles including real structures of materials, interphase boundary and creating models with more than one reinforcement particle.

References

[1] "Tribological properties of heterophase composites with an aluminium matrix". In: *Journal of Achievements in Materials and Manufacturing Engineering* 15 (2006), pages 53–57.

[2] Myalski, J., Wieczorek, J., and Płachta, A.: "Physical and mechanical properties of composites with aluminium alloy matrix designed for metal forming". In: *Solid State Phenom* 212 (2014), pages 59–62.

High Strength Forging Steels for Energy Efficient Process Chains

Hans Henning Dickert*, Jens Gervelmeyer, Oliver Rösch
Steel Application Development, Georgsmarienhütte GmbH
Neue Hüttenstraße 1, 49124 Georgsmarienhütte

1 Introduction

Steel research and materials optimisation today is strongly driven by energy efficiency and the reduction of CO_2 emissions. Within the Automobile Industry multiple light weight design approaches are used to reduce the total weight of the car and increase the fuel efficiency. This can be done by applying new vehicle concepts, structural design of single parts or alternative manufacturing technologies e.g. tailor welded blanks or tailor rolled products.

More important for the steel industry is the use of alternative high strength steels to reduce cross sections and realize the downsizing of components. Especially for highly loaded components within the engine or the power train forged steel offer highest strength levels to moderate costs.

Aim of the current steel development is to provide steels with superior toughness and highest strength with respect to static as well as dynamic loads. One way to provide the required mechanical properties are the Quenching & Tempering (Q&T) steels. The disadvantage of this steel group is their long processing chain which is very time, cost and energy intensive.

Therefore steel grades are developed that offer comparable mechanical properties as Q&T steels but without further heat treatment after forging. To realize such energy efficient process chains precipitation hardened ferritic pearlitic (PHFP) as well as bainitic steel grades can be applied.

2 Steel Concepts

The commonly used forging steels for automotive applications are on the one hand the precipitation hardening ferritic-pearlitic steels (PHFP-steel) and on the other hand the quenched and tempered (Q&T) forging steels. In order to obtain similar strength properties in ferritic-pearlitic precipitation hardening steels than in Q&T steels, the microstructure and the mechanical properties of these steels are controlled by adding further microalloying elements (V, Nb and Ti), which have a significant influence in the precipitation strengthening and the grain size control [2]. The advantages of these newly developed PHFP-M steels over Q&T steels are the elimination of an additional heat treatment step which includes a hardening, tempering and stress relieving due to a controlled cooling directly from the forging heat (Figure 1), an improved machinability and more consistent properties [3, 4]. However, forging steels with ferritic/pearlitic microstructures suffer

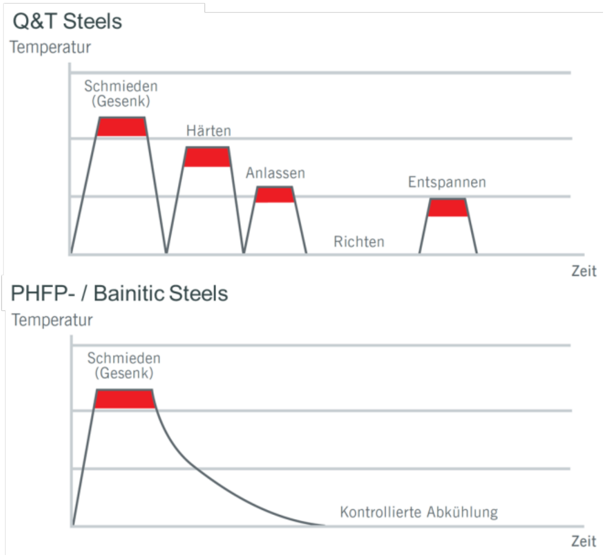

Figure 1: Advantages in the production process of PHFP- & Bainitic steels compared to Q&T steels [1]

compared to the Q&T steels from relatively low values of yield strength and toughness [5]. In order to improve the toughness while maintaining high strength values a bainitic microstructure can be employed [6–8]. The possibility of the achievable tensile strength in dependence of microstructural features for PHFP-M and high strength bainitic steels is presented in (Figure 2) [9]. While the increase in strength for the PHFP-M steel should be achieved by reduction of the ferritic volume fraction, the decrease in the lamellae spacing λ and the addition of precipitates of microalloying elements, the aimed for microstructure in the bainitic steel consists next to the precipitates of microalloying elements of bainitic ferrite and fine dispersed carbides or retained austenite as the bainitic second phase [10].

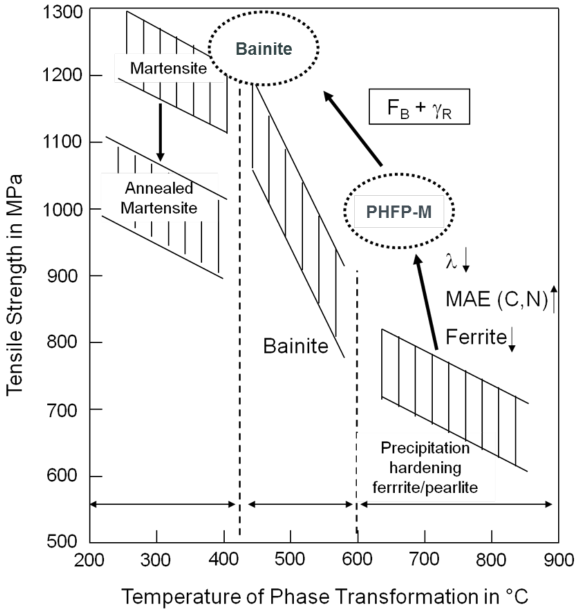

Figure 2: Achievable tensile strength levels as influenced by transformation temperature, microstructure and steel concept [9]

3 Industrial application

During the last years Georgsmarienhütte GmbH, together with partners from forging industry, developed multiple steels for automotive application. Two of them which are already in serial production are shown hereafter.

3.1 46MnVS5 - High Strength PHFP-M Steel

The first steel is developed for connecting rods. A high yield ratio is desired as on one hand high yield strength is needed for lightweight design and on the other hand the ultimate tensile strength should not exceed 1200 N/mm^2 so that a cost efficient machining is guaranteed. Furthermore connection rods need very low fracture toughness as they are manufactured by fracture splitting. Aim of the development was the substitution of the patented steel grade 36MnVS4.

Figure 3 compares steel grades for connection rods. In the past the strength increase of grades with fully pearlitic microstructures was realised by precipitation hardening. Therefore higher Vanadium contents were added which leads to increasing alloy surcharges. But the combination of the fully pearlitic matrix and a high amount of precipitates also leads to high ultimate tensile strength values which are detrimental for machining. The grade 36MnVS4 uses lower carbon contents to adjust a ferritic pearlitic microstructure with high amounts of ferrite. This is helpful for machining but very high vanadium contents are needed to increase the yield strength.

For the newly developed 46MnVS5 a compromise in the carbon content is made so that both ferrite content as well as ultimate tensile strength is between the two grades 36MnVS4 and 70MnVS4-high. Thermodynamic tools like JMatPro and ThermoCalc were applied to optimize the microalloying concept. In contrast to the existing grades not only Vanadium was used for precipitation hardening. Additional Niobium in combination with an increased Nitrogen content help to increase the volume fraction of fine dispersed carbonitrides. Through this alloying concept the yield strength can reach the same level as the 36MnVS4 but with a dramatic reduction of Vanadium content and costs. Furthermore the new steel grade is not covered by the above mentioned patent.

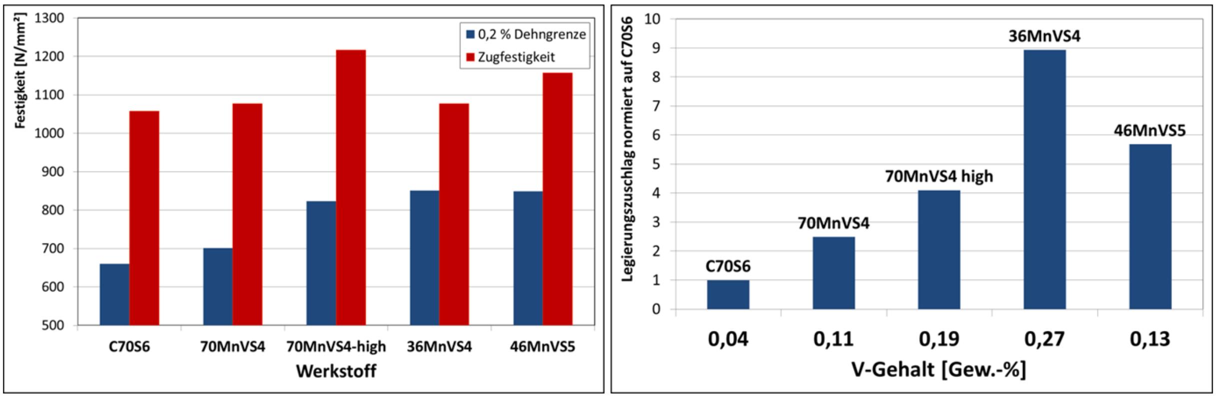

Figure 3: Development of steel grades for connecting rods - Left: Mechanical Properties, Right: Relative alloy surcharge in dependence of Vanadium content

3.2 H2 - High strength and ductile bainitic steel for structural applications

Although PHFP-M steels reach attractive yield strength levels their toughness is still weak compared to Q&T steels. Therefore the bainitic steel H2 was developed at GMH together with Hirschvogel Automotive Group. The newly developed micro-alloyed low carbon steel is based on a Manganese and Chromium rich concept similar as it is used in the carburizing steel 16MnCr5. These high amounts of Manganese and Chromium shift the ferrite pearlite transformation to longer times so that a fully bainitic microstructure can be adjusted during continuous cooling directly after forging. Additionally the yield strength is increased by applying a microalloying concept similar to that of PHFP-M steels. In total mechanical properties can be achieved that are comparable to Q&T steels. The data in Table 1 show a comparison of the mechanical properties of an injector body which is used in today's common rail diesel injection systems. They were produced from three different kinds of steel by warm forging. It is obvious that the air hardenable H2 steel shows similar mechanical properties as a quench and tempered 42CrMo4. This applies to yield strength as well as notch impact energy.

Table 1: Mechanical properties of warm forged injector bodies [11]

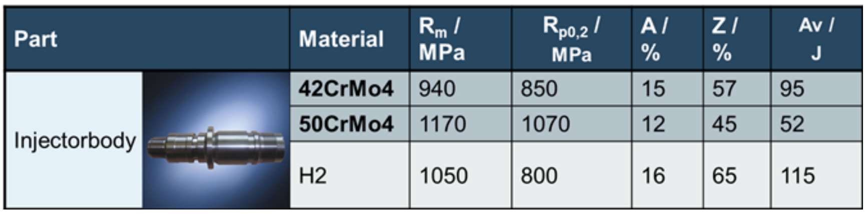

Part		Material	R_m / MPa	$R_{p0,2}$ / MPa	A / %	Z / %	Av / J
Injectorbody		**42CrMo4**	940	850	15	57	95
		50CrMo4	1170	1070	12	45	52
		H2	1050	800	16	65	115

A further advantage of the H2 steel is its cost-efficient alloy design without molybdenum as an alloying element. Together with the savings in heat treatment the H2 show the potential to replace more costly alloying resources but still yielding a highest strength and toughness values. This shows the perspective towards high strength parts at attractive cost levels.

4 Conclusion

By means of joined ventures between steel manufacturers and steel users it is possible to find solutions for the challenges of todays and future steel applications for the OEM. New high strength forging steels can replace Q&T steels and meet the requirements of the automobile industry for fuel efficiency and lightweight design. The development and optimization of steel grades offers the opportunity for customers in their production processes to save energy and time. However, it was shown, that these goals can be reached without losing superior mechanical properties.

References

[1] Moeller: *Handbuch Konstruktionswerkstoffe.* Hanser, 2008.

[2] Erisir, E. et al.: *19th International Forging Congress.* 2008, Chicago.

[3] Gladman, T.: *The Physical Metallurgy of Microalloyed Steels.* The Institute of Materials, London, 1997, pages 341–348.

[4] Cristinacce, M. and Reynolds, P. E.: “Fundamentals and Applications of Microalloying Forging Steels”. In: edited by C. J. Van Tyne, G. Krauss, and D. K. Matlock. TMS, Warrendale, PA, 1996, pages 29–43.

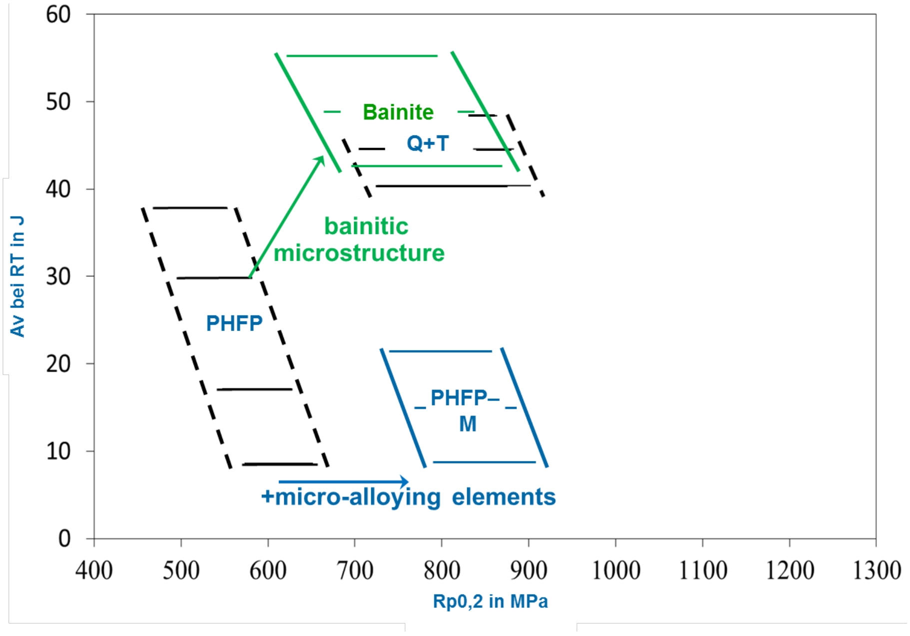

Figure 4: Correlation between toughness and yield strength for different steels, schematic [12]

[5] Lemaitre, C. and Dierickx, P.: "Steels for high performance diesel engines". In: *New Development in Long and Forged Products Proceedings* (2006), pages 29–36.

[6] Honeycombe, R. W. K. and Bhadeshia, H. K. D. H.: *Steels Microstructure and Properties.* 2nd edition. Edward Arnold, London, 1995.

[7] Bhadeshia, H. K. D. H.: *Bainite in steels-Transformations, microstructure and properties.* 2nd edition. The Institute of Metals, 2001.

[8] Wang, J., Wolk, P. J. van der, and Zwaag, S. van der: "On the influence of alloying elements on the bainite reaction in low alloy steels during continuous cooling". In: *Journal of Materials Science* 35 (2000), pages 4393–4404.

[9] Keul, C. and Bleck, W.: "New Microalloyed Steels for Forgings, The 6th International Conference on High Strength Low Alloy Steels (HSLA Steels'2011), 31.05.-02.06.2011, Beijing, China". In: *Journal of Iron and Steel Research International* 18.Supplement 1-1 (May 2011) (2011), pages 104–111.

[10] Langeborg, R., Sandberg, O., and Roberts, W.: "Fundamentals of Microalloying Forging Steels". In: TMS, Warrendale, PA, 1987, pages 39–54.

[11] Beyer, C. et al.: "Konstruktion". September 9-2013, IW 6.

[12] Arndt, J.: "Neue AFP-Stähle für hochbeanspruchte Fahrwerke". In: *Schmiede-Journal* 3 (2004), pages 17–18.

Potenziale übereutektoider Stähle durch den Einsatz von Kornfeinungsmitteln im Strang- und Formguss

Michel Wurlitzer
TU Clausthal
Institut für Metallurgie, Abteilung für Gießereitechnik, Robert-Koch-Straße 42, 38678 Clausthal-Zellerfeld
michel.wurlitzer@tu-clausthal.de

Übereutektoide Stähle finden in vielen hochbeanspruchten Bereichen des Maschinen- und Anlagenbaus Anwendung. Ihre anspruchsvollen gießtechnologischen Eigenschaften führen jedoch aus wirtschaftlichen, als auch technologischen Gründen zu einem begrenzten Anwendungsfeld. Insbesondere die Erstarrungsmorphologie ist Ausgangspunkt zahlreicher Probleme. Die heterogene Keimbildung als Weg der Gefügebeeinflussung kann daher ein Mittel der Wahl sein, um beispielsweise Seigerungen zu minimieren und eine anschließende Wärmebehandlung zu verkürzen. Im Folgenden soll der Stand der Technik in diesem Bereich kurz dargestellt und die aktuellen Probleme am Beispiel einiger Voruntersuchungen aufgezeigt werden, um damit einen Ausblick auf die Entwicklungen der nächsten Jahre in diesem Bereich zu geben.

1 Einleitung

Der Einsatz in sicherheits- und betriebsrelevanten Bauteilen im Automobil- und Anlagenbau erfordert die Erfüllung höchster Qualitätsansprüche bei der Herstellung von Wälzlagerstählen [1]. Die Abweichung von vorgegebenen Fehlertoleranzen und Ausfallwahrscheinlichkeiten sind aus diesem Grund in der Regel mit hohen Kosten verbunden. Insbesondere das Erreichen einer hohen Verschleißbeständigkeit, dem Widerstand gegen Materialermüdung und die thermische Stabilität des Gefüges sind dabei betriebsrelevante Eigenschaften der eingesetzten Stähle [1–3]. Die Optimierung der zugehörigen Herstellungsverfahren und die Reduzierung der Ausschussquote sind somit aus ökonomischer, als auch ökologischer Sicht sinnvoll.

Der Ausgangspunkt zur Erzeugung von Wälzlagerstählen und der geforderten Eigenschaften ist die chemische Zusammensetzung der Stahlschmelze nach ISO 683-17 [4]. Anschließend wird der Stahl überwiegend im kontinuierlichen Stranggussverfahren vergossen [5]. Die dabei ablaufende Erstarrung verläuft dendritisch und endet in einer ausgeprägten Sumpfspitze. Die starke Seigerungsneigung der legierten Elemente führt zu einer verstärkten konstitutionellen Unterkühlung an der Phasengrenze, was eine dendritische Erstarrung begünstigt. In der Sumpfspitze ergibt sich dadurch ein frühzeitiges Ende der Massenspeisung, die nicht durch interdendritische Speisung ausgeglichen werden kann und zur sogenannten „V“-Seigerung führt.

Diese, hier für einen Wälzlagerstahl beschriebenen, typischen Eigenschaften erstrecken sich auf das gesamte Feld der übereutektoiden Stähle. Diese neigen aufgrund ihres ausgeprägt großen Erstarrungsintervalls, dargestellt in Abbildung 1, zu den genannten Effekten.

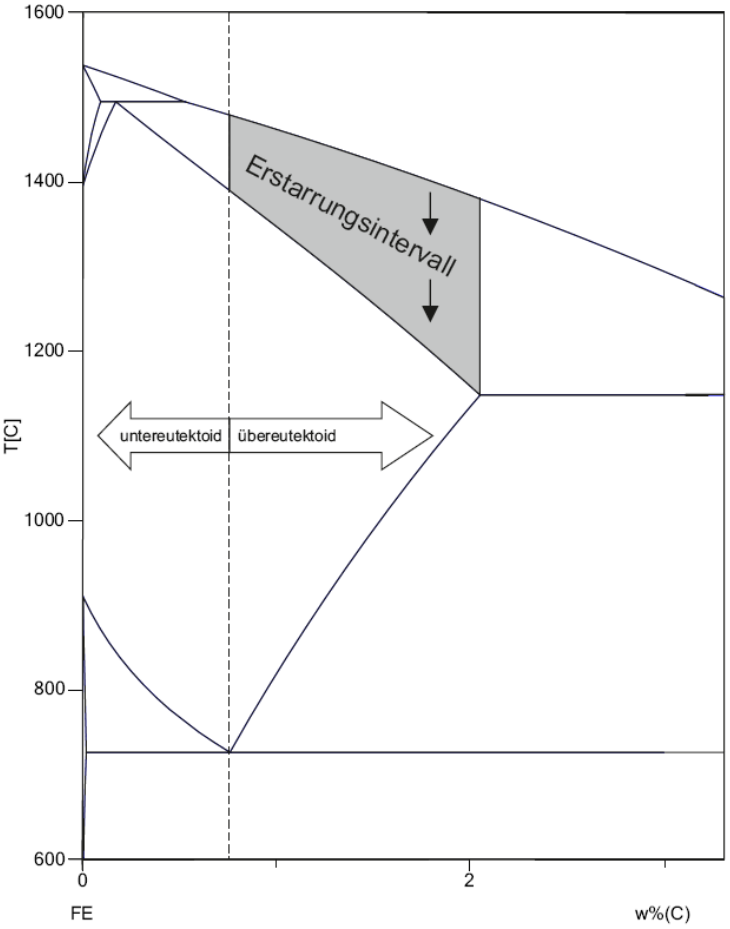

Abbildung 1: Darstellung des Erstarrungsintervalls übereutektoider Stähle im System Fe-C berechnet mit Thermocalc (TCFE7).

In den letzten Jahrzehnten wurden deshalb zahlreiche Anstrengungen unternommen, um diese Effekte zu minimieren und die Homogenität des Stahls zu verbessern. Mit Ausnahme der Softreduction zielen dabei alle Verfahren auf eine bevorzugt globulare Erstarrung und einer geringeren konstitutionellen Unterkühlung [6, 7]. Mit der Wirkung, dass Makroseigerungen reduziert und der Zeitraum der Massenspeisung verlängert wird.

2 Theoretische Grundlagen

Mit der Marktdurchdringung der mikrolegierten Stähle hat sich das Interesse an den Möglichkeiten der heterogenen Keimbildung gestärkt. Die heterogene Keimbildung beruht auf nichtmetallischen Verbindungen, die grobdispers bis kolloiddispers in der Schmelze vorliegen und als Keim dienen. Der heterogene Keim setzt dabei die zur homogenen Keimbildung nötige Oberflächenbildungsenthalpie herab.

Um die Wirkung des heterogenen Keims und dessen Bedeutung zu verstehen, ist zu nächst die homogene Keimbildung zu betrachten. Bildet sich ein annähernd runder Keim, so beträgt die Bildungsenthalpie der homogenen Keimbildung Δg_k gleich dem Energiebetrag der ebenen Grenzfläche Δg_V und dem Enthalpiebetrag der gekrümmten Grenzfläche Δg_O. Dies sind jeweils Funktion des Kugelvolumens V, bzw. der Kugeloberfläche O, dargestellt in Gleichung 1 [8]

$$\Delta g_K = \Delta g_V + \Delta g_O = V \Delta G_V + O \Delta G_O \tag{1}$$

Während Δg_V stets negative Werte mit einer Radiusabhängigkeit in dritter Potenz annimmt, ist Δg_O stets positiv und in zweiter Potenz vom Radius abhängig. Dies führt dazu, das erst nach überschreiten eines kritischen Radius ein stabiles Wachstum beginnt. Der kritische Radius verringert sich dabei mit dem Grad der Unterkühlung der Schmelze.

Die heterogene Keimbildung setzt nun voraus, dass die zur Keimbildung notwenige Energiebarriere im Vergleich zur homogenen Keimbildung herabgesetzt wird Gleichung 2. Dies ist gültig für Benetzungswinkel $\theta < 180°$ [8].

$$\Delta g_{K,heterogen} < \Delta g_{K,homogen} \tag{2}$$

In den vergangenen zwei Jahrzenten wurden dazu mehrere Stähle patentiert, was ein verstärktes Interesse an der sogenannten Dispersoid-Metallurgie zeigt. Bei den niedriglegierten, untereutektoiden Stählen konnten damit nicht zu Letzt aufgrund der Erfolge im IF-Bereich höchste Qualitätsansprüche erfüllt werden [9, 10]. Bei den übereutektoiden können keine marktreifen Stähle festgestellt werden. Dies liegt insbesondere an zwei Faktoren. Zum einen ist für die Bildung der nötigen Kolloide/Dispersoide eine exakt gesteuerte Desoxidations- und Entschwefelungsbehandlung notwendig und zum anderen ist Sicherzustellen, dass keine Agglomeration der Dispersoide stattfindet. Dies führt insbesondere bei Wälzlagerstählen zu Fehlstellen und frühzeitigem Bauteilversagen.

3 Forschungsvorhaben

Aus diesem Grund wurde in den vergangenen Jahren eine marktreife Kornfeinungslegierung auf Basis eines Ferrosiliziums entwickelt, die sicherstellen soll, dass die Dispersoide in einem Größenbereich von etwa 1µm liegen und homogen verteilt sind. Partikel mit diesem Durchmesser besitzen eine ausreichend niedrige Oberflächenregie und sind bei mechanisch zyklischer Belastung zu vernachlässigen. Es konnte gezeigt werden, dass die Verwendung zu einer Verringerung der Seigerungen führt und verbesserte mechanische Eigenschaften zu erwarten sind (Abbildung 2). Die dazu zur Verfügung stehenden Daten wurden jedoch nur im Labormaßstab erzeugt. Ein Einsatz der entwickelten Kornfeinungslegierung in Industriebetrieben findet nicht statt. Dies ist insbesondere auf fehlende Untersuchungen im Bereich der Agglomeration und die Abhängigkeit des Impferfolgs von der Stahlzusammensetzung zurück zu führen [11].

Die Kornfeinende Wirkung ist dabei sowohl für die Primärerstarrung in Form kleinerer Dendriten und kürzerer Dendritenarmabstände, als auch in einem thermomechanischen behandelten Wälzlagerstahl in Form kleinerer Ferritkörner festzustellen [12, 13]. In Abbildung 3 ist dies für einen 100Cr6 mit dem genannten Kornfeinungsmittel untersucht worden und es ist zu erkennen, wie sich das Fremdsubstart (schwarz) übwiegend im Zentrum der Dendriten befindet. Das hat in diesem Fall zu einer Kornfeinung geführt. Jedoch ist dies nicht für alle Dispersoide festzustellen. Aufgrund dessen in diesem Bereich weitere

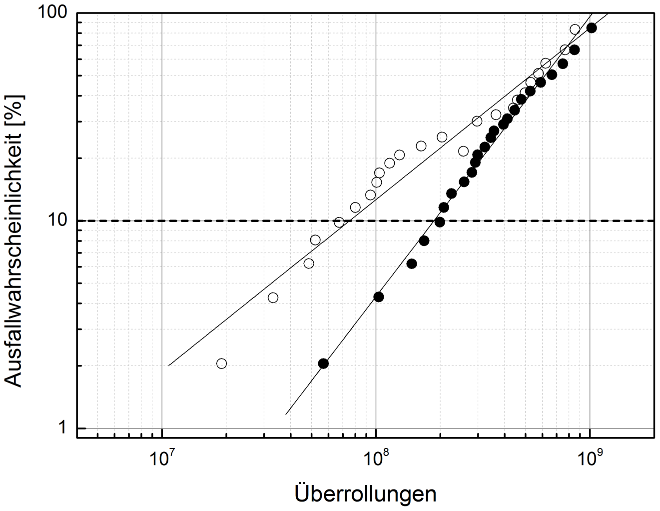

Abbildung 2: Ausfallwahrscheinlichkeit von Wälzlagerkugeln aus 100Cr6 mit (gefüllte Punkte) und ohne Kornfeinungsmittel (leere Punkte) [12].

Untersuchungen unternommen werden sollen, die die Abhängigkeiten der kornfeinende Wirkung aufzeigen sollen.

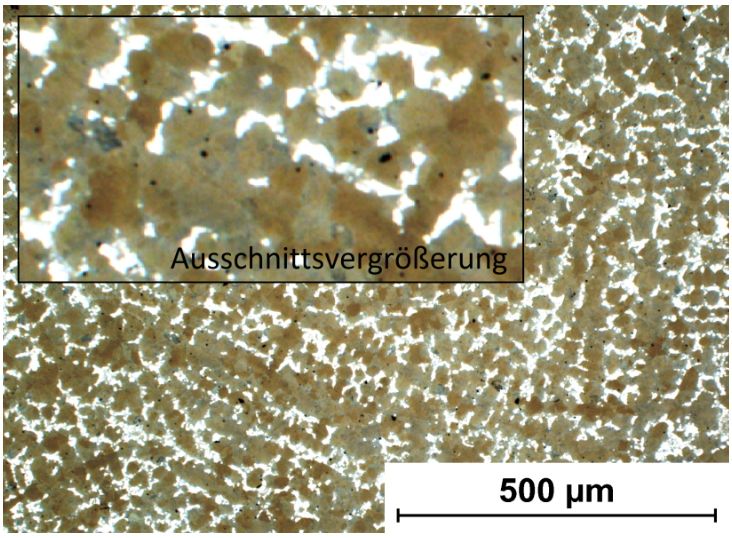

Abbildung 3: 100Cr6 mit Fremdsubstrat versetzt und mit Nital geätzt zur Darstellung des Primärgefüges.

Ein weiteres Kriterium für den Erfolg der Kornfeinung ist, das die Dispersoide im Stahl nicht als kritische Diskontinuitätszonen auftreten. Deshalb ist der Durchmesser der Dispersoide so einzustellen, dass diese auf der einen Seite eine optimale Kornfeinung gewährleisten und auf der anderen Seite nicht rissfördernd wirken. Ein großer Dispersoid bietet den Vorteil einer besseren Benetzbarkeit, jedoch ist in diesem Fall mit verstärkter Rissbildung im Bauteil und einer verringerten Dispersoidzahl bei gleicher Zugabemenge zu rechnen. Kleine Dispersoide sind aufgrund der hohen Oberflächenenergie und des hohen Krümmungsradius schlechter benetzbar, was zu einer verringerten kornfeinenden Wirkung führt. Gleichzeitig erhöht sich jedoch die Anzahl bei gleicher Zugabemenge und die rissfördernde Wirkung lässt nach. Aufgrund dessen ist ein Substrat auszuwählen, dass eine möglichst hohe Benetzbarkeit aufweist. Dies geht mit der Gitterpassung von Substrat und Metallmatrix einher [11, 14, 15]. Der Zusammenhang zwischen Dispersoidgröße und den Prozessparametern ist nach aktuellem Stand der Technik noch nicht hinreichend geklärt weshalb ein Teil der Forschungsbemühungen sich auf den Bereich der Kolloidagglomeration konzentriert. In Abbildung 4 sind die Dispersoide gut zu erkennen, die den geforderten Größenbereich von 1-2 µm überschreiten.

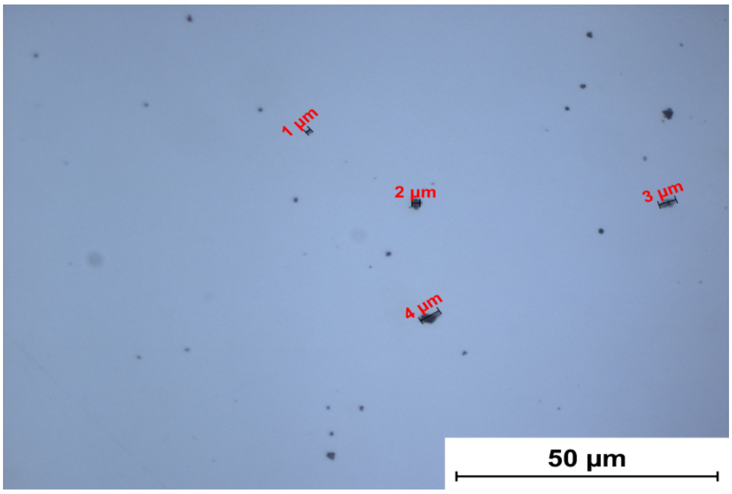

Abbildung 4: Dispersoide in ungeätzter Stahlmatrix.

Um die Größenverteilung genauer darzustellen, wurden Lichtmikroskopieaufnahmen eines 100Cr6 behandelt mit dem verfügbaren Impfmittel mittels Software untersucht und das Ergebnis in einem Histogramm dargestellt (Abbildung 5). Ist zu entnehmen, dass über 80% der Dispersoide eine Größe von 1 µm to 2 µm aufweisen, die restlichen sind in diesem Fall kleiner als 4.5 µm. Es ist somit festzustellen, das mit dem bisherigen Impfmittel bereits gute Ergebnisse erzielt werden können jedoch ein Teil der Dispersoide größer als gefordert ist. An dieser Stelle sollen die Untersuchungen ansetzen und klären, inwieweit Zusammensetzung von Impfmittel und Stahl Einfluss nehmen können. Hierbei sind insbesondere Gehalte von Sauerstoff und Schwefel relevant. Desweiteren soll geklärt werden, ob während der Erstarrung Ansammlungen der zugegebenen Dispersoide in bestimmten Bereichen auftreten.

4 Zusammenfassung und Ausblick

Die Dispersoid-Metallurgie als Lösungsansatz gießtechnologischer Probleme ist vielversprechend. Untersuchungen zeigen, dass Vorgaben erfüllt werden können und eine Verbesserung erzielt werden kann. Die derzeit noch bestehenden Risiken aufgrund fehlender Untersuchungen und ausbleibendem industriellem Einsatz bietet daher ein interessantes Untersuchungsfeld im Bereich übereutektoider Stähle.

Der Schwerpunkt der Untersuchungen soll dabei drei wesentliche Punkte umfassen. Zum einen soll die Bedeutung der Stahlzusammensetzung genauer untersucht werden, des Weiteren ist die Zeitabhängigkeit in der Zugabe zu klären und als dritter Punkt sollen die Einflüsse auf die nachfolgenden Verarbeitungsschritte geklärt werden.

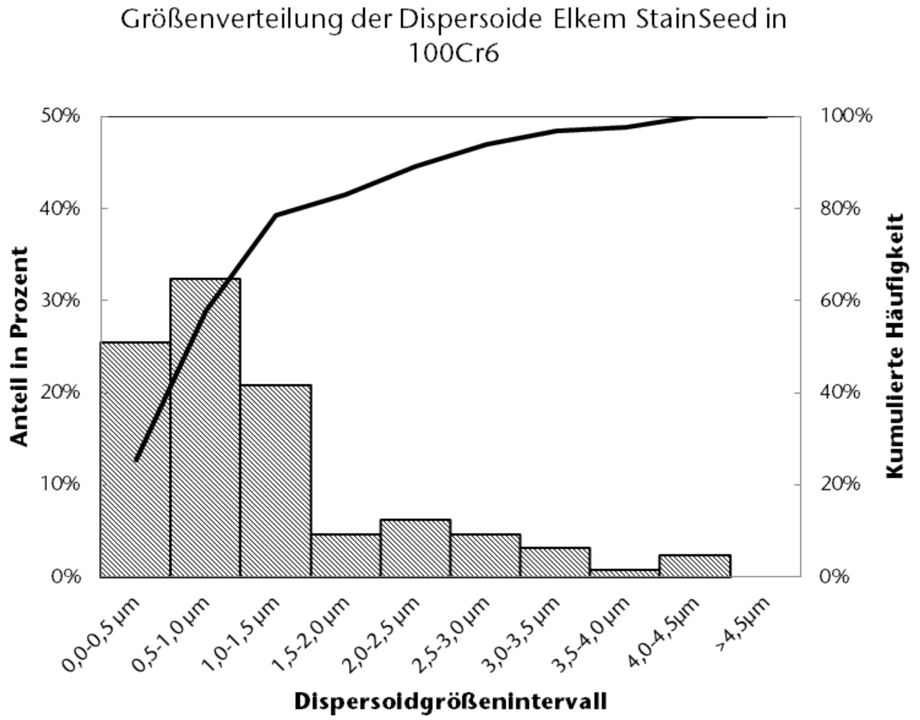

Abbildung 5: Verteilung der Dispersoidgröße in der Stahlmatrix für einen 100Cr6 behandelt mit Ce-haltigem Fremdsubstrat.

Die Verbesserung der gießtechnologischen Eigenschaften durch Fremdsubstrate würde die Konkurrenzfähigkeit übereutektoider Stähle insgesamt verbessern. Vor allem eröffnet sich hiermit eine Behandlungsmöglichkeit, die nicht an das Gießverfahren gekoppelt ist und damit sowohl für den Strang, als auch für den Formguss geeignet ist. Die veränderten Erstarrungsbedingungen würden zu weniger Seigerungen führen, die wiederum in einer Verkürzung der Wärmebehandlung münden. Das würde bedeuten, dass diese gießtechnologische Optimierung gleichzeitig mit einer Energieeffizienzsteigerung einhergeht. Außerdem führt das gefeinte Korn zu einer Feinkornhärtung, was die mechanischen Eigenschaften verbessern würde. Das bedeutet, dass dies nicht nur beim Stahlproduzenten, sondern auch beim Stahl verarbeitenden Betrieb zu einer Verbesserung führt.

Literaturverzeichnis

[1] H. K. D. H. Bhadeshia: “Steels for Bearings”. In: *Materials Science* 57 (2012), Seiten 268–435. URL: `BhadeshiaH.K.D.H..2012.pdf`.

[2] Harris, T. A. und Kotzalas, M. N.: *Essential concepts of bearing technology*. 5. ed. Band / Tedric A. Harris; Michael N. Kotzalas ; 1. Rolling bearing analysis. Boca Raton, Fla.: CRC Press, 2007. ISBN: 9780849371837.

[3] Choi, B.-Y.: “Characterization and transformation of 0.52%c steels for wheel bearing units produced by high frequency induction hardening after hot forging”. In: *Journal of Korean Institute of Metals and Materials* 48.12 (2010), Seiten 1103–1108. URL: `http://www.scopus.com/inward/record.url?eid=2-s2.0-78751497730\&partnerID=40\&md5=c81001fb183b1d4a9b5579116a25dfa5`.

[4] Normensausschuss Eisen und Stahl: *Für eine Wärmebehandlung bestimmte Stähle, legierte Stähle und Automatenstähle (683–17)*. 2014.

[5] Kemper, G.: *Strangguss 2014 - Effeizient, Sicher, Zukunftsorientiert*. Düsseldorf, 6.11.2014.

[6] LI, J. et al.: “Columnar to Equiaxed Transition During Solidification of Small Ingot by Using Electric Current Pulse”. In: *Journal of Iron and Steel Research International* 16.1 (2009), Seiten 7–12. URL: `http://ac.els-cdn.com/S1006706X10600192/1-s2.0-S1006706X10600192-main.pdf?\textunderscoretid=6a697e52-85fe-11e4-b72d-00000aab0f6b\&acdnat=1418829028\textunderscore170a96b711221e8c5a616da0ef5be8b9`.

[7] Senk, D.: “Erstarrungsstruktur und Makroseigerung in stranggegossenen Drahtgüten und ihre Beeinflussung durch eine harte Sekundärkühlung”. Dissertation. Clausthal-Zellerfeld: Technische Hochschule Clausthal, 1985.

[8] Frohberg, M. G.: *Thermodynamik für Werkstoffwissenschaftler, -ingenieure und Metallurgen: [eine Einführung].* 2., stark überarb. Aufl., unveränderter Nachdr. Weinheim: Wiley-VCH-Verl, 2009. ISBN: 9783527309221.

[9] Hahne, C.: "Verbesserung des Reinheitsgrades von 100Cr6 durch verlängertes Tiefvakuum und Argonspülen unter Stickstoffatmosphäre sowie Variation des feuerfesten Materials in der Pfanne und beim Vergießen". Dissertation. Aachen und Aachen: Techn. Hochsch, 2004.

[10] Zhang, L. und Thomas, B. G.: "State of the Art in Evaluation and Control of Steel Cleanliness". In: *ISIJ International* 43.3 (2003), Seiten 271–291. URL: `Zhang.2003.pdf`.

[11] C. Van Der Eijk: *INGROS: Final Technical Report.* Herausgegeben von SINTEF Materials Technology. Trondheim, 20.01.2004. URL: `http://nordicinnovation.org/Global/\textunderscorePublications/Reports/2004/Inclusion\%20Engineering\%20and\%20Grain\%20Size\%20Control\%20of\%20Steels\%20-\%20INGROS.pdf`.

[12] Kim, K.-H. und Bae, C.-M.: "Reduction of segregation during casting of 100Cr6 bearing steel by cerium inoculation". In: *Metals and Materials International* 19.3 (2013), Seiten 371–375. ISSN: 1598-9623. DOI: `10.1007/s12540-013-3001-2`.

[13] Zhang, G.-H. et al.: "Effects of Mn, Si and Cr addition on the dissolution and coarsening of pearlitic cementite during intercritical austenitization in Fe-1mass%C alloy". In: *Materials Characterization* 81 (2013), Seiten 56–67. ISSN: 10445803. DOI: `10.1016/j.matchar.2013.04.007`.

[14] C. Van Der Eijk et al.: *Grain Refinement of folly Austenetic Stainless Steels Using a Fe-Cr-Si-Ce Master Alloy.* 11.2001.

[15] Ole Svein Klevan Ystein Grong: "Verfahren zur Kornfeinung von Stahl, Kornfeinungslegierung für Stahl und Herstellungsverfahren für Kornfeinungslegierung". Patent DE 60129004 T2. 2007.

Microstructure and mechanical properties of WE43 magnesium matrix composite with addition of 5% SiC particles

Adam Gryc[1], Michał Dudek[2], Tomasz Rzychoń[3]
Silesian University of Technology
ul. Krasińskiego 8, 40-019 Katowice, Poland
[1]gryadam@wp.pl, [2]mdudek215@gmail.com, [3]Tomasz.Rzychon@polsl.pl

Abstract

In the paper the microstructure and mechanical properties of WE43 magnesium matrix composite with addition of 5% SiC particles are described. To fabricate the composites stir casting technology was used. The microstructure investigation showed the existence of α-Mg matrix, β–Mg_5RE eutectic compound, agglomerates of ZrSi2 particulates, yttrium oxide - Y_2O_3 and small Y-Nd-rich sharp-edged particles. Small YSi_2 particles in the vicinity of SiC particles were found. The transitional matrix-reinforcement layer is mainly composed of Si, Y and Zr. The agglomerates of SiC particles and material defects were also reported. The hardness of fabricated composite is 68±5 HV2, tensile strength R_m=146±7 [MPa], yield strength $R_{0,2}$=110±6 [MPa] and elongation A5=3,3±0,4 [%].

1 Introduction

Magnesium alloys have been increasingly used in recent years due to their low density and good mechanical properties at ambient temperature. In addition, magnesium alloys possess good damping capacity, excellent castability and superior machinability [1]. The major drawbacks of mentioned alloys are limited mechanical properties at elevated temperatures and low corrosion resistance.

One possible way to increase the high-temperature mechanical properties of cast magnesium alloys is the addition of expensive rare earth metals (yttrium, neodymium or gadolinium) [2]. The Mg-Y-Nd system is one of the most promising candidates for application in aerospace and automotive industry due to its good castability, creep resistance and corrosion resistance up to relatively high temperatures (300 °C) [3]. The best creep resistance and the highest strength properties among commercial magnesium alloys are presented by WE43 and WE54 alloys and are achieved by conventional age-hardening treatment, involving the formation of metastable β'' ($Mg_3(Y_{0,85}Nd_{0,15})$) and β' ($Mg_{12}NdY$ or $Mg_{24}Y_2Nd_3$), intermediate β_1 (Mg_3RE, RE = Nd, Ce, La, Gd) and equilibrium β ($Mg_{14}NdY$ in WE54, $Mg_{14}Nd_2Y$ in WE43) phases as dispersed precipitates, strengthening the alloy [2, 4–7].

Considerable improvement of mechanical properties can be also achieved through reinforcing with ceramic particles. The incorporation of particles causes a substantial increase of strength and stiffness as well as the creep resistance and wear resistance. Silicon carbide (SiC) particulates are the most preferred reinforcements primarily because enhanced properties can be easily achieved with little or no penalty on the low density of magnesium alloys [2, 6].

2 Material and experimental methods

2.1 Material

The investigated samples were obtained from 5 different casts of WE43 magnesium matrix composite with addition of 5 weight % of SiC particles (average size of 45 µm). The composition of the matrix alloy is given in Table 1.

Table 1: The composition of WE43 matrix alloy (wt%) [8]

Mg	RE (Nd, Dy, Ib)	Y	Zr	Zn	Mn	Fe	Ag
Balance	3,4	4,1	0,49	0,01	0,01	0,001	<0,01

2.2 Composite fabrication technology

To fabricate the composite ingots stir casting technology was applied. In the process, the reinforcing phases are distributed into molten magnesium by mechanical stirring. The final distribution of the particles in the solid depends on material properties and process parameters such as the wetting conditions of the particles with the melt, strength of mixing, relative density, rate of solidification, geometry and placement of the mechanical stirrer in the melt, melting temperature and characteristics of the particles added. The stirring process needs to be judiciously controlled in order to prevent the entrapment of gases and inclusions (magnesium alloys are sensitive to oxidation; once the gases and inclusions are entrapped, the increased viscosity of the vigorously stirred melt prevents easy removal of these detriments) [1].

Referring to the previous research, the stirring and casting temperatures were set to 720 °C. 1 kg of WE43 alloy was placed in a mild steel crucible preheated to 450 °C in electric resistance furnace. To prevent exposure of the melt to air, the inert atmosphere of argon was used. The furnace temperature was raised to 720 °C and the melt was homogenised for 10 min. Subsequently the Mg-Y, Mg-Zr and Mg-Nd hardeners were added. SiC particles (previously preheated up to 200 °C to improve the wetting conditions and to eliminate adsorbed water and gases from the surface of SiC particles) were introduced into the vortex of the melt during stirring with stainless steel impeller (150 rpm, 10 min). The ingots were casted into graphite forms [9].

2.3 Experimental methods

The samples were prepared for investigations following the guidelines of Struers specimen preparation system. Photomicrographs were acquired with an Olympus GX71 light microscope, equipped with the Olympus DP70 12 Megapixels digital camera, using the bright field technique and Hitachi S-3400N Scanning Electron Microscope, fitted with X-radiation EDS detector (Thermo NORAN System Six), using BSE imaging technique. EDS analysis and microstructure observations were performed with an accelerating voltage of 15 keV in high vacuum. Mechanical properties of as cast and heat treated samples were evaluated in terms of their hardness and tensile properties. Hardness measurements were carried out on Vickers hardness tester (Duramin A5) at the load of 2 kg. The tensile tests were carried out on a Zwick Kappa 50DS machine. The length of the specimen was 60 mm, the gage length was 30 mm and the diameter of the reduced section was 6 mm.

3 Results

3.1 Light microscope investigation

Light microscope investigation of fabricated composites allowed the preliminary identification of microstructure constituents and showed the existence of eutectic compound (Figure 1, pt 1) and SiC particles (Figure 1, pt 2) in the matrix. The fine sharp-edged precipitates (Figure 1, pt 4) and agglomerates of irregular particles (Figure 1, pt 3) were observed. Significant amount of oxides (Figure 1, pt 5) and the interfacial products at the interface between the matrix and SiC particles (Figure 1, pt 6) were also found.

3.2 Scanning electron microscope investigation

Scanning electron microscope investigation allows the detailed analysis of microstructure of the fabricated composites. EDS analysis provide information about the chemical composition of identified constituents (Table 2). The microstructure consists of α-Mg matrix (Figure 2, pt 1), β-Mg_5RE eutectic compound (Figure 2, pt 2), agglomerates of $ZrSi_2$ precipitates (Figure 2, pt 3), yttrium oxide - Y_2O_3 (Figure 2, pt 4), fine YSi_2 precipitates

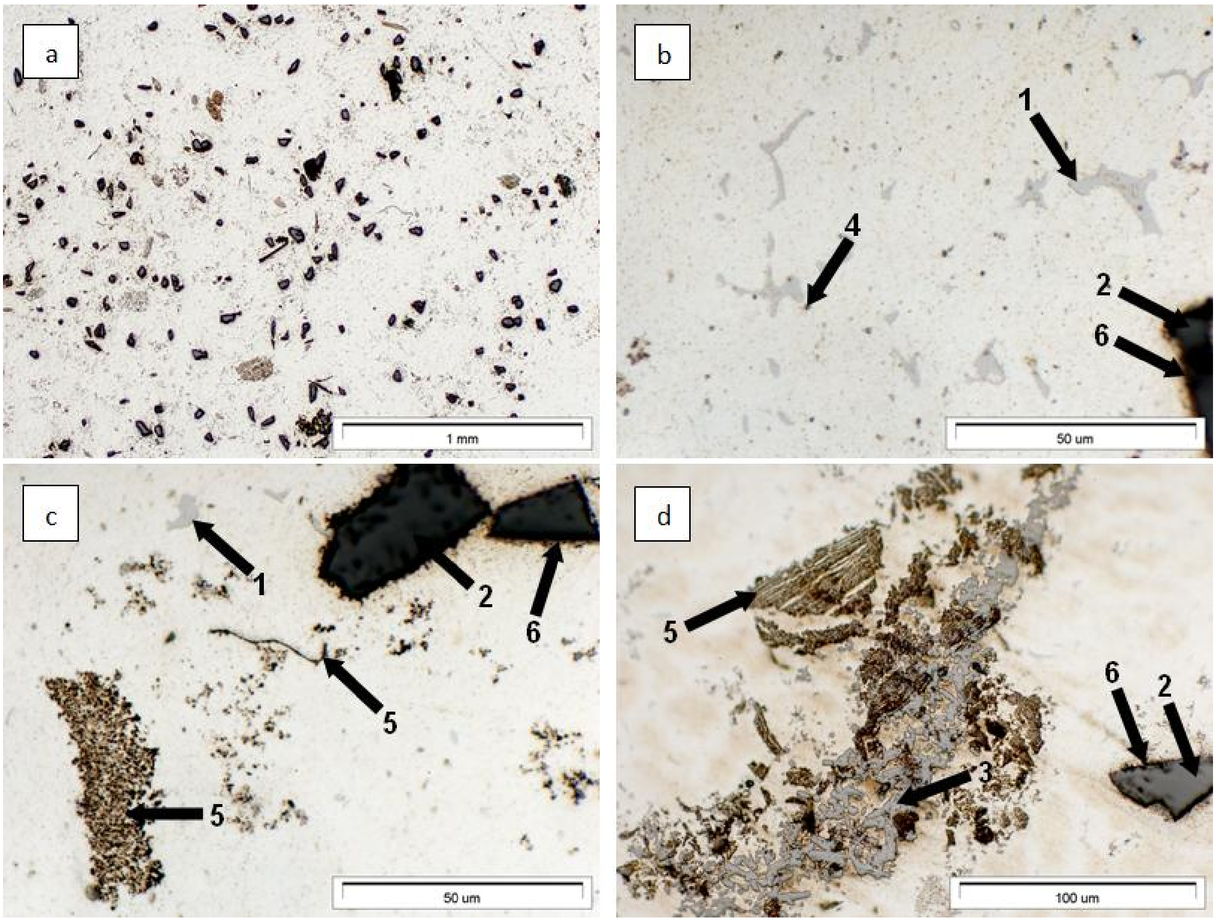

Figure 1: Microstructure of WE43 magnesium matrix composite with addition of 5% SiC particles.

(Figure 2, pt 5) in the vicinity of SiC particles (Figure 2, pt 6) and small Y-Nd-rich sharp-edged particles (Figure 2, pt 7). The transitional layer (Figure 2, pt 8) is mainly composed of Si, Y and Zr. The agglomerates of SiC particles (Figure 2a) and pores at the interface between α-Mg matrix and SiC particles (Figure 2c) were also observed.

Table 2: Results of EDS analysis (at%)

	Mg-K	Al-K	Si-K	Y-L	Zr-L	Nd-L	Dy-L
1	99.4			0.6			
2	88.3			4.6		7.2	
3	76.4			13.4	10.2		
4	68.2			31.8			
5	18.3		39.9	33.1		5.8	2.9
6			100.0				
7	93.1			2.0		4.9	
8	31.1	1.1	35.2	9.3	20.8	1.1	1.4

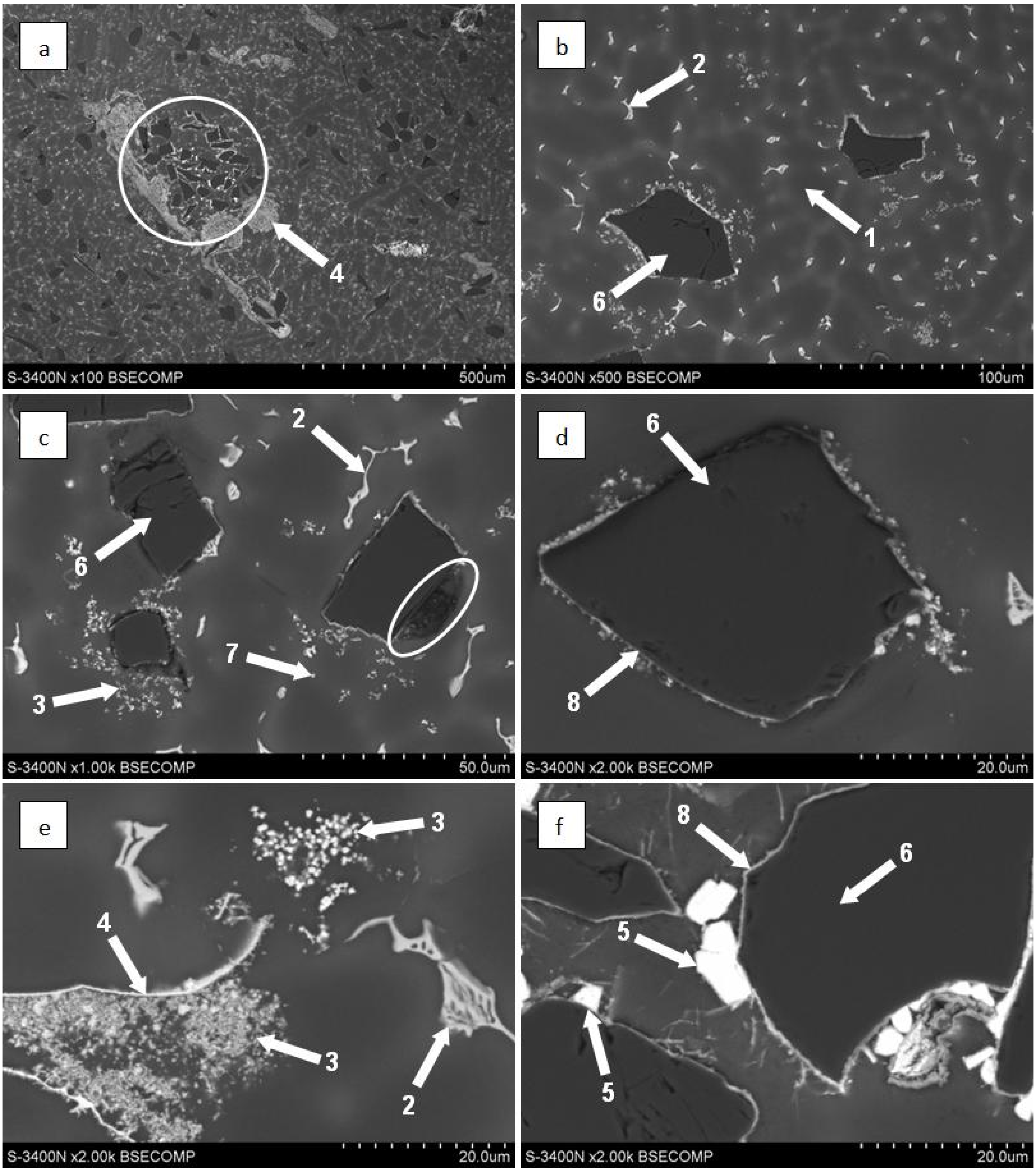

Figure 2: SEM photomicrographs of WE43 magnesium matrix composite with addition of 5% SiC particles.

3.3 Mechanical properties investigation

In Table 3 the results of HV2 microhardness test and uniaxial tensile test for WE43 alloy with and without the addition of 5% SiC particles are given. Tensile strength, yield strength and elongation of WE43 alloy with addition of 5% SiC particles have been deteriorated in comparison to as-cast WE43 alloy. The increase of hardness of the alloy containing SiC particles was noticed.

Table 3: Results of mechanical properties investigation

Material	HV2 hardness	Tensile strength R_m [MPa]	Yield strength $R_{0,2}$ [MPa]	Elongation A_5 [%]
WE43	59±4	166±18	113±9	6,7±1,5
WE43 + 5% SiC	68±5	146±7	110±6	3,3±0,4

4 Conclusions

- The microstructure of WE43 matrix composite with addition of 5% SiC particles consists of αMg matrix, β-Mg_5RE eutectic compound, agglomerates of $ZrSi_2$ particulates, yttrium oxide - Y_2O_3, small YSi_2 particles in the vicinity of SiC particles and small Y-Nd-rich sharp-edged particles.
- The transitional matrix-reinforcement layer is composed of Mg, Si, Y, Zr, Re (Nd, Dy) and Al with traces of O and C. The cause of oxygen presence might be the incomplete elimination of adsorbed gas from the surface of SiC before stirring process.
- The agglomerates of SiC particles and material deficiencies were also reported. Their presence may point to potential mistakes in stirring process and could be the direct reason of mechanical properties deterioration (in the areas of significant agglomeration of normally highly brittle hard particles, weak bonds are formed in the material).
- In comparison with WE43 alloy without the addition of SiC, hardness of fabricated composites has been raised at the expense of tensile strength, yield strength and elongation. The SiC particles were found to be source of microcracks initiation and in consequence the reduction of mechanical properties of WE43 matrix composite.

5 Acknowledgement

The present work was supported by the National Centre for Research and Development under the research project LIDER/29/198/L-3/11/NCBR/2012.

References

[1] Ye, H. Z. and Liu, X. Y.: “Review of recent studies in magnesium matrix composites”. In: *Journal of Materials Science* 39 (2004), pages 6153–6171.

[2] Rzychoń, T., Dyzia, M., and Pikos, I.: “Microstructure of WE43 Magnesium Matrix Composite Reinforced with Ceramic Particles”. In: *Solid State Phenomena* 211 (2014), pages 101–108.

[3] Mengucci, P. et al.: “Structure evolution of a WE43 Mg alloy submitted to different thermal treatments”. In: *Materials Science and Engineering* A 479 (2008), pages 37–44.

[4] Rzychoń, T. and Kiełbus, A.: “Microstructure of WE43 casting magnesium alloy”. In: *Journal of Achievements in Materials and Manufacturing Engineering* 21.1 (2007), pages 31–34.

[5] Kiełbus, A. and Rzychoń, T.: “Mechanical and creep properties of Mg-4Y-3RE and Mg-3Nd-1Gd magnesium alloy”. In: *Procedia Engineering* 10 (2011), pages 1835–1840.

[6] Trojanová, Z. et al.: “Acoustic emission from deformed Mg-Y-Nd alloy and this alloy reinforced with SiC particles”. In: *Journal of Alloys and Compounds* 504 (2010), pages L28–L30.

[7] Gryc, A., Dudek, M., and Rzychoń, T.: “Microstructure of WE43 Magnesium matrix composite reinforced with silicon carbide”. In: *Proceedings XXI. International Students’ Day of Metallurgy.* 2014, pages 38–41.

[8] Kiełbus, A., Stopyra, M., and Jarosz, R.: “Influence of sand-casting parameters on microstructure and properties of magnesium alloys”.

In: *Archives of Metallurgy and Materials* 58 (2013), pages 635–640.

[9] Dudek, M., Gryc, A., and Rzychoá, T.: "Characteristic of microstructure of WE43 magnesium alloy reinforced with silicon carbide after solution heat treatment". In: *XVI Międzynarodowa Studencka Sesja Naukowa „Materiały i Technologie XXI wieku"*. 2014, pages 37–40.

Einfluss von Mikrolegierung auf die Phasenumwandlung und Mikrostruktur eines 3.5% Medium-Mangan-Stahls

P. Peißl[1], R. Schneider[1], M. Rahofer[1], L. Samek[1], E. Arenholz[2]
[1]FH Oberöstereich, [2]voestalpine Stahl GmbH
[1]Fakultät für Technik und Umweltwissenschaften, 4600 Wels, Austria; [2]4020 Linz, Austria

Kurzfassung

Medium-Mangan-Stähle gehören zur 3. Generation der Advanced-High-Strength-Steels (AHSS). Sie weisen hohe Festigkeiten bei guten Dehnungen auf. Zusätzlich kann durch gezielte Zugabe von Legierungselementen wie Nb die Ausbildung der Gefügestrukturen bei unterschiedlichen Glühbehandlungen weiter beeinflusst werden. Neben der Dilatometrie zur Bestimmung der Umwandlungskinetik wurden Restaustenitmessungen mittels Röntgendiffraktometrie und Härteprüfungen durchgeführt. Für die Darstellung mittels Lichtmikroskop und Rasterelektronenmikroskop wurden Aufnahmen von der Mikrostruktur mit unterschiedlich angewandten Ätztechniken (Nital, Klemm-I, Marshall) erstellt. Aus der Gesamtheit der genannten Untersuchungen konnten Zeit-Temperatur-Umwandlungs-(ZTU)-Schaubilder erstellt werden. Zusätzliche Glühversuche im interkrititischen Temperaturbereich geben Aufschluss über den Einfluss von Niob auf die Entwicklung der Mikrostruktur. Neben dem starken Kornfeinungseffekt von Nb konnte, anhand des ZTU-Schaubilder, auch eine Verschiebung der Umwandlungen von Austenit in Ferrit, Bainit bzw. Martensit festgestellt werden. Das Gefüge setzt sich, je nach Abkühlrate, aus Martensit oder einer Mischung aus Ferrit, Bainit und Martensit zusammen. Interkritische Glühungen führen zu deutlich höheren Gehalten an Restaustenit.

Schlüsselwörter: Medium-Mn-Stähle, Niob, Metallografie, Dilatometrie, Röntgendiffraktometrie, Restaustenit, AHSS

1 Einleitung

Steigende Anforderungen an Gewichtsreduktion, Treibstoffeffizienz und die Sicherheiten im Crashverhalten in der Automobilindustrie sind der treibende Faktor für die Entwicklung neuer Stahlsorten und deren Wärmebehandlung. Durch die starke Konkurrenz von Bauteilen aus Aluminium, Kunststoffen oder Faserverbundwerkstoffen, wurde die Entwicklung im Bereich der Advanced High Strength Steels kurz AHSS in den letzten Jahren stark vorangetrieben. Die Eigenschaften, der als erster Generation der AHSS bezeichneten DP (Dualphasen) und TRIP (Transformation Induced Plasticity) Stähle, ermöglichen eine Minimierung der Blechstärke oder Steigerung der Sicherheit, durch höhere Festigkeiten bei guter Bruchdehnung des Stahles [1]. Hochfeste Stähle mit stark erhöhtem Mangangehalt, werden als TWIP (twinning induced plasticity) Stähle bezeichnet und der zweiten Generation der AHSS zugeordnet. Diese Stähle weisen höchste Festigkeiten (ca. 1000 MPa), bei Bruchdehnungen im Bereich von 50 % auf. [2] Die dritte Generation der AHSS wurde entwickelt um die Lücke in den Eigenschaften der ersten beiden zu schließen. Potentielle Kandidaten für die Erfüllung dieser Anforderungen sind die sogenannten Medium-Mangan-Stähle mit Mangangehalten zwischen 3 und 10 %.

Die Ziele moderner Werkstoffkonzepte umfassen einerseits die Legierungen und andererseits die exakte Einstellung einer bestimmten Gefügestruktur, bestehend aus Martensit, Ferrit und Restaustenit, realisiert durch unterschiedliche Wärmebehandlungen. Um eine deutliche Festigkeitssteigerung durch den TRIP-Effekt erreichen zu können, wird der Restaustenit bei langen Glühungen im interkritischen Bereich, durch die Wechselwirkung von Mangan im Ferrit und Austenit stabilisiert. [3–5] Für diese Stabilisierung werden zurzeit zwei unterschiedliche Wärmebehandlungsrouten angewandt. Die erste wird als ART (Austenite Reverted Transformation) Route bezeichnet [6–9] und besteht aus zwei Wärmebehandlungsschritten. Die zweite und einfachere Route wird als reine Haubenglühung durchgeführt. Beim ART-Zyklus (Abb. 1, rot) ist der Haubenglühung im interkritischen Bereich noch eine kontinuierliche Glühung mit anschließender Abschreckung aus dem Austenitgebiet, vorgeschalten. Die kurze Austenitisierung mit anschließender Abschreckung führt zu einem feinen, lattenförmigen und vollmartensitischen Gefüge. Durch die anschließende Haubenglühung im interkritischen Bereich wird die Diffusion von Mangan und Kohlenstoff in den, bevorzugt zwischen den Martensitlatten gebildeten, Austenit ermöglicht. Dadurch kommt es zu einer chemischen und mechanischen Stabilisierung des Austenits, welcher bis auf Raumtemperatur stabil ist [4, 5, 7, 8, 10]. Bei einer reinen Haubenglühung (Abbildung 1, blau) wird das martensitische Ausgangsgefüge durch Abkühlung nach dem Warmwalzen eingestellt.

Die Zugabe von Mikrolegierungselemente wie Niob und deren Wirkung auf das Gefüge sind seit der Einführung des thermomechanischen Walzens (TM-Stähle) bestens bekannt. Sie verzögern die Rekristallisation während des Walzvorganges und sind zusätzlich starke Karbid- und Nitridbildner. Mikrolegierungselemente wurden auch in den AHSS der ersten Generation (DP, TRIP) verwendet um die Entwicklung des Gefüges, durch Kornfeinung und Austenitkonditionierung, beeinflussen zu können [11]. Die Kornfeinung kann dabei durch feinste Karbid- oder Nitridausscheidungen als auch nach [3] durch die gelösten Mikrolegierungselemente (solute drag effect) hervorgerufen werden.

2 Experimentelle Durchführung

Die vorliegende Untersuchung widmet sich zum Großteil der Ausbildung des Gefüges eines niedrig gekohlten Stahls mit 3.5 % Mangan (0.1C3.5Mn) und davon einer abgeleiteten Variante mit Mikrolegierungselementen wie Niob (0.1C3.5Mn-Nb). Die Wirkung

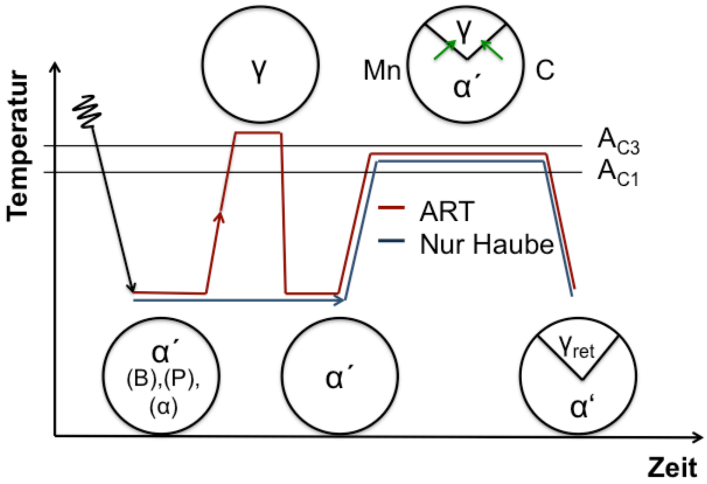

Abbildung 1: Schematische Darstellung der ART-Route (rot) und der reinen Haubenglühung (blau)
(α = Ferrit, α' = Martensit, B = Bainit, P = Perlit).

unterschiedlicher Abkühlraten auf die Umwandlung aus dem Austenitgebiet wurde mittels Dilatometrie untersucht. Daraus wurden ZTU-Schaubilder erstellt. Weiters wurden Haubenglühzyklen im interkritischen Bereich, also mit teilweiser Austenitisierung, durchgeführt.

Das Probenmaterial wurde von voestalpine Stahl GmbH zur Verfügung gestellt. Die Probenherstellung für die Untersuchungen im Dilatometer (Bähr 805 A/D) erfolgte durch Drahterodieren auf das Endmaß von 4 x 3 x 10 mm^3. Die für die Entwicklung der ZTU-Schaubilder angewandten Abkühlraten betrugen zwischen 0.03 und 100 K/s. Für die interkritischen Haubenglühungen wurde eine Glühdauer von 10h verwendet.

Die Präparation der Proben für die Untersuchung der Mikrostruktur erfolgte durch mechanisches Schleifen, Diamantpolieren und abschließendes mechanisch-chemischen Polieren (OP-S). Anschließend wurde mit Nital bzw. Klemm-I für die Darstellung des Gefüges bzw. zur Unterscheidung zwischen den Gefügebestandteilen geätzt. Die optische Erfassung der Mikrostruktur erfolgte mittels Lichtmikroskop und Rasterelektronenmikroskop. Zusätzlich wurde der Restaustenitgehalt (RA) mittels Röntgendiffraktometrie mit einer Mo-Röhre (nach ASTM E 975-03) ermittelt.

3 Ergebnisse

3.1 Umwandlungsverhalten aus dem vollaustenitischen Zustand

Das Ergebnis des ersten Teils des ART-Zyklus stellt die Einstellung eines üblicherweise vollmartensitischen Zustandes, erreicht durch schnelles Abkühlen aus dem Austenitgebiet, dar.

Dilatometeruntersuchungen

Die chemische Zusammensetzung hat in Verbindung mit der Abkühlgeschwindigkeit den größten Einfluss auf die Umwandlung aus dem Austenitgebiet in unterschiedliche Gefüge. Ausgewählte Abkühlkurven mit den jeweiligen Umwandlungsbereichen sind in Abbildung 2 dargestellt. Die Dilatometerkurven sind Ergebnisse aus Untersuchungen mit Abkühlraten von 0.03 K/s bis 100 K/s, welche die Ober- bzw. Untergrenze in dieser Versuchsreihe darstellen. Die charakteristischen Temperaturen (A_{c1} und A_{c3}) betrugen 660 °C und 810 °C für die Stähle mit bzw. ohne Mikrolegierung. Der Einfluss der unterschiedlichen Abkühlrate ist klar ersichtlich. Bei langsamer Abkühlung ist eine Ferritumwandlung beginnend bei ca. 600 °C, ersichtlich, welche durch Zugabe von Mikrolegierungselementen verstärkt wird. Verglichen mit der schnellsten Abkühlrate, bei der eine rein martensitische Umwandlung auftritt, weist die langsamste Abkühlrate zudem eine stark ausgeprägte Bainitumwandlung auf.

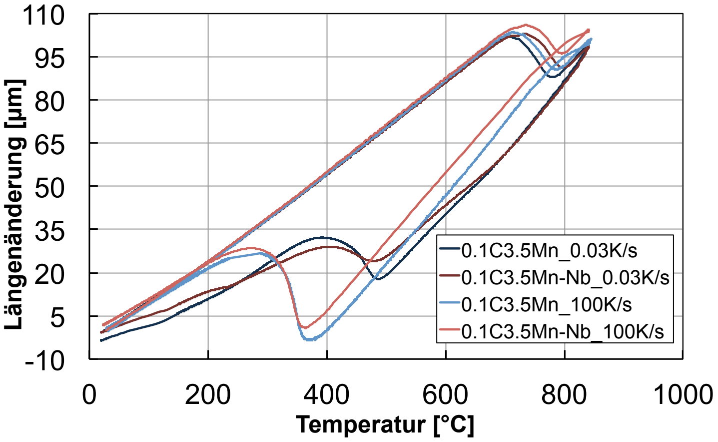

Abbildung 2: Dilatometerkurven bei unterschiedlichen Abkühlraten (100 K/s and 0.03 K/s).

Mikrostruktur

Untersuchungen der Mikrostruktur zeigen in Abbildung 3 den klaren Einfluss von Mirkolegierungselementen wie Niob auf die Gefügeausbildung, im Speziellen auf die Korngröße des entstehenden Gefüges, auf. Das Gefüge des Stahles 0.1C3.5Mn mit und ohne Mikrolegierungselement setzt sich aus Ferrit und Bainit bzw. Martensit zusammen.

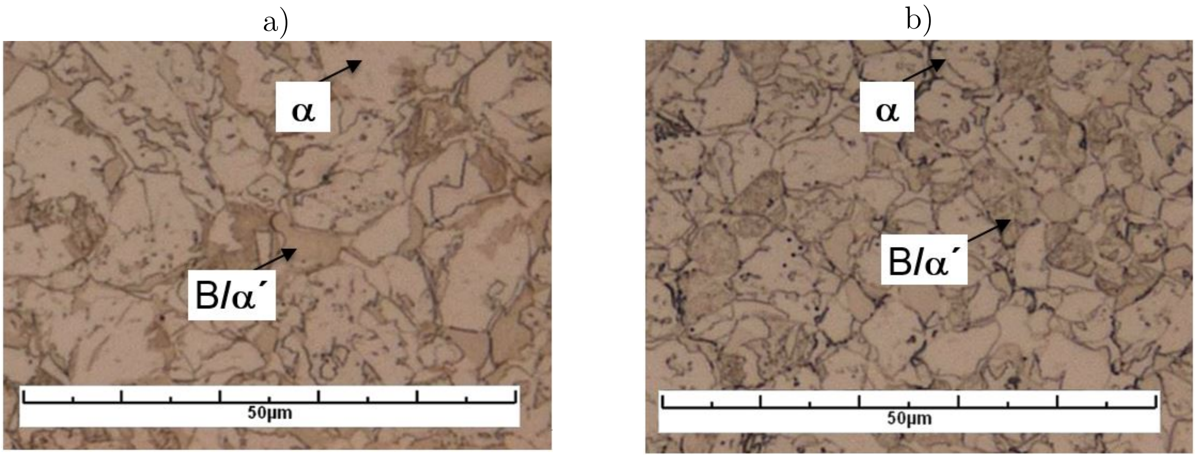
a) b)

Abbildung 3: Lichtmikroskopische Aufnahmen der Mikrostruktur der Stähle (a) 0.1C3.5Mn; (b) 0.1C3.5Mn-Nb bei einer Abkühlrate von 0.03 K/s; geätzt mit Nital (3%); Vergrößerung 1000x; α = Ferrit, α' = Martensit, B = Bainit.

Abbildung 4 zeigt die gleichen Stähle bei einer Abkühlrate von 100 K/s. Bei dieser Abkühlrate ist die Bildung von Martensit die dominierende Gefügeumwandlung während der Abkühlung. Generell kann wieder der Kornfeinungseffekt durch Mikrolegieren beobachtet werden.

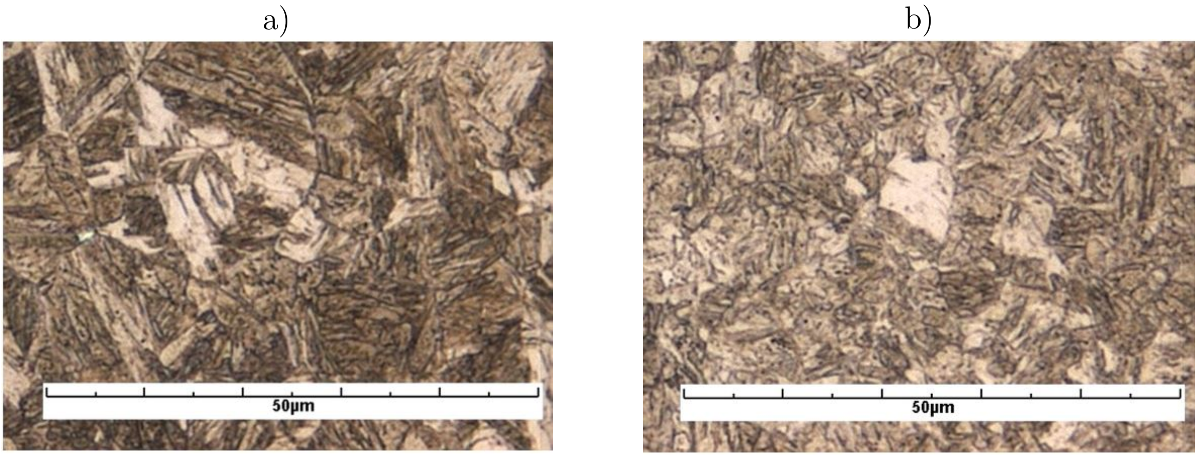
a) b)

Abbildung 4: Lichtmikroskopische Aufnahmen der Mikrostruktur der Stähle (a) 0.1C3.5Mn; (b) 0.1C3.5Mn-Nb bei einer Abkühlrate von 100 K/s; geätzt mit Nital (3%); Vergrößerung 1000x.

Vickers-Härteprüfung

Die Ergebnisse der Härteprüfung sind in Abbildung 5 als Funktion der Abkühlrate dargestellt. Mit Ausnahme des Bereichs zwischen einer Abkühlrate von 3 bis 10 K/s besitzt der mikrolegierte Stahl 0.1C3.5Mn-Nb durchwegs eine höhere Härte als der Stahl 0.1C3.5Mn. In diesem Bereich ist bei beiden Stählen auch ein starker Abfall der Härte ersichtlich. Bei hohen Abkühlraten von 100 bzw. 30 K/s weisen beide Stähle eine Härte im Bereich von 400 HV10 auf. Verglichen dazu liegt bei niedrigen Abkühlraten die Härte in einem Bereich von ca. 300 HV10.

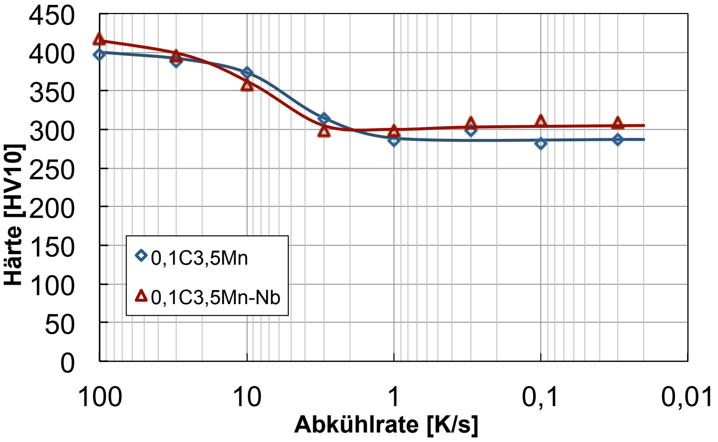

Abbildung 5: Vickers Härte als Funktion der Abkühlrate.

Restaustenitgehalte

Um den Gehalt an Restaustenit, nach der Abkühlung auf Raumtemperatur, ermitteln zu können wurden Messungen mit einem Röntgendiffraktometer durchgeführt. Abbildung 6 zeigt die Werte für die untersuchten Stähle. Bei hohen Abkühlraten (>10 K/s) liegen die RA-Werte beider Stähle im Bereich der Nachweisgrenze (≤ 2 Vol.-%). Bei niedrigen Abkühlraten (<10 K/s) weisen beide Stähle in einem Bereich zwischen 2 und 4 % leicht höhere RA-Werte auf.

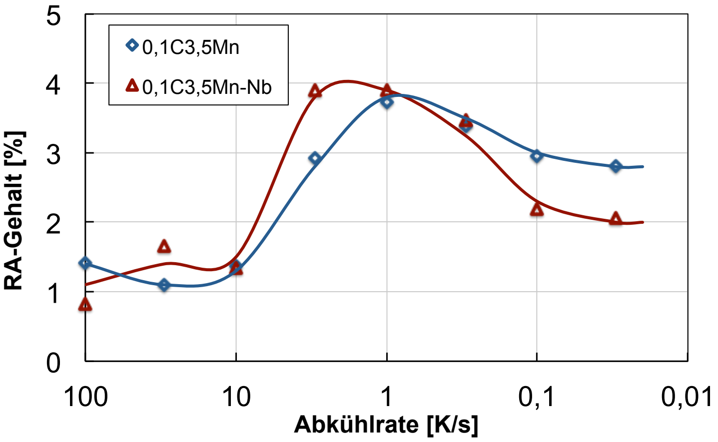

Abbildung 6: Restaustenitgehalt als Funktion der Abkühlrate.

Aus der Gesamtheit der Ergebnisse konnten ZTU-Schaubilder für die untersuchten Stähle erstellt werden. Der Einfluss der zusätzlich zugegebenen Mikrolegierungselemente ist klar ersichtlich, da die Umwandlungsbereiche von Ferrit und Bainit zu kürzeren Zeiten verschoben werden. Durch höhere Anteile an Ferrit und Bainit ist der Anteil von Martensit im Stahl 0.1C3.5Mn-Nb etwas geringer. Zusätzlich liegt die MS-Temperatur durch Mikrolegierungselemente wie Niob zum Teil niedriger als beim Stahl 0.1C3.5Mn.

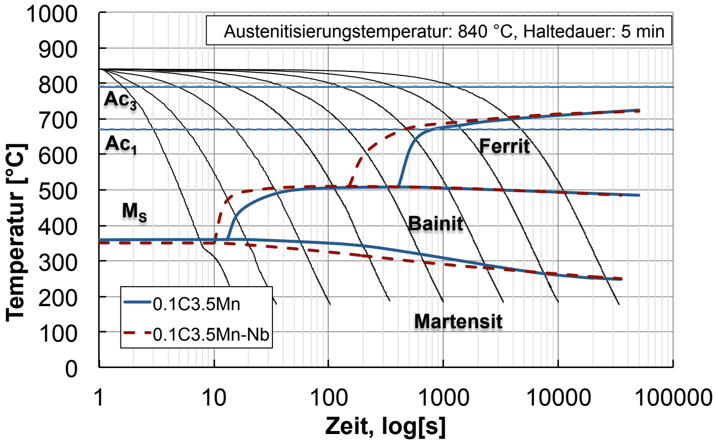

Abbildung 7: ZTU Diagramm für die Stähle 0.1C3.5Mn und 0.1C3.5Mn-Nb.

3.2 Entwicklung der Mikrostruktur bei interkritischer Glühung

Haubenglühzyklen

Die Haubenglühung im interkritischen Bereich, als Teil des ART-Zyklus (bzw. ohne vorangegangenen Austenitisierung) dient der Maximierung des Restaustenitgehaltes bei langen Glühzeiten in Abhängigkeit von der Glühtemperatur. Industrienahe Haubenglühzyklen mit unterschiedlichen Haltetemperaturen wurden in dieser Untersuchung durchgeführt und miteinander verglichen.

Härteprüfung

Abbildung 8 zeigt die Ergebnisse der Vickers-Härteprüfung in Abhängigkeit von der Glühtemperatur. Die Härte des mikrolegierten Stahles 0.1C3.5Mn-Nb liegt, mit Ausnahme der höchsten Glühtemperatur (700 °C), immer ca. 30 – 50 HV10 über jener des Stahles 0.1C3.5Mn. Beide Stähle zeigen einen ähnlichen Verlauf, welcher im Bereich zwischen 610 und 640 °C nur geringe Änderungen aufweist. Ein Anstieg der Härte ist, ab 640 °C, beim mikrolegierungsfreien Stahl stärker ausgeprägt.

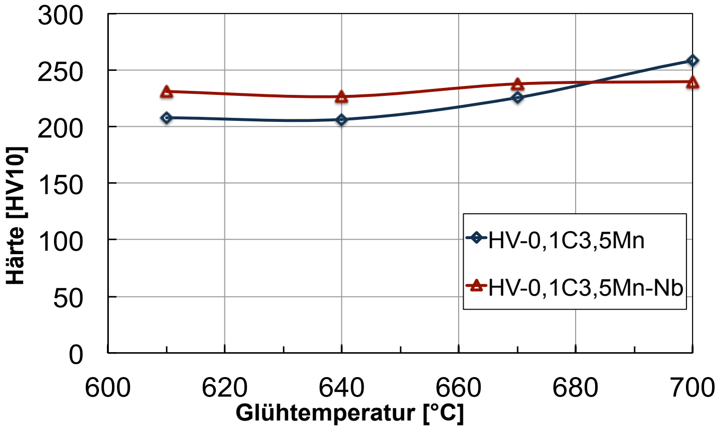

Abbildung 8: Verlauf der Vickers-Härte als Funktion der Haubenglühtemperatur.

Restaustenitgehalte

Die Restaustenitgehalte sind in Abbildung 9 in Abhängigkeit von der Haubenglühtemperatur dargestellt. Die maximalen Restaustenitgehalte (ca. 10 %) in dieser Untersuchung erreichte der mikrolegierte Stahl 0.1C3.5Mn-Nb im Bereich zwischen 640 und 670 °C. Im gleichen Temperaturintervall hat auch der Stahl 0.1C3.5Mn mit ca. 7 % sein Maximum. Von den unterschiedlichen Gehalten abgesehen, weisen beide Stähle einen ähnlichen Verlauf über der Glühtemperatur auf.

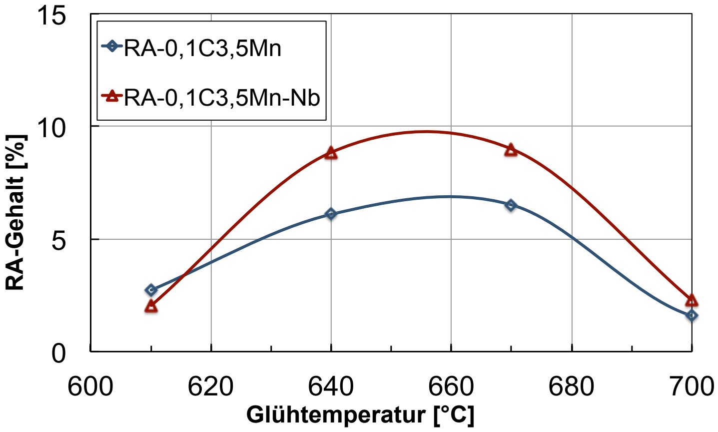

Abbildung 9: Restaustenitgehalt als Funktion der Haubenglühtemperatur.

Mikrostruktur

In Abbildung 10 sind die Gefüge der untersuchten Stähle nach einer Haubenglühbehandlung bei 670 °C dargestellt. Die Ätzung nach Klemm-I ermöglicht die Feststellung der Verteilung des Restaustenits, da dieser höher legiert ist und im Ätzbild hell bis weiß entwickelt wird. Die anodischen Bereiche wie Ferrit und Bainit werden in blauen bzw. braunen Tönen dargestellt. Beide Stähle zeigen ein eher globulares Gefüge, wobei der mikrolegierte Stahl wiederum ein deutlich feineres Gefüge aufweist. Der Restaustenit liegt in eher globularer Form vor und ist im Bereich der Korngrenzen angesiedelt.

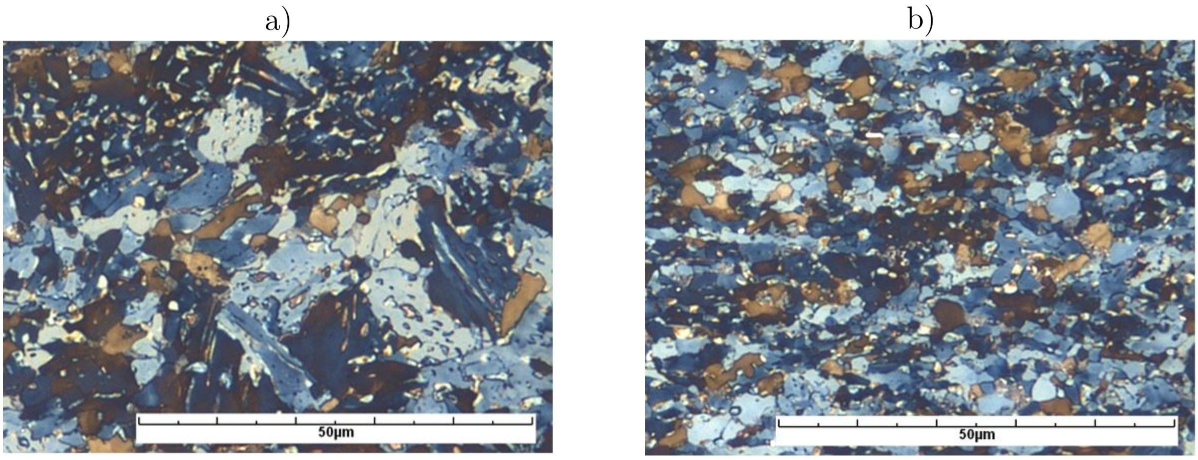

Abbildung 10: Gefügebilder der untersuchten Stähle bei einer Haubenglühtemperatur von 670°C; (a) 0.1C3.5Mn; (b) 0.1C3.5Mn-Nb; geätzt in Klemm-I Lösung.

4 Diskussion

Die entwickelten ZTU-Schaubilder zeigen die Phasenumwandlungen aus dem Austenitgebiet bei unterschiedlichen Abkühlraten. Mit Ausnahme der höchsten Abkühlrate entsteht bei allen anderen Abkühlraten ein Gefüge bestehend aus Ferrit, Bainit und Martensit. Die geringe Änderung der MS-Temperatur durch die Zugabe von Mikrolegierungselementen ist in guter Übereinstimmung mit mikrolegierten TRIP-Stählen aus [10] und auf das feinere Ausgangsgefüge zurückzuführen, welches die Martensitbildung erschwert. Nach [3] besteht auch ein Zusammenhang zwischen Mikrolegierungselementen wie Niob und dem Mangangehalt, welcher auf das Umwandlungsverhalten großen Einfluss hat. Die Beschleunigung der Ferrit- und Bainitumwandlung durch eine Mikrolegierung kann auf die größere Anzahl von Keimen an den Ausscheidungen und Korngrenzen zurückgeführt werden.

Die Härtesteigerung durch die Zugabe von Mikrolegierungselementen ist hauptsächlich auf deren starken kornfeinenden Effekt bzw. eine Ausscheidung von Sonderkarbiden zurückzuführen. Der starke Kornfeinungseffekt konnte allgemein gut nachgewiesen werden. Ein eindeutiger Einfluss der Mikrolegierung auf die ermittelten RA-Gehalte konnte nicht festgestellt werden.

Die erreichten Gehalte an Restaustenit nach den interkritischen Haubenglühungen sind in guter Übereinstimmung mit [5], wo ein maximaler RA-Gehalt von ca. 10 Vol.-% bei einer Glühtemperatur von 650 °C und vergleichbarer Kühlrate erreicht wurde. Die höheren RA-Gehalte beim mikrolegierten Stahl können auf die beschleunigte Bildung von Ferrit und die damit verbundene stärkere Anreicherung von C im Austenit zurückzuführen werden [12]. Bei 600°C wird während der Glühung bei beiden Varianten der Restaustenit durch eine hohe Anreicherung mit C und Mn sehr stark stabilisiert, sodass hier bei der anschließenden Abkühlung keine weitere Umwandlung auftritt. Bei einer interkritischen Glühtemperatur von 700°C ist die Stabilisierung des Austenits bei beiden Legierungsvarianten nicht ausreichend und es kommt zur Bildung von frischem Martensit welcher den verbleibenden Restaustenitgehalt wieder deutlich reduziert.

Die Gefügeuntersuchungen nach einer interkritischen Glühung zeigen die Stabilisierung des Restaustenits bis zu einem Gehalt von ca. 10 Vol.-% und seine polygonale Form an den Korngrenzen auf. Restaustenit in lattenartiger Anordnung wie in [6, 7, 9] beschrieben konnte nicht nachgewiesen werden, was darauf zurückzuführen ist, dass bei diesen Untersuchungen kein vollständiger ART-Glühzyklus angewandt wurde.

5 Zusammenfassung

Die Entwicklung von Gefüge, Härte und Restaustenitgehalt an zwei 3.5%-Mn-Stählen in Abhängigkeit von den angewandten Glühparametern kann wie folgt zusammengefasst werden:

- Nach dem Abkühlen aus dem Austenitgebiet liegt bei beiden Stählen ein Gefüge aus Ferrit, Bainit und/oder Martensit vor.
- Die ferritische und bainitische Umwandlung wird durch Mikrolegierung etwas beschleunigt.
- Die Zugabe von Mikrolegierungselementen wie Niob erhöht die Härte.

- Unabhängig von der Art der Wärmebehandlung konnte ein starker Kornfeinungseffekt durch Mikrolegieren festgestellt werden.
- Durch interkritische Haubenglühungen konnten höhere Gehalte an Restaustenit (bis 10 Vol.-%) stabilisiert werden.
- Der Restaustenit liegt nach interkritischen Haubenglühungen in polygonaler Form an den Korngrenzen vor.

Danksagung

Die Autoren danken der voestalpine Stahl GmbH für die finanzielle, materielle und ideelle Unterstützung des Projektes. Besonderer Dank gebührt der österreichischen Forschungsförderungsgesellschaft mbH (FFG) für die finanzielle Förderung im Rahmen des Projektes Nr. 841377.

Literaturverzeichnis

[1] Matlock, D. K. et al.: “Recent Developments In Advanced High Strength Sheet Steels For Automotive Applications: An Overview”. In: *Engineering Science and Technology, an International Journal* 1.15 (2012), Seiten 1–12.

[2] Aydin, H. et al.: “Effect of Heat Treatment on the Deformation Behavior During Cold Rolling of Medium Mn Steels”. In: *Materials Science and Technology (MS & T)*. 2012, Seiten 501–508.

[3] Grajcar, A., Kuziak, R. und Zaleckib, W.: “Third generation of AHSS with increased fraction of retained austenite for the automotive industry”. In: *Archives of civil and mechanical engineering* 3 (2012), Seiten 334–341.

[4] Steineder, K. et al.: “Microstructural evolution in 0.1%C5%Mn steel after intercritical annealing depending on temperature and cooling rate”. In: *Proceedings of European Conference on Heat Treatment, 21st IFHTSE Congress*. 2014, Seiten 301–308.

[5] Steineder, K. et al.: “Microstructural evolution of two low-carbon steels with a medium manganese content”. In: *Proceedings of 2nd HMnS Conference*. 2014, Seiten 351–354.

[6] Wang, C. et al.: “Development of Ultrafine Lamellar Ferrite and Austenite Duplex Structure in 0.2C5Mn Steel during ART-annealing”. In: *The Iron and Steel Institute of Japan* 51.4 (2011), Seiten 651–656.

[7] Arlazarov, A.: “Characterization of microstructure formation and mechanical behaviour of an advanced medium-mn-Steels”. In: *Materials Science and Technology (MS & T)*. 2012, Seiten 1124–1131.

[8] Schneider, R. et al.: “Metallographic investigation of Medium-Mn-Steels”. In: *Special editions of Practical Metallography*. Band 46. 2014, Seiten 77–82.

[9] Arlazarov, A. et al.: “Evolution of microstructure and mechanical properties of medium Mn steels during double annealing”. In: *Materials Science and Engineering A* 542 (2012), Seiten 31 –39.

[10] Beck, W., Frehn, A. und Ohlert, J.: “Niobium in dual phase and trip steels”. In: *Niobium - Science & Technology*. 2001, Seiten 727–776.

[11] DeArdo, A. J.: “Fundamental Metallurgy Of Niobium In Steel”. In: *Niobium - Science & Technology*. 2001, Seiten 427–500.

[12] Hausmann, K. et al.: “The influence of Nb on transformation behavior and mechanical properties of TRIP-assisted bainitic–ferritic sheet steels”. In: *Materials Science & Engineering A* 588 (2013), Seiten 142–150.

Material utilization of metallurgical fine grained waste

Romana Švrčinová, Jozef Vlček, Michaela Topinková, Miroslava Klárová
VŠB – Technical University of Ostrava
Department of Thermal Engineering, 17. listopadu 15 2172, 708 / 33 Ostrava – Poruba,
Czech Republic
E-Mail: romana.svrcinova@vsb.cz

Abstract

Czech Republic has a rich historical tradition in the production of iron and steel. Czech Republic is the major producer of iron and steel. During the manufacture of iron and steel are also produced waste products. The biggest problem metallurgical production is emerging solid waste. The aim of this study was to find suitable without cement binder. And then verify the possibility of pelletization fine grained metallurgical waste for recycling in the manufacturing process.

Keywords: binders, pelletization, fine-waste materials, ladle slags

1 Introduction

This work deals with the creation of compact high-tonnage fine-grained material from waste products generated during the production of iron and steel. These include waste slag which is an integral part needed in the production. Other wastes are ladle dust, wastes from aluminum dross, converter sludge and many others. These wastes contain significant proportions of ingredients that can be repatriated back in to the production process [1]. They are of lime, alumina and iron stakes. These materials are suitable for further use in steel production. Composition of the mixture influences the mechanical and physical properties of the final products. Ladle slag was used as a binder phases. This slag has suitable hydraulic properties. Slags that react with water are referred to as hydraulic binders. These are the substances that in contact with water solidify. During solidification occurs hydration original minerals and hydration products are insoluble in water [2, 3].

2 Experimental part

Pelletization process waste materials were carried out in several stages. In the first part, it was necessary to verify the hydraulic properties of the selected ladle slag. The chemical composition of the slag is specified in Table 1. These slags were finely ground. Slags grinding increases their surface area. The larger surface area of slags increases their reactivity. Water was added into the prepared slags. The prepared mixture was poured into metal molds. The size of each sample was 20×20×20 mm. After filling were molds vibrated for 2 minutes. Vibrating was achieved degassing the mixture. The samples were stored in the hydration box (an ambient relative humidity of 99%).

Table 1: Chemical composition of selected slags

Sample	**Slag**	**Chemical composition**						
		$Fe_{\sum}$	SiO_2	Al_2O_3	CaO	MgO	MnO	S
S1	Mixed ladle slag	1,34	13,55	21,83	55,62	4,99	0,40	0,85
S2	Ladle slag	0,70	11,90	17,80	54,80	5,80	0,17	0,85
S3	Ladle slag	0,80	22,80	14,40	51,20	5,70	0,40	1,10

Samples were pulled out from the mold after 24 hours. Samples were placed back in to the hydration box. Always 2, 7 and 28 days were chosen series of three samples for with the determination of compressive strength (PTL). Calculation of compressive strength was carried out according to Equation 1. Measured values of compressive strength are shown in Table 2.

$$PTL = \frac{F}{S} \tag{1}$$

Kde PTL is compressive strength (MPa)
F – power (N)
S – area (mm2)

Table 2: Measured values of compressive strength

Sample	**Average compressive strength (MPa)**		
	2 days	7 days	28 days
S1	2,11	2,14	2,07
S2	3,73	6,66	11,92
S3	8,41	8,96	12,38

Slags marked as S2 and S3 has suitable hydraulic properties. Slags S2 and S3 have a high compressive strength. Slags have compressive strength of about 12 MPa after 28 days of hydration. These values are important for the use of such slags as a binder phase for the preparation of fine grained compact samples from waste material. Slag S1 has a low compressive strength value of only about 2 MPa. The strength of about 2 MPa is sufficient of handling with the prepared samples.

The second stage of work was pelletization of fine grained waste materials. To create briquettes were used waste materials shown in Table 4 and coke which is needed for the metallurgical reaction. Ferric share is represented by ferric sludge which by chemical analysis containing 15.2 wt.% Fe and fine sludge KKO containing 63.0 wt.% Fe. In this work were used two types of dust from the ladle furnace. These dusts from ladle furnace have different chemical composition. Both types of ladle furnace dust by chemical composition contain high amounts of CaO (25% and 31%). The high lime content can cause after mixing with water volume increase, which will lead to the disintegration of the product. This hypothesis was confirmed. Dust mixture from the ladle furnace was mixed with water and poured into metal molds. At the beginning there was a hardening the mixture, but after approximately 24 hours the prepare samples started to disintegrate spontaneously. Before use dust from the ladle furnace, it was necessary to moisten and store 3 days for hydration box. Prepare dust already did not shown dimensional stability and are not subject to disintegration.

From the raw materials supplied was compiled mixture. Then the samples were created. Ingredients for the formed briquettes are given in Table 3.

Table 3: Ingredients for the mixture

Materials	**Briquettes**						
	A	B	C	D	E	F	G
	Composition (%)						
Technical Al_2O_3	15,0	15,0	15,0	15,0	15,0	15,0	15,0
Ferric sludge	-	-	-	15,0	15,0	15,0	15,0
Fine sludge KKO	15,0	-	15,0	-	-	-	-
KKO concentrate	-	15,0	-	-	-	-	-
Coke	5,0	5,0	5,0	5,0	5,0	5,0	5,0
Dust mixture from ladle furnace	30,0	30,0	30,0	30,0	30,0	-	-
Dust mixture from ladle furnace PP1	-	-	-	-	-	30,0	30,0
Slag S1	35,0	35,0	35,0	-	-	-	-
Slag S2	-	-	-	35,0	-	35,0	-
Slag S3	-	-	-	-	35,0	-	35,0
Humidity	-	-	22,0	22,0	22,0	22,0	22,0

The prepared mixtures were homogenized in a mixer for 2 minutes. The resulting mixture was then poured into metal mold with a diameter of 50 mm. The mixture was the draw force of approximately 20 kN and speed at 500 kN s^{-1}. It was created briquette 50 mm (±5 mm) in height and a diameter of 50 mm. The used as sample weight in the range of 200 g to 300 g depending on the composition of the raw material mixture. Figure 1 shows produced briquettes.

Figure 1: Produced briquettes A to G

Each series was prepared in a number of 6 pieces of briquettes. Prepared briquettes were stored hydration box at 2, 7 and 28 days. After 2, 7 and 28 days were performed on the prepared briquettes test compressive strength. They were two samples for each measurement. Measured values of compressive strength to the prepared briquettes are shown in Table 4.

Fine-grained waste materials were used for the preparation of briquettes without modification as supplied. The exceptions were slags that were finely ground.

Table 4: Compressive strength on the prepared briquettes

Days of hydration	**Briquettes** A	B	C	D	E	F	G
	Compressive strength (MPa)						
2 days	1,79	1,38	4,70	2,84	5,04	5,47	1,21
7 days	2,49	2,01	5,29	9,41	5,43	5,62	1,49
28 days	2,61	2,79	9,16	15,30	15,30	7,28	3,07

3 Conclusion

The aim was to create a compact sample of the raw material. Pelletization grained-wastes material is possible. For pelletization were used ladle slags with appropriate hydrating properties. The compressive strength of the samples was affected by the type of slags. The best compressive strength have sample D and E. In the sample D and E were used slag S2 and S3. These samples have a compressive strength 15.30 MPa after 28 days of hydration. Compressive strength produced briquettes also affects the amount of mixing water. This fact is confirmed a series of briquettes A and C. These briquettes have the same raw material composition, differing is only in the amount of mixing water. Sample A was formed without addition of water (for hydration were used the moisture of the raw materials). This sample has a compressive strength 2.61 MPa after 28 days of hydration. Sample C was created with a humidity of 22% and compressive strength this sample is 9.6 MPa.

4 Acknowledgement

This paper was created under the Project No. CV6005531 „Support and development of international relationship and mutual foreign activities of students and staff on FMMI“, funded by VŠB – Technical University of Ostrava, Czech Republic and SP2015/125 Thermal waste treatment and environmental protection.

References

[1] Botula, J.: *Recyklace odpadů kovových a kovonosných.* 1st edition. ISBN 80-248-0495-6. Ostrava: Vysoká škola báňská - Technická univerzita, 2003, page 86.

[2] Hlaváč, J.: *Základy technologie silikátů.* 1st edition. Praha: SNTL-Nakladatelství technické literatury, 1981, page 516.

[3] Bárta, R.: *Chemie a technologie cementu.* 1st edition. Praha: Nakladatelství československé akademie věd, 1961, page 1107.

The influence of glassy carbon quantity on tribological properties in aluminum based composites prepared via powder metallurgy

Aleksandra Miczek[a], Paweł Krzywda[b], Bartosz Hekner[c]
Silesian University of Technology
Faculty of Materials Engineering and Metallurgy, ul.Krasińskiego 8, 40-019 Katowice, Poland
[a]a.miczek@wp.pl, [b]pawel.krzywda@interia.pl, [c]bartosz.hekner@polsl.pl

Abstract

This paper presents the impact of glassy carbon on morphologies and tribological properties of metal matrix composites reinforced with Al_2O_3 particles. The materials were produced using a high energy milling process in a planetary mill and afterwards synthesized by a hydraulic press. The composites and the powders microstructure observation after milling process was conducted on scanning electron microscope (SEM).

In article the results of Al-Al_2O_3-GC composite tribological properties were presented. Friction tests were performed by pin-on-disc method under 35 and 50 N loads in constant parameters of velocity 0,05m/s at a distance 90m. The pin was made of cast iron (EN-GJL 300). The use of glassy carbon particles allows for correction of tribological properties. Among the analysed materials the most favourable results were obtained for the composite material with 5% glassy carbon addition.

Keywords: Metal Matrix Composites, glassy carbon, quantity, pin-on-disc, wear, friction.

1 Introduction

Nowadays, metal matrix composites (MMC) are widely used in various areas, e.g. automobile, aerospace, industry. Because of their numerous advantages like high strength and wear resistance they are used for instance in automobile brake rotors. The most common matrix used in MMC is aluminium with regard to its good corrosion resistance, low destiny. [1] A well- known tendency in metal matrix composites, which are used as a tribological materials is the ceramic particles reinforcement. The most popular are Al_2O_3 and SiC. Their use is connected with their good physical properties and economical aspects. [2, 3]

Glassy carbon is the amorphous one of the carbon phase. The appropriate properties like low share resistance and high hardness make them a proper solution for tribological applications. Glassy carbon addition reduces the friction coefficient value up to an advisable level and stabilized tribological properties. [3, 4]

Besides the classical metal- ceramic composites production methods, as casting, it is also used the powder metallurgy technology. This method consists of mixing the powders in a high energy mill where occur the bonding of the hard ceramic particles and the plastic matrix. Afterwards, the composite powders are pressed and sintered. It allows to obtain the composite material with uniform distribution of ceramic particles in the matrix. [5]

2 Experimental

Presented materials were obtained by powder metallurgy method. The initial materials to produce composites were powders of Al, Al_2O_3 and glassy carbon (GC) with parameters given in Table 1.

Table 1: Powders properties.

Material	Size [µm]
Al	45-63
Al_2O_3 (Martoxid®MR70)	0.1-3
GC	40-200

In the beginning, all components were subjected to a high-energy milling in a planetary mill Fritsch Pulverisette 6 Classic Line. The milling process was conducted with 650 rpm of velocity during 2 hours. The milling process was divided into the 24 cycles of 5 minutes of milling and 30 minutes of break. The grinding bowl and grinding media were made of steel. Subsequently, the obtained composite powders were synthesis in the Degussa press. The operation was conducted in vacuum 10-3 Torr with parameters presented in Table 2.

Table 2: Synthesis parameters.

	Stage	
	I	II
Time [min]	20	15
Temperature [°C]	480	640
Pressure [MPa]	10	

The analysis of the microstructure, shape and size of the composite powders and composite materials grains were made by using a scanning electron microscope SEM Hitachi S-3400N. During the observation secondary electron image (SE) applied an accelerating voltage of 25 kV was registered. Tribological properties of produced composite materials were assessed. The research was accomplished on the pin-on-disc tribometer at room temperature under the friction in air conditions with 35N and 50N of loads. The counterpart material was cast iron EN GJL300. The pin was sliding on the sample surface with $0.05\,\mathrm{m\,s^{-1}}$ velocity, on the distance of 90 m.

3 Results

The samples for further research were received. Their chemical composition was presented in Table 3.

Table 3: Materials composition.

Sample sign		**Composition** Mass fraction [g]	Proportional fraction [%]
Al-Al_2O_3	Al_2O_3	3	15%
	Al	17	85%
Al-Al_2O_3-5GC	Al_2O_3	3	15%
	Al	16.15	80%
	GC	0.85	5%
Al-Al_2O_3-10GC	Al_2O_3	3	15%
	Al	15.3	75%
	GC	1.7	10%
Al-Al_2O_3-15GC	Al_2O_3	3	15%
	Al	14.45	70%
	GC	2.55	15%

The composite powders microstructure observation indicated that after the high energy milling process, the aluminium particles have been deformed and flattened under the effect of collisions with the milling mediums and the walls of the milling bowl (Figure 1). The Al-Al_2O_3-15GC composite powder not only had it particles deformed but also it crumbled, that the powder has a finer grain than the other composite powders (Figure 1d). This fact is the evidence that the addition of a glassy carbon improves the milling process. The Al-Al_2O_3 powder without GC addition, only slightly deformed in the high energy milling process (Figure 1a).

The composite material microstructure was observed for rating the homogeneity of particles distribution in the volume of material. GC particles (shown as black areas) in heterogeneous composites (Al-Al_2O_3-5GC, Al-Al_2O_3-10GC, Al-Al_2O_3-15GC) are of comparable sizes, in spite of their various participation in materials (Figure 2). The composites with GC addition contain the pure aluminium space without reinforcement contribution (Figure 2b-d), which shows the problems of uniform distribution of reinforcement particles in the material. This may be caused by the inappropriate milling or synthesis parameters selection. For Al-Al_2O_3-5GC composite material the reinforcement particles have a good quality of bonding to the matrix (Figure 2b). The remaining materials have pores at grain boundaries.

The conducted friction tests were related to usable properties of composite materials assessment. The composites friction and friction coefficient were measured. Afterwards, on the basis of the results, the graphs of friction coefficient as a function of the distance (Figure 3) and mass loss of composite materials and counter sample material (Figure 4) were prepared.

The presented charts for friction coefficient as a function of the distance with the load 35N and 50N indicated that the most favourable properties had Al-Al_2O_3-5GC composite material with 5% GC addition. It is featured by friction coefficient stability over the whole

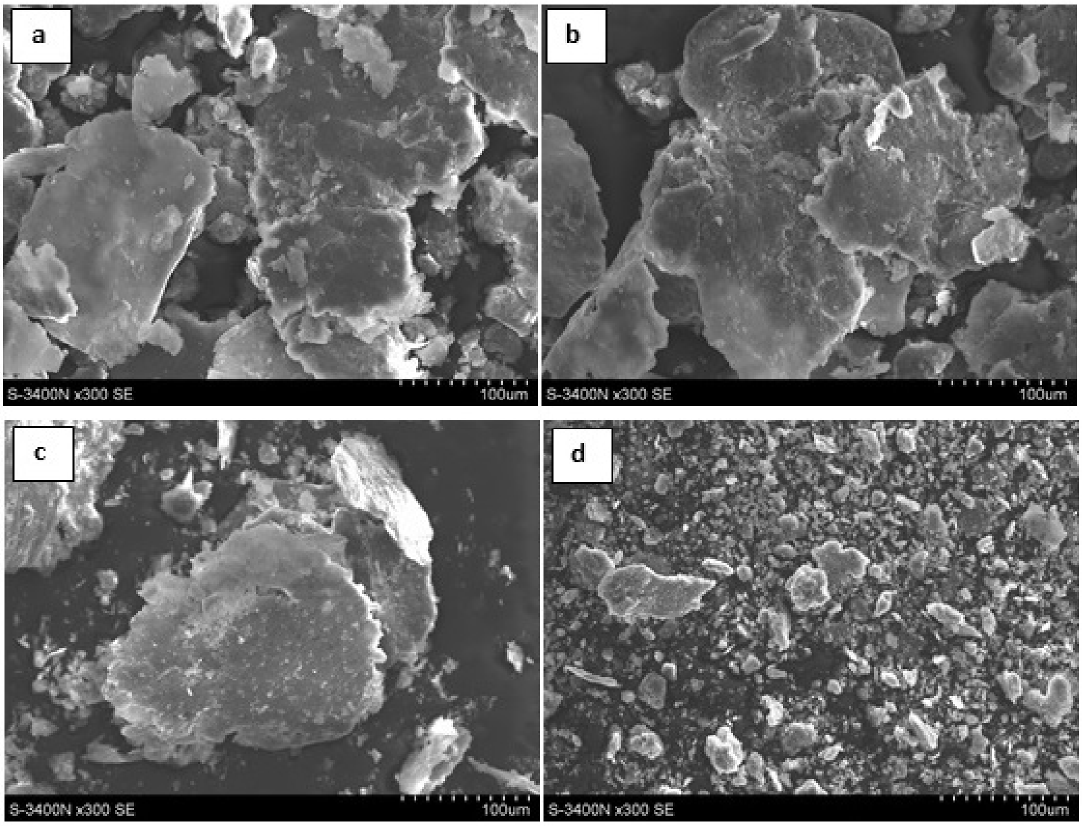

Figure 1: The microstructure of composite powders, SEM a) Al-Al_2O_3, b) Al-Al_2O_3-5GC, c) Al-Al_2O_3-10GC, d) Al-Al_2O_3-15GC.

range of distance. The sample Al-Al_2O_3-15GC had very unstable coefficient of friction in both load cases. This fact may indicate that the 15% GC addition is too much and it definitely excludes the usefulness of such material.

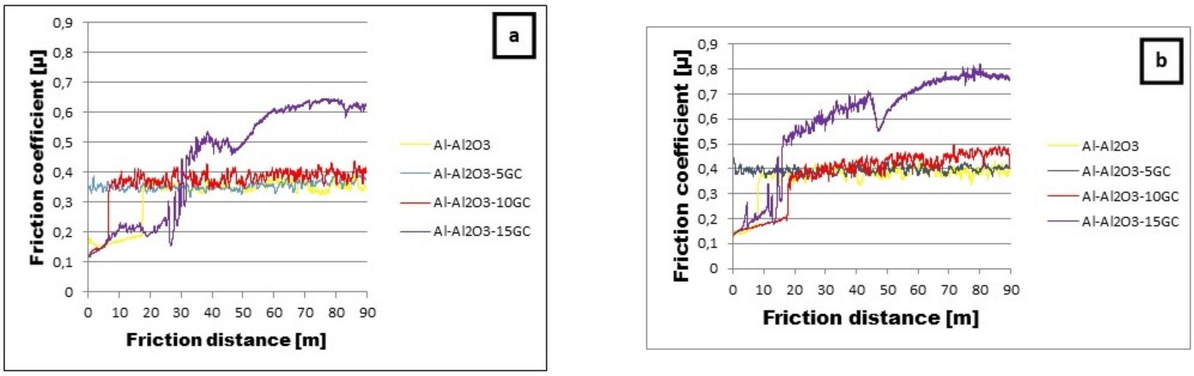

Figure 3: The friction coefficient as afunction of the distance a) 35 N, b) 50 N of loads.

The charts of composite materials and counter sample material mass loss illustrate both materials wear under dry conditions (Figure 4). According to the graphs the lowest attrition value characterized Al-Al_2O_3 sample. However, the GC application caused a decrease in counter sample wear. According to that the most beneficial properties have Al-Al_2O_3-5GC material, which characterized both, high wear resistance and almost zero mass loss of pin material (EN GJL300).

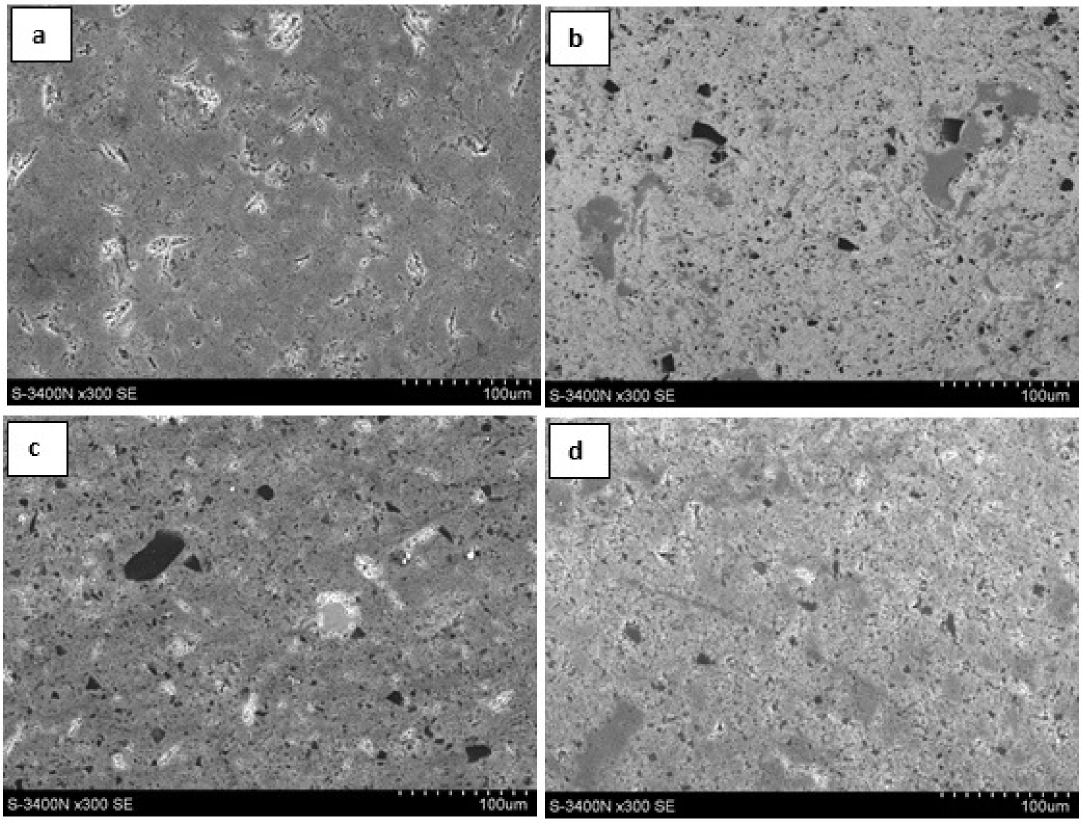

Figure 2: The microstructure of composite materials, SEM a) Al-Al_2O_3, b) Al-Al_2O_3-5GC, c) Al-Al_2O_3-10GC, d) Al-Al_2O_3-15GC.

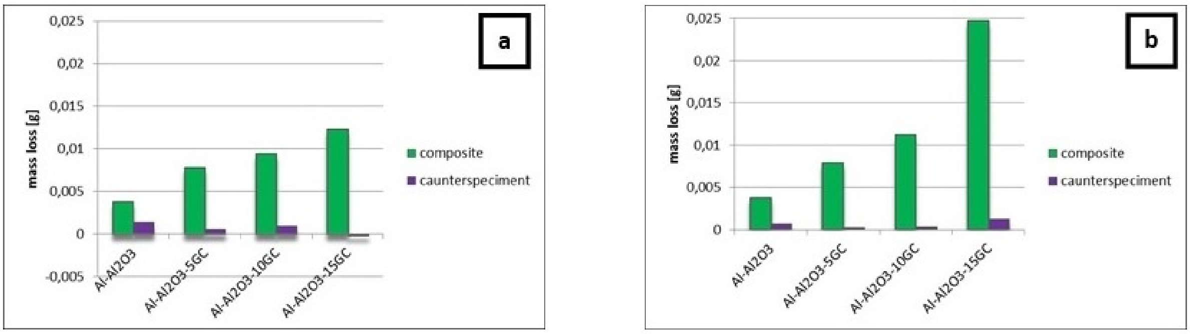

Figure 4: The mass loss of composite and counter sample materials with a) 35 N, b) 50 N of loads.

4 Conclusions

It is a possible to produce homogeneous and heterogeneous composites characterized by a good bonding between the matrix and the reinforcement particles. The engaged researches allowed to assess the impact of glassy carbon quantity on produced composite materials tribological properties. It was observed that GC addition improved the high energy milling process. The evidence of this statement could be more effective for more fragmented and deformed particles for materials containing GC. The friction tests proved that the most expedient properties from all analysed samples have Al-Al_2O_3-5GC composite material.

It revealed a stable friction coefficient. Furthermore, it has satisfactory wear resistance simultaneously has not caused the pin material wearing .

References

[1] Mazaheri, Y., Karimzadch, F., and Enayati, M. H.: "Nanoindentation study of Al356-Al2O3 nanocomposite prepered by ball miling". In: *Materials Science and Applications* 1 (2010), pages 217–222.

[2] Hafizpour, H. R., M.Sanjari, and Simchi, A.: "Analysis of the effect of reinforcement particles on the compressibility of Al-SiC composite powders using a neural network model". In: *Materials and Design* 30 (2009), pages 1518–1523.

[3] Hekner, B. et al.: "The manufacturing process and tribological properties of aluminum based composite reinforced with aluminum oxide particles and glassy carbon additions". In: *Materiały i technologie XXI wieku' XVI Międzynarodowa Studencka Sesja Naukowa*. 2014, pages 136–139.

[4] Myalski, J.: *Kształtowanie właściwości tribologicznych kompozytów zawierających węgiel szklisty*. 2011.

[5] Hekner, B. et al.: "Aluminum - ceramic composite materials reinforced with nanoparticles prepared via powder metallurgy method". In: *Composites Theory and Practice* 3 (2013), pages 203–207.

Tagungsbeitrag der Lech-Stahlwerke GmbH

Dr.-Ing. Jörg Lauscher
Lech-Stahlwerke GmbH
Industriestraße 1, 86405 Meitingen

1 Die Lech-Stahlwerke GmbH in Bayern

1.1 Gründung der Lech Stahlwerke

1970 gegründet

-Einziges Stahlwerk in Bayern-
(bis heute)

Planproduktion 1972: 300.000 Betonstahlproduktion/Jahr

1.2 Die Produktion Heute, Bayerns größter Recyclingbetrieb

Erzeugung von bis zu 900.000 t Qualitätsstahl, insgesamt >1,1 Mio. t/a

LSW – Bayerns größter Recyclingbetrieb

Verwertete Schrottmengen in 1.000 Tonnen seit Produktionsbeginn am 19.03.72

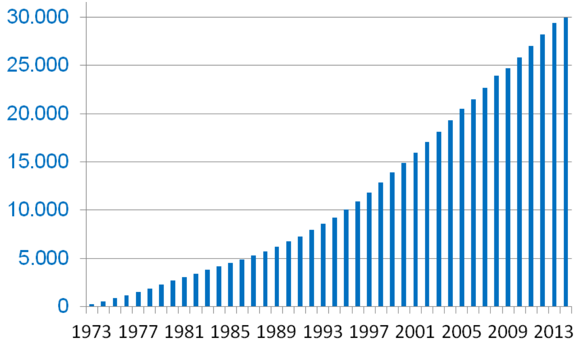

... mehr als 30 Mio. Tonnen recycelter Schrott
– das entspricht ca. 38 Mio. VW Golf.

2 Produktionsanlagen

2.1 LSW Process Chain for high grade steel

Two redundant melting lines

Schmelzbetrieb:

EAF →

→ LF →

→ VD →

→ SS

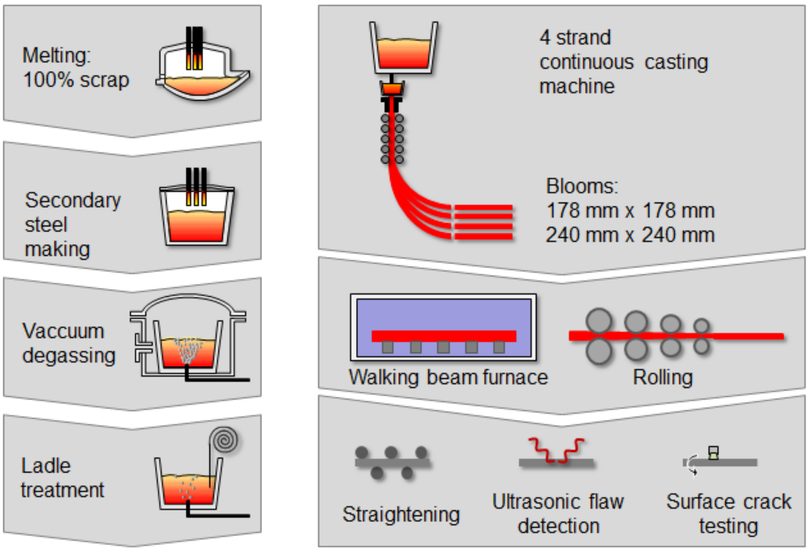

2x **Elektrolichtbogenöfen** mit bis zu 87 MVA Transformatoren und 12 MW Leistung: Kapazität 100 Tonnen
Tap to Tap-Zeit 1 Stunde
2x **Pfannenöfen** mit bis zu 25 MVA zur metallurgischen Behandlung und Einstellung der chem. Analyse
Je 2x **Vakuumentgasung** und **Spülstände** zur Reinheitsgradsoptimierung

2.2 Gießbetrieb

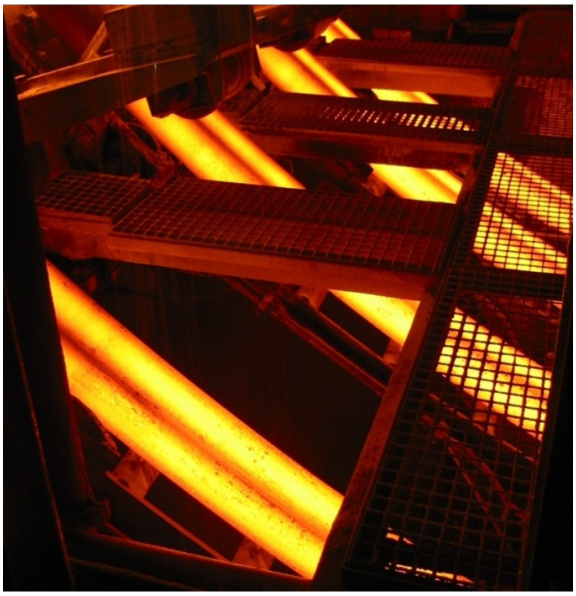

Gießbetrieb:

- 2 x 4-adrige Stranggießmaschinen für Vierkantformate von 130 bis 240 mm
- max. Länge: 6000 mm

2.3 Warmwalzwerk BST

Betonstahlwalzwerk:
Abmessungen 8 – 32 mm, max. Länge: 24m

2.4 Warmwalzwerk EST

Abmessungen
rund 31 – 65 mm, max. Länge: 12 m
rund 66 – 130 mm, max. Länge: 9 m
vierkant 50 -120 mm, max. Länge: 9 m

EST: Edelbaustahl

2.5 Adjustage / Nachbehandlung

„In der Adjustage werden unsere Produkte unterschiedlichen Wärmebehandlungen zugeführt und versandfertig gemacht.“

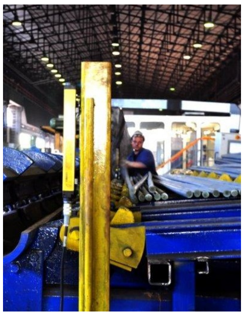

Richten

Verwechslungsprüfung

Wärmebehandlung

2.6 Qualitätssicherung

„In der Endkontrolle unterziehen wir unsere Erzeugnisse aufwendigen Prüfverfahren. So garantieren wir unseren Kunden ein Höchst-maß an Qualität und Sicherheit beim Einsatz unserer Produkte.“
Frühzeitige Erkennung von Oberflächenfehlern oder Einschlüssen sichern ein Höchstmaß an Qualität.

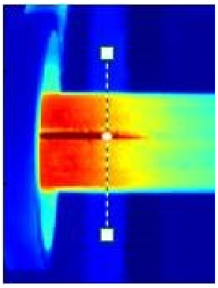

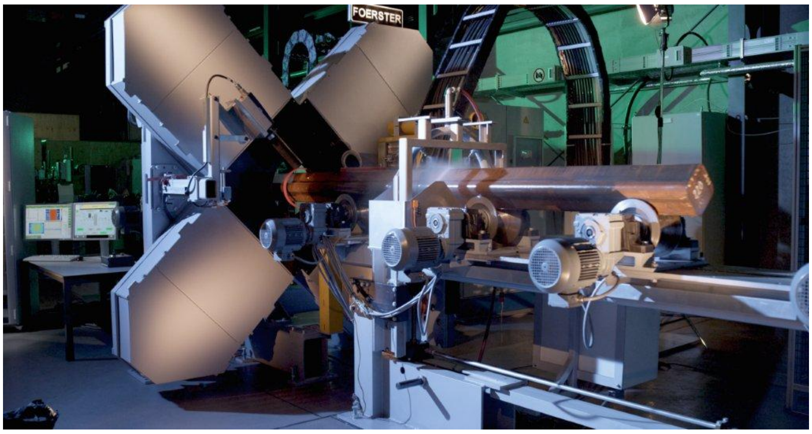

Fehlerprüfung für Stäbe als Ausgangsprodukt für Kurbelwellen, Motor- und Fahrwerkskomponenten.

Das **Wärmeflußthermographieverfahren** bei LSW setzt Maßstäbe: Prüfgeschwindigkeit **bis 1,5 m/s**; präzise und reproduzierbare Fehlererkennung; effektive Unterdrückung von Fehlanzeigen

2.7 Qualitätsmanagement

„In unseren Laboren stehen diverse Verfahren zur werkstofftechnischen Analyse zur Verfügung. Durch die Qualitätssicherung während des gesamten Produktionsprozesses und kontinuierliche Prozessoptimierung können Kundenanforderungen trotz sehr enger Toleranzen stets erfüllt und unsere Werkstoffe kontinuierlich weiterentwickelt werden.“

Richten

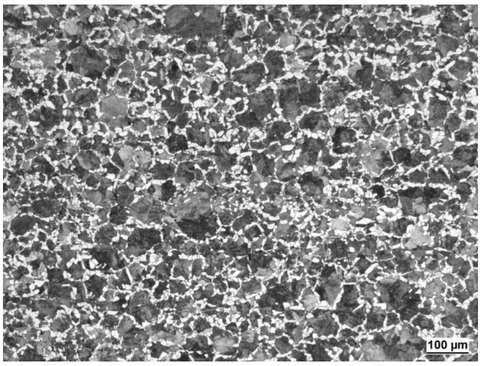

Verwechslungsprüfung

Wärmebehandlung

2.8 Lech-Stahl Veredelung

Richten, Wärmebehandlung, Schneiden, Schälen, Polieren, Endprüfung

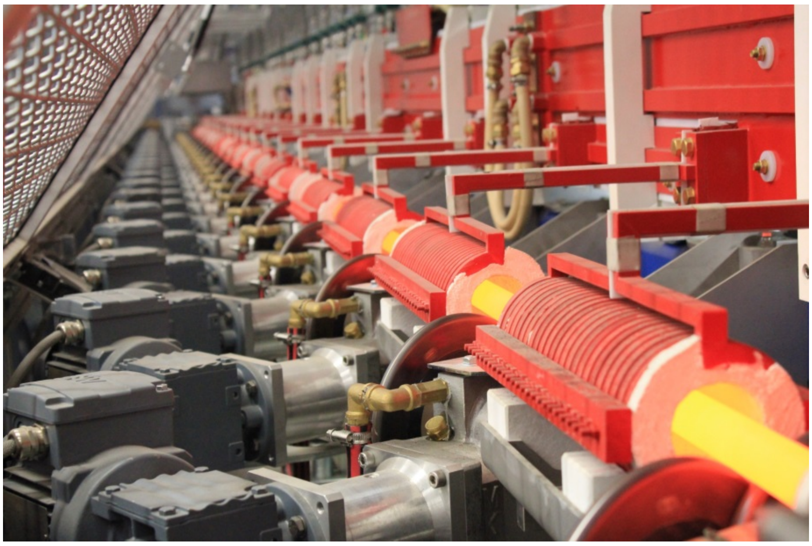

80 Meter lange Vergütungsanlage bei der LSV

3 Drei Sorten: Einsatzstähle, Vergütungsstähle, AFP-Stähle

3.1 Einsatzstähle

Der niedrige Kohlenstoffgehalt des Einsatzstahls reicht nicht für eine ausreichende Härtung des Bauteils aus. Daher werden diese Stähle in einer kohlenstoffhaltigen Atmosphäre bei Temperaturen von 850 - 1050°C geglüht also „eingesetzt“. Aufgrund der hohen Temperaturen kann der Kohlenstoff aus der Ofenatmosphäre von außen in die Oberfläche eindringen.

Damit wird der Kohlenstoffanteil in der Randschicht des Bauteils etwa vervierfacht. Die aufgekohlte Randschicht wirkt sich positiv auf die Bauteileigenschaften aus.

Ein geringer Kohlenstoffanteil im Inneren bedingt eine hohe Zähigkeit, während die Oberfläche eine erheblich höhere Härte und somit auch eine größere Widerstandsfähigkeit gegen äußeren Verschleiß zeigt.

Diese willkommene Eigenschaftskombination wird für Zahnräder, Wellen oder Bol-zen genutzt. Bekannte Vertreter dieser Gruppe bei den Lech-Stahlwerken sind Bauteile in Getriebe und Antrieben.

Antriebkreuz im Antriebsgelenk und Kardanwelle – 16MnCr5 / 20MnCr5

Getriebebauteil – ZF7B

3.2 Vergütungsstähle

Einsatzgebiet

dort wo hohe Festigkeit bei ausreichender Zähigkeit gefordert ist, z.B. Schrauben oder Kolben

Verarbeitung

Damit der Stahl noch gut schmiedbar ist, erfolgt das Vergüten nach der Umformung.
Schritt 1 Härtung: Erwärmen/Halten bei >850°C und Abschrecken in Wasser/Öl
Schritt 2 Zähigkeitssteigerung: Anlassen bei ca. 600°C und Abschrecken bzw. Abkühlen

Ergebnis

Ferrit-Perlitisches Walzgefüge wird über nadeligem Martensit zu angelassenem Martensit.

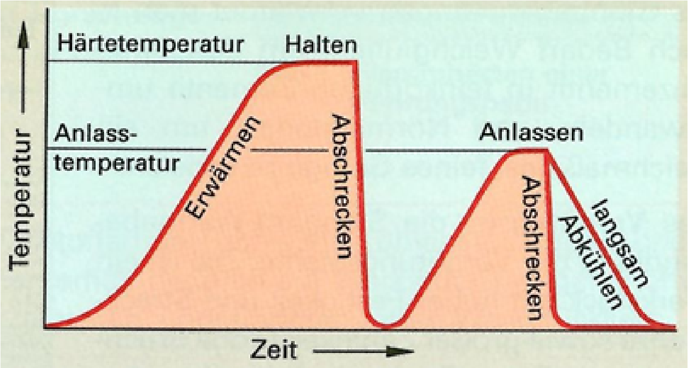

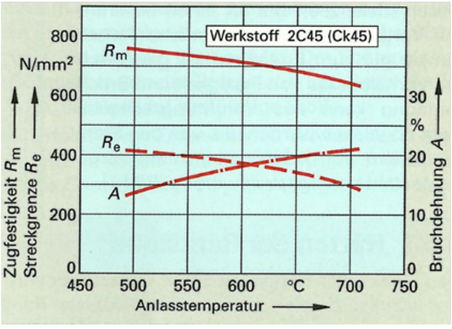

3.3 AFP-Stähle (Ausscheidungshärtende Ferritisch-Perlitische Stähle)

Einsatzgebiet

in der Edelbaustahlproduktion z.B. für Kurbelwellen, Pleuelstangen, Achsschenkel

Verarbeitung

Schritt 1 Warmschmieden: Zulegiertes Vanadium löst sich vollständig bei einer Tem-peratur von ca. 1250° auf
Schritt 2 kontrollierte Abkühlung: Entstehung von Vanadiumcarbiden sowie Carbonitriden

Ergebnis

kostengünstiger als Vergütungsstahl, da zeit- und energieaufwendige Vergütungsbehandlungen entfallen → Erreichung gewünschter mechanischer Eigenschaften

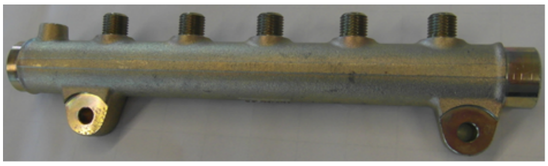

Rail für die Common-Rail-Einspritzung eines Dieselmotors

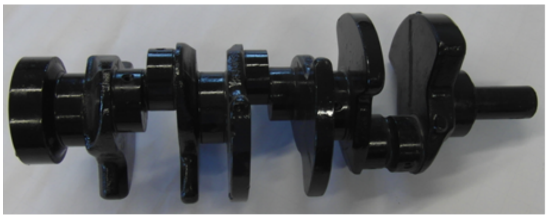

Kurbelwelle - 38 MnVS6

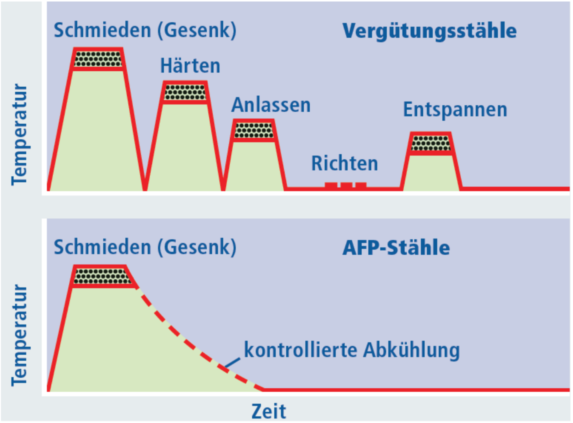

4 Schwerpunkt Automobilindustrie

„LSW ist einer der bedeutendsten Zulieferer der europäischen Schmiedeindustrie. In nahezu jedem europäischen Auto ist Qualitätsstahl der Lech-Stahlwerke verbaut. Darüber hinaus findet unser Stahl Einsatz vor allem im Maschinen- und Anlagenbau sowie der Werkzeug- und Kettenindustrie.“

5 Stahleinsatz in Projekten

„Der Einsatz unseres Stabstahls erfolgt in namenhaften Bauprojekten sowie im technischen Ingenieurbau in der ganzen Welt.“

Patentierte SAH-Gewindestahl-Produkte im Einsatz beim **Bau des neuen World-Trade-Center, NYC**

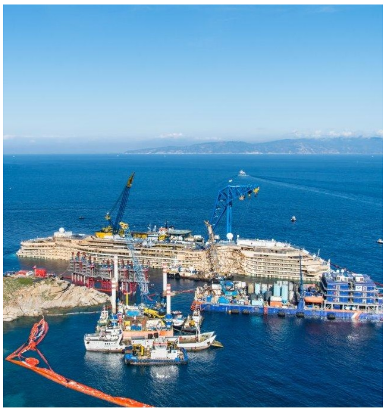

Gewindestahl-Sonderlösung für die **Bergung der Costa-Concordia**

WM-Finale 2010: **Soccer-City-Stadium (Johannesburg/SA)**, errichtet mit SAH-Know-How

Einfluss einer lauwarmen Umformung auf die Gefügeausbildung in einem umwandlungsträgen Vergütungsstahl und dessen Einfluss auf ausgewählte Eigenschaften

Paper zur Ingenieurarbeit vom 07.10.2014 für den XXII. ISDM 2015

E. Frank Sandig
TU Bergakademie Freiberg
sandigf@mailserver.tu-freiberg.de

1 Einleitung

Neuere Untersuchungen von härtbaren Stählen, insbesondere Vergütungsstählen, haben gezeigt, dass diese in der Nähe der M_s-Temperatur einen Transformation Induced Plasticity (TRIP)-Effekt aufweisen [1]. Dieser Effekt ist bereits von hochlegierten Stählen bei tiefen Temperaturen bekannt. Die Umwandlungsplastizität ermöglicht es, Vergütungsstähle lauwarm umzuformen und so mit reduziertem Energieaufwand und bei im Vergleich zum Presshärten höherem Umformgrad höchstfeste Formteile [1] oder hochfeste und bruchzähe Befestigungselemente [2] herzustellen.

Dieses Paper präsentiert ausgewählte Ergebnisse einer Ingenieurarbeit über die lauwarme Umformung eines umwandlungsträgen Vergütungsstahls [3].

Bezüglich der Ausnutzung des TRIP-Effekts bei der Herstellung höchstfester Formteile aus Vergütungsstahl mittels lauwarmer Umformung ist ein Patentantrag beim Deutschen Patent- und Markenamt anhängig [1]. Der Volltext der Ingenieurarbeit sowie zwei Präsentationen sind unter `http://sandig-fg.de` verfügbar.

2 Grundlagen

Bei der im Rahmen der in [3] untersuchten Legierung handelt es sich um einen umwandlungsträgen legierten Vergütungsstahl.

Tabelle 1: Ist-Analyse der untersuchten Legierung, Angaben in Masse-%

Fe	**C**	**Si**	**Mn**	**P**	**S**	**Cr**	**Ni**
93,3	0,355	0,426	0,449	0,0064	0,0069	2,08	3,25

2.1 Verformungsinduzierte Plastizität

Viele neu entwickelte sowie einige bereits länger bekannte Stahlwerkstoffe zeigen TRIP- und/oder Twinning Induced Plasticity (TWIP)-Effekte. Diese Effekte der verformungsinduzierten Plastizität sind für die Entwicklung neuer Werkstoffe von besonderem Interesse. TRIP bezeichnet die verformungsinduzierte Umwandlung von metastabilem Austenit in α'-Martensit oder ϵ-Martensit. Beide Arten haben einen ähnlichen Einfluss auf die mechanischen Eigenschaften der Legierung. Der α'-Martensit stellt die thermodynamisch stabilere Phase dar. TWIP steht für die verformungsinduzierte Bildung von Zwillingen im metastabilen Austenit. Da sich beide Effekte häufig überlagern, wird in der Literatur meist vom TRIP/TWIP-Effekt gesprochen [4]. Eine Besonderheit der verformungsinduzierten Gefügeumwandlung ist die gleichsinnige Zunahme von sowohl der Dehnbarkeit in Form der Bruchdehnung oder Gleichmaßdehnung als auch der Festigkeit des Werkstoffes. Abbildung 1 veranschaulicht diesen Effekt an Hand einer schematischen Spannungs-Dehnungs-Kurve [5].

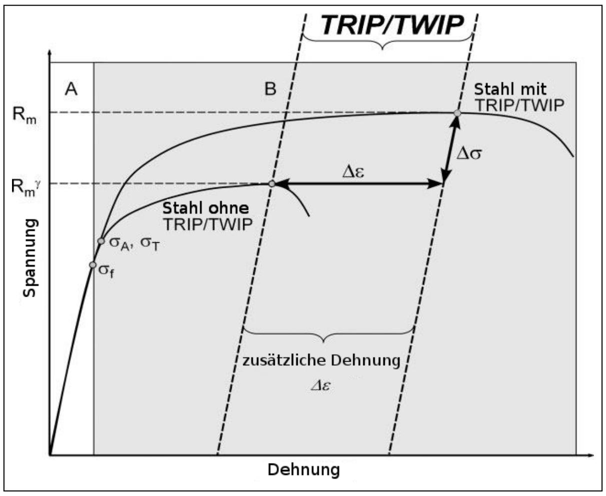

Abbildung 1: Schematischer Verlauf einer Spannungs-Dehnungs-Kurve mit und ohne TRIP/TWIP-Effekt [5]

Der Festigkeitszuwachs stammt einerseits von der Bildung einer neuen Phase mit höherer Festigkeit (Martensit), andererseits entsteht er durch die Behinderung des Versetzungsgleitens durch die neu gebildeten Phasengrenzflächen und entstandene Gitterdefekte [6]. Zur Erklärung des Dehnungszuwachses werden in der Literatur die Volumenzunahme bei der Martensitbildung, Scherbewegungen bei der Martensit- und der Zwillingsbildung sowie Verzögerung der Einschnürung durch lokal stärkere Verfestigung im Einschnürungsbereich genannt [4].

2.2 Thermodynamik der Martensitbildung

In metastabilen Stählen liegt im Austenit eine Triebkraft für die Martensitbildung vor. Diese reicht jedoch nicht für eine spontane Martensitbildung aus. Die thermodynamischen Zusammenhänge sind in Abbildung 2 dargestellt [5, 7]. Bei unterschreiten der Temperatur M_s bildet sich aus dem Austenit spontan 1 Vol.-% Martensit. Liegt die Temperatur darüber, so ist ein zusätzlicher mechanischer Energiebetrag aufzubringen. Unterhalb der

Temperatur $M_{s\sigma}$ setzt die Martensitbildung bereits bei elastischer Verformung ein. Dabei steigt zwar die Festigkeit, der Effekt führt jedoch nicht zu einer Erhöhung der plastischen Dehnung und ist daher nicht erwünscht. Mit M_d wird die obere Temperaturgrenze für verformungsinduzierte Martensitbildung bezeichnet. An dieser Stelle ist die Auslösespannung für die Martensitbildung gleich der Zugfestigkeit des Austenits. Bei $M_{s\sigma}$ ist die Auslösespannung dagegen gleich der Streckgrenze des Austenits. Der Bereich zwischen $M_{s\sigma}$ und M_d ist für die Ausnutzung des TRIP-Effektes von besonderer Bedeutung. In diesem Intervall kommt es zu dem erwünschten plastischen Dehnungszuwachs [4, 5, 7, 8].

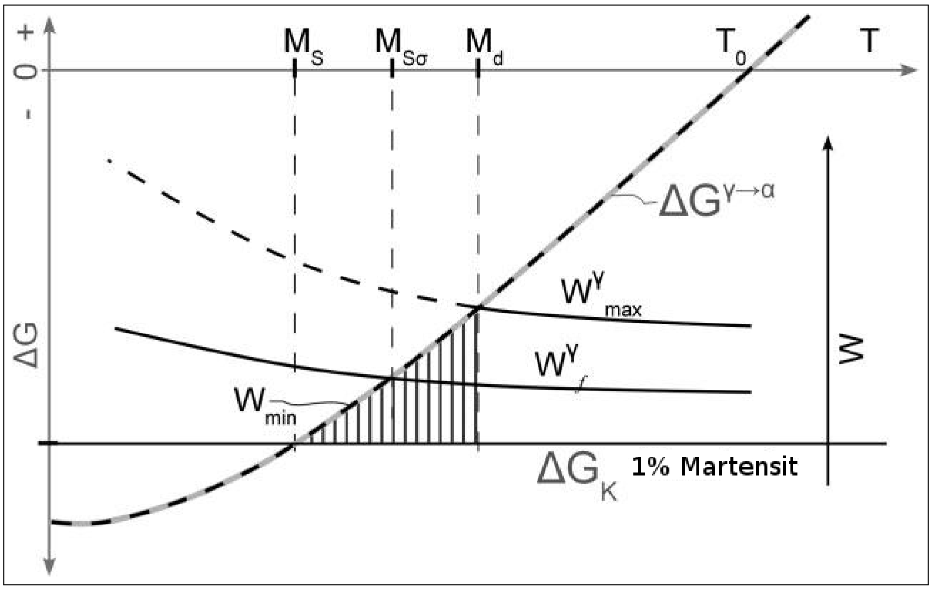

Abbildung 2: Thermodynamik der Martensitbildung, schematisch [5]

2.3 Lauwarme Umformung

Allgemeines

Der Begriff lauwarme Umformung bezeichnet eine Umformung bei Temperaturen von 200 °C bis 500 °C. In diesem Temperaturbereich kommt es nicht zu einer Rekristallisation. Während der Umformung verfestigt der Stahl. Bei lauwarmer Umformung während des isothermen Haltens in diesem Bereich wird nach Überschreiten eines kritischen Umformgrades ein TRIP-Effekt ausgelöst. Nahe der M_s-Temperatur sind bereits geringe Umformgrade ausreichend. Bei härtbaren Stählen werden mit diesem Vorgehen höhere Umformgrade als bei herkömmlichem Presshärten erreicht [1]. Abbildung 3 stellt einen lauwarmen Umformprozess schematisch mit Einordnung in ein ZTU-Diagramm dar.

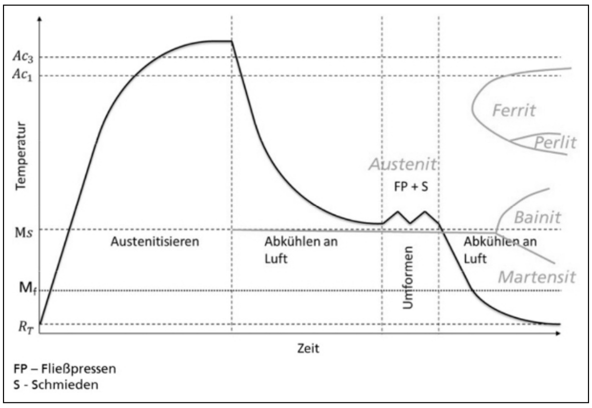

Abbildung 3: Schema eines Umformprozesses im metastabilen Austenitbereich [2]

Eigenschaftsverbessernde Mechanismen

Bereits seit längerer Zeit sind Mechanismen bekannt, welche bei lauwarmer Umformung zur Eigenschaftsverbesserung beitragen können. So kommt es zu einer Korngrößenverfeinerung des aus dem Austenit gebildeten Martensits [9–11]. Die Kaltverfestigung des Austenits wird an den Martensit vererbt [12–14]. Es bildet sich eine Verformungstextur aus [15–17]. An den Gleitlinien des Austenits kommt es zur feindispersen Ausscheidung von Carbiden [9, 18, 19]. Die Störstellen- und Versetzungszahlen nehmen zu [9, 13]. Darüber hinaus bilden sich Stapelfehler und Substrukturen aus [12]. Der TRIP-Effekt im metastabilen Austenitbereich wurde bislang nicht berücksichtigt. Bereits im Jahre 1968 stellte Wolfgang Lehnert bei einer Umformung nahe M_s einen Plastizitätszuwachs fest. Dieser Effekt konnte zum damaligen Zeitpunkt nicht erklärt werden [20]. Im Vergleich zu herkömmlichem Martensit entsteht bei lauwarmer Umformung ein feindisperser und höherfester Martensit mit verbesserten Zähigkeitseigenschaften. Unter Umständen kann somit eine Anlassbehandlung eingespart werden [2].

Umformversuche

Die Versuche zur lauwarmen Umformung im Rahmen der zu Grunde liegenden Arbeit [3] wurden in Form von Zylinderstauchversuchen durchgeführt. Dabei handelt es sich um eine Variante des Druckversuches mit zylindrischen Proben. Aus der aufgenommenen Kraft-Weg-Kurve wird die Fließkurve des Werkstoffes berechnet, wobei der Versuch nicht bis zum Bruch, sondern bis zu einem bestimmten Vergleichsumformgrad φ geführt wird [21]. Für die Fließspannung erhält man unter Voraussetzung eines einachsigen Spannungszustandes und mit Volumenkonstanz aus dem Kräftegleichgewicht an der Probe:

$$k_\mathrm{f} = \frac{F}{A_0}\frac{h}{h_0} = \frac{F}{\pi {r_0}^2}\frac{h}{h_0} \tag{1}$$

Diese Fließspannung wird schließlich über dem Vergleichsumformgrad

$$\varphi = \ln\left(\frac{h_0}{h}\right) = -\ln\left(1+\varepsilon\right) = -\varepsilon_\mathrm{w} \tag{2}$$

aufgetragen. Diese Beziehungen sind gültig, so lange die Ausbauchung der Probe vernachlässigt werden kann. Um dies möglichst lange sicherzustellen, werden die Stirnflächen der Probe geschmiert. Bei Stahlwerkstoffen sollte das Verhältnis $\frac{h}{2r_0} \approx 1{,}5 \dots 2$ betragen [21]. Die Abmessungen der verwendeten Zylinderproben betrugen $\varnothing 10\,\mathrm{mm} \times 18\,\mathrm{mm}$. Die Proben wurden mit $5\,\mathrm{K\,s^{-1}}$ auf 840 °C austenitisiert und nach einer Haltezeit von 10 min schnellstmöglich im Werkzeug auf Umformtemperatur abgekühlt. Die Umformtemperaturen betrugen 270 °C, 290 °C, 310 °C, 330 °C und 350 °C. Beginnend bei diesen Temperaturen erfolgte das Umformen von Material im Gusszustand und warmgewalztem Material jeweils bis zum Vergleichsumformgrad $\varphi = 0{,}3$, $\varphi = 0{,}6$ und $\varphi = 1{,}0$ mit stets der gleichen Umformrate von $\dot{\varphi} = 0.1\,\mathrm{s^{-1}}$. Die Proben mit der Ausgangshöhe von 18 mm besaßen nach der Umformung mit $\varphi = 0{,}3$, $\varphi = 0{,}6$ und $\varphi = 1{,}0$ jeweils eine Endhöhe von ca. 13.3 mm, 9.9 mm bzw. 6.6 mm hatten. Das entspricht einer relativen Änderung der Probenhöhe von 26,1 %, 45,0 % und 63,3 %.

3 Experimentelle Methoden

Im Rahmen der Ingenieurarbeit [3] kamen folgende experimentelle Methoden zum Einsatz: Digitale Lichtmikroskopie, Funkenspektrometrie, Dilatometrie, Härteprüfung nach Vickers sowie Zugversuche. Auf die Methoden wird in der Arbeit näher eingegangen.

4 Ausgewählte Ergebnisse

Das vorliegende Paper beschränkt sich auf Ergebnisse von Versuchen mit Material im Gusszustand. Zum warmgewalzten Material und den Eigenschaften angelassener Proben vgl. [3].

4.1 Charakterisierung des Gusszustands

Metallografie

Das Gussgefüge der Probenlegierung ist in Abbildung 4 dargestellt. Das Gefüge ist seigerungsreich und relativ grobkörnig mit einer feineren Substruktur. Es ist deutlich zu erkennen, dass es sich um ein massivmartensitisches Gefüge handelt. Dies ist auf die hohe Abkühlgeschwindigkeit beim Abgießen zwischen gekühlte Kupferplatten und den Kohlenstoffgehalt der Legierung von rund 0,36 % zurückzuführen.

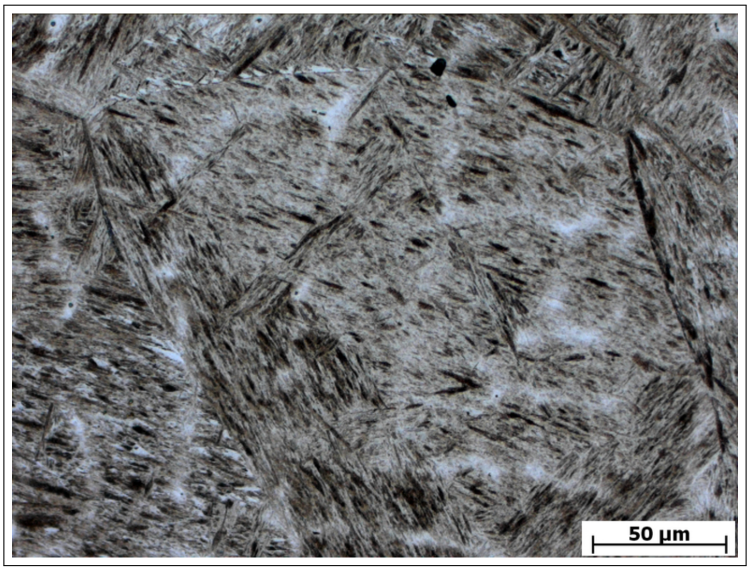

Abbildung 4: Gusszustand, 500x, Nital geätzt

Mechanische Eigenschaften

Die Härte des Materials im Gusszustand beträgt 627 HV10 mit einer Standardabweichung des Mittelwerts von 11 HV10. Diese hohe Härte ist, wie auch das Erscheinungsbild des Gefüges, auf die hohe Abkühlgeschwindigkeit in der wassergekühlten Kupferform zurückzuführen. Die folgende Tabelle 2 fasst die Ergebnisse der Zugversuche für den Gusszustand zusammen.

Tabelle 2: Ergebnisse der Zugversuche mit Material im Gusszustand

Kennung	Temperatur in °C	$R_{p0,2}$ in MPa	R_m in MPa	A_B in %	Z in %
AWI-G-Z4	19	1339	1932	10,3	14,2
AWI-G-Z5	19	1368	2022	7,1	17,5
Mittelwert	–	1354	1977	8,7	15,9

Der martensitische Gusszustand der Legierung AWI zeichnet sich durch eine sehr hohe Zugfestigkeit von ca. 2000 MPa und ebenfalls sehr hohe Streckgrenze von ca. 1400 MPa sowie eine für einen Gusswerkstoff unerwartet hohe Zähigkeit in Form der Bruchdehnung von ca. 9 % und der Brucheinschnürung von ca. 16 % aus. Die hohe Festigkeit entspricht bei einem Vergütungsstahl im martensitischen Zustand den Erwartungen. Die erhöhte Zähigkeit ist durch den relativ hohen Nickelgehalt der Probenlegierung von 3,25 % erklärbar, da Nickel als Legierungselement die Zähigkeit von Stahlwerkstoffen merklich erhöht [22].

4.2 Ergebnisse der lauwarmen Umformung

Gefügeentwicklung

Es folgt eine Gefügebeschreibung am Beispiel der aus dem Gusszustand lauwarm umgeformten Proben mit $\varphi = 1{,}0$ an Hand der Abbildungen 5 bis 9. Nach maximaler lauwarmer Umformung zeigen alle Proben ein Verformungsgefüge. Dieses zeigt sich jedoch noch immer als ähnlich seigerungsreich wie direkt nach dem Vergießen des Materials. Der Martensit erscheint als Massivmartensit und ist um so stärker strukturiert, je niedriger die Umformtemperatur bei Beginn der lauwarmen Behandlung war. Dieser Umstand ist dadurch zu erklären, dass es bei niedrigeren Temperaturen zu einer größeren Kaltverfestigung und geringeren Diffusion kommt. Bei der bei niedrigster Temperatur (M_s−20 K) umgeformten Probe setzte darüber hinaus bereits spontane Martensitbildung vor Beginn der Umformung ein, weshalb sich deren Gefüge (Abbildung 9) noch deutlicher abhebt. In allen Fällen handelt es sich um ein relativ feines Gefüge.

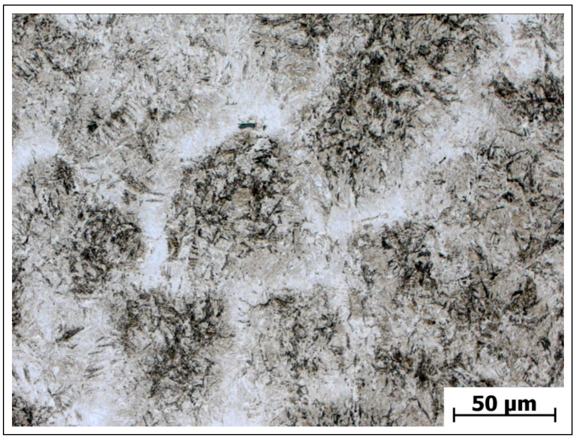

Abbildung 5: AWI-G-3, T_U=350 °C, φ=1,0, $\dot{\varphi}$=0.1 s^{-1}, Gusszustand, Nital geätzt, 500x

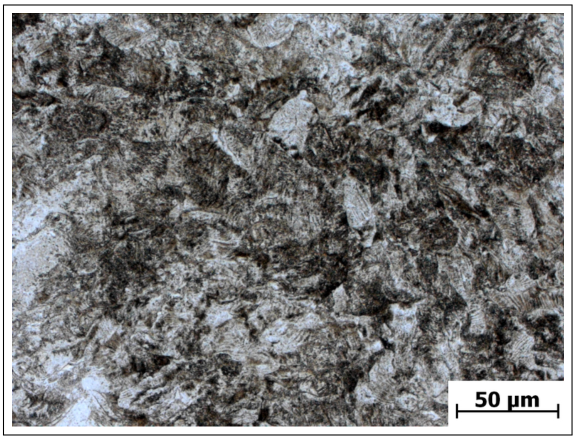

Abbildung 6: AWI-G-9, T_U=310 °C, φ=1,0, $\dot{\varphi}$=0.1 s^{-1}, Gusszustand, Nital geätzt, 500x

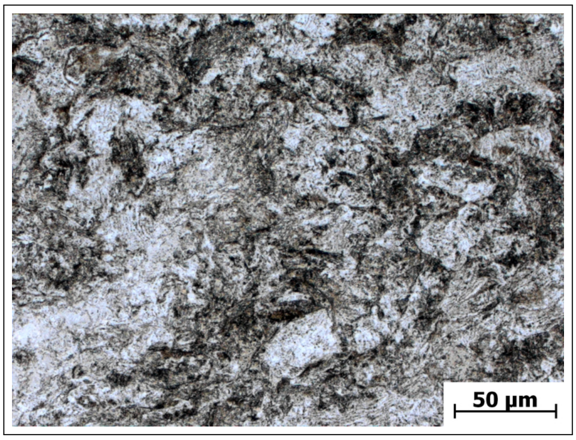

Abbildung 7: AWI-G-6, T_U=330 °C, φ=1,0, $\dot{\varphi}$=0.1 s^{-1}, Gusszustand, Nital geätzt, 500x

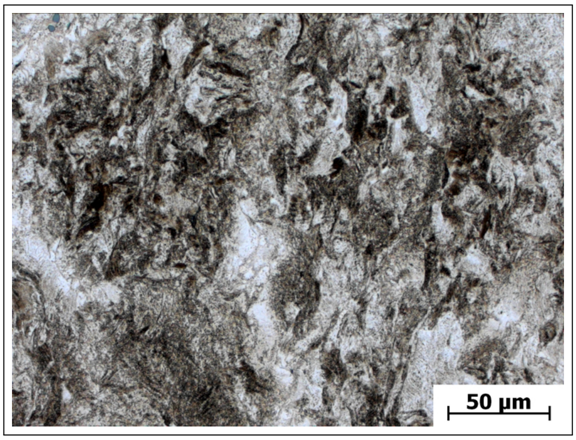

Abbildung 8: AWI-G-19, T_U=290 °C, φ=1,0, $\dot{\varphi}$=0.1 s^{-1}, Gusszustand, Nital geätzt, 500x

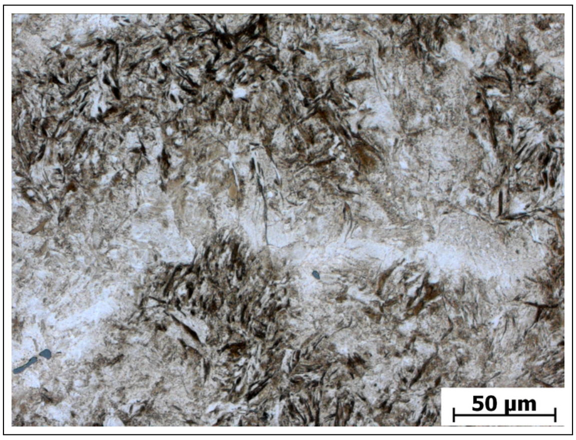

Abbildung 9: AWI-G-15, T_U=270 °C, φ=1,0, $\dot{\varphi}$=0.1 s^{-1}, Gusszustand, Nital geätzt, 500x

Mechanische Eigenschaften

Im Sammeldiagramm der Fließkurven für den Gusszustand, Abbildung 10, ist zu erkennen, dass die Festigkeit des Werkstoffes erwartungsgemäß mit fallender Temperatur zunimmt. Dabei fallen die Unterschiede bei niedrigeren Temperaturen größer aus. Die Proben ließen sich bei allen Temperaturen ohne Risse bis $\varphi = 1{,}0$ umformen, was die Erwartungen an den untersuchten Werkstoff bereits übertrifft. Es ist davon auszugehen, dass mit dem vorliegenden Werkstoff noch höhere Vergleichsumformgrade erreichbar sind. Die Fließkurven weisen im oberen Spannungsbereich Wendepunkte auf, welche bei niedriger Temperatur deutlicher hervortreten. Dabei handelt es sich um einen Reibungseffekt an den Stirnflächen der Proben. Diese Wendepunkte sind keinesfalls mit den typischen Wendepunkten des α′-TRIP-Effekts zu verwechseln und besitzen keine werkstoffkundliche Bedeutung. Sie treten bei Legierungen ohne Umwandlungsplastizität in gleicher Weise auf.

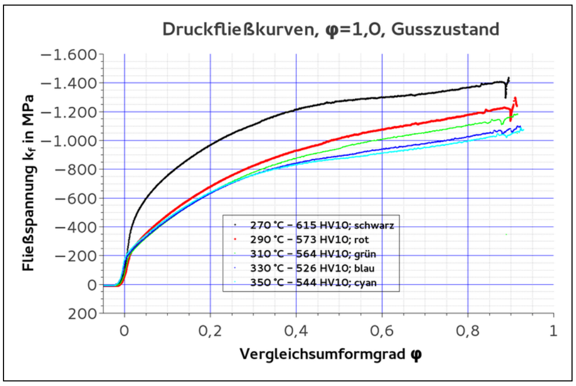

Abbildung 10: Sammeldiagramm der Fließkurven, Gusszustand

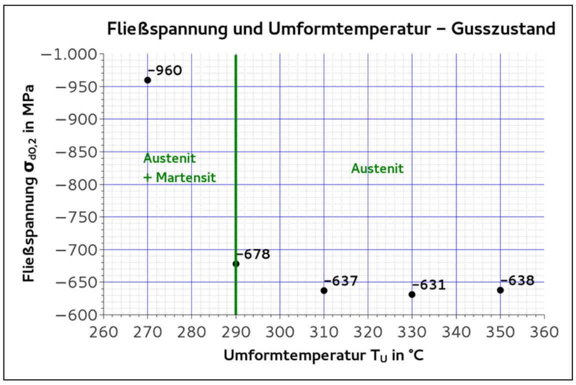

Abbildung 11: Abhängigkeit der Ersatzfließspannung $\sigma_{d0,2}$ von der Umformtemperatur, φ=1,0, Gusszustand

Zur Charakterisierung der Festigkeit des Werkstoffes bei unterschiedlichen Umformtemperaturen wurde die Ersatzfließspannung $\sigma_{d0,2}$ gewählt. Dabei handelt es sich um die Fließspannung bei einem Vergleichsumformgrad von $\varphi = 0{,}2$. Dieser Wert ist nicht mit der Ersatzstreckgrenze $R_{p0,2}$ aus dem Zugversuch zu verwechseln. $\sigma_{d0,2}$ markiert nicht den Übergang zwischen elastischem und plastischem Werkstoffverhalten, sondern liegt bereits deutlich im plastischen Bereich. Eine Darstellung der Temperaturabhängigkeit von $\sigma_{\mathrm{d}0,2}$ zeigt Abbildung 11. Die Werte wurden aus den Fließkurven für $\varphi = 1{,}0$ abgelesen. In der Darstellung von $\sigma_{\mathrm{d}0,2}$ über der anfänglichen Umformtemperatur bestätigt sich der Eindruck, welcher durch die Verläufe der Fließkurven entsteht. Tendenziell nimmt die Festigkeit mit fallender Temperatur zu. Dabei fällt der besonders große Sprung der Festigkeit zwischen $T_{\mathrm{U}} = 290\,°\mathrm{C}$ und $T_{\mathrm{U}} = 270\,°\mathrm{C}$ auf. Dieser ist auf die Tatsache zurückzuführen, dass beginnend bei 20 K unterhalb der Temperatur M_{s} ein Gefüge umgeformt wird, welches bereits merkliche Anteile an Martensit enthält. Dennoch kam es bei dieser Probe nicht zu einem Bruch.

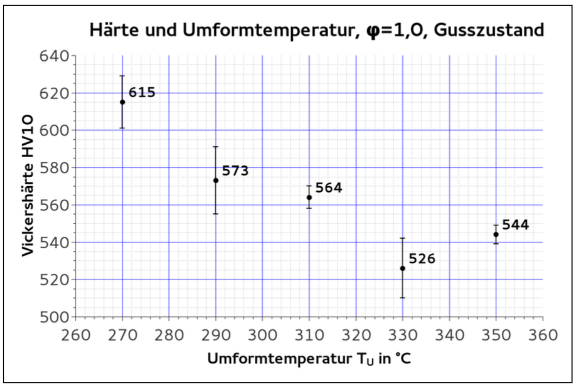

Abbildung 12: Abhängigkeit der Härte von der Umformtemperatur, φ=1,0, $\dot{\varphi}$=0.1 s^{-1}, Gusszustand

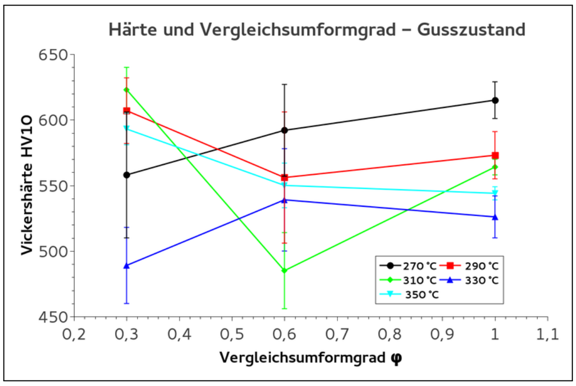

Abbildung 13: Abhängigkeit der Härte vom Vergleichsumformgrad für unterschiedliche T_{U}, Gusszustand

In Abbildung 12 sind die Härten der Proben mit $\varphi = 1{,}0$ nach lauwarmer Umformung bei verschiedenen Temperaturen und anschließender Abkühlung an Luft dargestellt. Tendenziell nimmt die Härte mit steigender Temperatur ab. Dies entspricht den Erwartungen, da die Kaltverfestigung bei niedrigerer Temperatur größer sein muss. Zusätzlich fällt die Martensitbildung jeweils unterschiedlich aus. Die Zunahme der Härte bei der Probe mit höchster anfänglicher Umformtemperatur ist durch Streuungseffekte, insbesondere die große Streuung bei der Probe mit $T_{\mathrm{U}} = 330\,°\mathrm{C}$, erklärbar. Betrachtet man die Entwicklung der Vickershärte mit dem Vergleichsumformgrad für unterschiedliche Temperaturen (Abbildung 13), so entsteht ein unkontrolliertes Bild durch das Zusammenwirken unterschiedlicher, teils gegenläufiger Prozesse bei der lauwarmen Umformung. Zum einen wirken die Bildung von Verformungsmartensit und Abkühlmartensit sowie die Kaltverfestigung des Austenits und des Martensits festigkeits- und damit tendenziell härtesteigernd. Zum anderen wirken bei Temperaturen im lauwarmen Bereich bereits ein Anlassen des Martensits sowie eine beginnende Erholung des kaltverfestigten Martensits und Austenits härtesenkend. Die Temperatur-Zeit-Verläufe der Proben sind dabei in jedem Fall, wie auch die Umformparameter, unterschiedlich. Damit erhalten die verschiedenen Prozesse in jeder Probe eine andere Gewichtung. So gibt es Proben mit der erwarteten Zunahme der Härte mit steigendem φ (270 °C, schwarz). In diesem Fall dominieren die verfestigenden Prozesse. Bei der höchsten Temperatur hingegen dominieren die entfestigenden Prozesse, so dass in diesem Fall die Härte bei kleinstem Vergleichsumformgrad am höchsten liegt (hellblau). In anderen Proben wiederum kommt es zunächst zu einer Abnahme bei mittlerem φ und zu einer späteren Zunahme der Härte bei $\varphi = 1{,}0$ (grün, rot). Schließlich nimmt die Härte in einem Fall (dunkelblau) zunächst zu und bei höherem Vergleichsumformgrad ab. In [3] wird gezeigt, dass diese Effekte durch eine Anlassbehandlung weitgehend ausgeglichen werden können.

5 Zusammenfassung

Der umwandlungsträge Vergütungsstahl AWI/Komatsu ist ein lufthärtender Werkstoff. Sein Gefüge zeigt sich in allen Zuständen als martensitisch. Das Umformvermögen des Werkstoffes im Temperaturbereich von 270 °C – 350 °C ist als sehr gut einzustufen. Insbesondere ist die gute lauwarme Umformbarkeit im Gusszustand bemerkenswert. Die Festigkeit des Werkstoffes im martensitischen Gusszustand liegt mit $R_\mathrm{m} \approx 2000\,\mathrm{MPa}$ und $R_\mathrm{p0,2} \approx 1400\,\mathrm{MPa}$ sehr hoch, wobei relativ hohe Zähigkeitswerte von $A_\mathrm{B} \approx 9\,\%$ und $Z \approx 16\,\%$ erreicht werden. Es ist zu erwarten, dass die Zähigkeit der Legierung AWI im warmgewalzten und insbesondere im vergüteten Zustand sehr hoch ausfallen wird. Auf Grund dieser Eigenschaften handelt es sich bei diesem Vergütungsstahl um einen viel versprechenden Konstruktionswerkstoff, welcher für die lauwarme Umformung geeignet ist.

Symbole

Symbol	**Einheit**	**Bedeutung**
A_0	mm^2	Ausgangsfläche
A_B	%	Bruchdehnung
F	N	Kraft
h	mm	Dicke / Höhe allgemein
h_0	mm	Ausgangsdicke
k_f	MPa	Fließspannung
M_d	°C	Temperatur für $\sigma_\mathrm{A}^{\gamma\rightarrow\alpha'} = R_\mathrm{m}^{\gamma}$ (TRIP-Ende)
M_s	°C	Martensit-Starttemperatur
$M_{\mathrm{s}\sigma}$	°C	Temperatur für $\sigma_\mathrm{A}^{\gamma\rightarrow\alpha'} = \sigma_\mathrm{f}^{\gamma}$ (TRIP-Maximum)
r_0	mm	Ausgangsradius
R_m	MPa	Zugfestigkeit
R_m^{γ}	MPa	Zugfestigkeit des Austenits
$R_\mathrm{p0,2}$	MPa	0,2 %-Proportionalitätsgrenze
T_U	°C	Umformtemperatur (lauwarm)
Z	%	Brucheinschnürung
ε	%/–	Dehnung, bezogene Dickenänderung
ε_w	–	wahre Dehnung
φ	–	Vergleichsumformgrad
$\dot{\varphi}$	s^{-1}	Umformrate
$\sigma_\mathrm{A}^{\gamma\rightarrow\alpha'}$	MPa	Auslösespannung für die Martensitbildung
$\sigma_\mathrm{d0,2}$	MPa	Ersatzfließspannung für φ=0,2
$\sigma_\mathrm{f}^{\gamma}$	MPa	Streckgrenze des Austenits

Literaturverzeichnis

[1] Weiß, A.: *Patent DE 10 2013 014 814 A1. Verfahren zur Herstellung eines hochfesten bzw. höchstfesten Formteils aus härtbarem Stahl.* Offenlegungsschrift. Deutsches Patent- und Markenamt, 5. März 2015.

[2] Autorenkollektiv: *Hochfeste und bruchzähe Befestigungselemente für Windkraftanlagen.* Projektskizze. Stahlzentrum Freiberg e. V., 2013.

[3] Sandig, F.: "Einfluss einer lauwarmen Umformung auf die Gefügeausbildung in einem umwandlungsträgen Vergütungsstahl und dessen Einfluss auf ausgewählte Eigenschaften". Großer Beleg (Ingenieurarbeit). Institut für Eisen- und Stahltechnologie der TU Bergakademie Freiberg, 7. Okt. 2014. URL: `https://www.dropbox.com/s/u7e7nyzdzezwanj/Grosser-Beleg_Sandig_2014_HP.pdf?dl=1`.

[4] Jahn, A.:
"Einfluss der Martensitbildung auf die mechanischen Eigenschaften von ein- und mehrphasigen gegossenen und warmgewalzten Cr-Mn-Ni-Stählen".
Veröff. Shaker-Verlag, Herzogenrath.
Dissertation. Institut für Eisen- und Stahltechnologie der TU Bergakademie Freiberg, 2012.
ISBN: 978-3-8440-0765-7.

[5] Kovalev, A.: "Characterization of the TRIP/TWIP effect in austenitic stainless steels using Stress-Temperature-Transformation (STT) and Deformation-Temperature-Transformation (DTT) Diagrams". In: *Steel Research International* 82.1 (2011). ISSN 0177-4832, Seiten 45–50.

[6] Weiß, A.:
"Hochfester und kaltumformbarer austenitischer Stahlguss mit TRIP-/TWIP-Eigenschaften".
In: *Gießerei* 100 (Apr. 2013), Seiten 54–65.
ISSN: 0175-1034.

[7] Heinemann, G.: "Virtuelle Bestimmung des Verfestigungsverhaltens von Bändern und Blechen durch verformungsinduzierte Martensitbildung bei metastabilen rostfreien austenitischen Stählen".
Dissertation. Eidgenössische Technische Hochschule Zürich, 2004.

[8] Koyro, N.: "Kaltwalzen von austenitischem Stahlguss mit Phasenumwandlungseffekten".
Experimentelle Studienarbeit. Institut für Eisen- und Stahltechnologie der TU Bergakademie Freiberg, 2013.

[9] Shyne, J. C., Zackay, V. F. und Schmatz, D. J.:
"The strength of Martensite Formed from Cold-Worked Austenite".
In: *Transactions of the American Society for Metals* 52 (1960), Seiten 346–360, 366–371.

[10] Potak, M.: "Thermomechanische Behandlung von Stahl auf hohe Festigkeit".
In: *Metallovedenie i termiceskaja obrabotka metallov* 5 (Mai 1961), Seiten 2–9.

[11] Kula, E. B. und Dhosi, J. M.:
"Effect of Deformation Prior to Transformation on the Mechanical Properties of 4340 Steel".
In: *Transactions of the American Society for Metals* 52 (1960), Seiten 321–328.

[12] Justusson, W. H. und Schmatz, D. J.:
"Some Observations on the Strength of Martensite Formed from Cold-Worked Austenite".
In: *Transactions of the American Society for Metals* 55 (1962), Seiten 640–653.

[13] Kogan, L. J. und Entin, R. J.:
"Einfluss der Verformung des unterkühlten Austenits auf die mechanischen Eigenschaften der Stähle".
In: *Metallovedenie i termiceskaja obrabotka metallov* 1 (Jan. 1962), Seiten 3–9.

[14] Schmatz, D. J. und Zackay, V. F.:
"Mechanical Properties of Deformed Metastable Austenite Ultra High Strength Steel".
In: *Transactions of the American Society for Metals* 51 (1959), Seiten 476–487.

[15] Ermakov, W. N.: "Thermomechanische Behandlung von Konstruktionsstählen".
In: *Metallovedenie i termiceskaja obrabotka metallov* 4 (Apr. 1963), Seiten 25–29.

[16] Pewsner, L. M.:
"Struktur und Eigenschaften von Konstruktionsstahl nach der Niedertemperatur-thermomechanischen Behandlung". In: *Metallovedenie i termiceskaja obrabotka metallov* 4 (Apr. 1963), Seiten 13–19.

[17] Drjukova, J. N.: "Anisotropie der Eigenschaften des Stahles nach der thermo-mechanischen Behandlung".
In: *Metallovedenie i termiceskaja obrabotka metallov* 2 (Feb. 1965), Seiten 41–43.

[18] Detert, K. und Schmidt-Krayer, C.: "Einfluss einer Austenitverformung vor der Martensitumwandlung in niedrig legierten Baustählen".
In: *Stahl und Eisen* 83 (1963), Seiten 449–457.

[19] McEvily, A. J.: "On the Formation of Alloy Carbides During Ausforming".
In: *Transactions of the American Society for Metals* 54 (1963), Seiten 753–767.

[20] Lehnert, W.:
"Thermomechanische Behandlung der Stähle, wichtigste Einflussgrößen und erreichbarer Effekt".
In: *Neue Hütte* 13.12 (Dez. 1968), Seiten 716–722.
ISSN: 0028-3207.

[21] Autorenkollektiv: *Umformtechnik, Plastomechanik und Werkstoffkunde.*
Herausgegeben von Winfried Dahl.
Verlag Stahleisen, Düsseldorf, 1993, Seite 89.
ISBN: 3-514-00402-1.

[22] Autorenkollektiv: *Stahlschlüssel-Taschenbuch.*
21. Auflage. Verlag Stahlschlüssel Wegst GmbH, Marbach/N., 2007. ISBN: 978-3-922 599-22-7.

The impact of glassy carbon particle size on tribological properties in aluminium based composites prepared via powder metallurgy method

Paweł Krzywda[a], Aleksandra Miczek[b], Bartosz Hekner[c]
Silesian University of Technology
Faculty of Materials Engineering and Metallurgy, Krasińskiego 8 STR, 40-019 Katowice, Poland
[a]pawel.krzywda@interia.pl,[b]a.miczek@wp.pl, [c]bartosz.hekner@polsl.pl

This paper presents the impact of glassy carbon particle size on the tribological properties of materials designed for high loaded friction point. Composite powders containing 15% Al_2O_3 5% glassy carbon particles (size: <40, 40-80, 80-120, 120-160, 160-200 µm) were produced by high energy milling in planetary mills. High energy milling process resulted in bonding of hard ceramic particles with a plastic matrix metallic. The bonding between ceramic and metal particles was obtained by the two-stage hot pressing in the semi-liquid state. Hardness was measured using the Brinell method and density was measured at a hydrostatic balance. The morphology and microstructure of materials was examined by scanning electron microscope (SEM). The tribological research was conducted at room temperature by the pin-on-disc method, at a distance of 90 m, with 35 and 50 N of load and 0.05 m/s of sliding speed.

Keywords: Aluminium matrix composites, alumina, glassy carbon, tribological properties, wear, friction.

1 Introduction

Metal matrix composites (MMC) have been used in industry due to the low density, good tribological properties and high corrosion resistance. Especially in the car and aircraft industry, gives rise to constant search for the possibilities of improving tribological properties. The use of traditional reinforcing particle of the Al_2O_3 type contributes to improvement of physical and mechanical properties [1].

Introduction of the glassy carbon to aluminum matrix composites reinforced with ceramic particles of Al_2O_3 decrease the coefficient of friction, and influences the less wear on the friction pair caused protective layers creation on the area of friction through the glassy carbon particles [2].

The most common method of producing the composites are casting methods. The disadvantage of these methods is the poor wettability of the ceramic particles by the liquid metal, resulting in weak bonding between matrix and reinforcement, moreover weakly coupled matrix particles are pulled out from the matrix material, which increases the friction pair wear. To eliminate all these defects is possible to use methods of powder metallurgy [3, 4].

The prepared powder mixture is subjected to high energy milling in order to obtain a good connection between the hard ceramic particles and the plastic matrix. However glassy carbon additive promotes the disintegration of aluminum matrix particles [4, 5]. In the second step, composites powder are prepared by hot pressing and sintering technologies. These processes have been used to obtain correct bonding between the matrix and reinforcement.

2 Experimental

Composite materials were produced by powder metallurgy method. Aluminum (99 % purity) used as a matrix material had size between 45 and 65 µm. Two types of reinforcing particles were applied. As a first type of reinforcement was α-Al_2O_3 – Martoxid® MR70 (98 % purity), while the second one were glassy carbon particles. Glassy carbon was obtained in laboratory at Silesian University of Technology. The composition of the powders are given in Table 1.

Table 1: The composition of the composite powders.

Composite	**Weight Fraction** [%]			**GC size** [µm]
	Al	Al_2O_3	GC	
Al – Al_2O_3	85	15	-	-
Al – GC<40	80	15	5	<40
Al – GC40-80	80	15	5	40-80
Al – GC80-120	80	15	5	80-120
Al – GC120-160	80	15	5	120-160
Al – GC160-200	80	15	5	160-200

All components were milled at planetary Fritsch Pulverisette 6 classic line in steel jars together with steel milling balls. Milling process was conducted in gas atmosphere – argon, on time 2 hours, realized in 24 cycles with 5 minutes milling time followed by 30 minutes breaks and a 16:1 ball to powder weight ratio. The next step to obtain composite materials was hot pressing on hydraulic Degussa press. Parameters of sintering shows Table 2. The process was carried out in two stages in the semi-liquid state.

Table 2: Parameters of sintering

	Stage	Temperature [°C]	Holding Time [min]	Punch press [MPa]	Chamber pressure
Hot pressing	I	480	20	10	10^{-3} Tor
	II	640	15		

Morphology and microstructure of composite powders and solid materials were observed using Scanning Electron Microscope Hitachi S-3400N, which register secondary electron (SE) image. It occurs at voltages of 25 kV.

The measurement hardness was performed Brinell method. The density of the materials tested was based on Archimedes' principle on hydrostatic weight.

Rating of tribological properties was a main part of experiment. Wear a pair of friction and coefficient of friction were analysed. Tribological tests were performed on all samples at room temperature. Under the conditions: load 35 N and 50 N, velocity of $0.05\,\mathrm{m\,s^{-1}}$ and distance -90 m, countersample material was cast iron (EN - GJL – 300).

3 Results and discussion

The milled composite powders as well as sintered specimens were observed using Scanning Electron Microscope. On Figure 1a. plastically deformed aluminium particles are visible. In powders with the glassy carbon an irregular edges and cracked large particles were detected (Figure 1b). This demonstrates the positive impact of a glassy carbon on milling process.

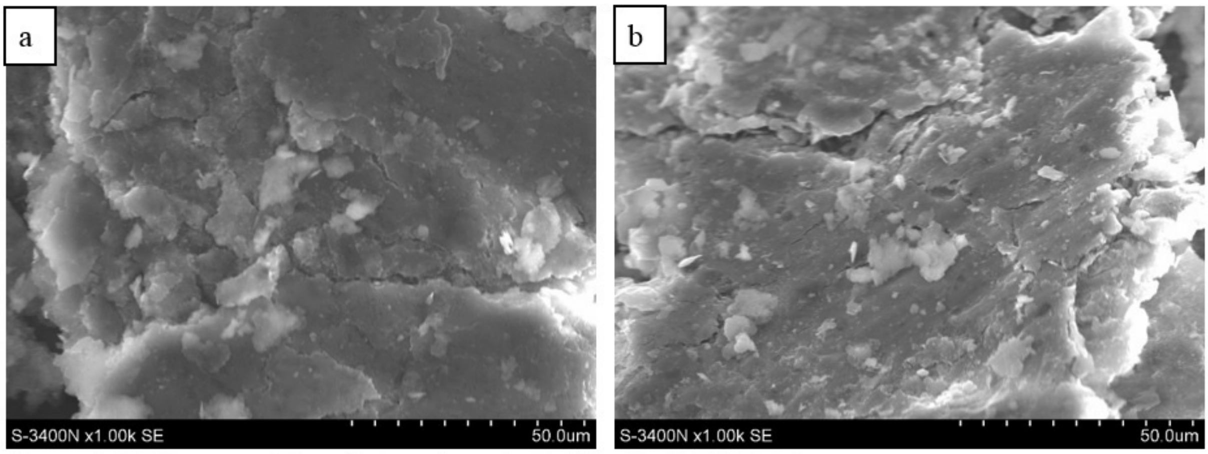

Figure 1: SEM images of the milled powders; a) Al-Al_2O_3; b) Al-GC120-160.

The smaller particles of the glassy carbon have a low tendency to cracking during the milling. For those materials conducted a detailed analysis of structure revealed pure aluminum areas without reinforcing particles (Figure 2a). The use of larger particles allows for improved fragmentation and led to uniform distribution of particles in the matrix without clusters or agglomerates (Figure 3b). The glassy carbon has typical irregular shape with sharp edges.

Table 3 presents the results of density and hardness. The highest density is characterized by a reference material Al-Al_2O_3. The glassy carbon additive to cause reducing the density of the material due to low density of glassy carbon material. The addition of the glassy carbon increases hardness, all the materials are similar in hardness. In the case of Al-GC160-200 a decreasing of hardness was observed but it was still higher than the reference material. A large standard deviation of results of hardness due to differences in hardness of the material depending on the measurement site. The area in the middle of the material revealed a lower hardness than at the edges.

Analysis of the influence of glassy carbon particle size on the tribological properties was main part of conducted research. Almost all composites have a higher coefficient of friction than the reference material (Figure 4). For the composite Al-GC40-80 a lower average

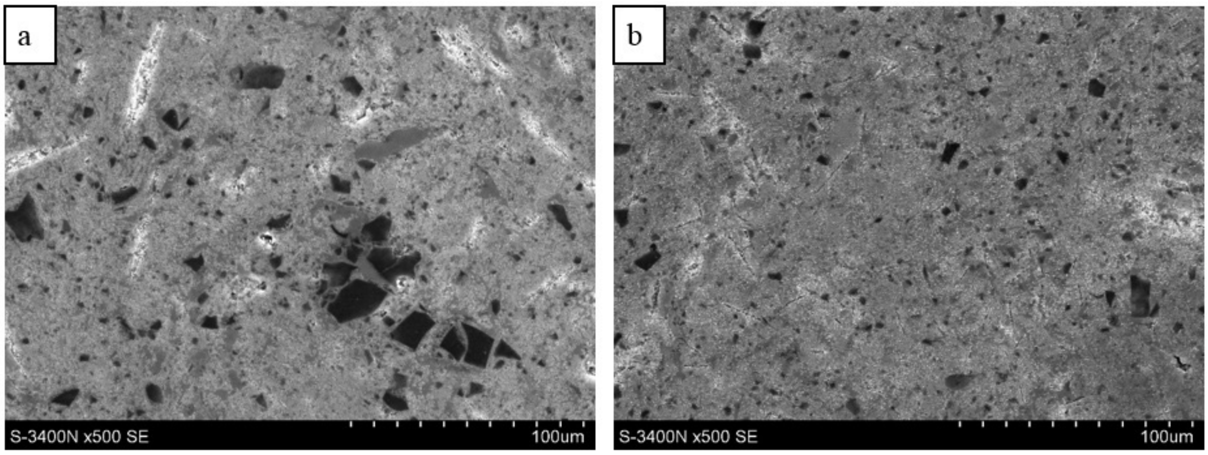

Figure 2: SEM images of the samples with 5wt%; a) Al-GC; b) Al-GC120-160.

Table 3: The results of measurements density and hardness.

Composite	Density [g/cm3]	Hardness, HB	Variation
Al – Al_2O_3	2.85	112.1	30.46
WS<40	2.66	115.8	15.59
WS40-80	2.62	125.4	12.12
WS80-120	2.66	132	14.32
WS120-160	2.69	138.8	13.31
WS160-200	2.66	117.4	10.71

coefficient of friction was measured, this may be caused by the formation of carbon film during friction. Differences in average coefficient of friction is also interesting. Composites with <40 and 120-160 µm glassy carbon particle size were characterized almost the same coefficient of friction under both loads. Significant increases were observed for materials Al-GC40-80 and Al-GC80-120. Only in application of the glassy carbon particles size 120-160 µm obtained a stable friction coefficient from the beginning to the end of the friction distance (Figure 3). This material was also characterized by the highest hardness (Table 3).

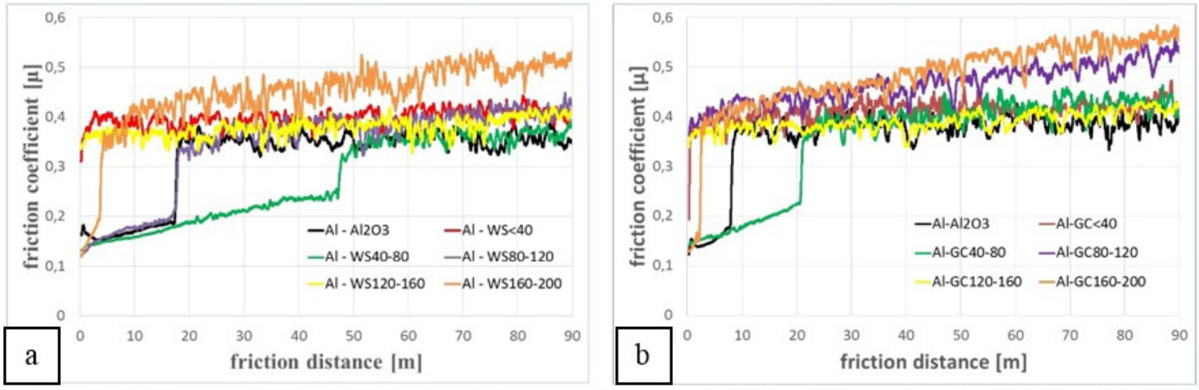

Figure 3: Frcition coefficient of tested materials as afunction of sliding distance. Load: a) 35 N and b) 50 N.

The smallest wear was observed for samples containing glassy carbon particles in size

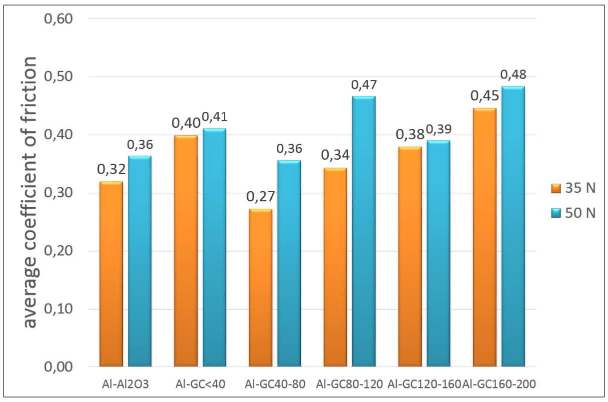

Figure 4: The influence of GC particles size on average coefficient of friction.

between 40 µm to 80 µm. It can be explained by smearing of those particles on the friction surfaces, what led to protective layer creation. The composites have a high coefficient of friction have also a high wear. The highest wear was observed for the Al-GC160-200 composite, which may be caused by the presence of voids and decrease the hardness of the material, it could be result in poorly chosen parameters of milling process or synthesis. Large particles occurred only in certain areas of material which could limit their positive impact during friction, e.g. The formation of protective layers.

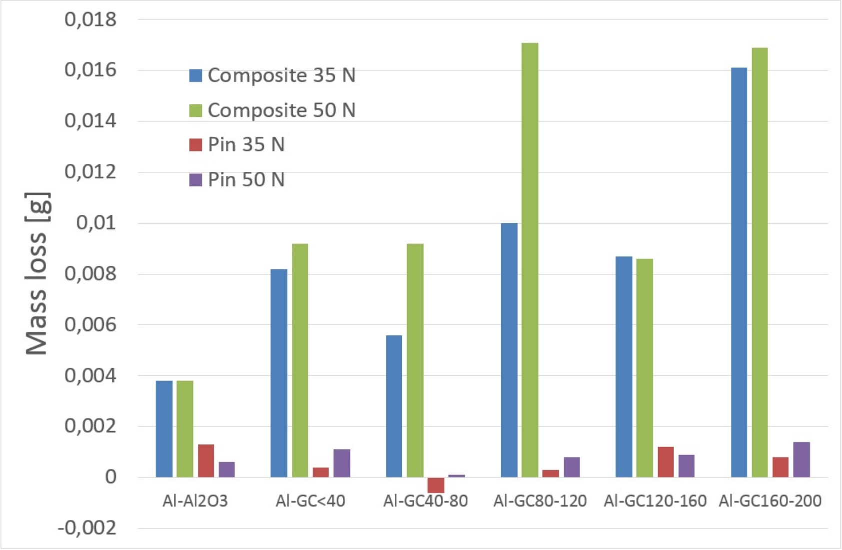

Figure 5: The composites and coutersample mass losses.

4 Conclusions

Based on the research results obtained, it has been found that:

1. It is possible to use high-energy milling and powder metallurgy methods to form good quality heterophases composites, what is extremely hard using classic method, like casting.
2. Glassy carbon additive decreased density of the material. Moreover, hardness of the composites increased.

3. Use a particle size between 120 µm to 160 µm is the most efficient fraction. The highest stabilization and with no differences in average coefficient of friction value under both analyzed loads.
4. The results of tribological tests are unsatisfactory. It was expected that the addition of glassy carbon reduces wear composite materials. However, despite the increased wear of composites, wear of countersample decreased. The lowest wear of cast iron EN - GJL – 300 was observed using carbon particles of size 1 µm to 120 µm.

References

[1] Myalski, J., Wieczorek, J., and A.Dolata-Grosz: "Tribological properties of heterophase composites with an aluminium matrix". In: *Journal of Achievements in Materials and Manufacturing Engineering* 15 (2006), pages 53–57.

[2] Hekner, B.: "Tribological characterization of aluminium-based composites with reinforcement of submicro SiC and Al_2O_3 particles with glassy carbon addition". In: *Proceedings XX. International Students' Day of Metallurgy.* 2013.

[3] Hekner, B. et al.: "Influence of carbon nanotubes and carbon particles on tribological properties in aluminum based composites". In: *Composites Theory and Practice* 1 (2014), pages 43–49.

[4] Hekner, B. et al.: "Aluminum - ceramic composite materials reinforced with nanoparticles prepared via powder methallurgy method". In: *Composites Theory and Practice* 3 (2013), pages 203–207.

[5] Adamczyk, B. and Hekner, B. In: *XVI Mįedzynarodowa Studencka Sesja Naukowa „Materiały i Technologie XXI wieku".* 2014, pages 103–106.

Calculation of surface tension of real steel grades at 1550 ℃

Aleš Kalup[1], Simona Zlá[1,2], Lenka Řeháčková[1], Monika Kawuloková[1,2], Bedřich Smetana[1,2]
VŠB-Technical University of Ostrava
[1]Department of Physical Chemistry and Theory of Technological Processes, Faculty of Metallurgy and Materials Engineering, VŠB-Technical University of Ostrava, 17. listopadu 15, Ostrava-Poruba, 708 33
[2]Regional material science and technology centre, VŠB-Technical University of Ostrava, 17. listopadu 15, Ostrava-Poruba, 708 33
ales.kalup@vsb.cz

Abstract

In the presented work, new thermodynamic approach based on basic thermodynamics was used for calculation of the surface tension of steel. Surface tension was computed for three steel grades and computed values were compared with experimental values at 1550 °C. Thermodynamic properties, which are necessary for this thermodynamic approach of surface tension, were calculated using Thermo-Calc software with TCFE7 database.

Keywords: surface tension, steel, Thermo-Calc, thermodynamic properties

1 Introduction

The surface properties of liquids and melts have attracted much more interest both physicist and metallurgists from the long past to the present day because of either scientific or technological importance [1–6]. During the soldering, brazing, sintering and dying, the knowledge of surface properties of the liquid state is required. Although there are a large number of methods to determine the surface properties of liquids such as surface tension, those suitable for liquid metals are limited by their chemical reactivity and high melting points [7].

In the past, many models were derived for the calculation of the surface tension [8]. Butler equation [9] is the most commonly used model for surface tension calculations, another commonly used models are Kohler model [10], Toop model [11] and Chou model [12]. In contrast to the above models, input data for our proposed approach are thermodynamic properties of the sample and experimental value of surface tension of standard. Input thermodynamic properties, such as Gibbs energy [13], can be obtained experimentally [14] or these properties can be obtained using specific software. In this work, all required thermodynamic properties were calculated using Thermo-Calc 4.0 with TCFE7 database.

2 Surface tension model

Surface tension is thermodynamically defined using the partial derivative of the Gibbs energy Equation 1 [15]:

$$\sigma = \left(\frac{\partial G}{\partial A}\right)_{T,p,n} \tag{1}$$

where σ is surface tension, G is Gibbs energy, A is surface, T is thermodynamic temperature, p is pressure and n is amount of substances. As it is not possible to maintain a constant temperature, it is necessary to express Gibbs energy by the first and second laws of thermodynamics Equation 2 – Equation 5:

$$dG = dU - d(TS) + d\,(p \cdot V) \tag{2}$$

$$dU = T \cdot dS + dW \tag{3}$$

$$dW = -p \cdot dV + \sigma \cdot dA \tag{4}$$

where U is internal energy, S is entropy and W is work. Combining of Equation 1 – Equation 4 can be obtained final equation Equation 5 for calculation of surface tension:

$$\sigma_{calc} = \left(\frac{\partial G}{\partial A} + S\frac{\partial T}{\partial A} - V\frac{\partial p}{\partial A}\right)_{n} \tag{5}$$

Equation 5 is derived for a constant amount of substances, so it can be used only for fully melted materials (above temperature of liquidus), where it is possible to assume minimal (if any) changes in phase composition.

3 Calculations

All thermodynamic properties from Equation 5, namely Gibbs energy, entropy, thermodynamic temperature, volume and pressure, were computed using Thermo-Calc 4.0 [16] with TCFE7 (Thermo-Calc Fe-based alloys) database [17].

The only one quantity that must be obtained by another way is surface of the system. Material tends to minimalize its surface (more precisely, the surface energy) with a given volume. Sphere has the smallest surface with a given volume, so this shape can be used for computing the surface from its volume Equation 6:

$$A = (36\pi)^{\frac{1}{3}} \cdot V^{\frac{2}{3}} \tag{6}$$

During experiments, many factors (i.e. wettability [18], effect of inert atmosphere) act to the sample, so the sample has shape different from ideal sphere. These effects cannot be described by mathematical formulas, it is necessary to use scale factor f. This factor represents the ratio between calculated and experimental values of the surface tension Equation 7 of standard:

$$f = \frac{\sigma_{calc,std}}{\sigma_{exp,std}} \tag{7}$$

where $\sigma_{calc,std}$ is surface tension of standard calculated using Equation 5 and $\sigma_{exp,std}$ is experimentally measured surface tension. Surface tension of sample is then recalculated using scale factor from Equation 7 and calculated value of surface tension from Equation 5 according to Equation 8:

$$\sigma_{result,sample} = \frac{\sigma_{calc,sample}}{f} \tag{8}$$

where $\sigma_{calc,sample}$ is surface tension of sample calculated using Equation 5 and $\sigma_{result,sample}$ is the resulting value of surface tension of sample.

4 Results and discusson

Three industrial-grade stainless steels (sample 1-3) and two standards (pure iron and Fe-20 wt.% Ni alloy) were used to validate suggested approach. Chemical composition of samples is given in Table 1.

Table 1: Chemical composition of steel samples (wt.%).

Sample	C	Cr	Ni	S	Mn	Al	O	Fe
1	0.067	18.24	8.15	0.002	1.77	0.001	0.0057	bal.
2	0.056	18.28	8.20	0.009	1.80	0.001	0.0090	bal.
3	0.045	16.49	0.30	0.003	0.48	0.001	0.0164	bal.

Experimental values of surface tension at 1550 °C were obtained from literature [19] for both standards and for three real steel grades. Experimental values of surface tension of both standards are given in Table 2.

All needed thermodynamic properties of standards and samples were calculated using Thermo-Calc software with TCFE7 database. This software allows calculations only in

Table 2: Surface tension of standards at 1550 °C ($N\,m^{-1}$).

Standard	σ_{exp}
Fe	1.670
Fe-20 wt. % Ni	1.489

the equilibrium state and also allows adding and excluding phases in its calculations. In this paper, only default setting with no changes in phase addition/exclusion was used (the “black box” mode) [20].

Surface tension for both standards was calculated and scale factors were obtained. These scale factors were used to calculation of surface tension of presented steels and obtained values of surface tension are given in Table 3. Values σ_{Fe} are obtained with the use of f_{Fe} (pure iron as a standard), values σ_{Fe20Ni} are obtained with the use of f_{Fe20Ni} (Fe-20 wt.% Ni alloy as a standard). Experimental values of surface tension of samples σ_{exp} are given in .

Table 3: Surface tension of samples at 1550 °C ($N\,m^{-1}$).

Sample	σ_{exp}	σ_{result}	
		σ_{Fe}	σ_{Fe20Ni}
1	1.354	1.265	1.296
2	1.320	1.342	1.376
3	1.472	1.526	1.565

Surface tension calculated with iron as a standard are always lower than values calculated with Fe-20 wt.% Ni alloy as a standard. For sample 1, calculated surface tension is lower than experimentally measured surface tension. For samples 2 and 3, surface tension computed with iron as a standard are closer to experimental values than surface tension computed with Fe-20 wt.% Ni alloy as a standard.

The difference between measured and calculated surface tension is always below 0.1 $N\,m^{-1}$. The highest difference (0.093 $N\,m^{-1}$; standard deviation is 6.32%) is for sample 3 with Fe-20 wt.% Ni alloy as a standard, the lowest difference (0.022 $N\,m^{-1}$; standard deviation is 1.67%) is for sample 2 with pure iron as a standard. The correlation between calculated and experimental values of surface tension is given in Figure 1.

Calculated values of surface tension are in very good agreement with experimental results. The small relative difference between measured and calculated values of surface tension may be caused by trace amounts of other elements which have not been determined.

5 Conclusions

New thermodynamic approach based on classical thermodynamics for computing of the surface tension was derived and tested using three real steel grades. Approach gives values that are in a very good agreement with experimentally obtained values of surface tension. Two different materials (pure iron and Fe-20 wt.% Ni alloy) were used as standards and values calculated according f_{Fe} and f_{Fe20Ni} are close to experimental values.

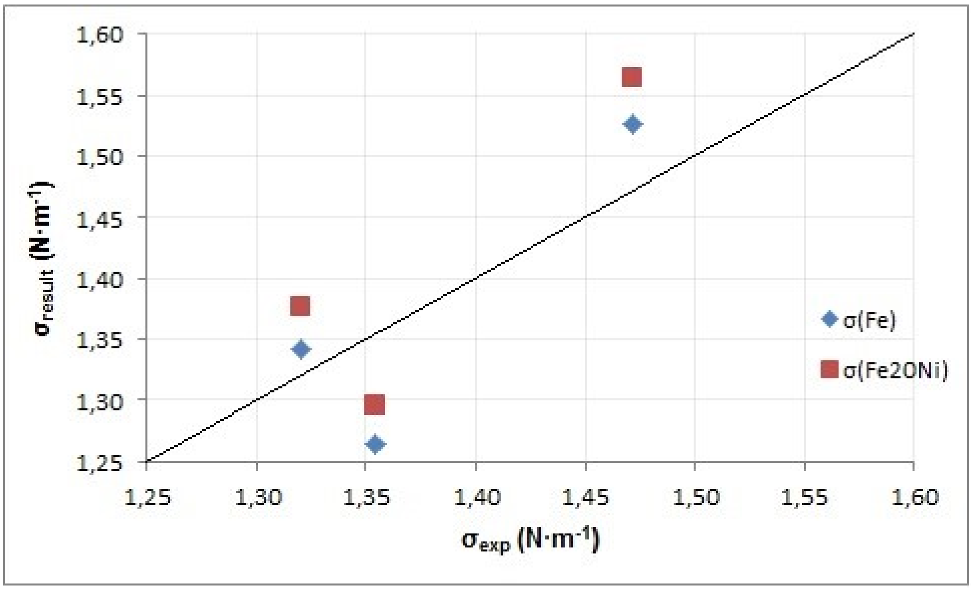

Figure 1: Correlation between calculated and experimental values of surface tension.

Because of the use of scale factor in these calculations, the standard has to be measured under same conditions as samples and the standard has to behave on the similar way, should have similar properties.

Acknowledgement

This paper was created on the Faculty of Metallurgy and Materials Engineering (FMME) in the Project No. LO1203 "Regional Materials Science and Technology Centre - Feasibility Program" funded by Ministry of Education, Youth and Sports of the Czech Republic. This work was also supported by Technology Agency of the Czech Republic (TA 03011277) and two SGS projects (SP2015/88 and SP2015/70). This paper was created under the Project No. CV6005531 „Support and development of international relationship and mutual foreign activities of students and staff on FMMI", funded by VŠB – Technical University of Ostrava, Czech Republic.

References

[1] Fowler, R. H. In: *Proceedings of the Royal Society of London* A 159 (1937), page 229.

[2] Kirkwood, J. G. and Buff, F. P. In: *Journal of Chemical Physics* 17 (1949), page 338.

[3] Lang, N. D. and Khon, W. In: *Physical Review* B 1 (1970), page 4555.

[4] Evans, R. In: *Journal of Physics* C 7 (1974), page 2808.

[5] Mahan, G. D. In: *Physical Review* B 12 (1975), page 5585.

[6] Zykova-Timan, T. et al. In: *Physical Review Letters* 94 (2005), page 176105.

[7] Korkmaz, S. D. and Korkmaz, S. In: *Applied Surface Science* 257 (2010), pages 261–265.

[8] Tanaka, T. In: *Treatise on Process Metallurgy: Process Phenomena* 2 (2014), pages 35–59.

[9] Picha, R., Vřešťál, J., and Kroupa, A. In: *Calphad* 28 (2004), pages 141–146.

[10] Yan, L. et al. In: *Calphad* 31 (2007), pages 112–119.

[11] Plevachuk, Y. et al. In: *Surface Science* 605 (2011), pages 1034–1042.

[12] Rosypalová, S. et al. In: *Proceedings of the 22nd International Conference Metallurgical and Materials Conference and Metal and Brno and Czech Republic* (2013), pages 80–85.

[13] Cotes, S., Guillermet, A. F., and Sade, M. In: *Materials Science and Engineering* A273–275 (1999), pages 503–506.

[14] Banerjee, A. et al. In: *Materials Letters* 59 (2005), pages 1219–1222.

[15] Meybodia, M. K. et al. In: *Chemical Engineering Research and Design* 95 (2015), pages 79–92.

[16] Andersson, J. O. et al. In: *Calphad* 26 (2002), pages 273–312.

[17] “Thermo-Calc Software TCFE7 Steels/Fe-alloys database version 7”. In: (). Accessed 23 Aug 2013).

[18] Tanaka, T., Lee, J., and Scheller, P. R. In: *Treatise on Process Metallurgy: Process Phenomena* 2 (2014), pages 61–77.

[19] Sharan, A. and Cramb, A. W. In: *Metallurgical and Materials Transactions* B 26B (1995), pages 87–94.

[20] Kalup, A. et al. In: *Proceedings of the 23rd International Metallurgical and Materials Conference and Metal and Brno and Czech Republic* (2014), pages 695–700.

Deutsche Edelstahlwerke - Tailor-made steel solutions

Dr.-Ing. Armin Krabiell
Deutsche Edelstahlwerke GmbH

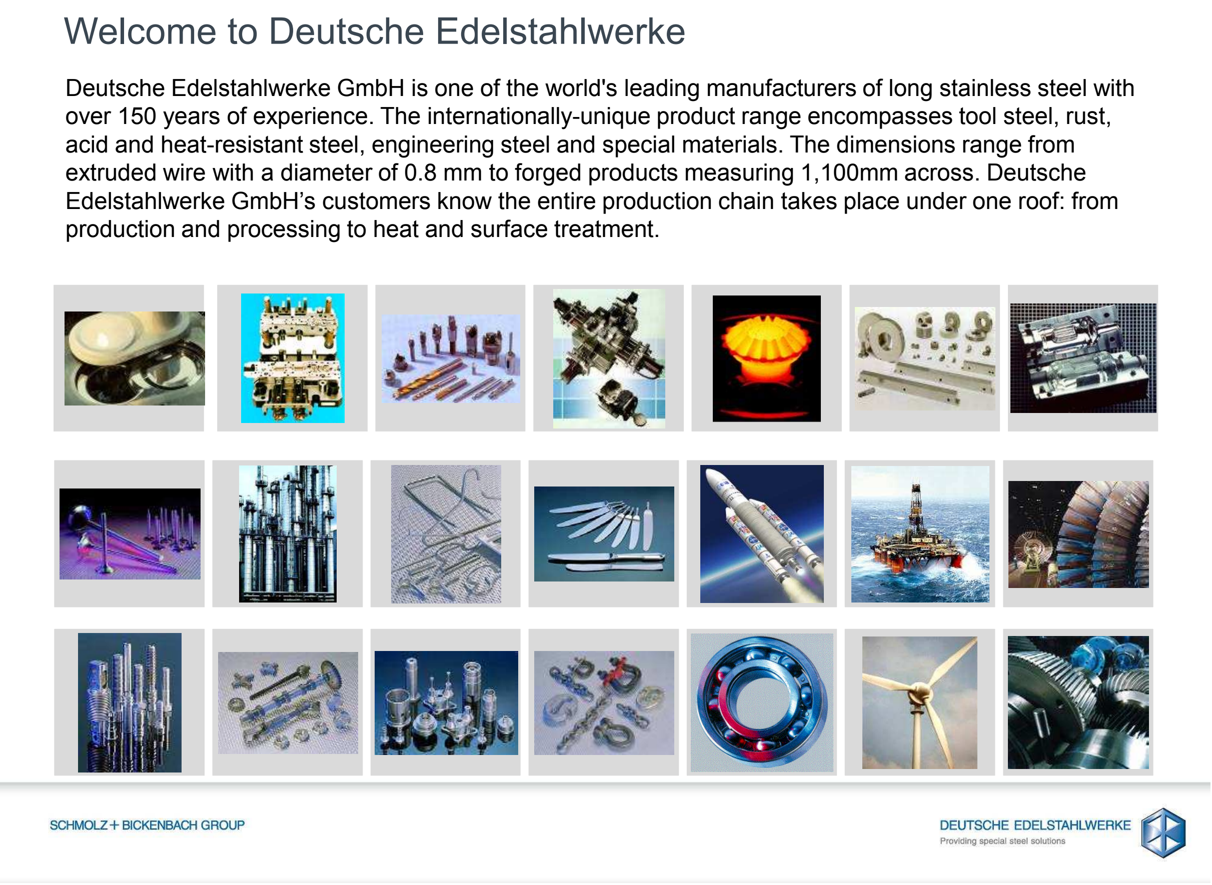

Welcome to Deutsche Edelstahlwerke

Deutsche Edelstahlwerke GmbH is one of the world's leading manufacturers of long stainless steel with over 150 years of experience. The internationally-unique product range encompasses tool steel, rust, acid and heat-resistant steel, engineering steel and special materials. The dimensions range from extruded wire with a diameter of 0.8 mm to forged products measuring 1,100mm across. Deutsche Edelstahlwerke GmbH’s customers know the entire production chain takes place under one roof: from production and processing to heat and surface treatment.

SCHMOLZ + BICKENBACH GROUP

DEUTSCHE EDELSTAHLWERKE
Providing special steel solutions

Characteristic of microstructure of WE43 magnesium matrix composite reinforced with carbon fibers

Michał Dudek[a], Adam Gryc[b], Tomasz Rzychoń[c], Maciej Dyzia[d]
Silesian University of Technology
Faculty of Materials Engineering and Metallurgy, Krasińskiego 8 STR, 40-019 Katowice, Poland
[a]mdudek215@gmail.com, [b]gryadam@wp.pl, [c]tomasz.rzychon@polsl.pl,
[d]maciej.dyzia@polsl.pl

Abstract

In the paper the microstructure of WE43 magnesium matrix composite reinforced with carbon fibres is presented. Sample of as-cast WE43 magnesium alloy reinforced with carbon fibre were investigated. The investigations on light microscope, scanning electron microscope and hardness tested. The transitional areas composed of magnesium, nickel, neodymium, yttrium and zirconium on the reinforcement – carbon fibres.

Keywords: Magnesium Alloys, Carbon Fibres, Composites, Magnesium Matrix Composites.

1 Introduction

Magnesium alloys are widely employed in aerospace and automotive industry, especially for components of aircraft and automotive engines, such as compressors' pistons and bodies. This employment is justified by the low density of these alloys, combined with high specific strength, good creep resistance up to 523 K and corrosion resistance.

The wide employment of magnesium alloys is justified by their low density, combined with high specific strength, corrosion resistance and good creep resistance up to 250 °C. The best creep resistance and the highest strength properties among commercial magnesium alloys are presented by the WE43 and WE54 alloys, containing yttrium and neodymium. Mentioned superior properties are achieved by conventional age-hardening treatment, typically involving a solution treatment of 8 h at 525 °C, a hot water quench and a subsequent ageing treatment of 16 h at 250 °C. Depending on the ageing temperature the formation of metastable β'' ($Mg_3(Y_{0,85}Nd_{0,15})$), β' ($Mg_{12}NdY$ or $Mg_{24}Y_2Nd_3$), intermediate β_1 (Mg_3RE, RE = Nd, Ce, La, Gd) and equilibrium β ($Mg_{14}NdY$ in WE54, $Mg_{14}Nd_2Y$ in WE43) phases as disperse participates, strengthening the alloy, in WE alloys has been reported. The addition of expensive rare earth elements is one of a few possible ways to increase high temperature mechanical properties of cast magnesium alloys [1, 2].

In case of difficult working conditions of engines' components, notably high stresses and creep, the further development of materials, based on magnesium alloys is necessary. The further improvement of magnesium based materials involves the usage of different kinds of reinforcement, creating magnesium metal matrix composites. In case of fibre reinforcement, according to the literature, the bending strength of unidirectionally reinforced with continuous carbon fibres magnesium matrix composite oscillates around 1000 MPa, with low density on the level of $1.8\,\mathrm{g\,cm^{-3}}$. These superior properties could be retained up to 300 °C [3, 4].

To fabricate the fibre-reinforced composites the pressure infiltration technology is commonly used. The process comprises preparing a perform of reinforcement, placing it into casting mold, pouring of the molten magnesium matrix and its solidification under high pressure. The pressure has to be properly controlled, due to the fact, that excessively high pressure could be the reason of turbulent flow of molten alloy and in consequence gas entrapment, causing the material porosity. The advantage of pressure infiltration in comparison with stir casting is the possibility of higher volume fractions of reinforcement (up to 40-50%) usage [4, 5].

2 Material and experimental methods

2.1 Material

The investigated samples were obtained from two casts of WE43 magnesium alloy with chemical composition given in Table 1, provided by Magnesium Electron Company, Manchester, England.

Table 1: Chemical composition of WE43 casting magnesium alloy, according to Magnesium Elektron UK (wt. %).

Mg	**RE**	**Y**	**Zr**
Balance	2,4-4,4	3,7-4,3	0,4 min

2.2 Composite fabrication technology

To fabricate the composite the pressure infiltration technology was used. The process comprises preparing a perform of reinforcement and placing it into the casting mold, pouring of the molten magnesium matrix and it is solidification under the high pressure. The pressure has to be properly controlled, due to the fact, that excessively high pressure could be the reason of turbulent flow of molten alloy and in consequence gas entrapment, causing the material porosity [4–6].

2.3 Experimental methods

Images of microstructure were acquired with an Olympus GX71 light microscope, equipped with the Olympus DP70 12 Megapixels digital camera, using the bright field technique and Hitachi S-4200 Scanning Electron Microscope, equipped with X-radiation EDS detector from Noran Instruments, using SE technique. EDS analysis were performed with an accelerating voltage of 15 keV.

The hardness of the sample was tested by using a Vickers hardness tester Duramin 5, a load of 0.2 kg.

3 Results

3.1 Light microscope investigation

The microstructure of WE43 matrix composite reinforced with carbon fibre consist of magnesium matrix (Figure 1c. point 1), eutectic compound (Figure 1c. point 2), small irregular particles (Figure 1c. point 3) and significant amount of shrinkage porosity (Figure 1c. point 4). Light microscope image of microstructure shows also reinforcement fibres (Figure 1c. point 5).

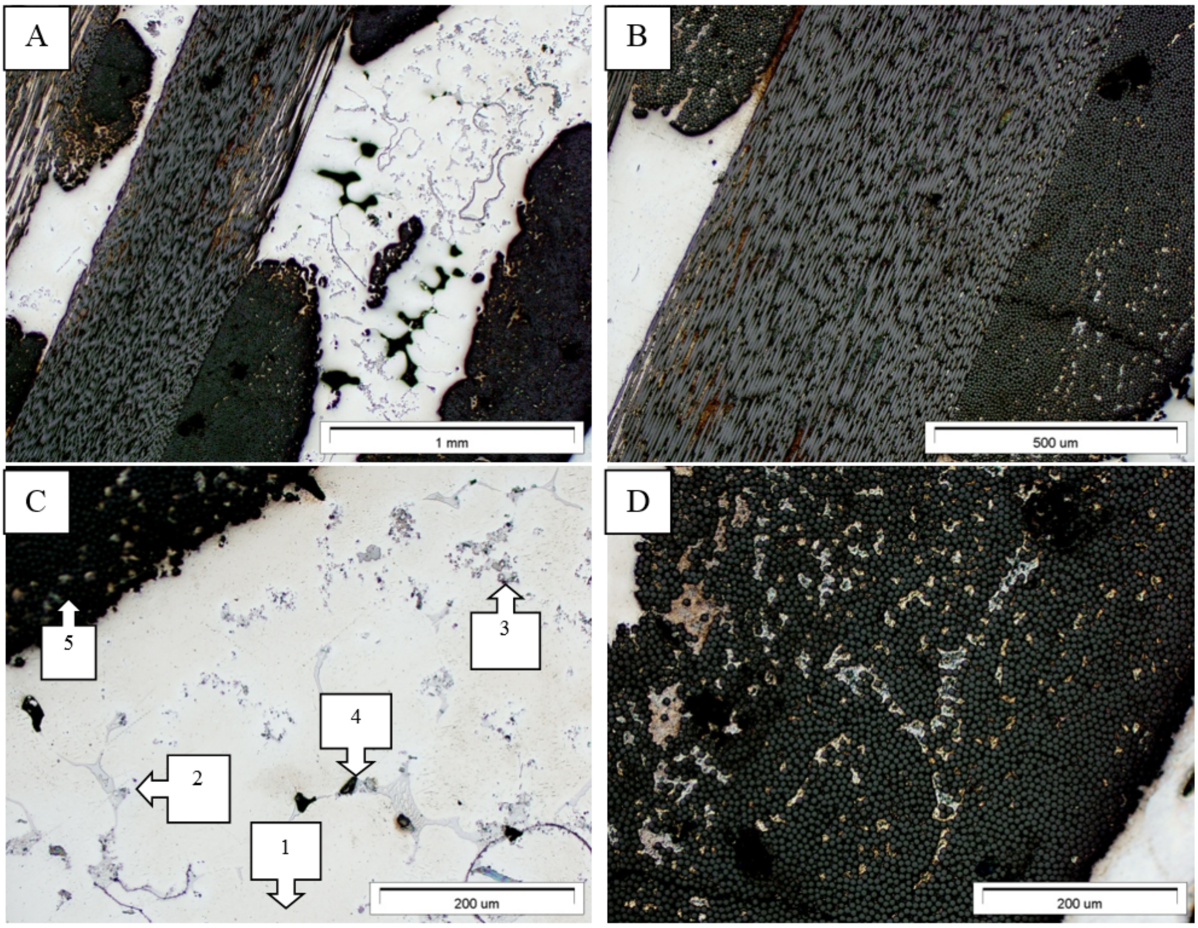

Figure 1: Light micrograph WE43 reinforced with carbon fibers.

3.2 Scanning electron microscope investigation

The SEM investigations and EDS analysis lead to determination of qualitative composition of particles. The eutectic compound is composed of magnesium, yttrium and dysprosium, is β-phase [4] (Figure 3. Point 2). Matrix composed of magnesium (Figure 3. point 5). Particles near to fibres were found to be appeared Mg, Dy, Y and Ca which is a contamination (Figure 3. point 1).

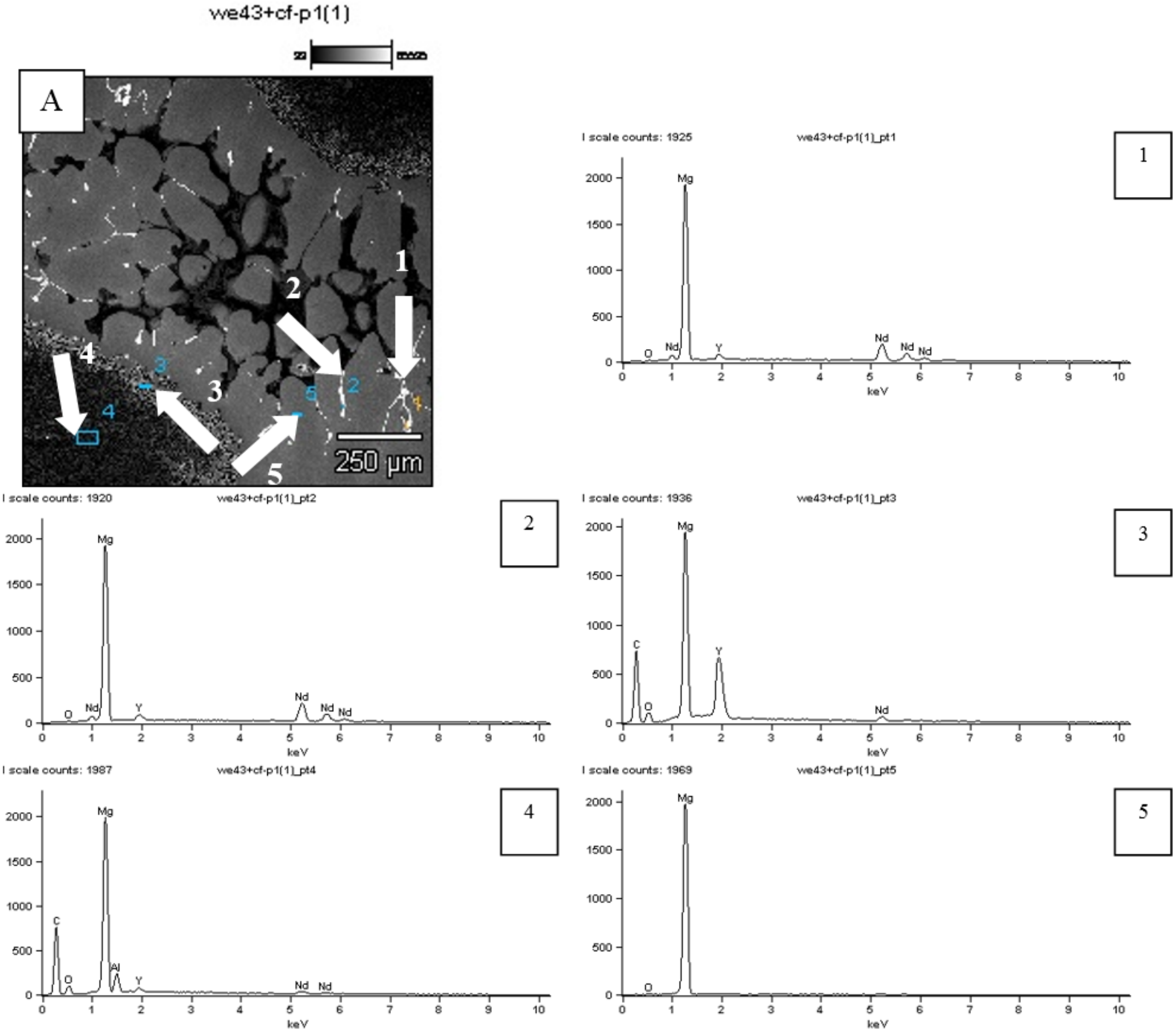

Figure 2: SEM micrograph with analysed points of WE43 reinforced with carbon fibers.

3.3 Hardness research

In Table 2 the results of HV0,2 microhardness test were made of matrix of sample on hardness tester Duramin 5 with a load of 0.2 kg. The average hardness is 54,6 HV0,2, standard deviation is 5,25.

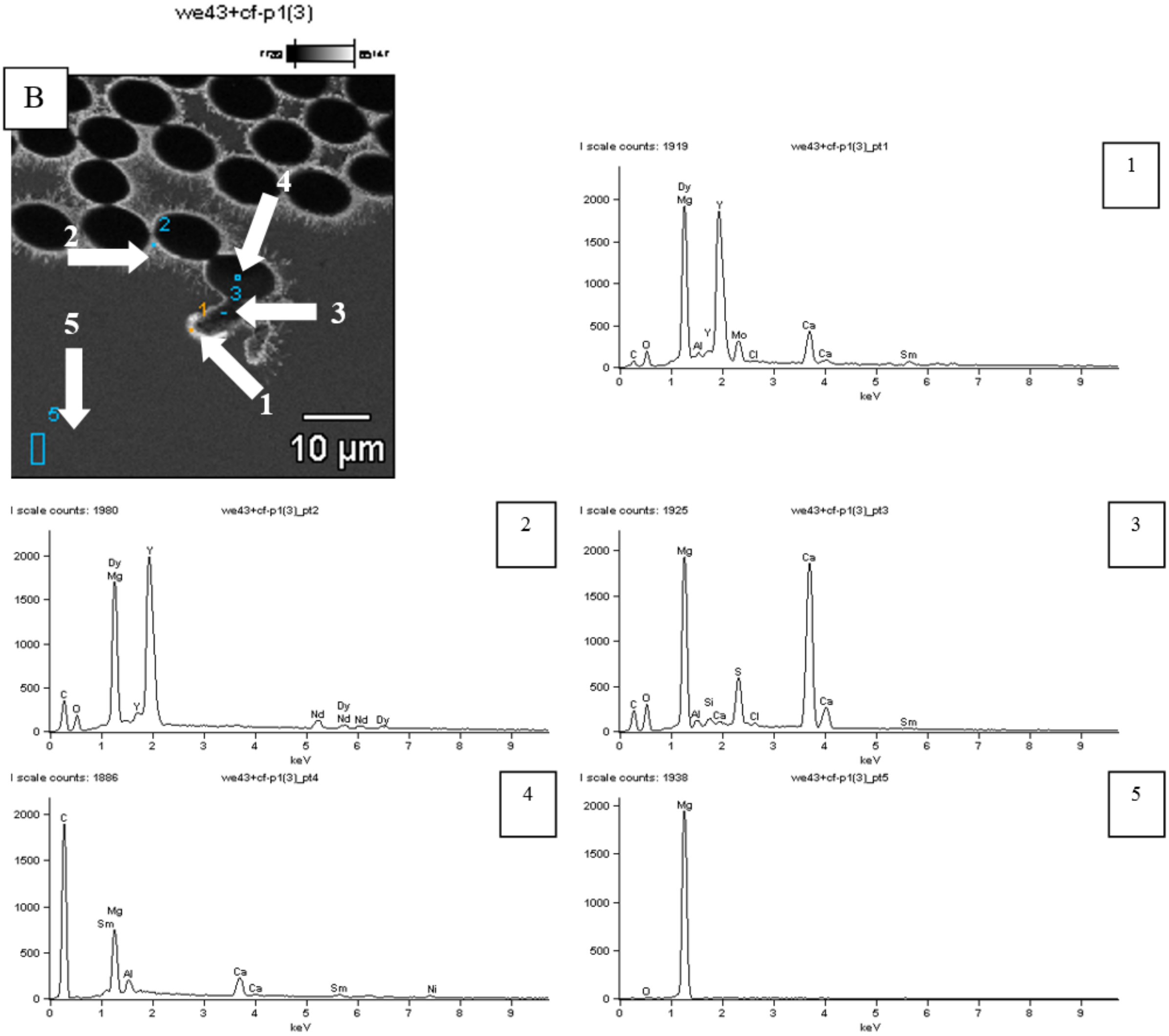

Figure 3: SEM micrograph with analysed points of WE43 reinforced with carbon fibers.

Table 2: Results hardness investigation.

HV0,2 Hardness	Average	Standard deviation
63	54,6	5,25
57		
56		
45		
58		
49		
54		
50		
56		
58		

4 Conclusions

Described investigations allowed the detailed analysis of fabricated composites in terms of microstructure and chemical composition. The following conclusions were drawn:

- In investigated samples the segregation of rare earth elements (neodymium and dysprosium), yttrium and zirconium to the matrix – reinforcement boundary was identified. This phenomenon caused the formation of small particles, consisting of mentioned elements in this area.
- The most probable reason of elevated concentration of oxygen in the transitional layer and matrix in the vicinity of reinforcement fibres was the fibres oxidation during the process of composite fabrication (the carbon fibres were not coated with protective coating).
- The hardness of matrix is 54,6 HV0,2.

References

[1] Rzychoń, T. and Kiełbus, A.: “Microstructure of WE43 casting magnesium alloy”. In: *Journal of Achievements in Materials and Manufacturing Engineering* 21 (2007), pages 31–34.

[2] Rzychoń, T., Dyzia, M., and Pikos, I.: “Microstructure of WE43 Magnesium Matrix Composite Reinforced with Ceramic Particles”. In: *Solid State Phenomena* 211 (2014), pages 101–.108.

[3] Gryc, A., Dudek, M., and Rzychoń, T.: “The influence of aluminium contamination on microstructure of WE43 magnesium matrix composite reinforced with carbon fibres”. In: *XVI Mįedzynarodowa Studencka Sesja Naukowa „Materiały i Technologie XXI wieku”*. 2014, pages 132–135.

[4] Ye, X. and Liu, Y.: “Review of recent studies in magnesium matrix composites”. In: *Journal of Materials Science* 39 (2004), pages 6153–6171.

[5] Dybowski, B. and Kiełbus, A.: “Non-metallic inclusions in the WE43 magnesium casting alloy”. In: *XV Mįedzynarodowa Sesja Studencka „Materiały i Technologie XXI wieku”*. 2013, pages 51–54.

[6] Chang, H.-W. et al.: “The role of Al_2Y in grain refinement in Mg-Al-Y alloy system”. In: *Journal of Magnesium and Alloys* 1 (2013), pages 115–121.

Metallographische Gefügecharakterisierung eines Medium-Mn-Stahles

M. Rahofer[1], R. Schneider[1], P. Peißl[1], C. Commenda[2], L. Samek[1], E. Arenholz[2]
[1]FH Oberöstereich, [2]voestalpine Stahl GmbH
[1]Fakultät für Technik und Umweltwissenschaften, 4600 Wels, Austria; [2]4020 Linz, Austria

Kurzfassung

Zur Gefügecharakterisierung an einem Medium-Mn-Stahl mit 5 Gew.% Mn wurden verschiedene Ätzmethoden herangezogen. Die weiteren Untersuchungen erfolgten sowohl lichtoptisch als auch mittels Rasterelektronenmikroskopie. Zur Bestimmung des Restaustenitgehaltes wurde die Röntgendiffraktometrie verwendet. Die Ergebnisse zeigen die Gefügeentwicklung in Abhängigkeit von den vorangegangenen Glühprozessen. Eine vollständige

Austenitisierung führt, je nach Abschreckgeschwindigkeit, zu einem martensitischen oder martensitisch-bainitischen Gefüge. ART-(Austenite-Reversed-Transformation)-Glühungen im interkritischen Bereich ergaben Gefüge aus hoch angelassenen Martensitnadeln und sehr hohen Restaustenitgehalten.

Schlüsselwörter: Medium-Mn-Stähle, Metallographie, TRIP-Stähle, Restaustenit

1 Einleitung

In der vorliegenden Arbeit wurde das Gefüge eines Medium-Mn-Stahles in verschiedenen Wärmebehandlungszuständen untersucht. Bei Medium-Mn-Stählen handelt es sich um Legierungen mit 0,05-0,2 Gew.% C und 4-10 Gew.% Mn, die zur 3. Generation der AHSS (Advanced High Strength Steels) gezählt werden. Sie sind eine Weiterentwicklung der im Automobilbau verwendeten AHSS der 1. Generation, die z.B. Dualphasen-, Complexphasen- und TRIP-Stähle umfasst [1, 2]. Aufgrund ihrer sehr guten Eigenschaftskombination von Zugfestigkeit und Bruchdehnung gelten diese Stähle als vielversprechende Nachfolger der AHSS der 1. Generation [3–6]. Ihre hervorragenden mechanischen Eigenschaften beruhen auf dem TRIP-Effekt, der durch einen hohen Gehalt metastabilen Restaustenits erzielt wird. In Abbildung 1 ist ein für diese Stähle typischer ART (Austenite-Reversed-Transformation)-Glühzyklus [7] nach einem Warmwalzvorgang dargestellt, der schematisch das Prinzip der Restaustenitstabilisierung zeigt. Nach dem Walzen wird zunächst austenitisiert und abgeschreckt, um ein feines, lattenmartensitisches Gefüge einzustellen. Anschließend wird im Zweiphasengebiet Ferrit/Austenit geglüht, wobei Kohlenstoff und Mangan in den Austenit diffundieren, welcher sich vorzugsweise zwischen den Martensitnadeln bildet [8]. Der Austenit wird hierbei chemisch und mechanisch stabilisiert. Am Ende der Wärmebehandlung liegt ein feines Gefüge aus hoch angelassenem Martensit und Restaustenit vor.

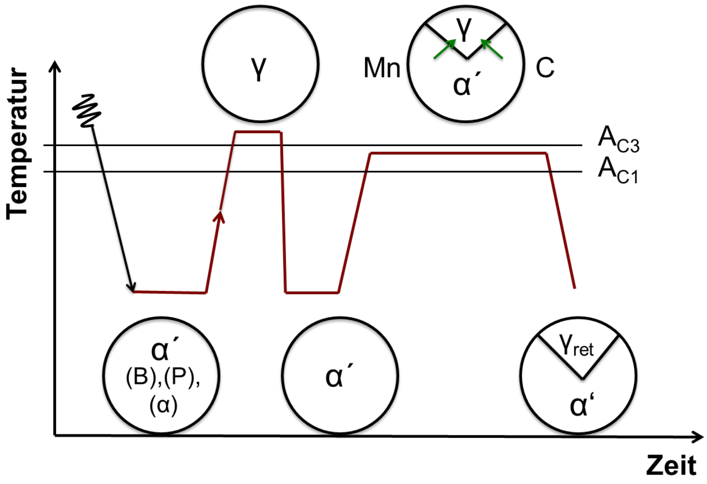

Abbildung 1: Typische Wärmebehandlung von Medium-Mn-Stählen.

2 Experimentelle Durchführung

Bei den untersuchten Proben handelte es sich um eine niedrigkohlige Legierung mit 5 Gew.% Mn. Die aus dem Austenitgebiet abgeschreckten Proben sowie die interkritisch geglühten Proben mit unterschiedlichen Korngrößen lagen als Warmband vor. Die mit vier verschiedenen Ätzmethoden kontrastierte, interkritisch geglühte Probe wurde kaltgewalzt. Die Wärmebehandlung der Proben erfolgte an einem Abschreckdilatometer mit unterschiedlichen Halte- und Abkühlzeiten. Um negative Effekte bei der röntgendiffraktometrischen Untersuchung (XRD) auszuschließen wurden die Proben in einer amorphen Matrix kalt eingebettet. Aufgrund der großen Empfindlichkeit des Restaustenits gegenüber mechanischen Einwirkungen erfolgte eine sehr schonende Präparationsroutine mit fein abgestuften Polierschritten. Für die lichtmikroskopische Untersuchung wurden die Schliffe mit den in [9] beschriebenen Ätzlösungen Nital, Marshall, Klemm-I und LePera kontrastiert. Die Bestimmung des Restaustenitgehaltes erfolgte mittels XRD (Mo-K_α Strahlung, 40kV Anregungsspannung) nach ASTM E 975-03 an den Ferritreflexen $\alpha[200]$, $\alpha[211]$, $\alpha[220]$ sowie den Austenitreflexen $\gamma[200]$, $\gamma[220]$ und $\gamma[311]$. Nach der Kontrastierung mit verschiedenen Ätzmitteln wurden die Proben lichtmikroskopisch und elektronenmikroskopisch (REM) untersucht.

3 Ergebnisse

3.1 Einfluss der Abkühlrate nach vollständiger Austenitisierung

Die nachfolgend dargestellten Ergebnisse beziehen sich auf die Abkühlung aus dem vollaustenitischen Zustand. Abbildung 2 zeigt die Gefüge bei rascher (100K/s) und langsamer (0,03K/s) Abkühlung nach einer Ätzung mit Nital. Bei der raschen Abkühlung ist ein lattenmartensitisches Gefüge zu erkennen. Das Gefüge der langsam abgekühlten Probe ist dagegen hauptsächlich bainitisch, was sich anhand lamellenartig geschichteter Strukturen zeigt. Die Austenitkorngrenzen zeichnen sich hier gut sichtbar ab.

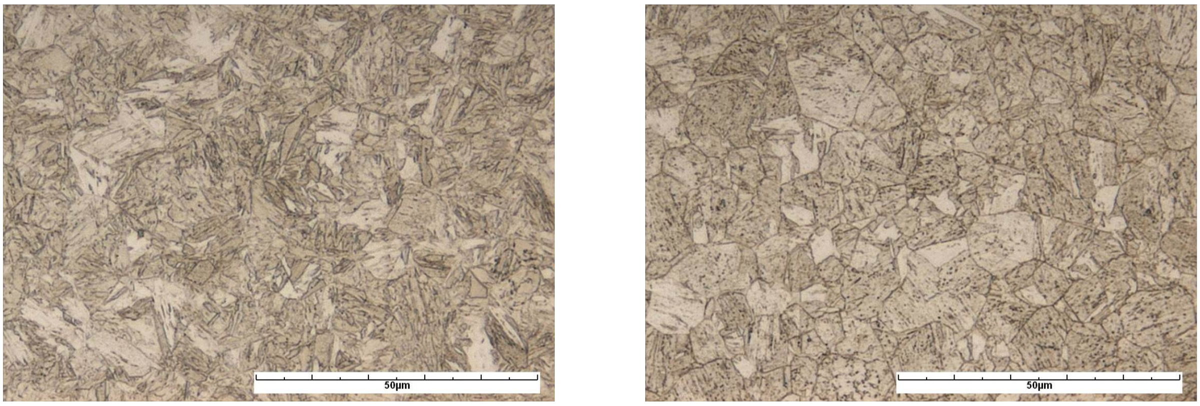

Abbildung 2: Gefüge des Stahles 0,1C5Mn nach einer Abkühlung mit 100K/s (links) bzw. 0,03K/s (rechts), Nitalätzung.

Vergleicht man die Nitalätzung mit der Ätzung nach Klemm in Abbildung 3, so ist eine gute Übereinstimmung zu erkennen. Bei der raschen Abkühlung ist, ebenso wie bei der Nitalätzung, ein martensitisches Gefüge festzustellen, wobei nach [9] blaue Bereiche auf Ferrit und braune Bereiche auf Martensit hinweisen. Aufgrund der raschen Abkühlung ist aber mit einem vollständig martensitischen Gefüge zu rechnen und die verschiedenen Färbungen lassen sich hier eher auf unterschiedliche Orientierungen der Nadelpakete zurückführen.

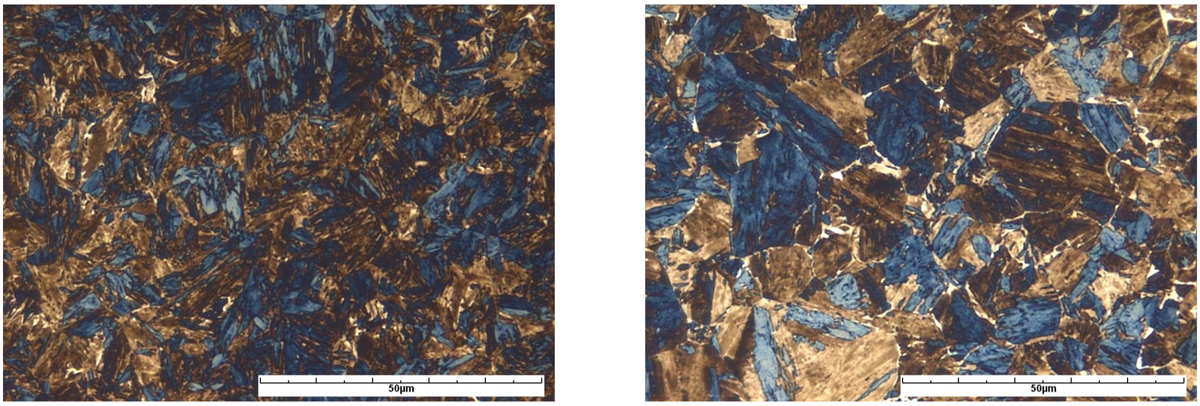

Abbildung 3: Gefüge des Stahles 0,1C5Mn nach einer Abkühlung mit 100K/s (links) bzw. 0,03K/s (rechts), Ätzung nach Klemm.

Bei der langsamen Abkühlung zeichnet auch die Ätzung nach Klemm (Abbildung 3 rechts) schichtartige Strukturen im Inneren der ehemaligen Austenitkristallite, was für den Bainit charakteristisch ist. Weiters weist die Färbung von Braun- bis Blauschattierungen auf den Ferrit des Bainits hin. Die ehemaligen Austenitkorngrenzen, die sich bei der Nitalätzung dunkel abzeichnen, sind bei der Ätzung nach Klemm teilweise weiß bis hellbraun gefärbt, wonach sie nach [9] Restaustenit oder Martensit zuzuordnen sind. Die sehr geringen Anteile an weißen Bereichen stehen mit dem röntgendiffraktometrisch bestimmten Restaustenitanteil von < 2 % in guter Übereinstimmung. Die REM-Aufnahmen der Nital-geätzten Proben in Abbildung 4 bestätigen die Ergebnisse der lichtoptischen Untersuchungen. Bei der schnellen Abkühlung zeigt sich wieder das martensitische Gefüge mit klar sichtbaren Nadelpaketen, während bei der langsamen Abkühlung zeilig-geschichtete Strukturen erkennbar sind, bei denen es sich um die Karbidausscheidungen des Bainits handeln dürfte. Die Bereiche an den Korngrenzen sind offenbar nicht vom Ätzangriff betroffen und unterscheiden sich demnach in ihrem elektrochemischen Potential gegenüber der Matrix [10]. In Übereinstimmung mit der Ätzung nach Klemm muss es sich daher um Restaustenit bzw. Martensit handeln.

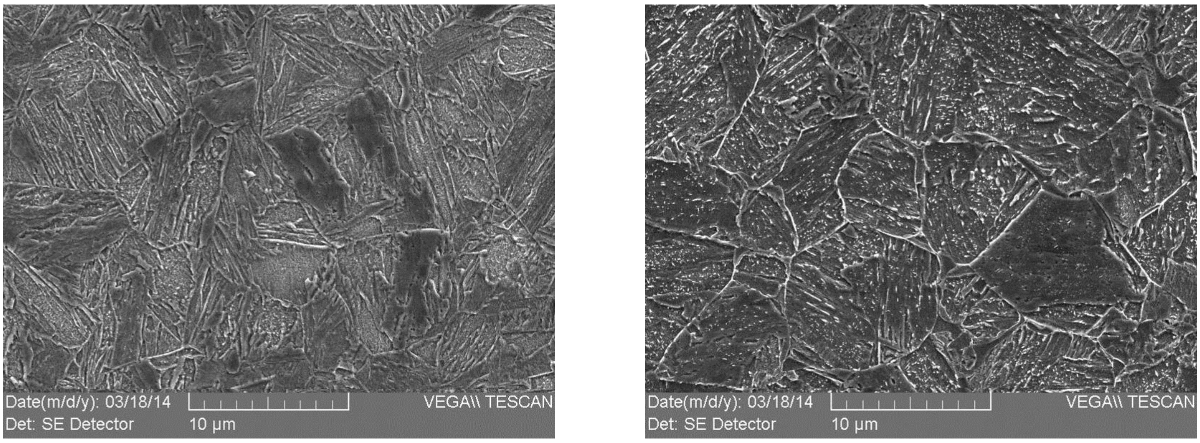

Abbildung 4: Gefüge des Stahles 0,1C5Mn nach einer Abkühlung mit 100K/s (links) bzw. 0,03K/s (rechts), Nitalätzung, REM.

3.2 Einfluss einer interkritischer Glühung

Die folgenden Gefüge (Abbildung 5 und Abbildung 6) sind jeweils durch einen ART-Glühzyklus entstanden (interkritische Glühung bei 670°C), wobei eine unterschiedliche Austenitkorngröße vor der interkritischen Glühung eingestellt wurde. Anhand der Nitalätzung in Abbildung 5 werden zunächst die unterschiedliche Strukturgrößen deutlich. Bei beiden Proben besteht das Gefüge aus paketartig geschichteten, hoch angelassenen Martensitnadeln.

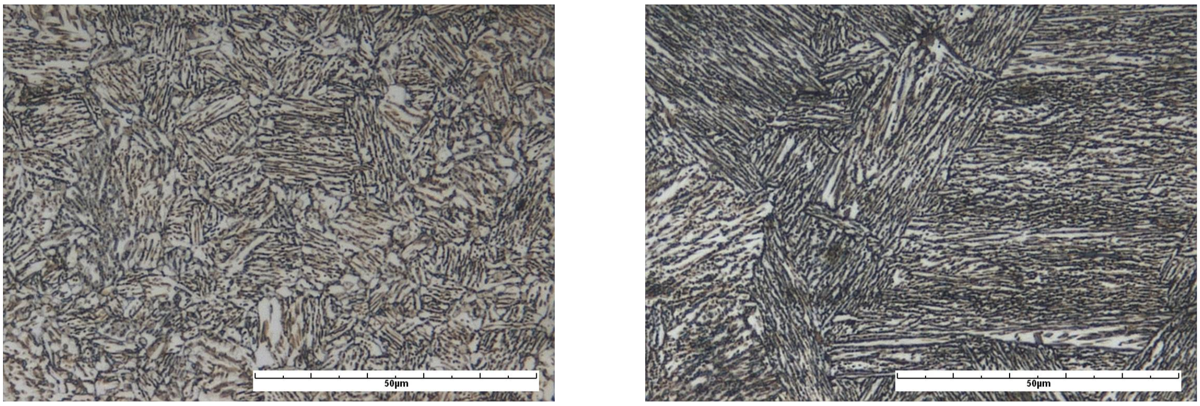

Abbildung 5: Gefüge des Stahles 0,1C5Mn, Nitalätzung, links: feines Korn, rechts: grobes Korn.

Durch die Ätzung nach Klemm zeigen sich zwischen den angelassenen Martensitnadeln weiße Bereiche, die nach [9] austenitisch sind. Diese Beobachtung wurde auch in [5], [7] und [11] gemacht, wo interkritische Glühungen ähnlicher Legierungen zu einem vergleichbaren Gefüge geführt haben. Die Klemm-Ätzung zeigt auch, dass die Morphologie des Restaustenits sich bei kleiner und großer Korngröße leicht unterscheidet. Bei kleinem Austenitkorn bildet sich der Restaustenit nicht nur in zeilig-gestreckter Form zwischen den angelassenen Martensitlamellen, sondern verstärkt polygonal eingeformt aus. Bei grobem Korn befindet sich der Restaustenit hingegen zum größten Teil zwischen den angelassenen Martensitnadeln und ist aufgrund der „vergrößerten“ Strukturgröße auch deutlicher zu erkennen. Dennoch ist bei beiden Korngrößen der Restaustenit in bestimmten Bereichen nicht mehr lichtoptisch auflösbar, da er zu fein ist. Bei der Ätzung nach Klemm, und besonders bei großer Korngröße, ist weiters erkennbar, dass die weißen Bereiche zwischen den Nadeln teilweise hellbraun gefärbt sind, was nach [9] auf neu gebildeten Martensit hinweist. Es ist daher davon auszugehen, dass sich aus dem Restaustenit bei der Abkühlung zum Teil wieder frischer Martensit gebildet hat.

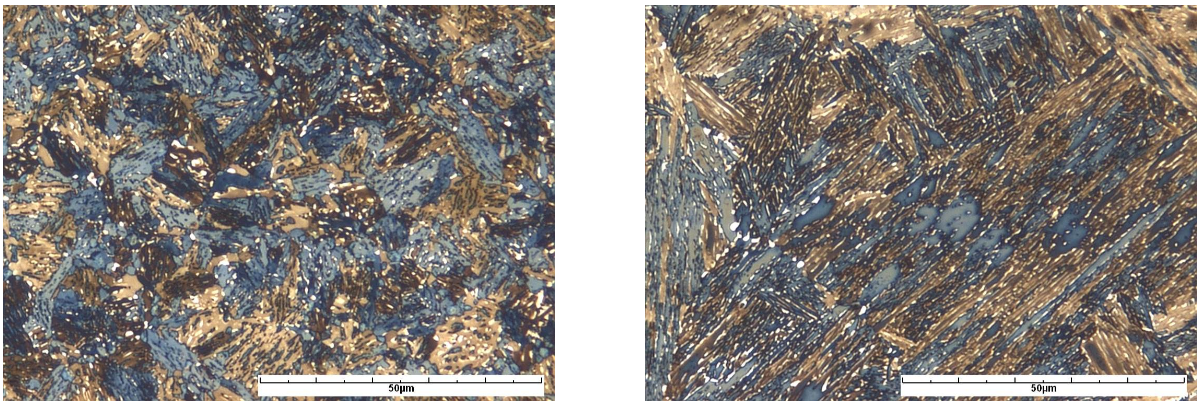

Abbildung 6: Gefüge des Stahles 0,1C5Mn, Ätzung nach Klemm, links: feines Korn, rechts: grobes Korn.

Aus dem Vergleich mit der Klemm-Ätzung lässt sich nun ableiten, dass die bei der Nitalätzung in unterschiedlich dunklen Schattierungen gezeichneten Bereiche zum Teil dem Restaustenit und, falls vorhanden, auch dem Martensit zuzuordnen sind. Die Nitalätzung eignet sich gut für die Beurteilung der Struktur und Geometrie der Gefügebestandteile, jedoch nicht für eine klare Unterscheidung der vorhandenen Phasen.

3.3 Gegenüberstellung verschiedener Ätzmethoden

An einer kaltgewalzten Probe, die einem ART-Glühzyklus unterzogen wurde (Austenitisierungstemperatur 810°C, interkritische Glühung bei 650°C) wurden vier verschiedene Ätzmethoden angewendet, die in Abbildung 7 gegenübergestellt werden. Wie bereits bei den vorhergehenden Proben besteht das Gefüge aus hoch angelassenen Martensitnadeln mit Restaustenit. Das nadelige Gefüge wird bei allen Ätzmethoden deutlich entwickelt, wobei die Ätzung nach Marshall die Struktur am gleichmäßigsten zeigt. Durch die Nitalätzung werden die ehemaligen Austenitkorngrenzen sichtbar, während anhand der Klemm-Ätzung die Lage und Verteilung des Restaustenits am besten erkennbar ist. Aufgrund der blauen bis braunen Färbung liegt hier nach [9] ein ferritisches Grundgefüge vor (hoch angelassener Martensit). Die weißen Bereiche sind dem Restaustenit zuzuordnen. Bei Ätzung nach LePera bleiben Martensit und Restaustenit gegenüber der ferritischen Matrix weiß [12]. Sie sind hier nicht eindeutig voneinander zu unterscheiden, was auch in [13] diskutiert wird. Der mittels XRD bestimmte Restaustenitgehalt beträgt bei dieser Probe 24%. Das Bild, das die Ätzung nach Marshall ergibt, deckt sich grundsätzlich mit der Ätzung nach LePera, da sowohl Martensit, als auch Restaustenit gegenüber dem Ferrit ein anderes elektrochemisches Potential aufweisen [10] und durch das Marshall-Ätzmittel gelöst werden. Analog zu den Ergebnissen in [5] lässt sich anhand der Marshall-Ätzung der Restaustenit indirekt nachzuweisen.

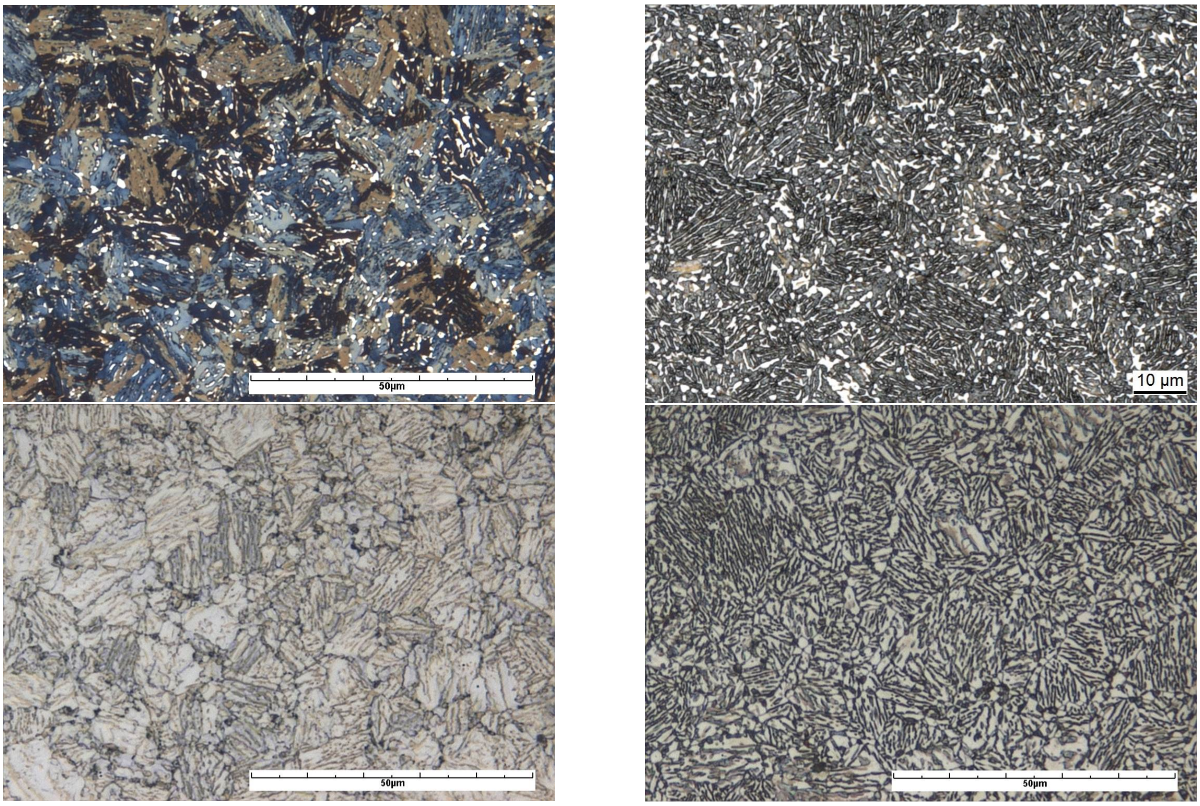

Abbildung 7: Gefüge des Stahles 0,1C5Mn nach einer interkritischen Glühung bei 650°C, links oben: Ätzung nach Klemm, rechts oben: Ätzung nach LePera, links unten: Nitalätzung, rechts unten: Ätzung nach Marshall.

4 Zusammemfassung

Mittels unterschiedlicher Ätzmethoden (Nital, Marshall, Klemm, LePera) werden verschiedene Gefügebestandteile von Medium-Mn-Stählen sehr gut sichtbar gemacht, wobei jede Ätzmethode andere Gefügemerkmale deutlicher entwickelt. Zur Quantifizierung des Restaustenitgehaltes ist aber eine alternative Ermittlung z.B. mittels Röntgendiffraktometrie notwendig, da die Austenitplatten zum Teil nur submikroskopisch klein zwischen den Martensitlatten eingebettet und lichtoptisch kaum mehr auflösbar sind. Durch die Ätzung nach Klemm kann allerdings die Lage und Form des Restaustenits gut sichtbar gemacht werden. Die Ätzung nach LePera zeigt zusätzlich neu gebildeten Martensit, lässt aber keine eindeutige Unterscheidung zwischen Restaustenit und Martensit zu.

Danksagung

Die Autoren danken der voestalpine Stahl GmbH für die finanzielle, materielle und ideelle Unterstützung des Projektes. Besonderer Dank gebührt der österreichischen Forschungsförderungsgesellschaft mbH (FFG) für die finanzielle Förderung im Rahmen des Projektes Nr. 841377.

Literaturverzeichnis

[1] Matlock, D. K. et al.: “Recent developments in advanced high strength sheet steels for automotive applications: an overview”. In: *Jestech* 15.1 (2012), Seiten 1–12.

[2] Jin, Y. S.: “Development of advanced high strength steels for automotive applications”. In: *La Metallurgia Italiana* 67 (2011), Seiten 43–48.

[3] Miller, R. L.: “Ultrafine-grained microstructures and mechanical properties of alloyed steels”. In: *Metallurgical Transactions* 3 (1972), Seiten 905–912.

[4] Dong, H. et al.: “The medium manganese steels: Phenomena and industry potentials”. In: *Proceedings of the 1st International Conference on High Manganese Steels*. 2011.

[5] Arlazarov, A. et al.: “Evolution of microstructure and mechanical properties of medium Mn steels during double annealing”. In: *Material Sciences and Engineering A* 542 (2012), Seiten 31–39.

[6] Huang, H., Matsumura, O. und Furukawa, T.: “Retained austenite in low carbon and manganese steel after intercritical heat treatment”. In: *Materials Science and Technology* 10.7 (1994), Seiten 621–626.

[7] Arlazarov, A. et al.: “Characterization of microstructure formation and mechanical behavior of an advanced medium Mn steel”. In: *Materials Science and Technology*. 2012.

[8] Wang, C. et al.: “Development of ultrafine lamellar ferrite and austenite duplex structure in 0,2C5Mn steel during ART-annealing”. In: *ISIJ* (2011).

[9] Voort, G. F. V.: *Metallography Principles and Practice.* McGraw-Hill Book Company, 1984.

[10] Angeli, J. und E. Füreder, A. C. K. und: “Ätztechniken für die Phasencharakterisierung von niedriglegierten Dual-Phasen- und TRIP-Stählen”. In: *Pract. Metallogr.* 43.10 (2006), Seiten 489–504.

[11] Steineder, K. et al.: “Investigation on the Microstructural Evolution in a Medium-Mn steel (X10Mn5) after Intercritical Annealing”. In: *HTM J. Heat Treatm. Mat.* 70.1 (2015), Seiten 19–25.

[12] Girault, E. et al.: “Metallographic Methods for Revealing the Multiphase Microstructure of TRIP-Assisted Steels”. In: *Materials Characterization* 40 (1998), Seiten 111–118.

[13] Merwin, M. J.: “Microstructure and Properties of Cold Rolled and Annealed Low-Carbon Manganese TRIP Steels”. In: *AIST Steel Properties & Applications Conference Proceedings*. 2007.

Paul Wurth - Technologies for hot metal production

Philipp Bermes[1], Laurence Kayl[2], Steffen Köhler[3], Christian Cortina[3]
Paul Wurth S.A.
[1]BF Process & Technology - Project Engineer, [2]Head of Corporate Communications,
[3]Corporate Marketing - Senior Manager, [4]Head of Human Resources

1 Our profile

The Paul Wurth Group is a leading player in the global market for design and supply of equipment and plant facilities for the ironmaking industry, especially when technically advanced solutions are required.

Headquartered in Luxembourg since its beginnings back in 1870, the company has developed in the course of its history into an engineering company which is active on the international market. As a result of its growth and expansion policy, the Group is today an established technology provider and supplier of complete plants for the primary stage of integrated steelmaking.

Thanks to its extensive experience and capacity to continuously innovate, Paul Wurth is a leading market player for the design and construction of complete blast furnace and coke oven plants. Agglomeration plants, direct reduction plants, environmental protection technologies for the iron and steel industry as well as waste treatment and recycling facilities complete Paul Wurth's product portfolio focused on the primary phase of steelmaking. In addition to its core competence in development and execution of new construction projects and modernizations, Paul Wurth also offers a full range of products and services in engineering, project management, site supervision, commissioning assistance, operator consulting and after-sales.

Besides the activities devoted to the iron and steel industry, Paul Wurth also offers, through its subsidiary Paul Wurth Geprolux, in the Greater Region of Luxembourg tailor-made services, in particular integral planning and multidisciplinary engineering for town planning, civil construction and infrastructure projects. Through its modern and performing subsidiary, CTI Systems S.A., Paul Wurth also supplies and installs integrated and automated intralogistics solutions for heavy-load applications.

With more than 1 500 employees and entities in around 20 countries, the Paul Wurth Group has a strong presence primarily in those regions of the world where a significant iron and steel industry operates.

2 Paul Wurth history

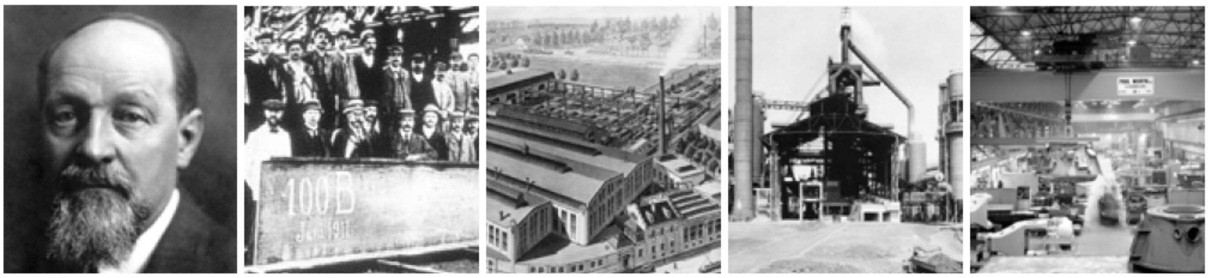

1870 Eugène Muller builds a boilermaking facility in Luxembourg Hollerich, known as „Kesselfabrek“.

1890 Business is taken over by Paul Wurth. The firm specialises in metal erection works, especially the construction of metal bridges and blast furnace shells.

1926 Paul Wurth sells his shares to ARBED.

1951 Paul Wurth acquires the licenses needed to supply complete blast furnaces with all accessories.

1954 Construction of a first blast furnace at S.A. Métallurgique d'Espérance-Longdoz in Seraing, Belgium.

1969 Invention of the Bell Less Top®, a revolutionary, innovative system for blast furnace charging.

1977 A first subsidiary is incorporated in Brazil. A worldwide network of entities is set up.

2003 Together with Dango & Dienenthal Maschinenbau, the joint venture TMT - Tapping Measuring Technology is created.

2004 Fabrication activities are transferred to Arcelor Dommeldange. Paul Wurth becomes a pure engineering company.

2004 Integration of Didier - M&P Energietechnik as Paul Wurth Refractory & Engineering GmbH, specialised in hot blast stove technology and refractory & lining concepts.

2005 Take-over of the blast furnace, coke making and direct reduction activities from SMS Demag S.p.A. and integration of the staff into the newly created Paul Wurth Italia S.p.A.

2009 50.4% shareholding in CTI Systems S.A., a leading provider of automated solutions for heavy-load applications. In 2011, the stake is increased to 75.2%. In 2013, the stake is brought to 100%.

2012 Creation of Paul Wurth IHI Corp., Ltd in Japan, a joint venture with IHI Corporation.

2012 SMS group acquires a majority stake in Paul Wurth, taking over the shares previously owned by ArcelorMittal and Luxempart. Paul Wurth becomes part of the SMS group.

2014 Paul Wurth takes over the cokemaking segment of the German company Schalker Eisenhütte Maschinenfabrik and reinforces its coke oven technology portfolio by adding coke oven machinery.

3 Technologies for hot metal production

Thanks to our extensive know-how in plant and mechanical engineering and our many years of experience in international project management, Paul Wurth is now the market leader in technologies for the primary stage of integrated steelmaking.

Paul Wurth's core competence is in the construction of complete blast furnaces and as part of this we can offer, from a single source, a complete range of products based on our proprietary technologies and customised solutions.

With its cokemaking and sintering technology, Paul Wurth also masters the processes and aggregates upstream of the blast furnace for preparing the burden materials. Finally, environmental and energy-efficient solutions for the iron and steel industry complete the offer. As a result of our full range of products we are able to support our customers in all the processes involved in producing hot metal so that they can achieve optimal, economically-viable production.

Figure 1: 1. Coal grinding, drying and pulverised coal injection plant, BFs 4 & 6, Trinecke Zelezarny, Czech Republic. 2. Bell Less Top®, US Steel Lake Erie, Canada. 3. INBA® slag granulation plant, BF3, Hyundai Steel, South Korea. 4. Dome replacement of hot blast stove No. 43, BF4, China Steel, Taiwan.

As a consequence, the entire iron and steelmaking process chain, from the ore to the finished end product, can be serviced within the SMS group, of which Paul Wurth has been a member since December 2012.

4 Values of Paul Wurth

The Paul Wurth Group's cohesion and performance are anchored in a set of shared core values and principles. Among the most important cornerstones of Paul Wurth's corporate culture are the health of its employees and contractors, safety at work and a zero accident policy. As well as the quality and reliability of our products, so, too, are sustainability and energy efficiency an integral part of our innovative projects and our development of environmentally-friendly technologies. But the success of the Paul Wurth Group depends above all on its employees and their innovation skills. Nurturing our talents is crucial to our corporate culture. These commitments, shared by all our employees, are the best means of ensuring the Group's international competitiveness, long-term growth and continuing success.

Figure 2: Blast furnaces No. 1, 2 and 3 at Hyundai Steel, South Korea.

5 Health and safety at work

Because we are a global company specialising in the construction of plants and machines, our site personnel works in a hazardous industrial environment, often in difficult conditions. Our prime objective is therefore to minimise possible risks for all those involved in our projects. In addition to providing regular, preventive safety training for our own employees and systematically applying safety standards in our products and services, we also regard it as our duty to support our customers' site safety efforts. Joint training sessions on site safety issues for the customer's site personnel and operators as well as detailed root cause analyses in the event of accidents or incidents are part of the mandatory safety plans.

Paul Wurth considers its employees to be the company‘s most important resource, which is why it places such importance on promoting health in the workplace. It is only by protecting and promoting the health of our employees that they can give us their best possible performance.

6 Innovation

In industry and technology businesses, R&D and innovation constitute key factors for identifying and developing new competitive advantages, condition precedent for any leadership position in international markets. Dedicating significant resources to R&D has thus always been and still continues to be of strategic importance for Paul Wurth. Investigating and developing technologies which improve the environmental footprint of steel production has been a constant pillar of Paul Wurth's R&D efforts.

Figure 3: 1. Industrial pilot plant for dry granulation of blast furnace slag. 2. Hot commissioning of dry slag granulation pilot plant.

7 International presence

As an international engineering company Paul Wurth has a presence in all the major iron and steelmaking markets of the world through its global network. We have always striven to adapt our operational entities, branches, representation offices and joint ventures to the market situation in order to be able to respond quickly, flexibly and in a targeted fashion to our customers' needs.

8 Employees

Our employees are crucial to the success of the Paul Wurth Group, as are their dedication and their pioneering innovation skills, which is why we continuously intensify our staff-development efforts.

We continued to expand our continuous training programme focusing on technology, languages and management and adapted it even better to meet our needs. For our future leaders, we provided targeted staff development, with particular emphasis on developing and testing a company-specific leadership-skills model which makes executives more aware of their key role in relation to employees, customers, internal processes and company growth and to this end we developed a leadership programme specially tailored to our needs.

Close contacts with numerous higher education institutions and student organisations is also in our focus. The overarching aim of the continuous cooperation between Paul Wurth and higher education and other training institutions is to have an input into shaping practical technical training that meets the needs of our industry.

Figure 4: Coal grinding, drying and pulverised coal injection plant, BFs 5 & 6, JSC Evraz Nizhniy Tagil, Russia.

Influence of the Second Cold Rolling and Slow Laboratory Heating to the 620 ℃ during High Temperature Annealing on precipitation in GOES

Anastasia Volodarskaja[1], Vlastimil Vodárek[1], Šárka Miklušová[2]
[1]VŠB – Technical University of Ostrava, [2]ArcelorMittal Frýdek-Místek a.s

1 Introduction

Magnetic properties (easy magnetization, low hysteresis loss and low eddy current losses) of grain oriented electrical steels (GOES) depend heavily on the sharpness of the Goss texture ({110}<001>). The perfection of the Goss texture in final GOES sheets is closely affected by the structure evolution during the manufacturing process. The high induction or permeability level is related to the fact that the easy magnetization direction <001> is parallel to the rolling direction of sheets [1]. Understanding of the texture selection mechanism in the abnormal grain growth is important for the quality of final GOES sheets. Factors which are considered to be important for the formation of the{110}<001> texture during the final high temperature annealing (HTA) include the initial Goss grains size, the misorientation of these grains in relation to the neighboring grains or significant texture components and inhibition effects of minor phase particles [2]. The necessary conditions for abnormal Goss grain growth are controlled by microstructural parameters. The inhibitor phase particles (MnS or AlN, depending on the technology) restrict ferritic grain growth during uniform grain growth after the primary recrystallization. Coarsening and dissolution of these particles during the later stage of high temperature annealing create the presumptions for growth of Goss grains. The role of copper addition to GOES has not been fully understood yet. The following mechanisms have been proposed:

- stabilization of austenite during hot rolling in two phase $\alpha+\gamma$ region,
- precipitation of ϵ - Cu,
- dissolution and reprecipitation of Cu_2S or complex (Mn, Cu)S,
- segregation of copper at grain boundaries,
- support of deformation by twinning and shear.

The AlN + Cu technology comprises following production steps: slab reheating, hot rolling and coiling, cold rolling and decarburization annealing (DCA), second cold rolling, HTA, thermal flattening.

This paper deals with minor phase evaluation in GOES after the following manufacturing steps: first cold rolling and DCA, second cold rolling and a slow heating to the temperature of primary recrystallization (620°C).

2 Experimental materials and procedures

Chemical compositions of three samples, manufactured by different steelmakers, are shown in the Table 1. All strips correspond to an AlN + Cu production technology.

Table 1: Chemical compositions of the investigated steels (after hot rolling), wt.%

Supplier	C	Mn	Si	P	S	Cu	Altotal	N2	Ti+Nb+V
A	0.032	0.25	3.14	0.014	0.009	0.51	0.015	0.0131	-
B	0.031	0.27	3.09	0.009	0.004	0.50	0.015	0.0091	0.007
C	0.026	0.25	3.16	0.007	0.004	0.50	0.016	0.0088	0.009

Hot rolling was carried out at 1250°C to the thickness of 2.00 mm, After pickling, the first cold rolling to mid-thickness of 0.6 – 0.65 mm was applied and it was followed by DCA at the temperature of 820°C in the atmosphere containing N_2 + 20 $\%H_2$. Carbon content of the steel after DCA was reduced to 0.003 wt. %. After the second cold rolling to the final thickness of 0.28 mm, the laboratory simulation of slow heating to the temperature of primary recrystallization (620°C) was provided.

Precipitation processes were studied on carbon extraction replicas in a transmission electron microscope JEM 2100. EDX technique was applied for identification of minor phases. Microtexture analysis on samples after slow laboratory heating was carried out using Electron backscatter diffraction (EBSD) in a scanning electron microscope FEI QUANTA FEG 450. The software OIM (EDAX/TSL) was used for indexing of Kikuchi diffraction patterns and for evaluation of the orientation data.

3 Results

Precipitation processes in the GOES strips during the first stage of the AlN + Cu production technology were particularly described in [3]. In the hot rolled strip ferrite grain boundaries were decorated by cementite, which formed during coiling. Inside grains a very low number density of TiN and AlN particles was observed. Also hot rolling was accompanied by dissolution of copper-bearing sulphides, which are less stable than sulphides of manganese [3].

DCA after the first cold rolling resulted in re-precipitation of Cu_2S and complex sulphides of manganese and copper. The size of most copper rich sulphides was less than 50 nm, Figure 1.Grain boundaries were decorated by both Si_3N_4 and AlN particles. This metastable nitride should gradually transform to AlN phase [4]. AlN particles precipitating during the DCA can dissolve some oxygen, silicon and manganese. Intragranular precipitation of AlN was very intensive and heterogeneous [3]. TiN particles were not affected by DCA. No ϵ - Cu particles were detected. The typical size of nitrides reached several tens of nanometres.

The second cold rolling did not significantly affect precipitation of minor phases, Figure 2. However, a high density of defects after the second cold rolling accelerated additional precipitation, coarsening and dissolution of minor phase particles during the HTA. Similarly like in the case of the sheets after cold rolling and DCA the following phases were identified:

- AlN,
- Si^3N^4,
- Cu_2S, and complex (Mn, Cu)S,
- TiN.

The size and surface density of precipitates were comparable too.

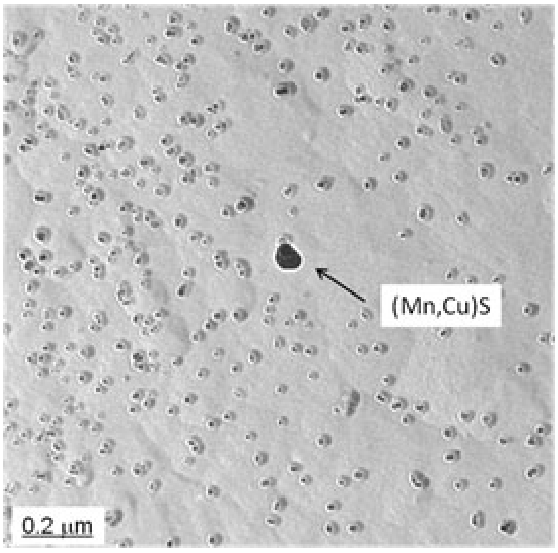

Figure 1: Precipitation of AlN in the sample after cold rolling and DCA, supplier B.

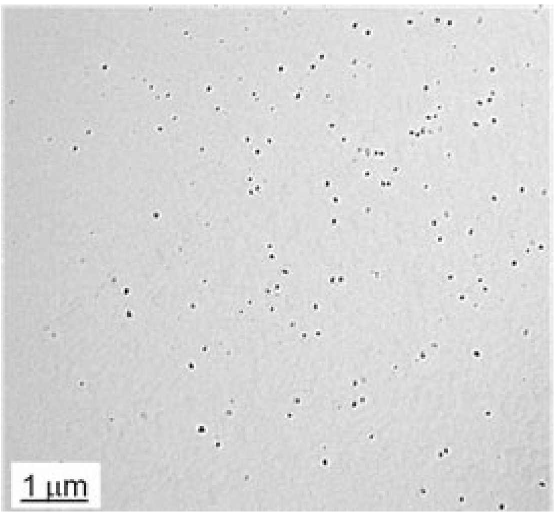

Figure 2: Precipitation of AlN in the sample after second cold rolling, supplier A.

After the second cold rolling laboratory simulation of a slow heating rate to the temperature of primary recrystallization (620°C) was provided. Heating rate in a protective nitrogen atmosphere was v = 25°C/h. The microstructure analysis after the heating was carried out using EBSD technique in the middle of the sheet thickness, Figure 3a. The microstructure consists of small equiaxed recrystallized grains and non-recrystallized grains (misorientation inside grains is greater than 2°). Figure 3b shows the grain orientation spread chart. The fraction of deformed structure in sheets from suppliers A, B and C was 11.45 %, 6.42 % and 8.73 %, respectively. It is obvious that the fraction of non-recrystallized structure in all sheets was approximately equivalent. It means that the temperature of the beginning of the primary recrystallization was approximately the same for all samples. Figure 3c shows that the number of grains with the orientation close to the Goss texture was low (≤15°). The rest of recrystallized grains have the deviation from the ideal Goss texture greater than 15°.

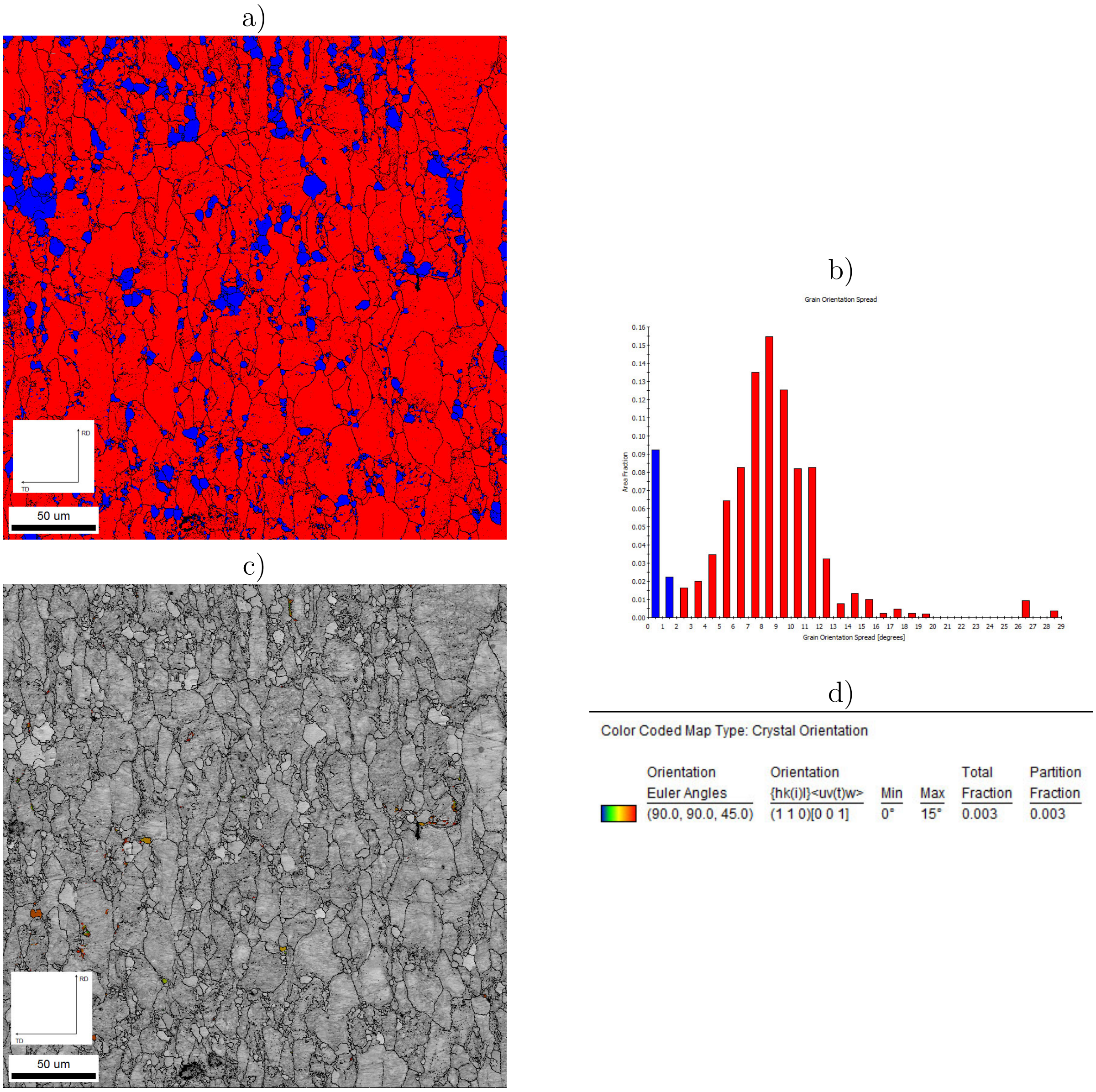

Color Coded Map Type: Crystal Orientation

	Orientation Euler Angles	Orientation {hk(i)l}<uv(t)w>	Min	Max	Total Fraction	Partition Fraction
▨	(90.0, 90.0, 45.0)	(1 1 0)[0 0 1]	0°	15°	0.003	0.003

Figure 3: Microstructure and microtexture of samples after the slow heating to the 620°C, supplier A: a) recrystallized (blue) and deformed (red) fractions of microstructure, b) grain orientation spread chart, c) grains close to the Goss orientation + high angle boundaries ($\theta > 15°$), d) the legend for Figure 3c.

In the sheets after the slow heating to the 620°C the surface density of precipitates was less than in the sheets after the second cold rolling, Figure 4. Using EDX technique the following phases were identified:

- AlN,

- Si_3N_4,
- TiN,
- Cu_2S, and complex (Mn, Cu)S.

Figure 5 shows the typical EDX spectrums for different types of precipitates which were identified. In case of Si_3N_4 phase it was determined that this type of minor phases dissolved some manganese ($Si : Mn = 5 : 1$). Particles with a low aluminium content and the atomic ratio $Si : Mn = 5 : 1$ could represent an initial stage of "in situ" transformation of Si_3N_4 to AlN. No ϵ - Cu particles were observed.

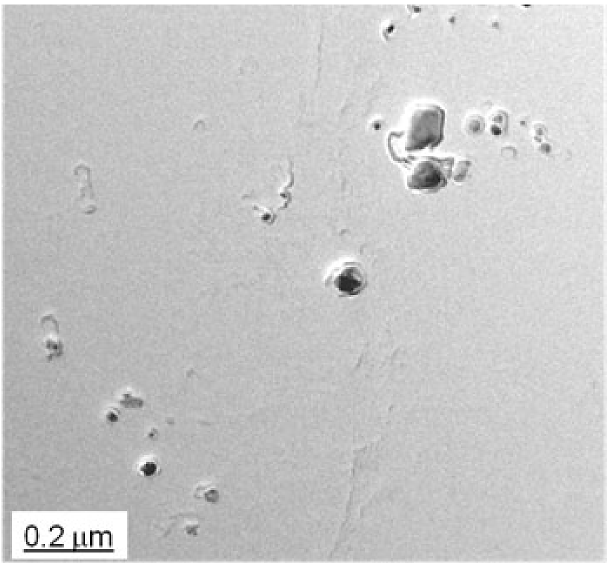

Figure 4: Coarsening of precipitates during the slow heating to the 620°C, supplier A.

4 Conclusions

The same types of precipitates were presented in samples after the first cold rolling and DCA, the second cold rolling and the slow heating to the 620°C.The following phases were identified Si_3N_4, AlN, TiX, Cu_2S and (Mn, Cu)S. It was expected because all those types of minor phases are stable in ferrite to the temperature 850°C. It was surprising that after the slow heating to the 620°C the surface density of precipitates was less than in the sheets after DCA. The possible reason of decreasing of the surface density of minor phases is coarsening of precipitates because all types of nitrides were stable during the slow heating to the temperature of the primary recrystallization. In this case the Gibbs free energy decreasing was connected to reduction of interface between precipitates and matrix. It means dissolving of small precipitates and coarsening of big ones.

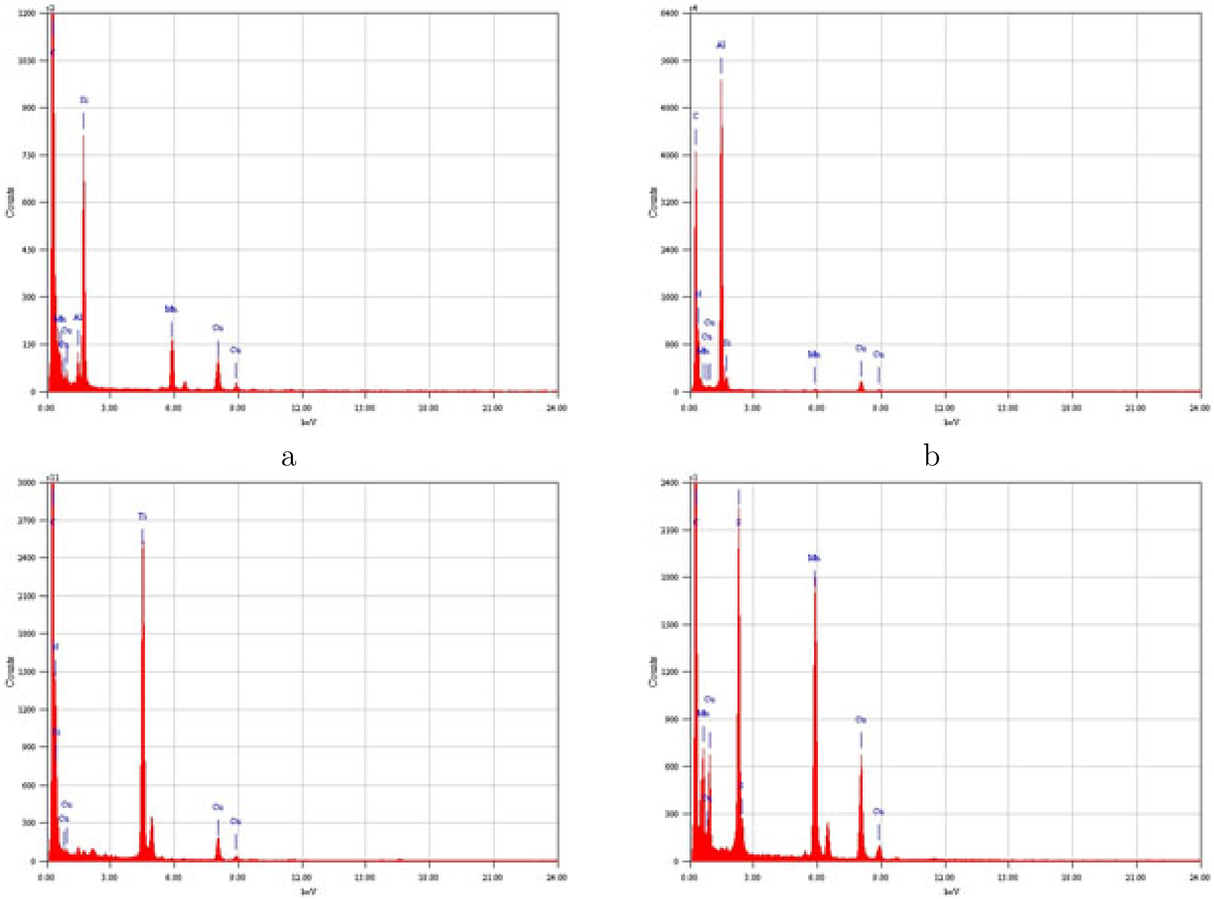

a b

c d

Figure 5: The typical EDX spectrums for precipitates observed in the samples after the slow heating to the 620°C: a) Si_3N_4, b) AlN, c) TiX, d) (Mn, Cu)S.

Acknowledgements

This paper was prepared with the financial support of the project No. CV6005531 “Support and development of international relationship and mutual foreign activities of students and staff on FMMI” and the project “SP 2015/70 Specific research in the metallurgical, materials and process engineering”, both funded by VŠB – Technical University of Ostrava, Czech Republic, FR-TI3-053 and the Project No. LO1203 "Regional Materials Science and Technology Centre - Feasibility Program" funded by Ministry of Education, Youth and Sports of the Czech Republic.

References

[1] Bernier, N. et al.: “EBSD study of angular deviations from the Goss component in grain-oriented electrical steels”. In: *Micron* 54 (2013), pages 43–51.

[2] Rollett, A. et al.: *Recrystallization and related annealing phenomena.* Elsevier, 2004.

[3] Vodárek, V. et al.: “Microstructure Characterization of GOES after Hot Rolling and Cold Rolling+ Decarburization Annealing”. In: *Proc. Metal* (2013).

[4] Stoyka, V, Kovac, F, and Sidor, Y: “Effect of second phase particles topology on the onset temperature of abnormal grain growth in Fe-3% Si steels”. In: *Metalurgija* 47.1 (2008), pages 37–41.

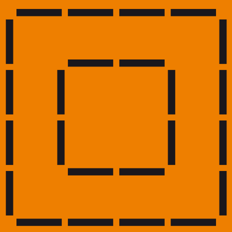

You know how to think precisely and how to get the best results.

How do you get two same-sized squares, containing all of the sticks, by moving only four of them?

DO YOU SOLVE COMPLEX SITUATIONS?

Developing steel means shaping the future

Would you like to design new steel tubes in order to improve the efficiency factor of power plants? Would you like to shape new steel car bodies to make them lighter and safer? Or are you keen on managing big blast furnaces or an impressive hot strip mill? Then we can offer you a perfect opportunity: join our research department or become a member of our production or sales team.

You will have

lots of benefits. Your start in our company will be accompanied by a development program which is especially tailored to your needs. Your job will offer you a wide range of responsibility and space to realize your own ideas. Our salary and pension schemes are above-average.

We expect

communicative people, who enjoy working in teams. And we need your curiosity and creativity to remain on the top as a steel and technology group. So if you think that this fits to your future plans, have a look at our website to learn more about Salzgitter as employer of choice.

www.salzgitter-ag.com

We want to reach the best results – with you!

Salzgitter AG is one of the leading steel and technology companies in Europe with a business volume of 9 billion euro and a worldwide workforce of around 25,000 employees.

The product portfolio includes a wide variety of strip steel products. Furthermore, Salzgitter AG manufactures filling and packaging plants for the beverages, food and non-food industry.

Deutschlands
beliebteste Arbeitgeber
TOP100
universum
Studierende 2014

Salzgitter AG
Abteilung Führungskräfte
Markus Rottwinkel
Eisenhüttenstraße 99
38239 Salzgitter
karriere@salzgitter-ag.de

SALZGITTER**AG**
Stahl und Technologie

Fabrication of homogenous YBCO + Cu powders composite

Marcin Godzierz
Silesian University of Technology
ul. Krasińskiego 8, 40-019 Katowice, Poland
godzierz@gmail.com

Abstract

This publication describes two different methods for the preparation of a composite green body of superconducting YBCO (yttrium-bar-copper-oxygen) powders, mixed with the surface-oxidized copper powder. The Meissner effect behavior, better known as a magnetic levitation has been selected as a test of successful sample preparation.

This phenomenon was not observed in compressed pellets that suggests necessity of subsequent heat treatment (sintering) for this type of superconducting composites.

1 Introduction

Superconductors are now practically used in several devices, including applications in medicine (magnetic resonance imaging), superconducting energy bins and mostly in science and engineering. The usage of superconductors in construction of magnetic train led to a new standard and extremely fast journeys. These materials are promising because of generating extremely strong magnetic field with low power consumption. However, their production is relatively expensive.[1]

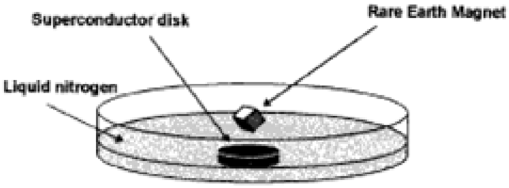

Figure 1: The Meissner Effect[2].

Not only the zero resistance is a factor of the classification as a superconducting material. In superconductors, there is also the phenomenon of magnetic field lines rejection from a perfect diamagnetics known as the Meissner effect in superconductors (Figure 1). This phenomenon can be controlled also by the shape of the element, due to the fact that most of the high-temperature superconductive materials are ceramics, could be the reason of some (technological) problems.[3]

Problems in fabrication of ceramic materials are strongly related to the shape of the final product and cause difficulties in production of superconducting wires and tapes. Therefore, the emphasis is placed on the wires and tapes produced by PIT (powder in tube) method and as metal matrix composites, allowing the possibility of plastic reprocessing of the materials. One of the mentioned methods is pressing and sintering of ceramic-metal homogenous powders.[4]

2 Material and experimental methods

2.1 Material

The used material was a fragmented powder of $\mathrm{YB_2C_3O_y}$ with the grain size between 0.1 mm and 0.045 mm and grain size under 0.045 mm. The transition temperature of the ceramics in the superconducting state ($\mathrm{T_K}$) is about 90 K. The second component of a composite was surface-oxidized copper powder which volume content is equal to 15%.

2.2 Powder's preliminary research

X-ray diffraction analysis (XRD) of a solid sample of YBCO was executed in order to verify the purity of the powder. The study was performed using the Philips X'Pert3 diffractometer, equipped with a strip detector PIXcel, monochromator, Soller slits 0.04° and a lamp with a copper anode ($\lambda_{\mathrm{CuK}\alpha} = 1.541\,78$ Å) fed a current of 30 mA at a voltage of 40 kV. Registration was performed by continuous increments of 0.026° in the range of 10 to 95° 2θ. Phases were identified using ICDD PDF-4+ database.

XRD patterns shown the following phases (Figure 2):

1. CuO – monoclinic,
2. $\mathrm{Ba_2Cu_3O_{6.74}Y}$ – orthorhombic,
3. $\mathrm{BaCuO_2}$ – cubic,
4. $\mathrm{Ba_2Cu_3O_7Y}$ – orthorhombic lattice (ambiguous identification).

X-ray diffraction patterns confirm that the solid sample composition corresponds to the typical superconducting material composition YBCO 123.

3 Results

3.1 Preparation of the sample

Solid YBCO sample was crushed in a hydraulic press, and subsequently manually grounded in a porcelain mortar. Sieve analysis was performed to determine the average grain size by means of a sieve mesh size equal to 0.1 mm and 0.045 mm. Superconducting powders with grain size of 0,1÷0,045 with volume fraction of approx. 70% and grains finer than 0.045 mm (about 15 volume percent). The mixture was homogenized manually with

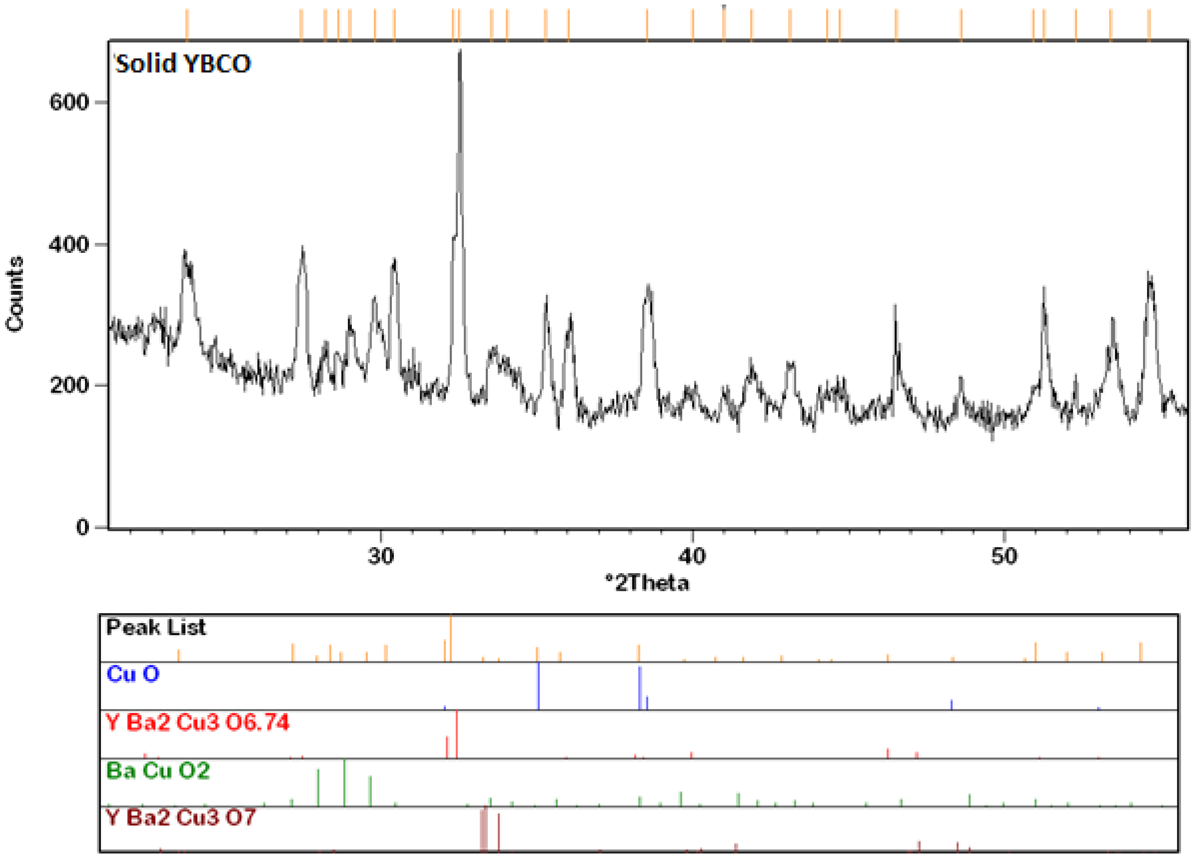

Figure 2: X-ray diffraction pattern of solid samples of YBCO.

the surface-oxidized copper powder and separated into two samples. The samples were pressed under various conditions. Compression parameters are presented in Table 1.

Table 1: Parameters of pressing YBCO + Cu composite.

	Sample 1	Sample 2
Sample weight [g]	3	13
Sample diameter [mm]	12,5	30
Pressure [MPa]	480	354
Binder	-	ethanol

3.2 Meissner effect

The presence of the Meissner effect was tested by immersing the sample in liquid nitrogen (77K), and holding it there for a period of 2 minutes. Neodymium magnets are then placed over the sample and there was no reaction near the cooled composite.

4 Conclusions

1. The addition of about 15% by volume of oxidized copper surface eliminates or reduces the properties of superconducting YBCO ceramic, which is not a good

thing.

2. Second theory is associated with fact that these samples were only pressed, so the Meissner effect could occur in each grain separately, limited to local behavior. This is bound up with fact that in the pressed ceramics, grains are not bonded together, and have no electrical contact between them.

It should be noted that both of the following conclusions are equally probable, and one of them could be excluded after sintering green body.

Acknowledgment

The author would like to thank Professor Michał Żelechower for discussion and advice; Dr. Tomasz Pawlik for providing laboratory and support; Dr. Julian Plewa for samples.

References

[1] Wong, K. W. et al.: “Superconductors having continuous ceramic and elemental metal matrices”. In: *International application published under the Patent Cooperation Treaty* (1993).

[2] *http://neon.mems.cmu.edu/cramb/27-100/lab/S00_lab3/lab3.html.* 2015.

[3] Plecháček, V. et al.: “Batch production of YBCO disks for levitation applications”. In: *Elsevier* (2012).

[4] Matsunami, T. et al.: “Variation of applied field angular dependence of critical current density in YBCO thin films deposition against temperature and composition”. In: *Elsevier* (2012).

Optimization of manufacturing technology of cast metal foams with stochastic system of inner cells

Ivana Kroupová
VŠB-Technical University of Ostrava
Department of Metallurgy and Foundry Engineering, FMME

Abstract

Since the discovery of porous metallic materials numerous methods of production have been developed. Porous metallic materials can be made from liquid metal, from powdered metal, metal vapours, or from metal ions. The aim of the paper is to introduce casting methods of manufacturing of metallic foams from aluminum alloys. The works deals with an optimization of procedure for production of cast metallic foams with use of disposable evaporate pattern for investment casting. The experimental part stresses the solution of metal fluidity into complicated cavity of the pattern, which is an exact negative of the initial model of polymeric foam. Attention in the experimental part is also devoted to the chosen moulding material – plaster. Suitably proposed procedure of manufacturing of plaster mould, drying process and subsequent annealing have principal influence on the final properties of the mould and therefore on the quality of the resulting casting of the metallic foam.

Keywords: Metal foam, aluminum foam, manufacturing of metal foam, polymer foam, plaster mould.

1 Introduction

Metallic foams and porous metals are materials which contains in their structure artificially created pores. These pores give them specific properties such as: large rigidity maintaining low density, high temperature conductivity, capability to absorb energy etc.

The first mention of metal foams come already from the beginning of the 20th century when these porous metal materials started to be used for engineering purposes. In the twenties of the last century there began to be produced and commercially used the foams produced by sintering of metal powders that were used for manufacture of filters, batteries and self-lubricating bearings. In the French patent from the year 1925 we can find the mention of metal foams made by material foaming, thirty years later in the United States their commercial use begun. But the extensive research and development activities started in the nineties and it continues up to now [1].

At VŠB – Technical University of Ostrava (Department of Metallurgy and Foundry Engineering) the research dealing with optimization of manufacture of this unique material by a foundry way is currently underway.

1.1 Metallic foam manufacture

Since the discovery of porous metallic materials numerous methods of production have been developed. Some technologies are similar to those for polymer foaming, others are developed with regard to the characteristic properties of metallic materials, such as their ability to sintering or the fact that they can be deposited electrolytically [2].

According to the state, in which the metal is processed, the manufacturing processes can be divided into four groups. Porous metallic materials can be made from [3, 4]:

- liquid metal (e.g. direct foaming with gas, blowing agents, powder compact melting, casting, spray forming)
- powdered metal (e.g. sintering of powders, fibres or hollow spheres, extrusion of polymer/metal mixtures, reaction sintering)
- metal vapours (vapour deposition)
- metal ions (electrochemical deposition)

1.2 Properties and utilization of metal foams

Foams and other highly porous materials with cell structure are known for a combination of many interesting physical and mechanical properties, such as e.g. high stiffness at low density, high thermal conductivity, the ability of energy absorption etc. (Figure 1).

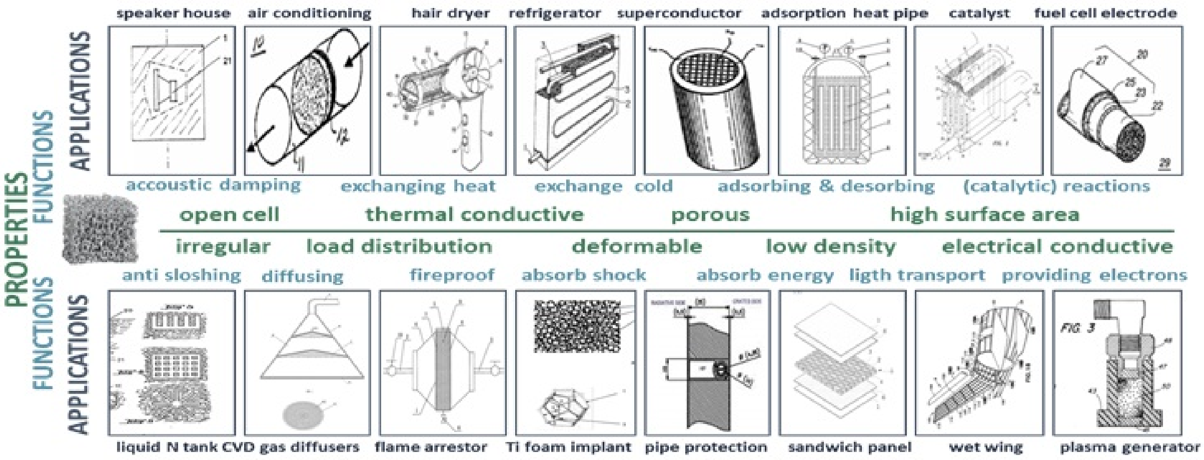

Figure 1: Applications of cellular metals [5].

2 Casting methods of production of metal foams with stochastic system of inner cells

The most common foundry method of manufacture the metal foams with open pores is a method with the use of a disposable evaporable polymeric pattern – polymeric foams (most commonly polyurethane foam – PU foam).

The principle consists in casting the polymeric foam with the refractory material, followed by drying and annealing of the mould when the foam pattern is evaporated. Molten metal is then poured in the resulting cavity. After removing the heat-resistant material the cast metal foam with open pores is obtained which is an exact copy of the foam pattern (Figure 2) [6].

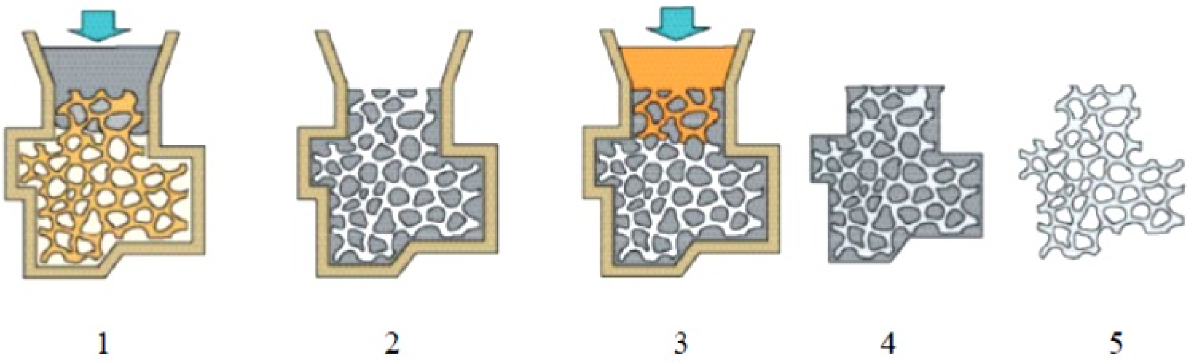

Figure 2: 1 – polymer foam infiltrate with plaster, 2 – remove polymer, 3 – infiltrate with metal, 4 – metal foam in mould, 5 – remove mould, final metal foam.

3 Polymer foam

Polymeric foams are used in numerous application areas. They are used as filters, isolators or noise suppressors. They may contain two dominant forms of pores, namely open or closed pores.

Particularly the choice of suitable foam has a cardinal influence on the final shape and properties of metallic foam. It depends both on the actual material, from which the foam is made, and on its porosity or on thickness of the fibres.

For manufacture of patterns for investment casting, which are then used to create the metallic foam, polymeric foams are used with a fully open structure, i.e. that they do not contain any closed cells. Such types of foams are produced by thermal reticulation process, in which all of the cell membranes, which remained after the foaming, are broken and they coalesce with cell ribs (see Figure 3). The actual ratio of foam ribs makes only 3 – 5 % of the volume of foam, depending on the type of foam.

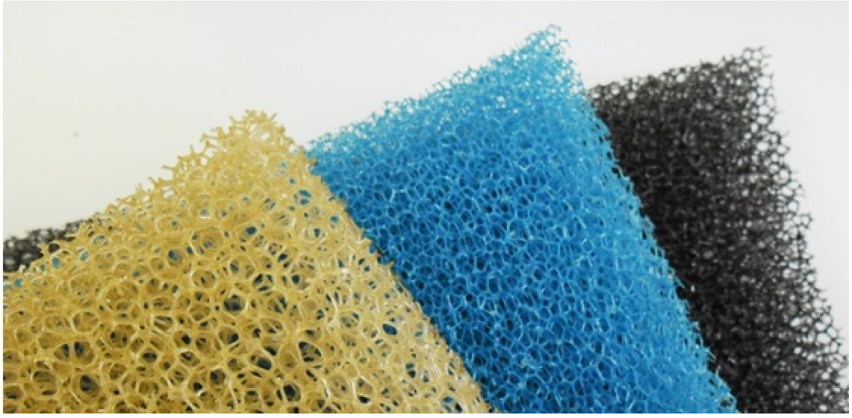

Figure 3: Examples of various types of used polymeric foams.

3.1 Surface treatment of polymeric foam

Particularly the issue of penetration of metal into the pattern cavities is crucial in the technology using the polymeric pattern. Several possibilities exist for increasing the penetration of metal, e.g. heating of the pattern to a higher temperature (800 °C), modification of the gating system, die casting. If these methods fail, it is then necessary to influence the penetration by modifying the pattern as such – by changing the thickness of the polymeric foam fibres.

Two procedures for increasing the thickness of the foam pattern fibres were verified – soaking of the pattern into wax and spraying the pattern with one or two layers of acrylic paint.

Spraying with one layer of paint appeared to be the most effective procedure. The series of thus manufactured of castings manifested a minimum scrap factor, good penetration in castings. The amount of sprayed coating was determined by weighing the sample before and after application of the paint (see Table 1). The average weight of the sprayed coating was 0.65 g.

Table 1: Evaluation of the mass of the sprayed coating.

coating	sample 1 [g]	sample 2 [g]	sample 3 [g]	sample 4 [g]	sample 5 [g]
before ap.	1.9859	1.9862	1.9539	1.9913	2.0173
after ap.	2.6007	2.6104	2.5844	2.6145	2.7799
mass	0.6148	0.6242	0.6305	0.6232	0.7626
Ø			0.65106		

4 Plaster mould manufacture

The plaster which serves as a filling material needs to be mixed in an exact proportion of water – plaster. On one part of water two and a half parts of plaster are used. It is appropriate to mix the plaster under reduced pressure to avoid the formation of air bubbles which could negatively affect the plaster mould. Such a mould, after thermal treatment, could crack or collapse under the influence of expansion of the closed air.

Making of a mould then consists in casting the pattern with the plaster and at the same time the plaster must fill all the pattern cavities. The pattern is stuck on an accessory silicone hat that serves for creating the gate. A metal cover (cuvette) is put on the hat and the plaster is cast into the system prepared in such a way. The made up moulds are left for two hours on the air and then they are dried at temperature 40 °C for 2 h.

After drying of moulds a next step follows – their annealing. During annealing the free water and the chemically bound water are removed and the PU foam is evaporated.

For casting of various alloys (Cu alloys, Al alloys) it is necessary to define different annealing cycles. For casting the Cu alloys with higher melting temperature (higher casting temperature) it is necessary to anneal the plaster moulds to higher temperatures – to eliminate the thermal shock during casting, and to increase the melt fluidity into the complex mould cavity. Annealing cycles can be seen in Table 2.

Table 2: Annealing cycles of plaster moulds.

	temperature, increase, soak at temperature	temperature, increase, soak at temperature	temperature, increase, soak at temperature
cycle 1	120 °C; 8 °C/min; 8 h	320 °C; 10 °C/min; 8 h	800 °C; 20 °C/min; 10 h
cycle 2	120 °C; 8 °C/min; 8 h	550 °C; 10 °C/min; 8 h	1100 °C; 20 °C/min; 10 h
cycle 3	120 °C; 8 °C/min; 8 h	550 °C; 10 °C/min; 8 h	1000 °C; 20 °C/min; 10 h

The most commonly used is the annealing cycle No 1 which is suitable for the subsequent casting of Al alloys (low melting temperature or low casting temperature).

But for casting of Cu and Fe alloys it is necessary to increase the annealing temperature, i.e. to heat the moulds to higher temperatures. Therefore the annealing cycle No 2 was recommended. This annealing cycle proved to be unsuitable – the moulds annealed to such high temperatures show impaired collapsibility after metal casting.

A plaster sample has been subjected to differential thermal analysis (DTA) in which it was found that at temperatures of 1100 °C the CaSO4 is disintegrated to CaO and SO3 (degradation of the mould).

After the evaluation of the plaster DTA the annealing cycle No 3 was designed. The moulds annealed in such a way have good collapsibility after casting but for casting the Cu and Fe alloys the mould temperature is too low. When casting these alloys the metal misruns into the mould cavity due to high temperature jump. On the contrary for casting the Al alloys the mould prepared in such a way is “overheated“.

5 Conclusion

At application of the technology using polymeric foam as a disposable evaporate pattern the molten metal is poured into the cavity of the plaster pattern. This cavity is very complicated. We therefore encounter a non-penetration of metal into the entire cavity of the pattern. Several possibilities for increasing metal penetration were verified (heating of the pattern to a higher temperature (800 °C), modification of the gating system, die casting). Another option for influencing the metal penetration consists in modification of the foam pattern as such – by changing the thickness of the polymeric foam fibres. Spraying with one layer of paint appeared to be the most effective procedure. The series of thus manufactured of castings manifested a minimum scrap factor and good penetration in castings.

The proper choice and processing of a material suitable for manufacture of the mould are then essential for this production process. The plaster (Satin Cast 20) is an ideal solution – it can faithfully copy the complex shape of the foam pattern and at the same time to resist high temperatures. The key step to making the resulting plaster mould is then especially the annealing cycle. The annealing cycle must ensure the annealing of moulds to sufficiently high temperature to avoid heat shock or the metal misrun into the all mould cavity. At the same time, however, the annealing cycle shall not exceed the temperature at which the degradation of the plaster mould occurs – in the case of the Satin Cast 20 plaster it is 1100 °C.

Acknowledgement

This work was elaborated within the research project TA02011333 supported by the Technology Agency of the Czech Republic, project No. CV6005531 „Support and development of international relationship and mutual foreign activities of students and staff on FMMI“, funded by VŠB – Technical University of Ostrava, Czech Republic and project of specific research VŠB - Technical University of Ostrava – SP2015/78 and SP2015/70.

References

[1] Lefebvre, L.-P., Banhart, J., and Dunand, D.: “Porous metals and metallic foams: current status and recent developments”. In: *Advanced Engineering Materials* 10.9 (2008), pages 775–787.

[2] Lichy, P., Bednarova, V., and Elbel, T.: “Casting routes for porous metals production”. In: *Archives of foundry engineering* 12.1 (2012), pages 71–74.

[3] Banhart, J.: “Manufacturing routes for metallic foams”. In: *Jom* 52.12 (2000), pages 22–27.

[4] Bednářová, V., Lichý, P., and Tomá-Elbel, A.-H.: “Cast cellular metals with regular and irregular structures”. In: *Materiali in tehnologije* 48.2 (2014), pages 175–179.

[5] http://www.aulive.com/blog/2014/03/26/3-ways-how-patents-can-help-to-find-new-clients-markets-and-applications/.

[6] Banhart, J.: “Manufacture, characterisation and application of cellular metals and metal foams”. In: *Progress in materials science* 46.6 (2001), pages 559–632.

Ingenieurbeschäftigung und -bedarf im Maschinen und Anlagenbau

Dr. Franz Beneke
VDMA
FV Hütten- und Walzwerkeinrichtungen, Gießereimaschinen und Thermoprozesstechnik

Der VDMA

VDMA

Führender Wirtschaftsverband Europas im Maschinen- und Anlagenbau

- Mehr als 3.100 Mitgliedsunternehmen
- über 1 Million Beschäftigte (2014)
- 219 Mrd. € Umsatz (2014)
- Exportanteil rund 75%
- rund 16% aller Maschinenexporte weltweit
- mittelständisch geprägt

VDMA | FV Hütten- und Walzwerkeinrichtungen, Gießereimaschinen und Thermoprozesstechnik Dr. Franz Beneke

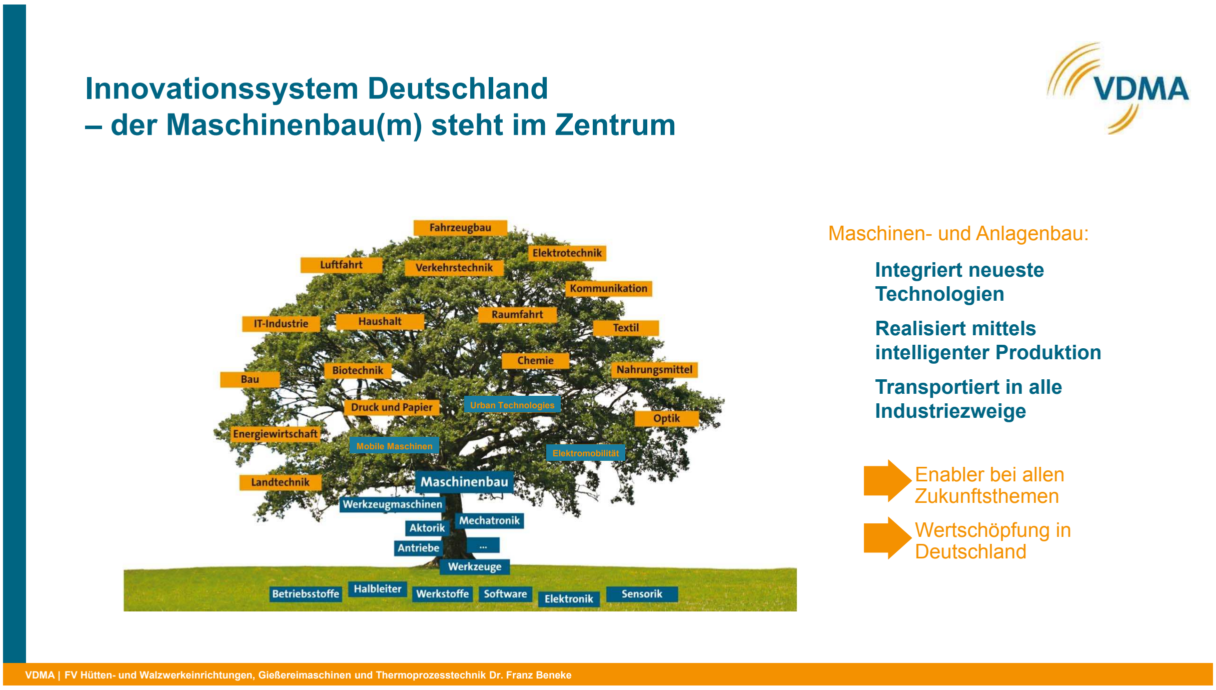

Innovationssystem Deutschland – der Maschinenbau(m) steht im Zentrum

Maschinen- und Anlagenbau:

Integriert neueste Technologien

Realisiert mittels intelligenter Produktion

Transportiert in alle Industriezweige

Enabler bei allen Zukunftsthemen

Wertschöpfung in Deutschland

VDMA | FV Hütten- und Walzwerkeinrichtungen, Gießereimaschinen und Thermoprozesstechnik Dr. Franz Beneke

Der VDMA und die Wissenschaft

Forschungsstark und Bedarf nach hochqualifizierten Fachkräften

- ca. 5 Mrd. Euro F&E-Ausgaben - 11% der F&E-Ausgaben im verarbeitenden Gewerbe
- 183.000 Ingenieure in den VDMA-Mitgliedsunternehmen
- 14.000 Doktor-Ingenieure - ca. 7,7% aller beschäftigten Ingenieure in der MB-Industrie
- 23% aller Unternehmen halten exklusive Doktor-Ingenieur-Stellen vor

VDMA | FV Hütten- und Walzwerkeinrichtungen, Gießereimaschinen und Thermoprozesstechnik Dr. Franz Beneke

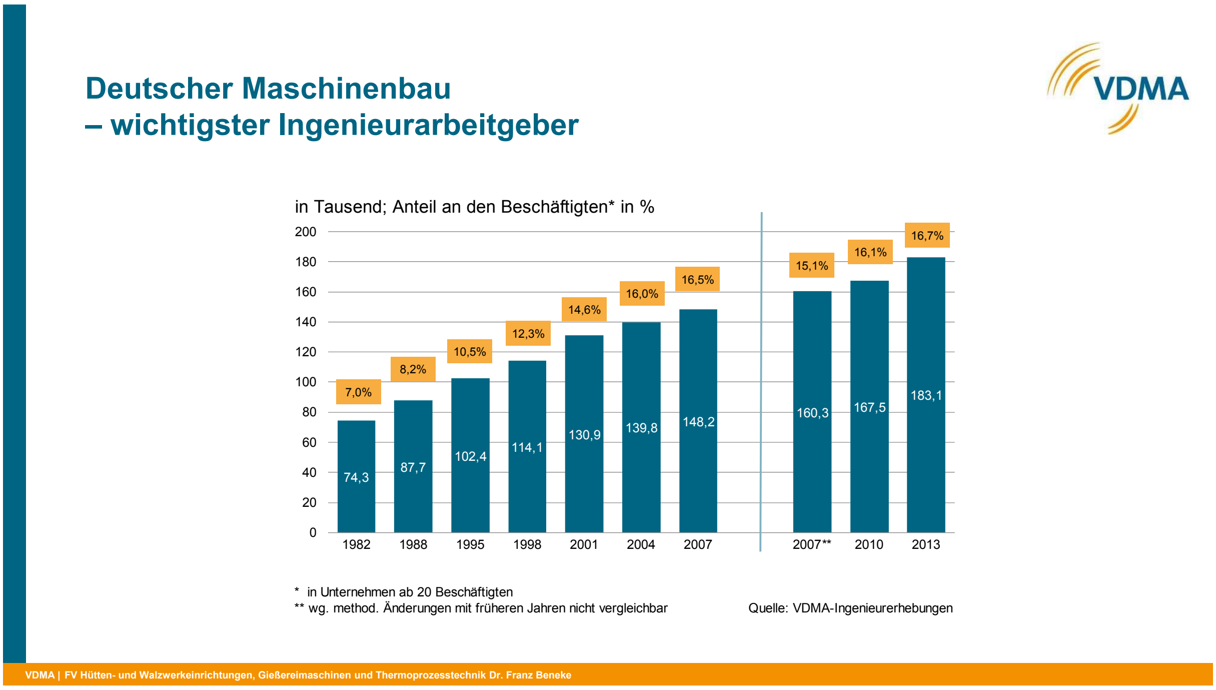

Deutscher Maschinenbau
– wichtigster Ingenieurarbeitgeber

* in Unternehmen ab 20 Beschäftigten
** wg. method. Änderungen mit früheren Jahren nicht vergleichbar

Quelle: VDMA-Ingenieurerhebungen

VDMA | FV Hütten- und Walzwerkeinrichtungen, Gießereimaschinen und Thermoprozesstechnik Dr. Franz Beneke

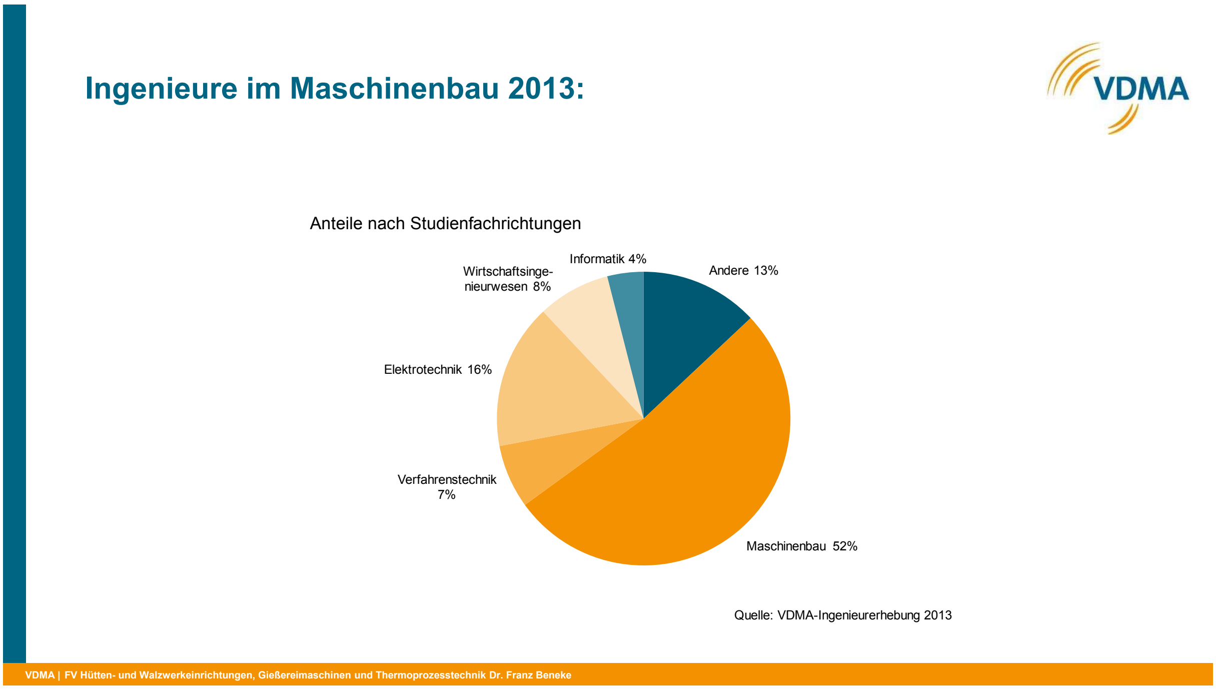

Ingenieure im Maschinenbau 2013:

Quelle: VDMA-Ingenieurerhebung 2013

VDMA | FV Hütten- und Walzwerkeinrichtungen, Gießereimaschinen und Thermoprozesstechnik Dr. Franz Beneke

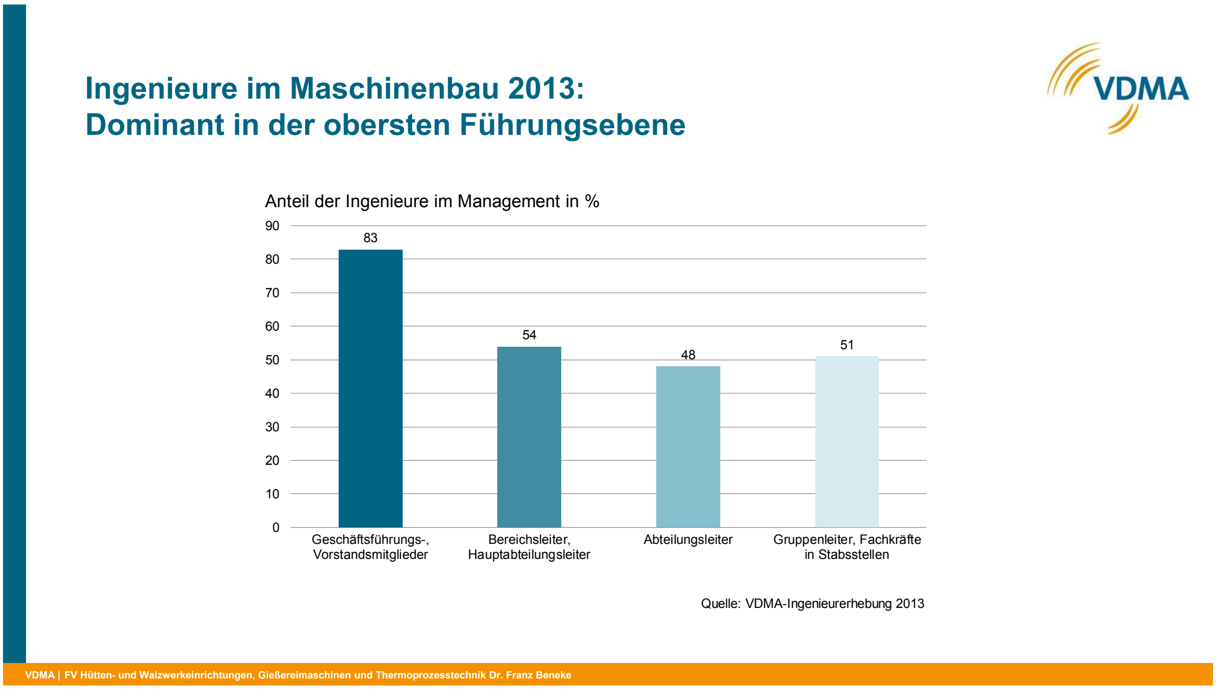

Ingenieure im Maschinenbau 2013: Dominant in der obersten Führungsebene

Quelle: VDMA-Ingenieurerhebung 2013

VDMA | FV Hütten- und Walzwerkeinrichtungen, Gießereimaschinen und Thermoprozesstechnik Dr. Franz Beneke

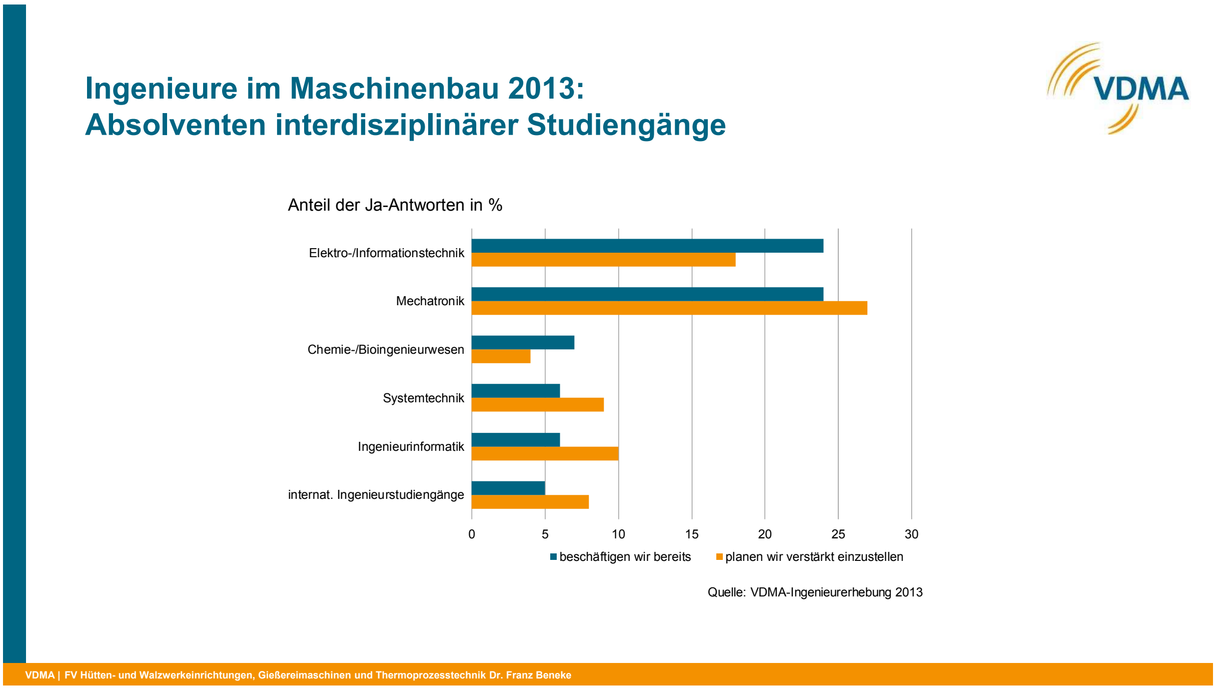

Ingenieure im Maschinenbau 2013: Absolventen interdisziplinärer Studiengänge

Quelle: VDMA-Ingenieurerhebung 2013

VDMA | FV Hütten- und Walzwerkeinrichtungen, Gießereimaschinen und Thermoprozesstechnik Dr. Franz Beneke

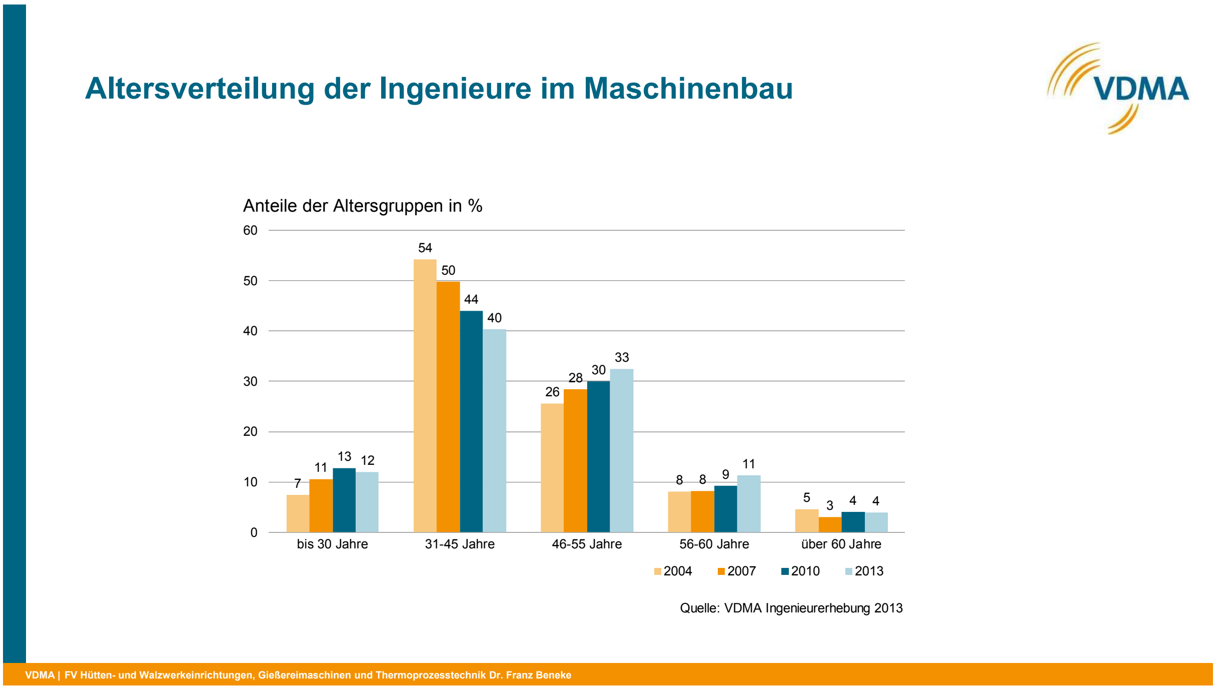

Altersverteilung der Ingenieure im Maschinenbau

Quelle: VDMA Ingenieurerhebung 2013

VDMA | FV Hütten- und Walzwerkeinrichtungen, Gießereimaschinen und Thermoprozesstechnik Dr. Franz Beneke

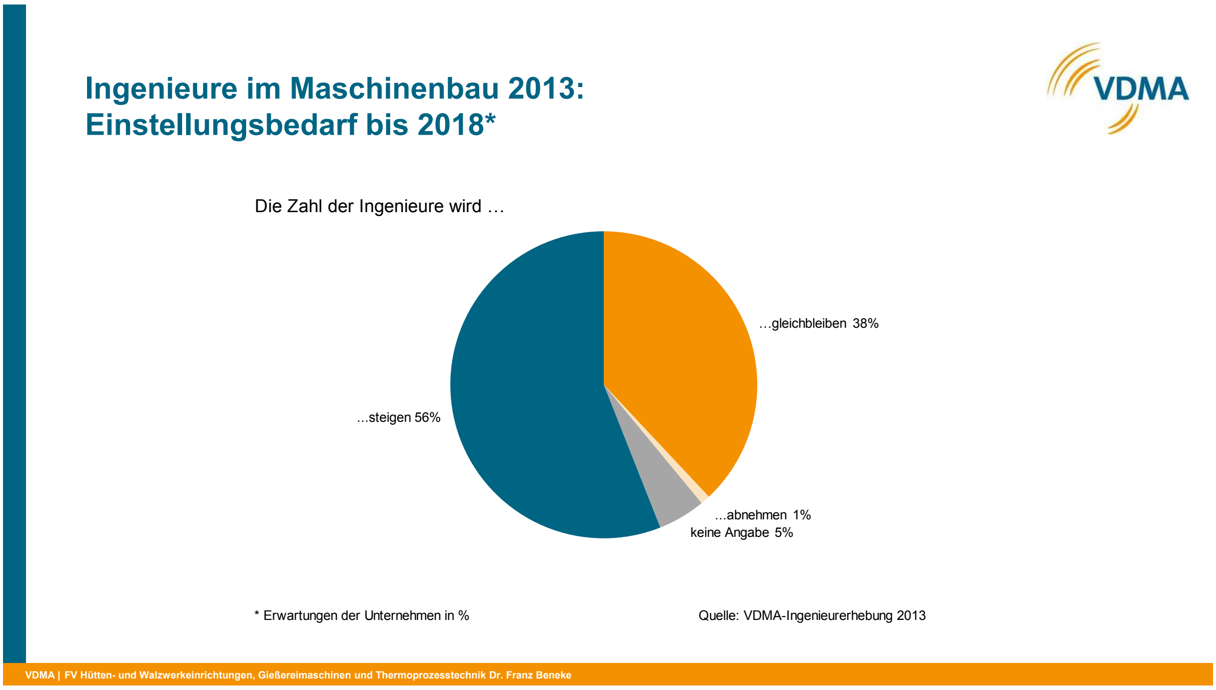

Ingenieure im Maschinenbau 2013: Einstellungsbedarf bis 2018*

* Erwartungen der Unternehmen in %

Quelle: VDMA-Ingenieurerhebung 2013

VDMA | FV Hütten- und Walzwerkeinrichtungen, Gießereimaschinen und Thermoprozesstechnik Dr. Franz Beneke

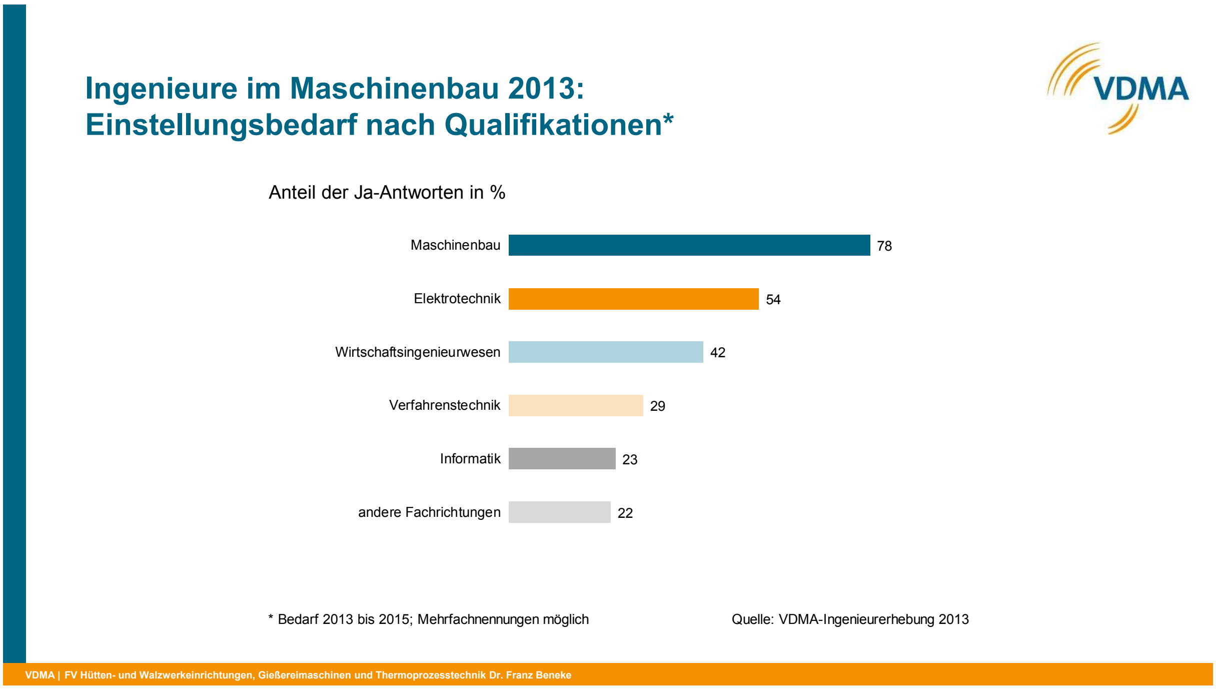

Ingenieure im Maschinenbau 2013: Einstellungsbedarf nach Qualifikationen*

Anteil der Ja-Antworten in %

* Bedarf 2013 bis 2015; Mehrfachnennungen möglich

Quelle: VDMA-Ingenieurerhebung 2013

VDMA | FV Hütten- und Walzwerkeinrichtungen, Gießereimaschinen und Thermoprozesstechnik Dr. Franz Beneke

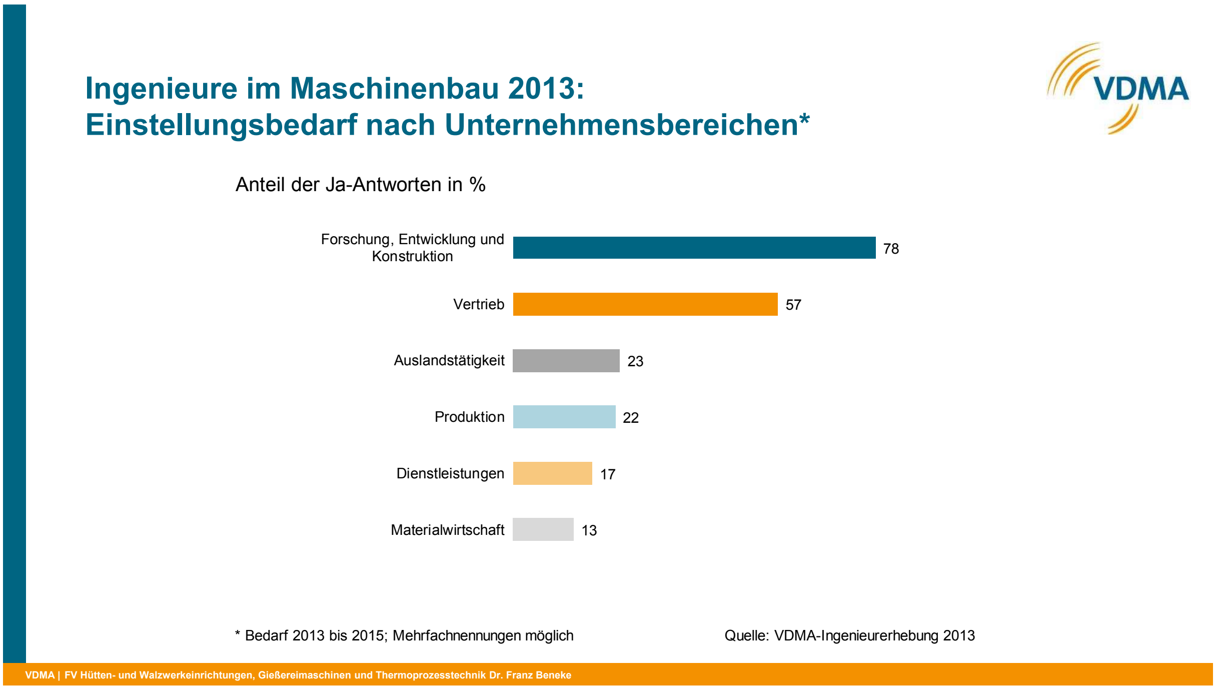

Ingenieure im Maschinenbau 2013: Einstellungsbedarf nach Unternehmensbereichen*

Anteil der Ja-Antworten in %

* Bedarf 2013 bis 2015; Mehrfachnennungen möglich

Quelle: VDMA-Ingenieurerhebung 2013

VDMA | FV Hütten- und Walzwerkeinrichtungen, Gießereimaschinen und Thermoprozesstechnik Dr. Franz Beneke

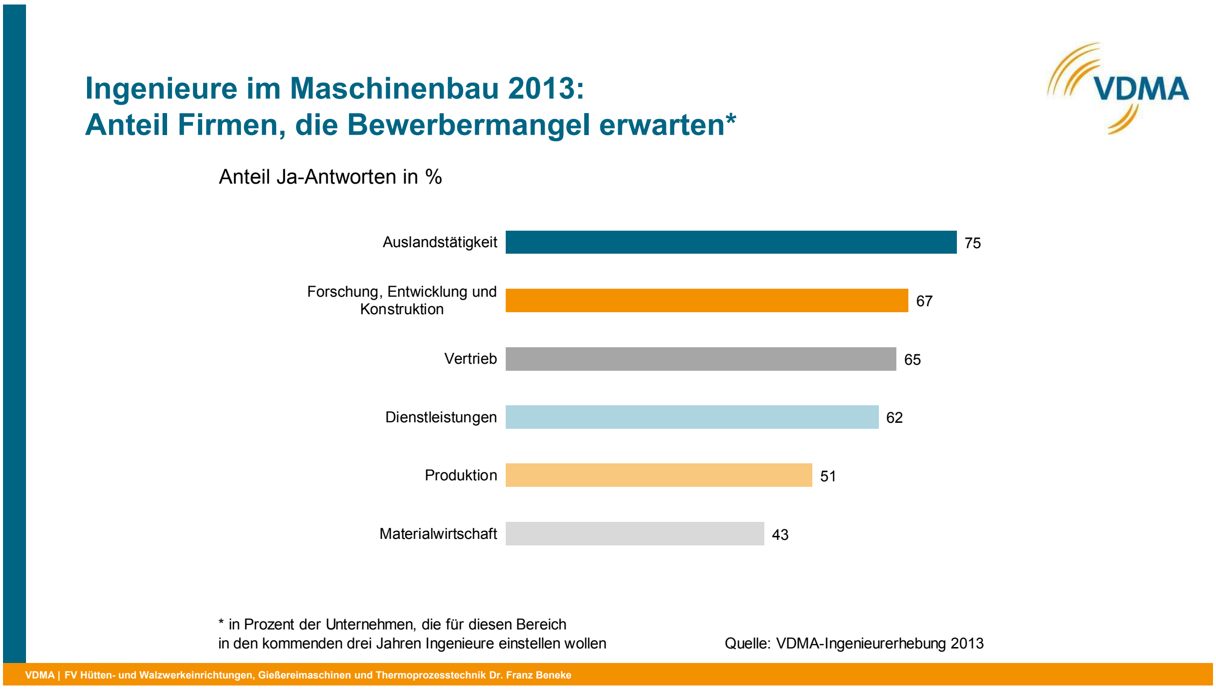

Ingenieure im Maschinenbau 2013:
Anteil Firmen, die Bewerbermangel erwarten*

Anteil Ja-Antworten in %

* in Prozent der Unternehmen, die für diesen Bereich in den kommenden drei Jahren Ingenieure einstellen wollen

Quelle: VDMA-Ingenieurerhebung 2013

VDMA | FV Hütten- und Walzwerkeinrichtungen, Gießereimaschinen und Thermoprozesstechnik Dr. Franz Beneke

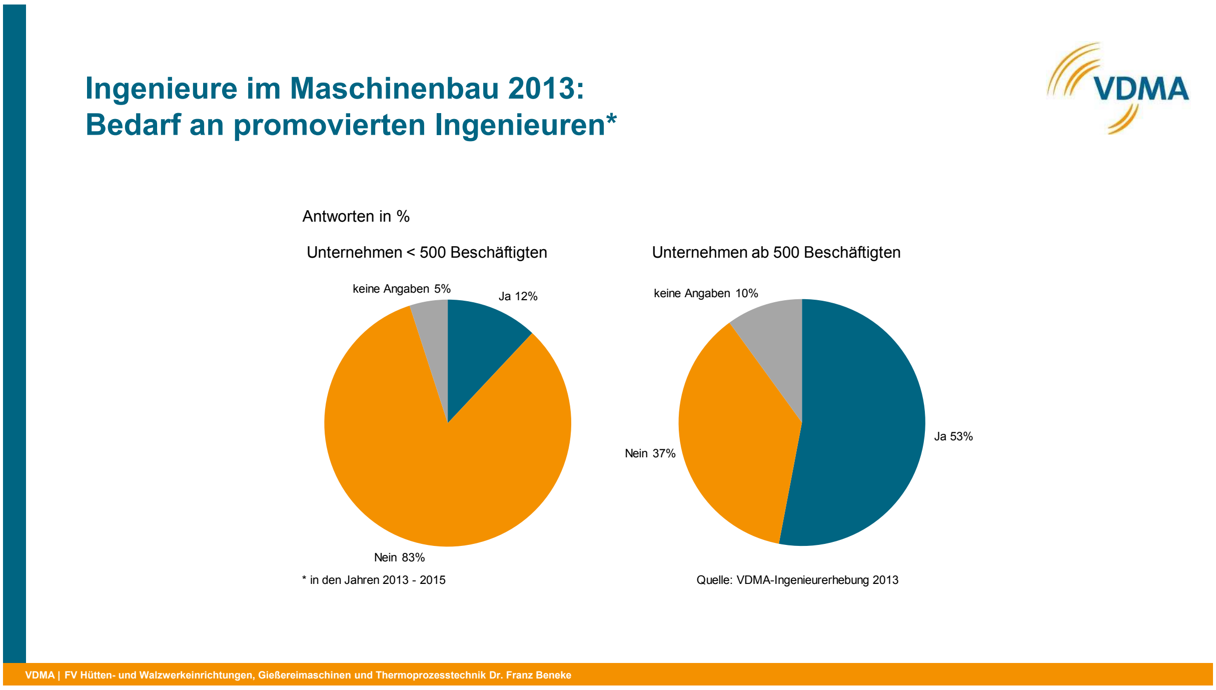

Ingenieure im Maschinenbau 2013:
Bedarf an promovierten Ingenieuren*

Antworten in %

* in den Jahren 2013 - 2015

Quelle: VDMA-Ingenieurerhebung 2013

VDMA | FV Hütten- und Walzwerkeinrichtungen, Gießereimaschinen und Thermoprozesstechnik Dr. Franz Beneke

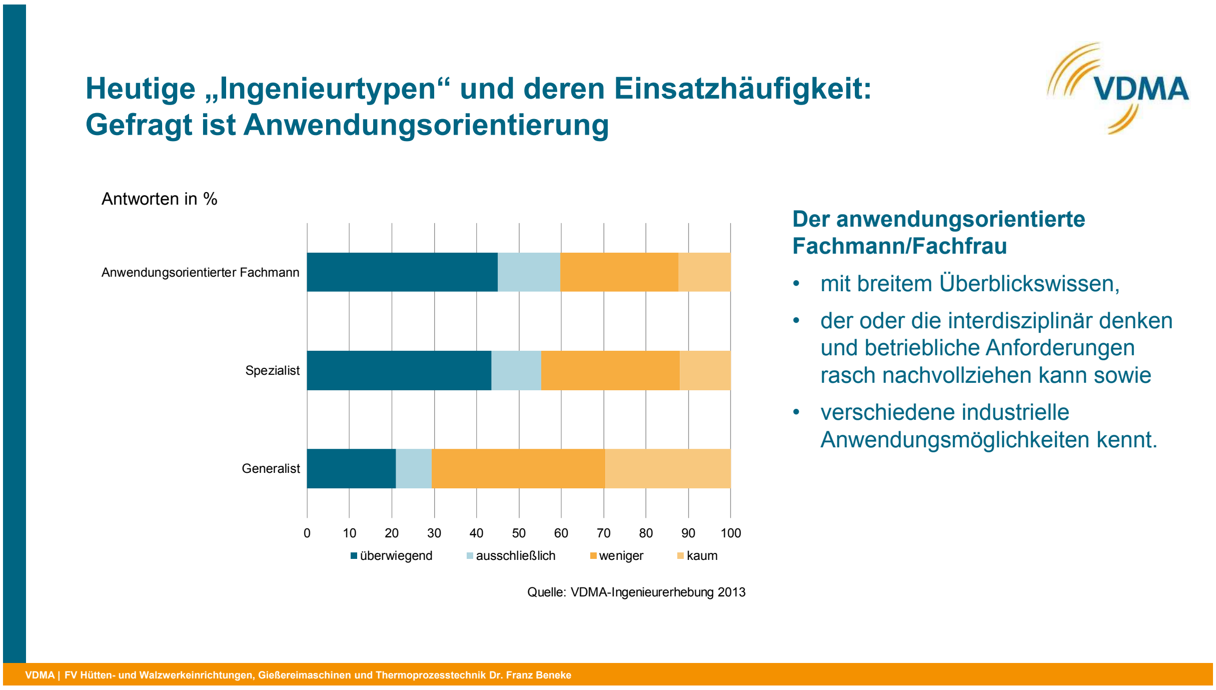

Heutige „Ingenieurtypen“ und deren Einsatzhäufigkeit: Gefragt ist Anwendungsorientierung

Antworten in %

Quelle: VDMA-Ingenieurerhebung 2013

Der anwendungsorientierte Fachmann/Fachfrau

- mit breitem Überblickswissen,
- der oder die interdisziplinär denken und betriebliche Anforderungen rasch nachvollziehen kann sowie
- verschiedene industrielle Anwendungsmöglichkeiten kennt.

VDMA | FV Hütten- und Walzwerkeinrichtungen, Gießereimaschinen und Thermoprozesstechnik Dr. Franz Beneke

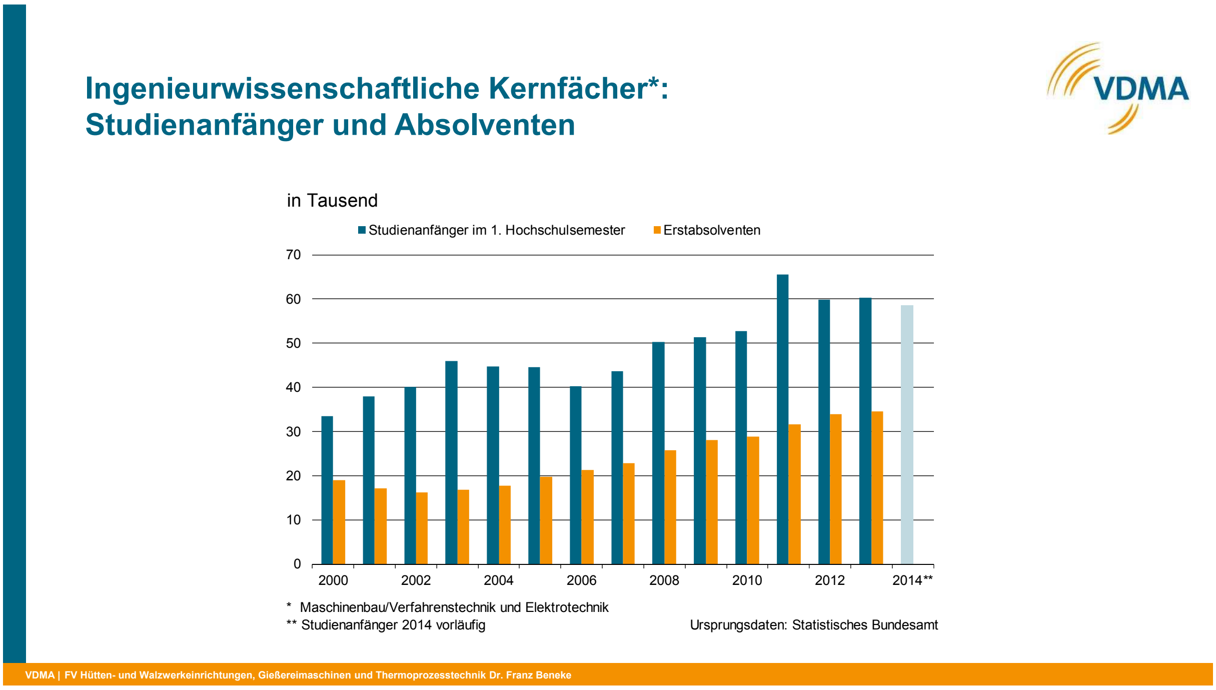

Ingenieurwissenschaftliche Kernfächer*: Studienanfänger und Absolventen

in Tausend

* Maschinenbau/Verfahrenstechnik und Elektrotechnik
** Studienanfänger 2014 vorläufig

Ursprungsdaten: Statistisches Bundesamt

VDMA | FV Hütten- und Walzwerkeinrichtungen, Gießereimaschinen und Thermoprozesstechnik Dr. Franz Beneke

Effect of alkaline reserve in cardboard on corrosion aggressiveness towards lead.

Kristýna Strachotová
Institute of Chemical Technology Prague

High sensitivity of lead to organic compounds leads to degradation of historical lead objects stored in the depositories of museums or archives. High concentration of organic compounds in the atmosphere of depositories is caused by degradation of organic materials (wood glue, leather, paper). Organic materials are stored together with lead objects or they are used as a packaging material.

This study was aimed on the influence of packaging material properties to aggressiveness towards lead by the resistometric method. Especially, the effect of alkaline reserve was studied by using model samples with the four different value of alkaline reserve.

The results showed that aggressiveness of packaging material is determined by a complex influence of material properties. Although the alkaline reserve was a significant factor in reducing the aggressiveness of the packaging material, its value in the packaging material had not a direct effect.

Technology of soluble cores for high-pressure die castings

E. Adámková*, P. Jelínek
VŠB – Technical University of Ostrava
Department of Metallurgy and Foundry, 17. listopadu 15 / 2172, 708 33
Ostrava-Poruba, Czech Republic
Corresponding author. E-mail address: eliska.adamkova@vsb.cz

Abstract

The greatest potential in high – pressure die casting technology represents the cores of inorganic salts. Therefore the interest in new manufacturing processes of “soluble” cores

(Verlorene Kerne, Lost Cores) is growing. The article gives the results of the production of salt cores by high-pressure squeezing and shooting with using a binder (alkali silicates). Special attention is paid to the shape of cooking salt NaCl crystals of different provenance with additives and the influence on strength properties of cores. A technology of bonding the salt cores is developing. Salinity of circulating water is studied and it is checked with the aid of electrical conductance.

Keywords: Salt cores, manufacture by squeezing and shooting, the use of cooking salts, bonding of cores, salinity of cleaning water, electric conductance

1 Introduction

The rising demands on the complexity of castings cannot be met in the die casting technology with the existing simple metal cores. Therefore the interest in new manufacturing processes of “soluble” cores (Verlorene Kerne, Lost Cores) is growing [1]. The greatest potential represents the cores of inorganic salts which must meet a number of requirements as follow:

- Dimensional accuracy
- Bench life (hydration)
- Strength even under increased temperatures (up to 700 °C)
- Smoothness of precast cavities (Ra)
- Ease solubility in water

According to some authors the salt cores are suitable for lower speeds of filling the mould (under 35 m/s) with limited post pressing, i.e. suitable e.g. for the „rheocasting“ technology [2]. The contribution deals with the development of salt cores by the method of high-pressure squeezing of crystalline salts and shooting with the use of binders (alkali silicates), the application of cooking salts of different provenance, gluing of cores and with recycling the brine.

2 New manufacturing processes of “soluble” cores

- Sand cores – made by the technology of PUR Cold – Box (binder – polyurethanes) or Warm – Box (alkaline silicates). Precast holes are geometrically precise but the cores are removable with difficulties (in case of organic binders by annealing which is often recommended to be performed simultaneously with heat treatment of castings of some Al-alloys) [3]. Metal penetration can be avoid by optimization of base sands granulometry and with the aid of protective coatings. Sometimes it is proposed to dip the cores in binders (resin, water glass).
- Cores of the plastics (polyoxymethylene) – are made by machining the blocks. They are removed by combustion of cores residues.
- Cores of low melting metals, e.g. Zn-alloys (ZnAl4CU1) [2]. They are melted out by additional annealing of castings. The surface of holes is of high quality corresponding to the die casting process.

- Cores of inorganic salts:
    - Hollow cores combined with a metal pipe [4, 5].
    - Full cores of crystalline salts or their melts [6].

The use of salt cores is already a longer time known with gravity or low-pressure casting processes (pistons of internal combustion engines) but for demanding high-pressure casting an intensive research is only realized [4–6] in spite of a fact that the beginnings go back to the 70th-80th years of the last century.

3 Salt cores

They are developed basically in the manufacturing technology of salt cores. Each of them has its merits and shortcomings (Table 1).

Table 1: Advantages and disadvantages of technologies for preparation of cores.

	High-pressure squeezing	Shooting (binder alkali silicate)	Casting of molten salts with post pressing
Advantages	- High cold and hot strengt - Minimum porosity (2 - 6 %) - Simple manufacturing process - No protection against penetration is needed - Cores can be machined - Accuracy of precast holes - Good solubility in water - High resistance to rehydration	- Possibility of using the existing core machines - Manufacture of complex shapes - Excellent solubility in water	- High cold and hot strengths - Minimum surface porosity - No surface protection is necessary - High accuracy and smoothness of precast holes
Disadvantages	- Designed for simpler shapes - Non-uniform degree of compaction (one-way pressing)	- Lower strengths - Higher hygroscopicity of cores - High porosity (30 - 35 %) - Worse surface quality (protective coatings)	- Expensive special equipment and demanding preparation - Volume shrinkage during solidification - More difficult solubility (high water consumption) - High energy consumption

3.1 Salt cores manufactured by squeezing

Our first experiments resulted from KCl and NaCl of chemical purity (p.a.). Although the physic-chemical properties of both salts don't differ substantially, the KCl in all parameters shows significantly higher cold and hot strengths (up to 650 °C) (Table 2) which is explained at first by different angularity and shape of grains which is also confirmed by C. R. Loper too.

Table 2: Bending strength of pressed cores (100 kN, 56 MPa).

	Holding in air 48 h [MPa]	Hot 650 °C [MPa]	Residual strength 650 °C/1 h [MPa]
KCl, p.a. $^{+)}$	7.53	> 8.9	8.49
NaCl, p.a. $^{+)}$	3.63	5.33	2.55

Angularity of salt grains: $KCl^{+)}$ = SPHT 3 0.778
$NaCl^{+)}$ = SPHT 3 0.906

Further growth of cold and hot strength was achieved by applying of composite salts resulting from an assumption that the additives of the $ZrSiO_4$, Al_2O_3, Fe_2O_3 a SiO_2 type of defined concentration and granulometry will interfere the long dislocation lines with particles of high heat resistance dispersed in the salt matrix (KCl, NaCl). Composite salts have brought as follows:

- The growth of cold and hot strengths (650 °C) and namely the highest one with the $\alpha - Al_2O_3$ additive. Primary bending strength exceeded 9 MPa which is approximately a triple of strength of the PUR Cold – Box cores.
- Residual strengths after the exposure of cores to 650 °C/1 h were by 10-20 % higher than primary strengths.
- With the growth of pressing forces (up to 200 kN) the porosity of cores was decreasing under 6 % (the cores are of a glassy, monolithic character), their strength is growing but the smoothness of precast holes too (Ra < 5 µm). Mean diameter of pores kept around 0.0618 µm.
- Cores can be mechanically machined.
- With strengths of cores the high kinetics of dissolving in water doesn't decrease (20 °C).

Spontaneous destructions of cores caused by residual stress after high-pressure squeezing can be prevented by special thermal treatment and modifications of the pressing element. Contrary and volume pressing are tested (3D).

3.2 Salt cores manufactured by shooting

They require the use of binders hardenable with the heat of core boxes or cold hardenable, e.g. with a gaseous medium (TEA – PUR Cold – Box). Our research was focused on environmental friendly inorganic binders (Na – silicates) made by a direct production (M < 2.1) hardened by a dehydration process, the Warm – Box technology (up to 250 °C). After shooting the mixture the cores are hardened in a hot core box (7.5 – 8.0 bar, 190 °C).

The achieved real porosity of cores ranged in the interval of 21.3 – 23.5 % (apparent porosity of 35 – 45 %) which correlated with bending strength of 1.5 – 3.5 MPa. It is ca $\frac{1}{3}$-$\frac{1}{2}$ of strength of cores squeezed from the mixture of the same composition. In this case the metal penetration must be avoided by a surface protection with the aid of alcohol-based protective coatings. Otherwise during storing this cores are also exposed to higher rehydration (Figure 1).

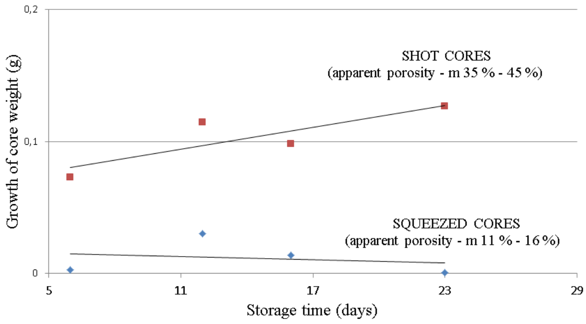

Figure 1: Comparison of hygroscopicity of squeezed and shot cores of the same composition (conditions RH 35 – 58 %, T = 20.7 – 24.9 °C).

In case of short-term storage the growth of weight is insignificant. During solution in water the cores behave in a similar way.

4 Application of cooking salt

Five types of cooking salts (No 1÷5) were chosen from the commercial offer and they were compared with a standard of NaCl, p.a. (No 6). Chemical composition (Table 3) can be evaluated from two points of view as follow:

- Health point of view
- Technological point of view

From the point of view of health the cooking salts contain health useful elements, iodine and fluorine, and namely in a form of compounds (KIO_3, KI, NaF) in amounts 15 – 58 (max. 205) mg/kg. But for manufacture of salt cores the technological points of view are much more important, the parameters limiting their quality. In some salt kinds the additives preventing the grain sticking, so called „anticaking agents“ are found. For this purpose the K_2CO_3, $CaCO_3$, $MgCO_3$, SiO_2, $K_4[Fe(CN)_6].3H_2O$ additives are used. Especially the occurrence of carbonates is characteristic for Alpine salts. Anticaking additives adversely influence the manufacturing technology of salt cores, and namely both the high-pressure squeezing and the shooting too. Gluing – binding properties are deteriorating (Figure 2) and namely both by the recrystallization way (squeezing) and by binding between the salt grains and alkali silicate (shooting) too.

In general, by squeezing the significantly higher strengths were achieved for all kinds of salts. The lowest strengths had the cores with cubic regular shape of grains („Alpine salt, Nos 3, 4 – recrystallized salts) (Figure 4), while the highest strengths were achieved for crushed rock salts (Nos 1, 2) (Figure 3) and sea salt (No 5). But this is not valid for the standard (NaCl, p.a., No 6). A „dipyramidal, regular“ shape of grains gives high

Table 3: Chemical composition of chosen cooking salts.

Salt sample	**Trade name**	**Additives**		**Presence of compounds**
1	Edible rock salt with iodine and fluorine (finely ground)	F I	max. 250 mg/kg 27±7 mg/kg	NaF KIO_3
2	Edible rock salt with iodine (finely ground)	I	20-35 mg/kg	KI KIO_3
3	Alpine salt with iodine (vacuum treated)	NaCl $CaCO_3$ $MgCO_3$ KIO_3 I	98.8 % min. 0.9 % min. 0.2 % 33-58 mg/kg 20-34 mg/kg	$CaCO_3$ $MgCO_3$ KIO_3
4	Alpine salt with fluorine and iodine (vacuum treated)	NaCl $CaCO_3$ $MgCO_3$ KIO_3 I F	98.0 % min. 0.7 % min. 0.1 % 33-58 mg/kg 20-34 mg/kg max. 250 mg/kg	KIO_3 $CaCO_3$ $MgCO_3$ NaF
5	Fine sea salt with iodine (evaporated from sea water)	I	15-35 mg/kg	KIO_3
6 Standard	NaCl, p.a. (chemically pure)	Fe Heavy metals (Pb) SO_4 Ca Mg I Br	max. 0.0003 max. 0.0005 % max. 0.005 % max. 0.005 % max. 0.002 % max. 0.008 % max. 0.01 %	

strengths both of squeezed and shot cores. This shape is closest to the globular shape of the quartz base sand what is an advantage both for shooting and squeezing (Figure 5).

5 Checking the state of concentration of salts in circulating wash water (kinetics of dissolution of cores, changes in electric conductance and pH of the system)

For measuring the state of salt concentration in the waste brine the signalling of the change of pH and electric conductance of the system was used. The measurement was carried out on cylindrical shot cores of chemical composition: NaCl, cooking salt + NaCl dust + graphite + water glass. It was dissolved in water under temperature of 19.5 ÷ 20.0 °C and different NaCl concentration in wash water (standard – pure water; the amounts of 145 g and 240 g NaCl in water). The measurement was based on a consideration that during removing the cores with already used water the solubility will decrease (the growth of the brine concentration) which is also confirmed with results given below (Figure 6).

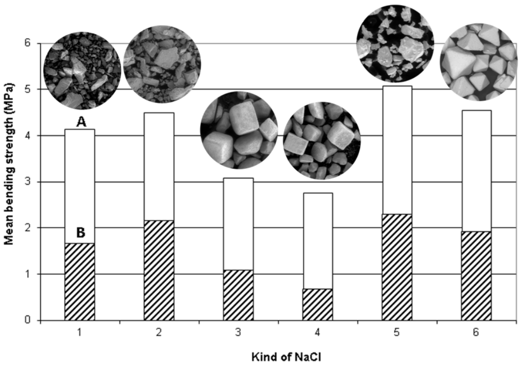

Figure 2: Comparison of strengths of salt cores squeezed and shot from different kinds of cooking salts (mean value from 6 cores; the fraction 0.063 ÷ 1.0 mm; A = SQUEEZED CORES (104 MPa); B = SHOT CORES (the binder Na – SODIUM SILICATE, 7.5-8.0 bar).

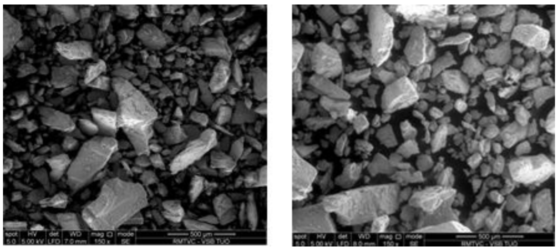

Figure 3: Shattered surface of crushed rock salts (samples Nos 1, 2) and EDX analysis of chemical composition.

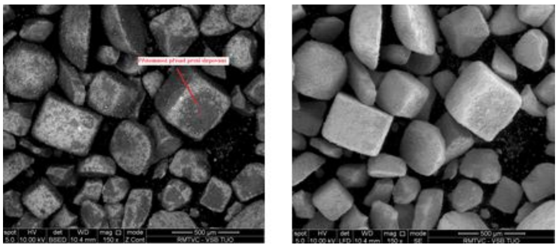

Figure 4: Regular cubic grains of Alpine salts (samples Nos 3, 4) and EDX analysis confirming the presence of anticaking additives on the salt grain surface ($MgCO_3$, $CaCO_3$).

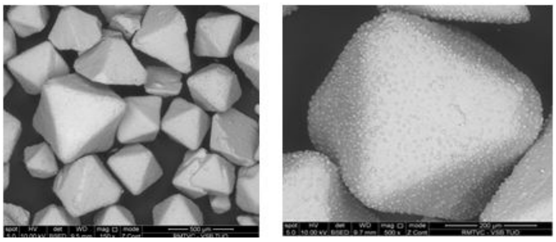

Figure 5: Dipyramidal regular shape of NaCl, p.a. – standard (sample No 6) and EDX analysis of chemical composition.

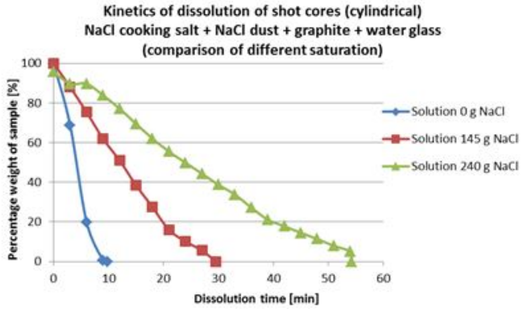

Figure 6: Comparison of dissolving the salt cores in two types of saturated solutions and in pure water.

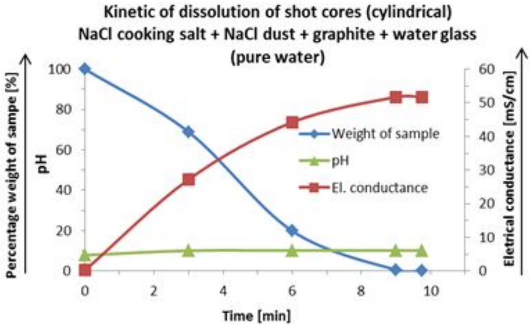

Figure 7: Kinetics of dissolution of salt cores in dependence on pH and electric conductance.

While in case of pure water the sample was dissolved for 9 minutes, with 145 g of NaCl present in the solution it was already 30 minutes and with amount of 240 g of NaCl the sample was dissolved for 54 minutes. Figure 7 shows a significant growth of electric conductance with the loss of weight of the salt core (growth of concentration of NaCl in pure water). On the contrary the pH value of the system increased from a neutral level to alkaline values (pH around 9) for a short time and with further enrichment of salts in water it wasn't further changed.

It turns out that the best criterion for the evaluation of reversal usability of wash water is electric conductance. Therefore for a specific chemical composition of the salt core a critical value of electric conductance can be determined which still allows the effective solubility of cores of the given composition. The methodology has a task to indicate a critical concentration of the brine still applicable in the closed circuit of wash water.

6 Conclusion

Salt water soluble cores offer a considerable potential even for so demanding manufacturing technology of castings as is high-pressure casting process. For developed methods of squeezing and shooting of cores with use of inorganic binders of composite composition a significant influence of granulometry and the shape of grains was proved but above all the unwanted presence of „anticaking“ additives in cooking salts. A way of gluing the salts cores and the combination with metal cores too is studied. The attention was paid to the kinetics of dissolving the cores and to study of critical salinity of circuit water during cleaning of castings.

Acknowledgements

The research was funded by the project of the Technological Agency of the Czech Republic TA 02011314 and projects of specific research in metallurgical, material and process engineering SP 2015/78, SP 2015/70. This paper was created under the Project No. CV6005531 „Support and development of international relationship and mutual foreign activities of students and staff on FMMI“, funded by VŠB – Technical University of Ostrava, Czech Republic.

References

[1] Pacyniak, T. and Kaczorowski, R.: “Ductile cast iron obtaining by Inmold method with use of LOST FOAM process”. In: *Archives of Foundry Engineering* 8.3 (2008).

[2] Michels, H., Bünck, M., and Bührig-Polaczek, A.: “Suitability of lost cores in rheocasting process”. In: *Transactions of Nonferrous Metals Society of China* 20 (2010), s948–s953.

[3] Holtzer, M. and Dańko, R.: “Teoria i praktyka regeneracji oraz zagospodarowania zużytych mas formierskich i rdzeniowych”. In: *Rozdział w monografii "Postępy teorii i praktyki odlewniczej". Wyd. PAN Oddział Katowice. Komisja Odlewnicza, Katowice–Gliwice* (2009), pages 133–152.

[4] Fuchs, B., Eibisch, H., and Körner, C.: “CORE VIABILITY SIMULATION FOR SALT CORE TECHNOLOGY IN HIGH-PRESSURE DIE CASTING.” In: *International Journal of Metalcasting* 7.3 (2013).

[5] Yaokawa, J. et al.: “Strength of salt core composed of alkali carbonate and alkali chloride mixtures made by casting technique”. In: *Materials transactions* 48.5 (2007), pages 1034–1041.

[6] Jelínek, P. et al.: “Development of Foundry Cores Based on Inorganic Salts”. In: *Materials and technology* 47.6 (2013), pages 689–693.

Hydrogen diffusion in the trip 800 C-Mn-Si-P steel

Taťána Kulová, Jaroslav Sojka
VŠB – Technical University of Ostrava

1 Introduction

Transformation induced plasticity (TRIP) steel represents one kind of advance high-strength steels (AHSS) and it demonstrates superior mechanical performance of a high strength and a very good fracture toughness [1]. The properties of TRIP steels depend on an optimal chemical composition and it is essential to include elements that inhibit cementite and/or carbide precipitation to ensure that a sufficient quantity of retained austenite (RA) remains in the steel microstructure at ambient temperature [2]. Unfortunately, TRIP steel is susceptible to hydrogen embrittlement. The susceptibility to hydrogen embrittlement is closely related to hydrogen diffusion characteristics. Nevertheless, there are only few literature data concerning hydrogen diffusion characteristics in the TRIP steels.

In the presented paper hydrogen diffusion characteristics were studied in the C-Mn-Si-P TRIP 800 steel in three different states: in as-received state after hot and cold rolling and subsequent heat treatment; and furthermore after 5% and 10% tensile deformation.

2 Material and experimental procedure

Experiment was performed on the TRIP 800 steel based on C-Mn-Si composition but with increased phosphorus content. The chemical composition of the studied steel is given in Table 1.

Table 1: Chemical composition of the studied TRIP 800 steel (wt.%).

C	**Mn**	**Si**	**P**	S	Cr	Ni	Cu	V	Al	Nb
0.20	**1.50**	**1.50**	**0.050**	0.005	0.16	0.15	0.06	0.02	0.006	0.02

Details concerning steel manufacturing and its heat treatment can be found in [2]. Microstructure of the studied steel was observed by means of light microscopy (LM) and scanning electron microscopy (SEM); retained austenite content was determined by means of X-ray analysis using Co K_α source (λ=0.179 02 nm).

Electrochemical hydrogen permeation tests were carried out using a Devanathan-Stachurski two-component cell, separated by a steel membrane – working electrode. Both sides of the working electrode were polished mechanically up to 1200 grinding paper. After that, exit side of the working electrode was palladium coated to prevent from the hydrogen atom recombination during permeation experiments [2]. The solution for hydrogen charging of the steel was 0.05M H_2SO_4, while the hydrogen exit cell was filled with 0.1M NaOH solution. The exit cell was deaerated by argon bubbling before and during experiments. The hydrogen permeation current was recorded using a VOLTALAB 40 potentiostat during experiments.

After an output current stabilization, the entry side of the specimen was polarized anodically at a current density of $35\,\mathrm{mA\,cm^{-2}}$. After that two build-up transients were recorded, the first one at the charging current density of $-20\,\mathrm{mA\,cm^{-2}}$, the second one at the charging current density of $-35\,\mathrm{mA\,cm^{-2}}$. Before ending the experiment hydrogen charging was stopped and a decay transient was also recorded.

3 Result and discussion

Microstructure. Microstructure of the studied steel was the same from the viewpoint of both light microscopy (LM) and scanning electron microscopy (SEM). The fine-grain microstructure consisted predominantly of proeutectoid ferrite and bainite. In some locations, it was possible to assume the presence of small regions of martensite. It was impossible to identify any retained austenite using either light or scanning electron microscopy. Figure 1 shows the microstructure of the studied steel in as-received state (without deformation) and Figure 2 shows the microstructure after 10% tensile deformation. The content of retained austenite was determined using X-ray diffraction analysis. A mean value of 9.0±2.0 % of retained austenite was obtained for the studied steel in the as-received state. The amount of retained austenite decreased for the states after 5% and 10% tensile deformation.

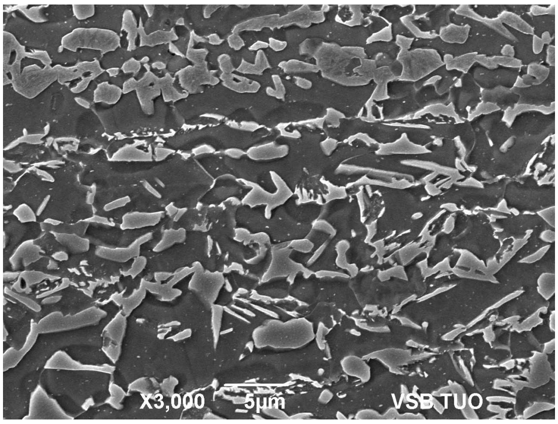

Figure 1: Microstructure of the TRIP steel in as-received state (SEM).

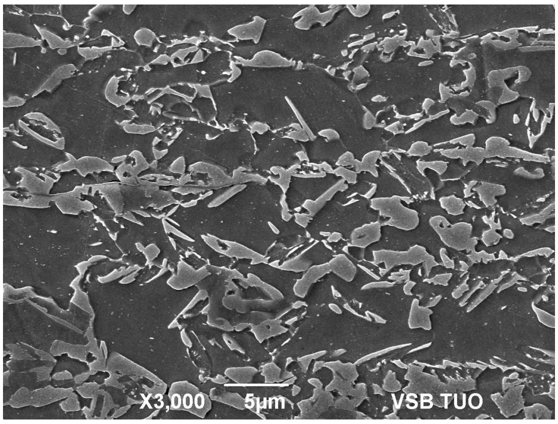

Figure 2: Microstructure of the TRIP steel after 10% deformation (SEM)

Hydrogen Diffusion Characteristics. Hydrogen diffusion coefficients were calculated using the time-lag method according to Equation 1:

$$D = \frac{L^2}{6t_l} \tag{1}$$

where L represents the membrane thickness and t_l corresponds to the time where the permeation currents reaches 63% of its steady-state value. Sub-surface hydrogen concentration was calculated by the following equation:

$$C_H^0 = \frac{i_\infty L}{DF} \tag{2}$$

where i_∞ is a steady-state current density and F is Faraday's constant. For the correlation between experimental results and a theoretical model, Equation 3 was used to calculate a normalized hydrogen flux $\frac{J_t}{J_\infty}$:

$$\frac{J_t}{J_\infty} = \frac{2}{\sqrt{\pi\tau}} \sum_{n=0}^{\infty} \exp\left[-\frac{(2n+1)^2}{4\tau}\right] \tag{3}$$

where τ is dimensionless time equal to $\frac{Dt}{L^2}$.

Hydrogen diffusion coefficients are shown in Figure 3 for all three studied states.

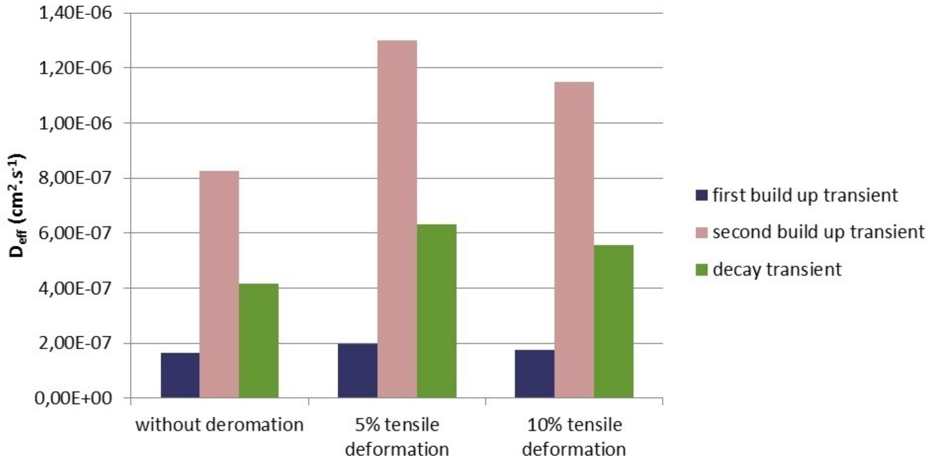

Figure 3: Hydrogen diffusion coefficients Deff for all studied states.

It is obvious from Figure 3 that the lowest values of hydrogen diffusion coefficient were always obtained for the first build up transient. It can be related to hydrogen trapping in both reversible and irreversible traps. The hydrogen diffusion coefficients corresponding to the first build up transient were higher for the states after tensile deformation. Probably, formation of martensite facilitates hydrogen diffusion in the TRIP steel. Hydrogen diffusion coefficients corresponding to the second build up transient were markedly higher and confirmed that most of traps were filled by hydrogen during the first build up transient. Nevertheless, values of hydrogen diffusion coefficients still remained lower in comparison with conventional steels having bcc lattice. For decay transients hydrogen diffusion coefficients were situated between values obtained for the 1st and 2nd build up transient. The obtained results are in a good agreement with findings of Zakroczymski [3]. According to him during the first build up transient hydrogen trapping can be expected and during decay transient hydrogen detrapping can be expected, influencing thus values of hydrogen diffusion coefficient. An example of fitting experimental results with the theoretical curve of normalized hydrogen flux $\frac{J_t}{J_\infty}$ is shown in Figure 4 for the second build up transient after 5% tensile deformation. Measured data fitted well with the theoretical curves for the second build up transient in all studied states. However, for the first build up transient and for the decay transient, the measured data were shifted to longer time in comparison with the theoretical curves confirming thus the important role of hydrogen trapping and detrapping [3].

Hydrogen sub-surface concentration was calculated for the first build up transient using Equation 2. The obtained results are presented in Table 2. The hydrogen sub-surface concentration was very high in all three states. The high sub-surface concentration of hydrogen in the studied TRIP steel can, at least partially, explain its rather high susceptibility to hydrogen embrittlement [2].

4 Conclusion

Results of the study of hydrogen diffusion characteristics in the C-Mn-Si-P TRIP 800 steel in three different states can be summarized as follows:

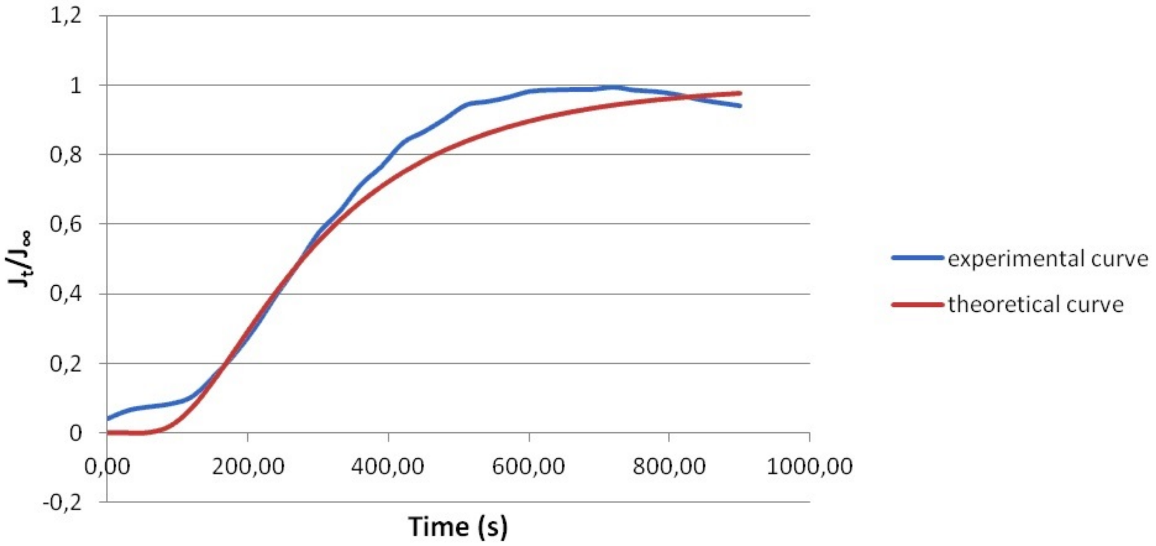

Figure 4: Fitting of the experimental data with the theoretical curve for the 2nd build up transient after 5% deformation.

Table 2: Hydrogen sub-surface concentration during the first build up transient (mass ppm).

As-received	5 % tensile deformation	10 % tensile deformation
20,9	36.9	27.0

The values of hydrogen diffusion coefficients in the TRIP 800 C-Mn-Si-P steel were rather low and lay between $1.30 \cdot 10^{-6} \mathrm{cm}^2\,\mathrm{s}^{-1}$ and $1.64 \cdot 10^{-7} \mathrm{cm}^2\,\mathrm{s}^{-1}$. The highest values of hydrogen diffusion coefficient were observed during the 2nd build up transient where the role of hydrogen trapping was limited.

The decrease of retained austenite content resulted in the increase of hydrogen diffusion coefficient.

The comparison of experimental data with the theoretical model showed a good fitting for the 2nd build up transient, while during the 1st build up transient and during the decay transient a shift of experimental data to longer time was observed.

Very high sub-surface concentration of hydrogen was determined in all three states of the studied steel especially for the state with 5% tensile deformation.

Acknowledgement

This paper was prepared with the financial support of the project No. CV6005531 “Support and development of international relationship and mutual foreign activities of students and staff on FMMI” and the project “SP 2015/70 Specific research in the metallurgical, materials and process engineering”, both funded by VŠB – Technical University of Ostrava, Czech Republic.

References

[1] De Cooman, B.: “Structure–properties relationship in TRIP steels containing carbide-free bainite”. In: *Current Opinion in Solid State and Materials Science* 8.3 (2004), pages 285–303.

[2] Sojka, J. et al.: “Effect of hydrogen on the properties and fracture characteristics of TRIP 800 steels”. In: *Corrosion Science* 53.8 (2011), pages 2575–2581.

[3] Zakroczymski, T: “Adaptation of the electrochemical permeation technique for studying entry, transport and trapping of hydrogen in metals”. In: *Electrochimica acta* 51.11 (2006), pages 2261–2266.

Bedeutung der Industriebrennertechnik

Joachim G. Wünning
WS Wärmeprozesstechnik GmbH

Die Nutzung des Feuers durch den Menschen gehört zu den entscheidenden Kulturtechniken die zur Zivilisation der Menschheit geführt haben. Das Feuer wurde zur Erzeugung von Heizwärme, Licht und zum Kochen, aber auch für frühe technische Anwendungen wie der Metallgewinnung und zum Brennen von Keramik genutzt.

Die Feuerungen waren offene oder eingefasste Feuerstellen und wurden überwiegend mit Holz beheizt. Auch in der frühen Phase der Industrialisierung wurden Feuerungen noch sehr einfach betrieben. Beim Dampfkessel etwa, wurde der Brennstoff, Holz oder Kohle, vom Heizer in den Dampfkessel geschaufelt. Man kennt das Bild des geschwärzten Heizers auf Lokomotiven oder im Kesselraum von Dampfschiffen. Diese schweißtreibende Tätigkeit wurde, durch den Einsatz von Brennern, überfällig.

Heutzutage wird der größte Anteil der eingesetzten Brennstoffe mit Hilfe von Brennern verfeuert. Ein weiterer Teil, vorwiegend flüssiger Brennstoff, wird in Verbrennungsmotoren eingesetzt.

Grob ein Viertel des in Deutschland verbrauchten Brennstoffes wird zur Erzeugung von Raumwärme und Warmwasser , ein weiteres Viertel zur Erzeugung von Prozesswärme und ein Drittel zur Erzeugung von mechanischer Energie. Der restliche Verbrauch verteilt sich auf Beleuchtung, Kälte und sonstige Anwendungen. Auf der Internetseite des Bundeswirtschaftsministeriums (www.bmwi.de) finden sich umfangreiche Energiedaten.

Die Verbrennung von zumeist fossilen Brennstoffen ermöglicht unseren modernen Lebenstil und unsere Anforderungen an Komfort, Mobilität, Kommunikation und Konsum. Auf der anderen Seite führt diese Verbrennung der fossilen Brennstoffe zur Schädigung unsere Umwelt durch Schadstoffbelastung und einer Beeinflussung des Weltklimas durch Kohlendioxidaustoss. Der Streit über die Kontrolle von Rohstofffeldern führt oft zu regionalen Konflikten und kriegerischen Auseinandersetzungen. Trotz unterschiedlicher Ansichten über die Reichweiten der fossilen Brennstoffvorräte weiss man, dass diese endlich sind. Es gibt also gute Gründe, fossile Brennstoffe als etwas Wertvolles zu betrachten und nicht weiterhin verschwenderisch mit dieser Ressource umzugehen.

Bei der Entwicklung der Brenner und Industriebrenner gibt es einige Entwicklungsschwerpunkte, die nachfolgend erläutert werden

1 Automatisierung

Ein wesentliches Merkmal eines Brenners ist die Verwendung von fließfähigen Brennstoffen. Brennstoff wird dabei, meist durch Druck, zum Brenner geführt und dort mit Luft verbrannt. Neben gasförmige und flüssigen Brennstoffen kann auch Kohle verwendet werden, wenn diese aufgemahlen und mit Transportluft fließfähig gemacht wird.

Heute werden moderne Industriebrenner oft über Datenbusverbindungen angesteuert und so können eine Vielzahl von Informationen an und vom Brenner übermittelt und archiviert werden. Heute werden Industriebrenner in der Regel vollautomatisch betrieben und überwacht.

2 Sicherheit

Das Glutbett einer Rostfeuerung oder einer Feuerstelle stellt eine kontinuierliche Zündquelle zur Verfügung. Bei dem Einsatz von Brennern muß aber sichergestellt werden, dass der Brennstoff in einer Flamme zuverlässig verbrannt wird. Beim Verlöschen der Flamme könnte sich im Brennraum ein unverbranntes Brennstoff/Luft-Gemisch ansammeln, das dann zu einer Verpuffung oder Explosion führen kann. Beim Verlöschen der Flamme muss deshalb die Brennstoffzufuhr sofort unterbrochen werden.

Sichere Verbrennung muss durch die Brennerkonstruktion gewährleistet sein und kann über eine Flammenüberwachung sichergestellt werden. Bei Brennraumtemperaturen oberhalb der Selbstzündtemperatur muss gewährleistet sein, dass genügend Sauerstoff (Luft) zugegeben wird und das eine ausreichende Mischung mit dem Brennstoff erfolgt. Eine detektierbare Flamme ist dann nicht mehr notwendig und der Brennstoffumsatz kann z.B. mit flammloser Oxidation erfolgen.

3 Vielfalt

Ging es zu Beginn de Industrialisierung vorangig um den Ersatz der Rostfeuerung, so entwickelten sich im Laufe der Zeit unterschiedlichste Arten von Brennern für eine Vielzahl von Anwendungen. Beispiele sind der Brenner eines Raketentriebwerkes, der Brenner eines Gasherdes, der Flachflammenbrenner in einem Schmiedeofen, der Brenner in einem Flugtriebwerk oder der 40 Megawatt Kohlenstaubbrenner im Dampfkessel eines Kohlekraftwerks. Industriebrenner unterscheiden sich heute grundlegend, je nach Art des Brennstoffes, der Einsatztemperatur, der Brennerleistung und vielen anderen Merkmalen. Ein Gebläsebrenner, der zur Erzeugung von Heizwärme konzipiert ist, kann beispielsweise nicht einen Flachflammenbrenner in einem Schmiedeofen ersetzen.

4 Effizienz

In den meisten Fällen übersteigt der Wert des umgesetzten Brennstoffes den Wert des Brenners um ein Vielfaches. Bei einem derzeitigen Industrie-Erdgaspreis von 4 ct/kWh betragen die Betriebskosten eines 100kW Erdgasbrenners 4 €/h. Bei einem Brennerpreis von beispielsweise €2000 wären schon nach 500 Betriebsstunden, also weniger als einem Monat, die Betriebskosten höher als die Anschaffungskosten des Brenners. Es war also, seit es Brenner gibt, ein Entwicklungsschwerpunkt diese möglichst effizient zu gestalten. Bei Industriefeuerungen, insbesondere im Hochtemperaturbereich, ist die Verbrennungsluftvorwärmung die wirksamste Maßnahme zur Reduzierung der Abgasverluste. Modernste Brennersysteme wärmen die Verbrennungsluft fast bis auf Prozesstemperatur vor und ermöglichen so feuerungstechnische Wirkungsgrade von mehr als 80% auch bei Hochtemperaturprozessen. Damit sind diese Feuerungen einer elektrischen Beheizung deutlich überlegen, da hier die hohen Verluste im Kraftwerk berücksichtigt werden müssen.

5 Schadstoffe

Schadstoffe aus Feuerungen können unterschiedliche Ursachen haben haben. Diese sind: Begleitstoffe im Brennstoff, unzureichende Brennereinstellung, Brennerkonstruktion, Prozessführung und andere. In den letzten Jahrzehnten wurden, zumindest in den entwickelten Industrienationen, erhebliche Fortschritte erzielt. Durch besser aufbereitete Brennstoffe, Abgasreinigungssysteme, moderne Brennerkonstruktionen und korrekte Brennerwartung sind die Emissionen von Industriebrennern drastisch zurückgegangen. Auch bei der motorischen Verbrennung wurden Fortschritte erzielt, die Abgasemissionen aus dem Verkehrssektor sind aber meist deutlich höher als die von stationären Feuerungen.

6 Zukünftige Schwerpunkte

Die erreichten technischen Fortschritte hinsichtlich Effizienz und Schadstoffen müssen in den nächsten Jahren konsquent umgesetzt werden. Neben steigenden Energiepreisen weden auch gesetzliche Regelungen, wie Einführung von Energie-Management-Systemen (früher waren das die Wärmestellen) und schärfere Grenzwerte diese Entwicklung befördert.

Wichtig ist auch die exergetische Betrachtung der Energieformen. Elektrische Energie ist in dieser Hinsicht eine sehr wertvolle Energie und sollte deswegen vorwiegend zur Bereitstellung von mechanischer Energie, sowie für Beleuchtung und Elektronik verwendet werden. Elektromobilität wird dabei zumindest im lokalen Verkehr einen Beitrag zur Reduzierung unserer Abhängigkeit vom Öl sowie eine deutliche Verbesserung der Luftqualität in Städten leisten. Zum Verheizen ist diese Energieform viel zu Schade.

Aber auch Brennstoffe werden exergetisch besser genutzt wenn man sie nicht nur zum Heizen sondern zur gleichzeitigen Erzeugung von mechanischer oder elektrischer Energie nutzt. Besonders bietet sich das für die Niedertemperaturwärme, also beispielsweise der Heizwärme an. Aber auch bei höheren Prozesstemperaturen ist diese Kraft-Wärme-Kopplung sinnvoll. Bislang wurde vorrangig an die Nutzung der Abwärme zur Erzeugung von elektrischer Energie, etwa durch ORC-Anlagen, in Betracht gezogen. Viel bessere Ergebnisse sind aber denkbar wenn die Abwärme der Wärmekraftmaschine den Prozess beheizt. Durch eine geeignete Auslegung, beispielsweise einer Gasturbine, lassen sich die gewünschten Abwärmetemperaturen einstellen.

Der Weg zu einer nachhaltigen Energiewirtschaft wird weder durch gigantische Solarfelder in der Sahara noch durch riesige Windparks in der Nordsee erreicht werden. Auch der massive Ausbau der Stromtrassen oder "Big Data", also eine vollständige Vernetzung aller Verbraucher wird nicht die gewünschten Ergebnisse bringen. Eine gerechtere Verteilung der direkten und indirekten Kosten, die sich aus dem Verbrauch der fossilen Energieträger ergeben wird zu vielen Innovationen führen die zu einer erheblichen Steigerung der Energieproduktivität führen, ähnlich wie dies mit der gestiegenen Arbeitsproduktivität durch steigende Lohnkosten im letzten Jahrhundert gelungen ist.

Die Verbrennung und Industriebrenner werden weiterhin eine hohe Bedeutung haben, auch wenn die in ferner Zukunft eingesetzten Brennstoffe keine fossilen Brennstoffe mehr sein werden. Die speicher- und transportfähigkeit der Brennstoffe sowie deren hohe Energiedichte sind der Grund dafür.

Utilization of waste heat from heating slabs in push furnace for Kalina cycle

Miroslava Kukurugyová , Gustav Jablonsky, Augustín Varga, Jana Nalevanková
Technical University of Košice
Department of Furnaces and Thermal Technology, Faculty of Metallurgy, Technical University of Košice, Letná 9,Košice, 042 00, Slovakia
miroslava.popovicova@tuke.sk, gustav.jablonsky@tuke.sk

Abstract

Many of the metallurgy aggregates in the world provides some waste heat which could be successfully used for electricity generation. The cycles which used this low temperature sources are called binary cycles. There are ORC (Organic Rankine cycle) and Kalina cycle. The metallurgy aggregate used in this article is the push furnace from the company U.S.Steel Kosice in Slovakia. The waste heat from the existing push furnace is in this

case the source of heat for the Kalina cycle. Very similar process could be found in the Kashima steel company in Japan. In the Kashima steel company the waste heat from the converter is used for Kalina cycle which generates approximately 3MW of electricity.

In this paper the push furnace and the Kalina cycle are introduced. The Kalina cycle is the efficient power cycle that uses an ammonia-water mixture as the working fluid. Kalina cycle is principally a modified Rankine cycle.

Keywords: Push furnace, Kalina cycle, Waste heat.

1 Introduction

Push furnaces are used to heat up the material (there are billets and slabs) of a square, respectively rectangular cross-section, in process of rolling and forging. Push furnaces are continuously working furnaces, mostly working in counter-current, rarely co-current flows. Blooms are arranged side by side across of the whole hearth of the furnace. They move forward on the skid planks in the hearth of the furnace or on the hearth from the refractory materials due to the pusher. Near to the charging hole is the flue gas . At the other end of the furnace are heated billets taken from the furnace. Combustion gasses move against the movement of material and at the charging end of the furnace is usually conducts heat exchanger, with temperatures of 700 to 1100 ° C.

Thermal efficiency of furnaces is high approximately about 40-60% and is influenced by the amount of preheated combustion air and construction of the furnace. Modern furnaces have specific capacity of 800 - 1200 kg. m-2. h-1. Their maximum length is 35 m, and are limited of the performance. [1–3].

Slab heating in push furnaces is conditional on the forming process and also of the final heating temperature selection of the slab, before the hot rolling. It depends on many factors, especially the type of steel. It should be located from 100 to 150 ° C below the solidus curve.

2 Material and heat balance

Calculation of process heat balance is based on mass and energy conservation equation and and given that the energy source is a mixed is also necessary to elaborate stoichiometric combustion, where for defined fuel composition and for determined oxidizer the volume of oxidizer and volume of combustions generated by fuel burning will be determined. Based on mass conservation equation the material balance determination takes place before the heat balance determination.

2.1 Stoichiometric of the combustion

Burning of fuels leads to oxidation reactions - burning, which releases large amounts of thermal energy.

Gas fuels combustion Reactions of individual fuel combustible constituents with oxygen take place according to following equations

$$CO + \frac{1}{2} \cdot O_2 \rightarrow CO_2 \tag{1}$$

$$H_2 + \frac{1}{2} \cdot O_2 \rightarrow H_O \tag{2}$$

$$H_2S + \frac{3}{2} \cdot O_2 \rightarrow SO_2 + H_2O \tag{3}$$

$$CH_4 + 2 \cdot O_2 \rightarrow CO_2 + 2 \cdot H_2O \tag{4}$$

$$C_2H_6 + \frac{7}{2} \cdot O_2 \rightarrow 2 \cdot CO_2 + 3 \cdot H_2O \tag{5}$$

$$C_3H_8 + 5 \cdot O_2 \rightarrow 3 \cdot CO_2 + 4 \cdot H_2O \tag{6}$$

$$C_4H_{10} + \frac{13}{2} \cdot O_2 \rightarrow 4 \cdot CO_2 + 5 \cdot H_2O \tag{7}$$

$$C_5H_{12} + 8 \cdot O_2 \rightarrow 5 \cdot CO_2 + 6 \cdot H_2O \tag{8}$$

Gas in general can contain following components: CO, $\mathrm{H_2}$, $\mathrm{H_2S}$, $\mathrm{CH_4}$, $\mathrm{C_2H_6}$, $\mathrm{C_3H_8}$, $\mathrm{C_4H_{10}}$, $\mathrm{C_2H_4}$, $\mathrm{N_2}$, $\mathrm{O_2}$, $\mathrm{CO_2}$, which are stated in volume percentage. The goal of fuel combustion is to totally burn and use the total fuel energy.

For calculation of minimal (theoretic) oxygen volume to combust $1\,\mathrm{m}^3$ of gas fuel the following relation is used:

$$O_{2,min} = 2 \cdot \frac{CH_4}{100} + \frac{7}{2} \cdot \frac{C_2H_6}{100} + 5 \cdot \frac{C_3H_8}{100} + \frac{13}{2} \cdot \frac{C_4H_{10}}{100} + 8 \cdot \frac{C_5H_{12}}{100} + ... - \frac{O_2}{100} \tag{9}$$

To determine combustion air or air enriched by oxygen the following equation applies:

$$L_{min} = \frac{O_{2,min}}{\frac{B}{100}} \tag{10}$$

B – oxygen in air.(%)

Actual volume of oxidizer is calculated as follows:

$$L_{sk} = mL_{min} \tag{11}$$

To assure total fuel combustion and in assumption, that not all fuel and oxidizer molecules will during the burning reaction meet and react, so-called excess combustion air should be used „m“.

Volume of individual combustions items is calculated according to following relations:

$$V_{CO_2} = \frac{CH_4}{100} + 2 \cdot \frac{C_2H_6}{100} + 3 \cdot \frac{C_3H_8}{100} + 4 \cdot \frac{C_4H_{10}}{100} + 5 \cdot \frac{C_5H_{12}}{100} + \frac{CO}{100} + \frac{CO_2}{100} + ... \tag{12}$$

$$V_{H_2O} = 2 \cdot \frac{CH_4}{100} + 3 \cdot \frac{C_2H_6}{100} + 7 \cdot \frac{C_3H_8}{100} + 8 \cdot \frac{C_4H_{10}}{100} + 6 \cdot \frac{C_5H_{12}}{100} + \frac{H_2}{100} + ... \tag{13}$$

$$V_{N_2} = \frac{N_2}{100} + \frac{100 - B}{100} \cdot m \cdot L_{min} \tag{14}$$

$$V_{O_2} = \frac{B}{100} \cdot (m-1) \cdot L_{min} \tag{15}$$

The total combustions volume is calculated as follows:

$$V_{sp} = C_{CO_2} + V_{H_2O} + V_{N_2} + V_{O_2} \tag{16}$$

Statics of combustion is used to determine the amount of flue gases resulting from the combustion of the mixed gas depending on the excess of combustion air to the furnace exit, also in the area before and after the heat exchanger disposed in the exhaust line of pusher furnaces.

2.2 Heat balance

Equivalence between items of input and output of heat in a furnaces describes heat balance equation. Thus heat input into the furnace is equal the heat output from furnace:
(Q_{ch}) heat input = heat output (Q_s)

$$Q_{ch} + Q_f(Q_r) + Q_{ex(end)} = Q_{uz} + Q_{ned} + Q_{osp} + Q_{spp} + Q_{vyz} + Q_{vys} + Q_{szb} + Q_{chv} \dots \tag{17}$$

Q_{ch} – chemical heat of fuel (W),
Q_f – physical heat of fuel and air (W), or heat recovered -(Qr) (W),
$Q_{ex(end)}$ – heat from the exothermic reactions, respectively heat needed for the endothermic reaction, (W),
Q_{uz} – useful heat (W),
Q_{ned} – heat loss of burnout (W),
Q_{osp} – heat loss of flue gasses (W),
Q_{spp} – heat loss of aggregate workspace (W),
Q_{vyz} – heat loss of radiation through doors and openings (W),
Q_{vys} – heat loss of spurt from the oven doors and openings (W),
Q_{chv} – heat loss of cooling water (W),
Q_{szb} – heat loss of missing the calculation (W).

Heat input into the sintering process

Chemical heat of mixed gas

$$Q_{chem} = V_{zmesplynov} \cdot Q_{n,zmesiplynu} \tag{18}$$

$V_{zmesplynov}$ – total volume of burned gas mixture (m^3/s),
$Q_{n,zmesiplynu}$ – calorific value of gas mixture (J/m^3).

Physical heat of oxidizer depends on heat and volume of required oxygen, which defined by combustion statics:

$$Q_{fyz_vz} = V_{vz} \cdot c_{p,vz} \cdot t_{vz} \tag{19}$$

V_{vz} – actual volume of the combustion air, as determined by determining the excess O2 in the flue exhaust,

$c_{p,vz}$ – specific heat capacity of air (J/(m^3 K)),
t_{vz} – air temperature (°C).

Heat from oxidation of Fe

$$Q_{ox(red)} = \frac{5,65 \cdot 10^6 \cdot m_k \cdot a}{100} \tag{20}$$

$5,65 \cdot 10^6$ – amount of heat released rfom oxidation of 1 kg Fe (J/kg) [4],
m_k – mass of the heating metal (kg/s),
a – burnout value (%).

Heat used in the heating slabs process

Heat losses through walls of furnaces

$$Q_{sten} = \alpha_{celk} \cdot \left(t_{povrchu} - t_{okolia}\right) \cdot S_{povrchu} \tag{21}$$

α_{celk} – overall coefficient of heat transfer from furnaceś surface into the surroundings (W/(m^2 K)),
$S_{povrchu}$ – heat exchange surface side of aggregate (m^2),
$t_{povrchu}$ – surface temperature, (°C),
t_{okolia} – ambient temperature, (°C).

Radiation heat loss from doors and openings

$$Q_{vyz} = 5.67 \cdot \left(\left(\frac{T_{pec}}{100}\right)^4 - \left(\frac{T_{ok}}{100}\right)^4\right) \cdot S \cdot \Phi \tag{22}$$

T_{pec} – furnace temperature, (K),
T_{ok} – ambient temperature (K),
S – surface area, (m^2)
Φ – coefficient of shield (-).

Heat loss beaten through doors and openings

$$Q_{vys} = V_0 \cdot i_p \tag{23}$$

V_0 – volume gas flow rate at standard conditions,
i_p – enthalpy of gases, (J/kg).

$$i = c_p \cdot t \tag{24}$$

Heat loss of burnout In case, if there are CO, H_2, or CH_4, in combustions:

$$Q_{ned} = V_{spal} \cdot \left(127 \cdot 10^3 \cdot CO + 107 \cdot 10^3 \cdot H_2 + 358 \cdot 10^3 \cdot CH_4\right) \tag{25}$$

$V_s pal$ – volume of flue gas generated during the sinter process (m^3 / h) determined from stoichiometry combustion process technology,
CO, H_2, CH_4 – content of carbon monoxide, hydrogen, methane in wet flue gas ; (obj.%).

Heat carried away by outgoing flue gases

Heat loss by outgoing combustions through duct system depends on temperature of combustions measured in the duct work.

$$Q_{odch,spal} = V_{spal} \cdot c_{p,spal} \cdot t_{spal} \tag{26}$$

V_{spal} – volume of flue gas generated during the sinter process (m^3 / h) determined from stoichiometry combustion process technology,
$c_{p,spa}$ – specific heat capacity of flue gas (J/(m^3 K)),
$tspal$ – flue gas temperature (in duct system), (°C).

Useful heat - charge heating

$$Q_{ohrev} = m_{vsad} \cdot \left(c_{p,i2} \cdot t_{i2} - c_{p,i1} \cdot t_{i1}\right) \tag{27}$$

m_{vsad} – the amount of charge at the entrance to the technological operations, (kg/s),
t_{i1} – initial temperature of the processing operations, (°C),
t_{liatia} – temperature at the end of the technological operations, (°C),
$c_{p,i1}$ – mean specific heat capacity of the charge at the beginning of the technological operations, (J/(kg K)),
$c_{p,i2}$ – mean specific heat capacity of the charge at the end of the technological operations, (J/(kg K)).

Heat loss of cooling water

$$Q_{chv} = m_v \cdot c_v \cdot (t_2 - t_1) \tag{28}$$

m_v – mass flow of the cooling water (kg/s),
c_v – water capacity (J/(kg K),
t_2 – the water temperature at the exit of the furnace (°C),
t_1 – the outlet temperature of cooling water to the furnace (°C).

2.3 Seting of energy (heat) balance of the recuperator

To assess the recuperator state and heat work of pusher furnace is necessary to elaborated the material and heat balance of the heat exchanger.
(Q_h) heat input = heat output (Q_s)

$$Q_{spal1} = Q_{vz} + Q_{spal2} + Q_{st} \tag{29}$$

Q_{spal1} – heat transmitted by flue gases in front of recuperator (W),
Q_{vz} – change in the heat content of the air in the recuperator (W),
Q_{spal2} – heat carried away in the flue gas heat recovery (W),
Q_{st} – heat loss to the surrounding areas of recuperator (W).

Heat input

Heat carried away by outgoing flue gases from pusner furnace The heat transferred of flue gases to the heat exchanger is dependent on the flue gas temperature measured with thermocouple in front of the heat exchanger and the oxygen content in the flue gas O_2, which set the excess combustion air in front of the heat exchanger.

$$Q_{spal1} = V_{spal} \cdot c_{p,spal} \cdot t_{spal1} \tag{30}$$

V_{spal} – flue gas volume in front of the recuperator in the process of heating slab (m^3 / s) seting by the stoichiometry of the combustion and from the process technology,
$c_{p,spal}$ – mean specific heat capacity of the flue gases(J/(m^3 K)),
t_{spal1} – flue gases temperature in front of recuperator, (°C).

Heat output

Changing the heat content of the air in the recuperator

$$Q_{vz} = V_{vz} \cdot \left(c_{p,vz} \cdot t_{vz} - c_{p,vzo} \cdot t_{vzo}\right) \tag{31}$$

V_{vz} – volumetric flow rate of combustion air to the heat exchanger (m^3/s),
$c_{p,vz}$, $c_{p,vzo}$ – mean specific heat capacity of air at the outlet respectively inlet air temperature of the recuperator (J/(^{3} K)),
t_{vz}, t_{vz} – output respectively inlet air temperature in the recuperator (°C).

Heat carried away by outgoing flue gases from recuperator The heat carried away by outgoing flue gases from the heat exchanger is dependent on the flue gas temperature measured with thermocouple for heat recovery and gas oxygen content O_2 heat exchanger, which set the excess combustion air beyond the heat exchanger.

$$Q_{spal2} = V_{spal2} \cdot c_{p,spal} \cdot t_{spal2} \tag{32}$$

V_{spal2} – flue gas volume in front of the recuperator in the process of heating slab (m^3/s) seting by the stoichiometry of the combustion and from the process technology,
$c_{p,spal}$ – mean specific heat capacity of the flue gases (J/(m^3 K)),
t_{spal2} – flue gases temperature in front of recuperator, (°C).

Heat loss to the surrounding areas Q_{st} of heat exchanger can be neglected.

3 The inputs for modeling of the waste flue gases use from push furnaces

Based on the heat balance of the furnace and the heat exchanger was determined item of heat otgoing flue gases after recovery. The temperature of the flue gases after recovery is approximately 487 °C and heat is 50,5 MW. These values serve as the basis for their use.

In a first step move to a theoretical design of the heat exchanger flue gases - water, the water serves as a heat transfer medium to the Kalina cycle. The following table shows the amounts of heat that can be used, depending on the efficiency of the exchanger and the flue gas temperature leaving the exchanger to a stack.

Table 1: The amount of useful heat, depending on the efficiency of the heat exchanger and flue gas temperature beyond the heat exchanger in MW.

t_{osp} (°C)	efficiency				
	0,4	0,5	0,6	0,7	0,8
200	12,07815	15,09769	18,11723	21,13677	24,15631
210	11,66072	14,5759	17,49108	20,40626	23,32144
220	11,24214	14,05267	16,86321	19,67374	22,48428
230	10,81582	13,51978	16,22373	18,92769	21,63165
240	10,39466	12,99333	15,592	18,19066	20,78933
250	9,972359	12,46545	14,95854	17,45163	19,94472

Theoretical expected amount of useful heat in Kalina cycle is of about 16 MW. This amount will be affected by the inlet and outlet water conditions.

4 Kalina cycle

The Kalina Cycle is a power cycle technology based on the superior thermodynamic properties of mixtures. Binary geothermal power generation includes utilizing the heat from liquid dominated geothermal resources to produce power more efficiently than ever before, [5].

The cycle is “saturated” because there is no superheat in the cycle. The fluid is not boiled entirely in the vaporizer, and the vapour-liquid mixture is then separated afterwards. This is done in order to maximise the vapour temperature at the vaporizer outlet, [6].

The heated fluid at the station s1 enters the heat vaporizer. The fluid is then cooled down in the vaporizer, and leaves it at the station s2, [6].

Pre-heated (in the regenerators) liquid ammonia-water mixture enters the vaporizer at station 3. The fluid is boiled partly in the vaporizer. The liquid-vapour mixture leaves the vaporizer at station 4, and enters the separator, [6].

The separated liquid leaves the separator and enters the high temperature regenerator at station 7. After the high temperature regenerator the liquid is throttled down to the condenser pressure in station 8, and mixed with the turbine exit vapour from station 6, [6].

Saturated vapour of ammonia-vapour mixture consisting in the 95% of ammonia, [5].

The ammonia-rich vapour enters the turbine at station 5, and is expanded to the condenser pressure at station 6. The exit vapour mixed with the throttled liquid (now at the average ammonia concentration) from the high temperature regenerator enters the low temperature regenerator at station 9, [6].

The cooled fluid from the low temperature regenerator enters the condenser at station 10. The fluid gas now started to condense, and the ammonia concentration is not the same in the liquid or vapour phase. An absorption process is going on, where the ammonia rich

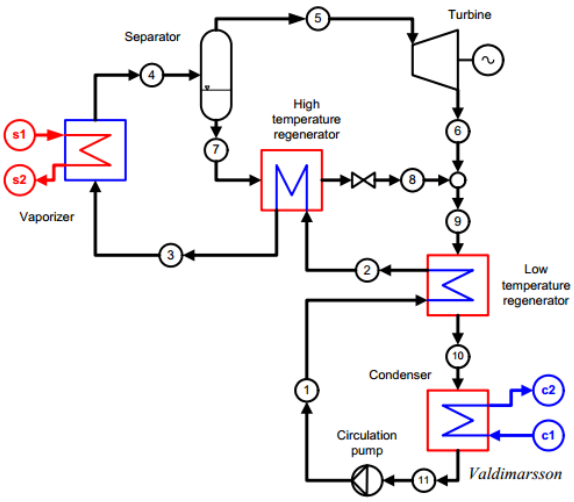

Figure 1: Flow diagram of a saturated Kalina cycle, [6].

vapour is absorbed into the leaner liquid, in addition to condensation due to lowering of the mixture temperature. The kinetics of the absorption process determines the rate of absorption, whereas heat transfer and heat capacity controls the condensation process, [6].

Finally all the mixture is in saturated liquid phase in the hot well of the condenser at station 11. The circulation pump raises the fluid pressure up to the higher system pressure level, and the liquid is then preheated in the regenerators in stations 1 through 3. The condenser shown here is water cooled, with the cooling water entering the condenser at station c1 and leaving at station c2, [6].

4.1 Modeling of Kalina cycle

Figure 2 shows the schema of the Kalina cycle. The cycle uses the waste heat from the push furnace in the form of the exhaust gases . At the exit of the push furnace the exhaust gases enter the heat exchangers and it heats up the water witch at the point A enters the evaporator of the Kalina cycle. The thermal power output is 16MWt. After the evaporator the water gets into the pre-heater and due to the pump (point C) it is pushed back to the cycle.

The Figure 3 shows the binary Kalina cycle with all calculated data. The outdoor temperature is an important temperature influencing most of the parameter in the power plant. In this case the sample temperature has been choose as 9,5 °C, because it is the annual average outdoor temperature in Slovakia.

With the increasing outdoor temperature the power output of the power plant will decrease. The inlet turbine pressure P7 was calculated as 28 bar, the turbine efficiency has been determinate as 85% and pump efficiency as 70%. Total mass flow of the ammonia water mixture has been calculated as 20,31 kg/s. The mass flow after the separator mostly consist of ammonia vapour and its total mass flow amount is 16,25kg/s.

The power output in this case has been calculated as 1,6 MWe. The Figure 4 and Figure 5 show how power output will change its value with the changing inlet turbine pressure and

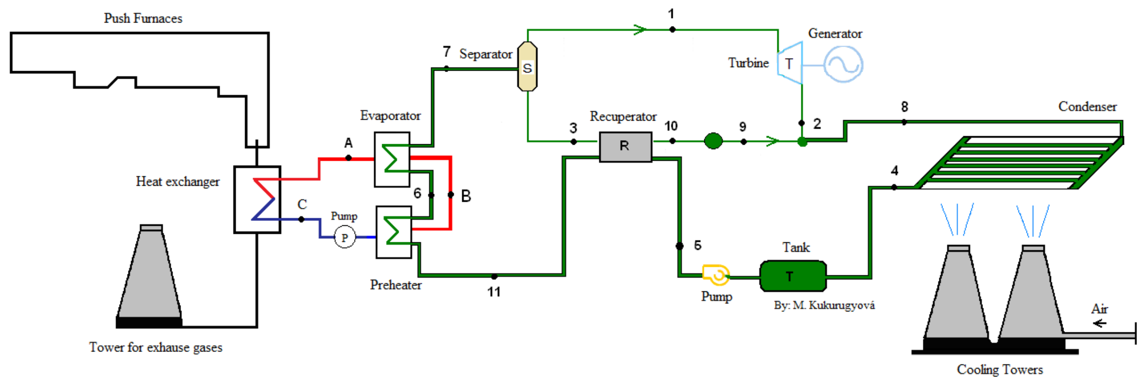

Figure 2: Schema of the Kalina cycle with push furnance.

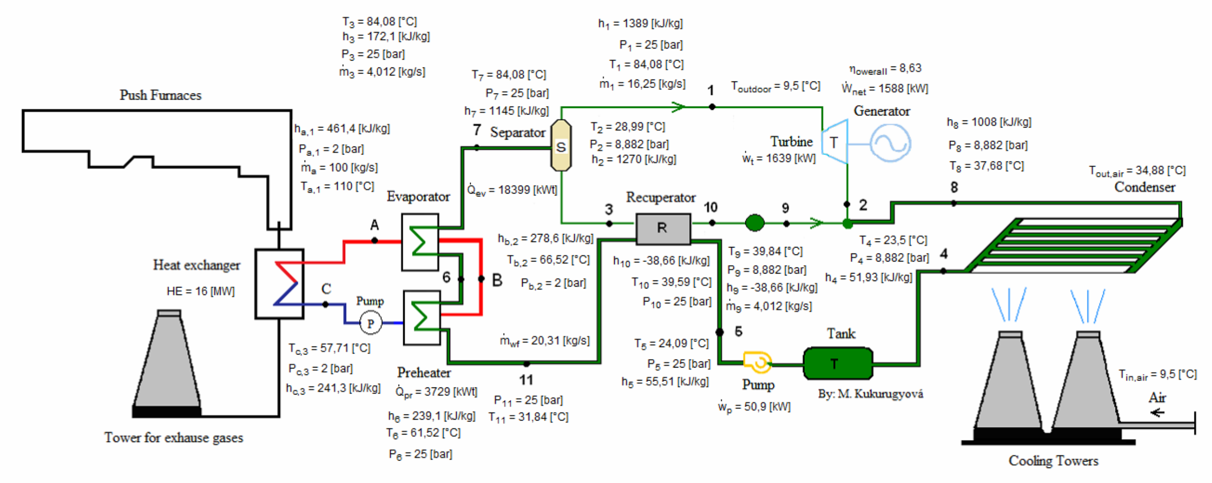

Figure 3: Kalina power plant with the output data.

outdoor temperature from -13 to 35 °C.

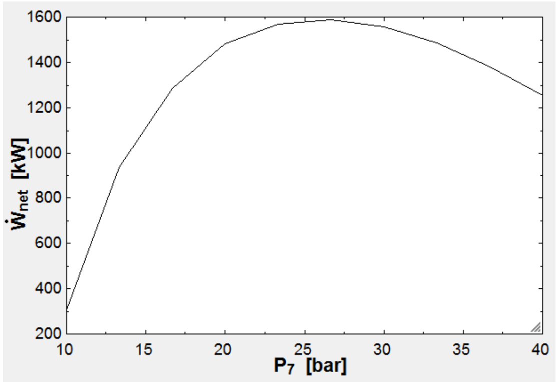

Figure 4: Power Output vs. Inlet Turbine Pressure.

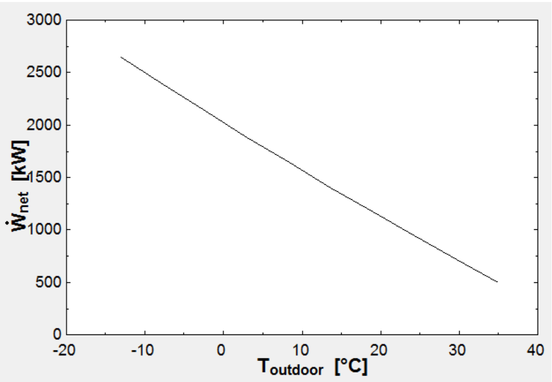

Figure 5: Power output vs. Outdoor Temperature.

5 Conclusion

Energy policy of every state in the Union is based on energy efficiency.

In many cases of the industrial sector is the significant amount of energy contained in the combustion products (same for push furnaces), where the waste heat is not anymore possible to use for any technological process. The use of exhaust energy for electricity and heat production is emerging as one of the options in increased overall efficiency.

Therefore the authors of this article strongly recommend in every possible cases use the waste heat from the combustion processes in binary cycles for the electricity production. In this case the Kalina cycle generate electricity of 1,6MWe from the 16MWt.

Acknowledgements

This publication was supported by the project VEGA 1/0252/13 and obtained results are part of the solution from this grant project.

References

[1] Tatič, M.: *Industrial furnaces I.* ISBN: 9788055302546. Košice: HF TU, 2009, page 225.

[2] Varga, A. et al.: *Thermal technology for metallurgists.* ISBN: 978-80-553-1590-4. Košice, 2013, page 280.

[3] Varga, A. and collective: *Optimisation of the combustion process NP, Final report.* Technical report. Košice: TUKE, Department of furnaces and thermal technology, 2015.

[4] Komorová, Ľ. and Imriš, I.: *Thermodynamic in metallurgy.* Bratislava, 1990.

[5] Mazurek, R.: “Modeling and Thermo-Economic Analysis of the Municipal CHP Station(PEC) in Stargard Szczecinski in Poland”. Master’s thesis. RES. Akureyri, 2011.

[6] Valdimarsson, P.: “Geothermal Power Plant Cycles and main components”. In: *Short Course on Geothermal Drilling, Resource Development and Power Plants.* Reykjavik, Iceland: University of Iceland, 2011.

Study of hydriding kinetics in Mg-Ni-MM alloys using GDS

V. Knotek, D. Vojtěch
Institute of Chemical Technology Prague
Department of Metals and Corrosion Engineering, Technická 5, 166 28 Prague 6, Czech Republic

Abstract

The main task for using hydrogen as energy carrier is to develop its safe and efficient storage. Storing hydrogen in the form of light metals hydrides seems to be very prospective. Magnesium alloys, as efficient hydrogen storage materials, have attracted great attentions recently. Magnesium shows excellent hydrogen storage capacity, but suffers from insufficient kinetics and thermodynamics. By empirical works, it was find out that some metal elements such Ni or rare earths could enhance magnesium properties. To obtain the best results it is necessary to understand the mechanism of catalytic function of some elements to hydriding process. Therefore in this study, we tried to evaluate the influence of alloying metal on the ability of magnesium alloy to absorb hydrogen.

Three binary Mg-Ni, one binary Mg-MM (MM = mischmetal containing Ce, La, Nd and Pr) and one Mg-Ni-MM alloys were hydrided by an electrochemical process. The amount of absorbed hydrogen as hydrogen profiles of alloys were determined by glow discharge spectrometry (GDS). The structures and phase compositions of the alloys both before and after hydriding were studied by optical and scanning electron microscopy, energy dispersive spectrometry and X-ray diffraction. Based on measured data the mechanism of catalytic effect of Ni and MM on hydriding of Mg-based alloys was suggested.

Keywords: electrochemical hydriding; glow discharge spectrometer; magnesium; nickel; rare earths

1 Introduction

Recently, hydrogen has been considered to be a promising energy carrier for use in various applications, for example in automotive industry. There can serve as an ideal fuel, because after burning of hydrogen or converting the chemical energy of hydrogen in the fuel cell, no harmful emissions are released. The main task still limiting the exploiting of hydrogen economy is hydrogen storage.

Storing hydrogen in the form of metallic hydrides seems to be promising due to the advantageous properties such as stability, safeness and easy handling. Magnesium-based hydrides have been taken great efforts in last two decades because magnesium is light, relatively inexpensive and capable to absorb up to 7.6 wt.% of hydrogen in the form of MgH_2. However, pure magnesium suffers from poor thermodynamics and slow kinetics of both hydrogenation and dehydrogenation. MgH_2 desorbs hydrogen very slowly if the temperature is below 573 K [1]. After the hydride layer is formed, MgH_2 prevents further diffusion of hydrogen into the material. Therefore the formation of MgH_2 is practically impossible in the bulk of pure magnesium [2]. Many efforts have been made to improve the hydrogenation characteristics of magnesium, including alloying with appropriate elements (Ni, Co, Al, Cu, La, Ce, Nd) [3–6], addition of transition metals oxides [7], mechanical alloying (MA) [8], preparing fine nanocrystalline or amorphous structure [9] and others.

For the preparation of metallic hydrides, we can use either a gas hydriding or an electrochemical hydriding process. Electrochemical hydriding is beneficial because it generates atomic hydrogen, which can easily penetrate the structure and form hydrides. Another benefit is its mild hydriding conditions. A one drawback of electrochemical hydiriding method is lower concentration absorbed hydrogen.

The main task to prepare alloys with superior kinetics to hydrogen absorption represents the understanding of hydriding mechanism. Unfortunately, the hydriding mechanism of Mg-based alloys and catalytic effect of some metals are still unknown. Therefore, in this work, we employed glow discharge spectrometer to study absorbed hydrogen after electrochemical hydriding. This unique method of hydrogen analysis allowed us to study the hydriding kinetics and the influence of alloying elements on absorption of hydrogen by Mg-based alloys. Based on the results, the hydriding mechanism of Mg-based alloys could be suggested.

2 Experiment

Three binary Mg-Ni alloys, one binary Mg-MM alloy (MM denotes mischmetal containing 45 % Ce, 38 % La, 12 % Nd, and 4 % Pr) and one ternary Mg-Ni-MM alloy, see Table 1, were investigated. Cylindrical ingots of alloys of 100 mm in length and 30 mm in diameter were prepared by pouring the melt into a brass mould. The ingots were cut to thin samples of 0.5 mm in thickness. Surface of samples was treated by grinding on P180-P2500 abrasive papers before electrochemical hydriding tests. Pre-treated samples were immediately put in electrochemically hydrididing cell.

Table 1: Chemical composition of hydrided magnesium alloys.

Alloy	**Element (wt. %)**		**Alloy**	**Element (wt. %)**	
	Ni	Mm		Ni	Mm
MgMM15	-	14.9	MgNi34	34.2	-
MgNi15	14.8	-	MgNi26MM12	25.6	12.0
MgNi26	26.4	-			

Samples of alloys for electrochemical hydriding were connected to a DC source as a cathode. The platinum electrod was placed opposite to the hydriding side of sample and used as anode. Electrochemical hydriding was carried out in 6 mol/l KOH solution at 80 °C. The current density was maintained at 100 A/m^2. Hydriding time was 480 min.

Hydrogen concentration profile in hydrided alloys was determined by glow discharge spectrometer (Horiba Jobin-Yvon, GD Profiler 2 (GDS)). Due to the fact that hydriding was performed in a strongly alkaline bath, formation of magnesium hydroxide and/or complex hydroxide surface layers could be expected. In order to minimize the influence of such layers on results of hydrogen profile analysis, oxygen was also analyzed to determine the exact position of hydroxide/metal interface. The GDS analyzer was calibrated with respect to MgH_2. Sputtering rate was determined by measurement of surface profile after analysis. The structures of the as-cast alloys were observed by light microscopy (LM), scanning electron microscopy (SEM, TESCAN Vega 3) and energy-dispersive spectrometry (EDS, OXFORD INSTRUMENT Inca 350). The phase compositions of the alloys both before and after hydriding were determined by X-ray diffraction (XRD, X Pert Pro, Cu Kα radiation).

3 Results and discussion

3.1 Structures of alloys

Icrostructures of the alloys are presented in Figure 1. The Mg-Ni alloys represent a typical eutectic system [10]. Hypoeutectic alloy such as MgNi15 (Figure 1a), consist of α-Mg dendrites (light) and α-Mg + Mg_2Ni eutectic mixture (dark). The MgNi26 alloy is close to the eutectic point (23,5 % Ni), and therefore, its structure is dominated by the α-Mg + Mg_2Ni eutectic mixture (Figure 1b). The MgNi34 (Figure 1c) alloy is hypereutectic and contain sharp-edged primary Mg_2Ni crystals (light) and an α-Mg + Mg_2Ni eutectic mixture (dark). The binary MgMM15 alloy also corresponds to a eutectic system, and its structure is very similar to MgNi15. The difference is in the composition of eutectic mixture, which is formed by α-Mg + Mg12MM eutectic mixture. The $Mg_{12}MM$ phase is a solid solution of isostructural $Mg_{12}Ce$, $Mg_{12}La$, $Mg_{12}Nd$ and $Mg_{12}Pr$ phases (space group I4/mmm) [10]. The MgNi26MM12 alloy is hypereutectic (Figure 1d), and it consists of primary Mg_2Ni crystals (light) and a ternary α-Mg+Mg_2Ni+$Mg_{12}Mm$ eutectic mixture (dark).

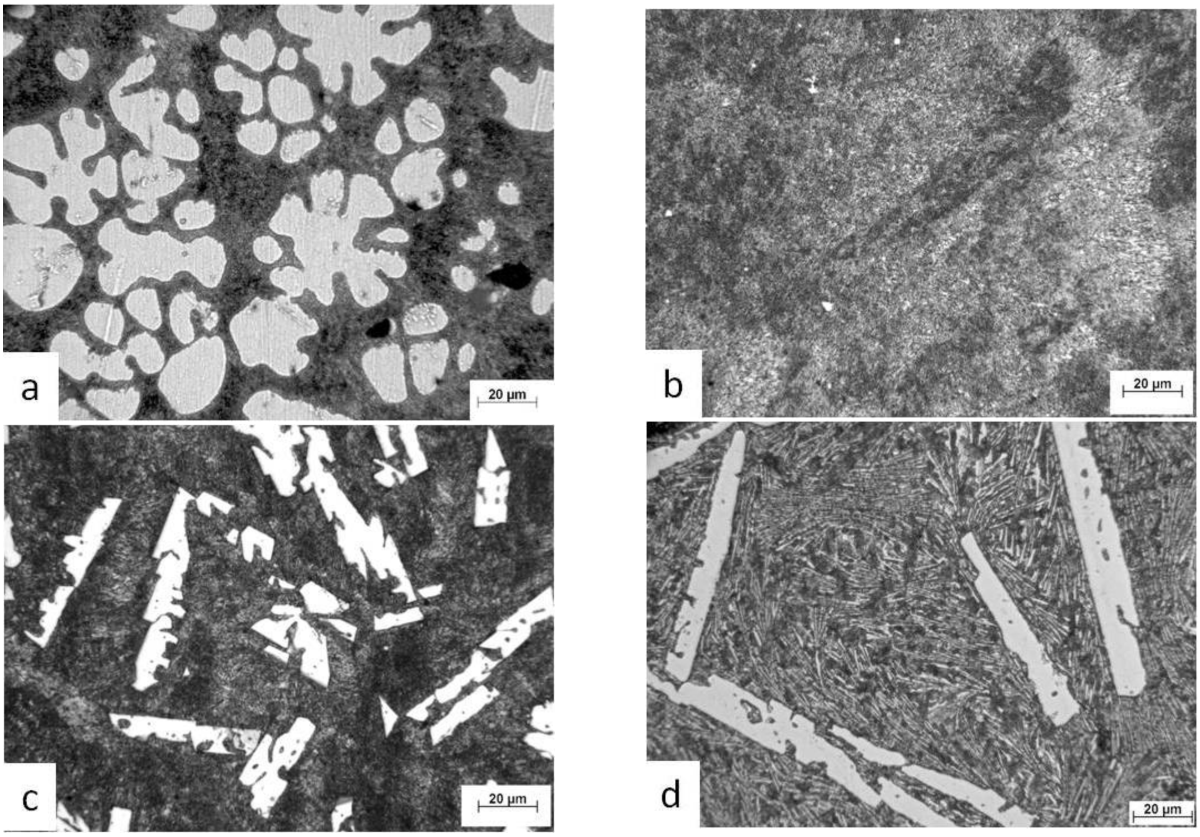

Figure 1: Microstructure of investigated alloys (LM) a) MgNi15, b) MgNi26, c) MgNi34, d) MgNi26MM12.

It is observed that in all investigated binary and ternary alloys, there are relatively significant volume fractions of eutectic structures. These structures are very fine. It means there is a high area of phase boundaries which represent efficient paths for hydrogen diffusion in materials.

3.2 Hydrogen concentration profiles

After GDS hydrogen analyzes we obtain hydrogen profile for each alloy. For investigated alloys, these hydrogen profiles are illustrated in Figure 2. In each profile, it can be determine two hydriding parameters, maximum surface concentration and penetration depth of hydrogen. Each profile can be also integrated to obtain the total amount of absorbed hydrogen. All hydriding parameters are summarized in Table 2.

One can see that the binary MgMM15 alloy reached the worst combination of hydriding parameters. The MgMM15 alloy absorbed minimal amount of hydrogen. In the case of the MgNi15 alloy the value of hydrogen surface concentration is the same, but depth of hydrogen penetration is explicitly higher, so the amount of absorbed hydrogen is higher. Therefore it can be assumed that Ni is more important element than Mm for electrochem-

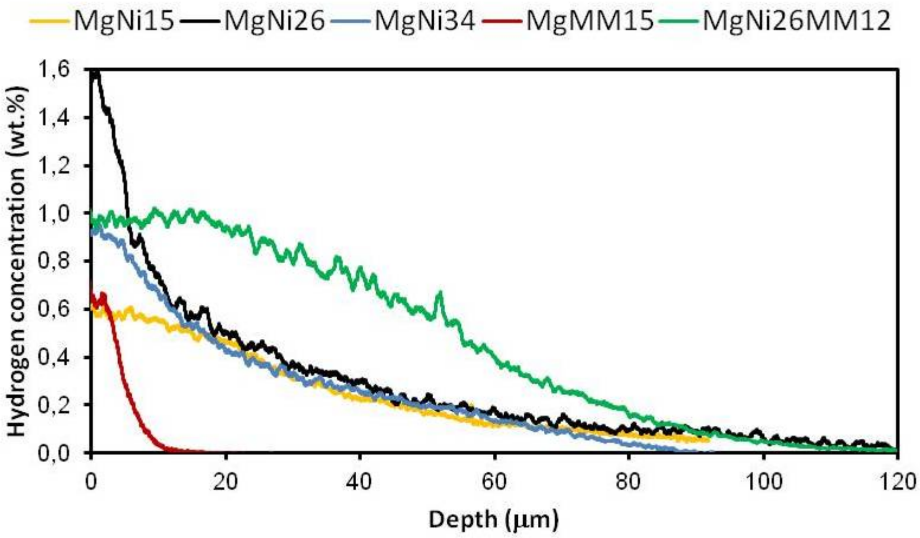

Figure 2: Hydrogen concentration profiles of investigated alloys after electrochemical hydriding (GDS).

ical hydriding.

Table 2: Hydriding parameters such as the maximum hydrogen concentrations on the alloy surface (C_{max}), the hydrogen penetration depths (X) and the total masses of hydrogen absorbed in the alloys (m) after electrochemical hydriding are listed.

alloy	C_{max} (wt.%)	X (µm)	m (µg)	alloy	C_{max} (wt.%)	X(µm)	m(µg)
MgNi15	0.6	90	74	MgMM15	0.6	12	13
MgNi26	1.6	120	170	MgNi26MM12	1.0	120	280
MgNi34	0.9	90	124				

The maximum value of hydrogen surface concentration is obtained for the Mg-26Ni alloy, the structure of which is eutectic (Figure 1b). When either primary α-Mg or primary Mg_2Ni form in the structure (Figure 1), all the hydriding parameters decrease. We believe that the higher volume fraction of eutectic is present at the structure of alloy, the better hydriding parameters are obtained. The eutectic structure is characterized by large volume fraction of interfaces where atomic hydrogen could proceeds faster than in primary dendrities. However, the MgNi26MM12 alloy is hypereutectic and the total mass of hydrogen absorbed in this alloy is much higher than for the MgNi26 alloy. This observation could be explained by the faster decreasing of H-concentration towards the alloy interior in the case of MgNi26 alloy (Figure 2), while the ternary alloy with mishmetal behaves in different manner - the maximum surface hydrogen concentration (C_{max}) is the same in the depth of 20 µm and then starts gradually decrease. Both nickel and mishmetal addition into magnesium supports the hydrogen absorption, but in different way. Nickel maximizes the maximum hydrogen concentration on the surface; therefore it probably supports hydrogen formation. The presence of mischmetal evidently decreases C_{max} parameter. On the other hand, Mm probably support inward hydrogen diffusion, while does not participate in formation of hydrides (lower maximum surface concentration).

3.3 Phase composition after hydriding

After electrochemical hydriding of investigated alloys the XRD analyses were carried out. In Figure 3, there is XRD patterns of the MgNi26 and MgNi26MM12 alloys after electrochemical hydriding. Figure 3 shows that the main hydriding product of the MgNi26 and MgNi26MM12 alloys is the MgH_2. The MgH_2 hydride was also detected in all other investigated alloys. It is surprising that no ternary or more complex hydrides, such as MmH_3, Mg_2NiH_4 and other which are often detected after hydriding in gaseous hydrogen at high temperatures and pressures, were found. This phenomenon could be explained by following hydriding mechanism. When atomic hydrogen is produced by electrochemical decomposition of water, it enters the cathode. Then hydrogen reacts with Mg phase to produce a layer of MgH_2. Such a layer would prevent hydrogen from further diffusion into cathode material. For this reason, it is likely that hydrogen also diffuses along interphase boundaries in the eutectic. Since Mg_2Ni and $Mg_{12}MM$ phases work as a catalysts and as mediums for fast exchange of hydrogen and dominate in the eutectic, presence of eutectic playing key role in to achieving deep penetration of hydrogen into the material and high hydrogen gravimetric densities. Since both Mg_2Ni and Mg_2NiH_x have hexagonal crystal lattice, these phases are not distinguishable in the XRD patterns in Figure 3.

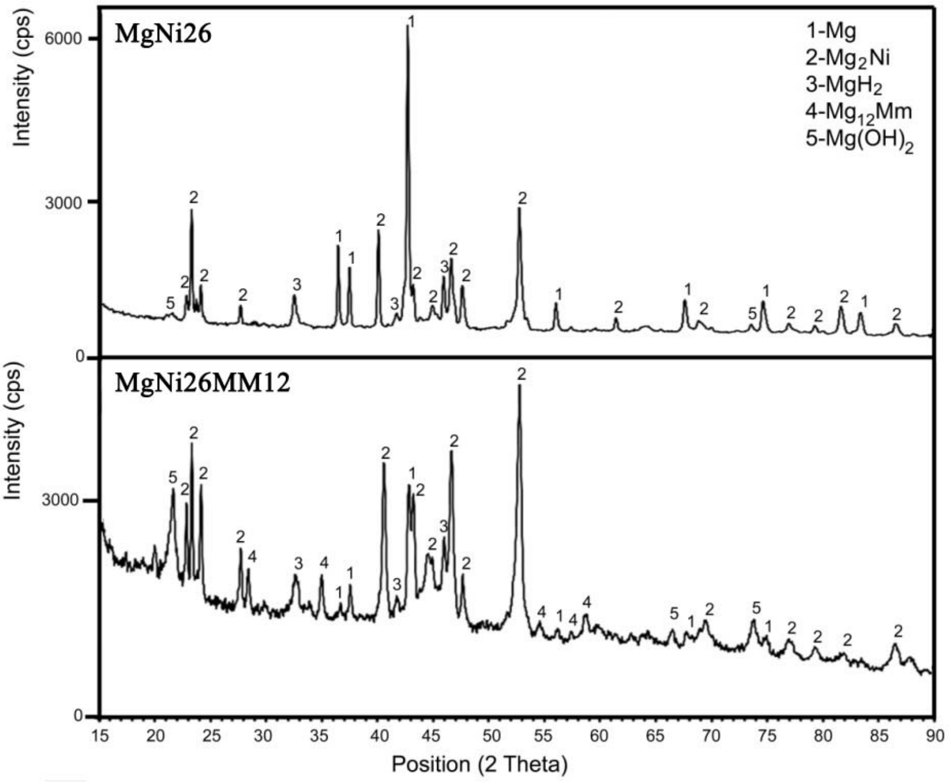

Figure 3: XRD patterns for the MgNi26 and MgNi26MM12 alloys after electrochemical hydriding.

4 Conclusions

The results of this work show that GD spectrometr is useful instrument to study an electrochemical hydriding process of Mg-based alloys. The influence of nickel and mischmetal on the hydriding kinetics in Mg-based alloys was described by this way. It is demonstrated that addition of Ni supports hydriding more than mischmetal in the case of binary alloys. In terms of hydrogen surface concentration, the best hydriding performance is observed for the MgNi26 alloy with a purely eutectic structure. Therefore we assume that presence of fine eutectic structure plays key role of electrochemical hydriding process. But in terms of total amount of absorbed hydrogen the ternary MgNi26MM12 alloys showed the best hydriding performance, although it has hypereutectic structure. The reason consists in the ability of MM to boost up a hydrogen diffusion inward material. In contrast to high-temperature and high-pressure hydriding processes, the only hydride formed during electrochemical hydriding was MgH_2.

Acknowledgements

Research on materials for hydrogen storage is financially supported by the Czech Science Foundation (project no. P108/12/G043).

References

[1] Denys, R. V. et al.: “New Mg–Mn–Ni alloys as efficient hydrogen storage materials”. In: *Intermetallics* 18.8 (2010), pages 1579–1585.

[2] Niemann, M. U. et al.: “Nanomaterials for Hydrogen Storage Applications: A Review”. In: *Journal of Nanomaterials* 2008 (2008), pages 1–9.

[3] Vegge, T. et al.: “Trends in hydride formation energies for magnesium-3d transition metal alloys”. In: *Journal of Alloys and Compounds* 386.1—2 (2005), pages 1–7.

[4] Sato, T., Blomqvist, H., and Noréus, D.: “Attempts to improve Mg2Ni hydrogen storage by aluminium addition”. In: *Journal of Alloys and Compounds* 356—357 (2003), pages 494–496.

[5] Tran, N. E., Imam, M. A., and Feng, C. R.: “Evaluation of hydrogen storage characteristics of magnesium–misch metal alloys”. In: *Journal of Alloys and Compounds* 359.1—2 (2003), pages 225–229.

[6] Wu, Y. et al.: “Microstructure and novel hydrogen storage properties of melt-spun Mg–Ni–Mm alloys”. In: *Journal of Alloys and Compounds* 477.1-–2 (2009), pages 262–266.

[7] Song, M.-Y. et al.: “Improvement of hydrogen-storage properties of Mg by reactive mechanical grinding with Fe2O3 prepared by spray conversion”. In: *Journal of Alloys and Compounds* 398.1-–2 (2005), pages 283–288.

[8] Au, M.: “Hydrogen storage properties of magnesium based nanostructured composite materials”. In: *Materials Science and Engineering: B* 117.1 (2005), pages 37–44.

[9] Lenain, C., Aymard, L., and Tarascon, J. M.: “Electrochemical properties of Mg2Ni and Mg2Ni2 prepared by mechanical alloying”. In: *Journal of Solid State Electrochemistry* 2.5 (1998), pages 285–290.

[10] Gale, W. F. and Totemeier, T. C.: *Smithells Metals Reference Book*. 8th edition. Amsterdam: Elsevier, 2004.

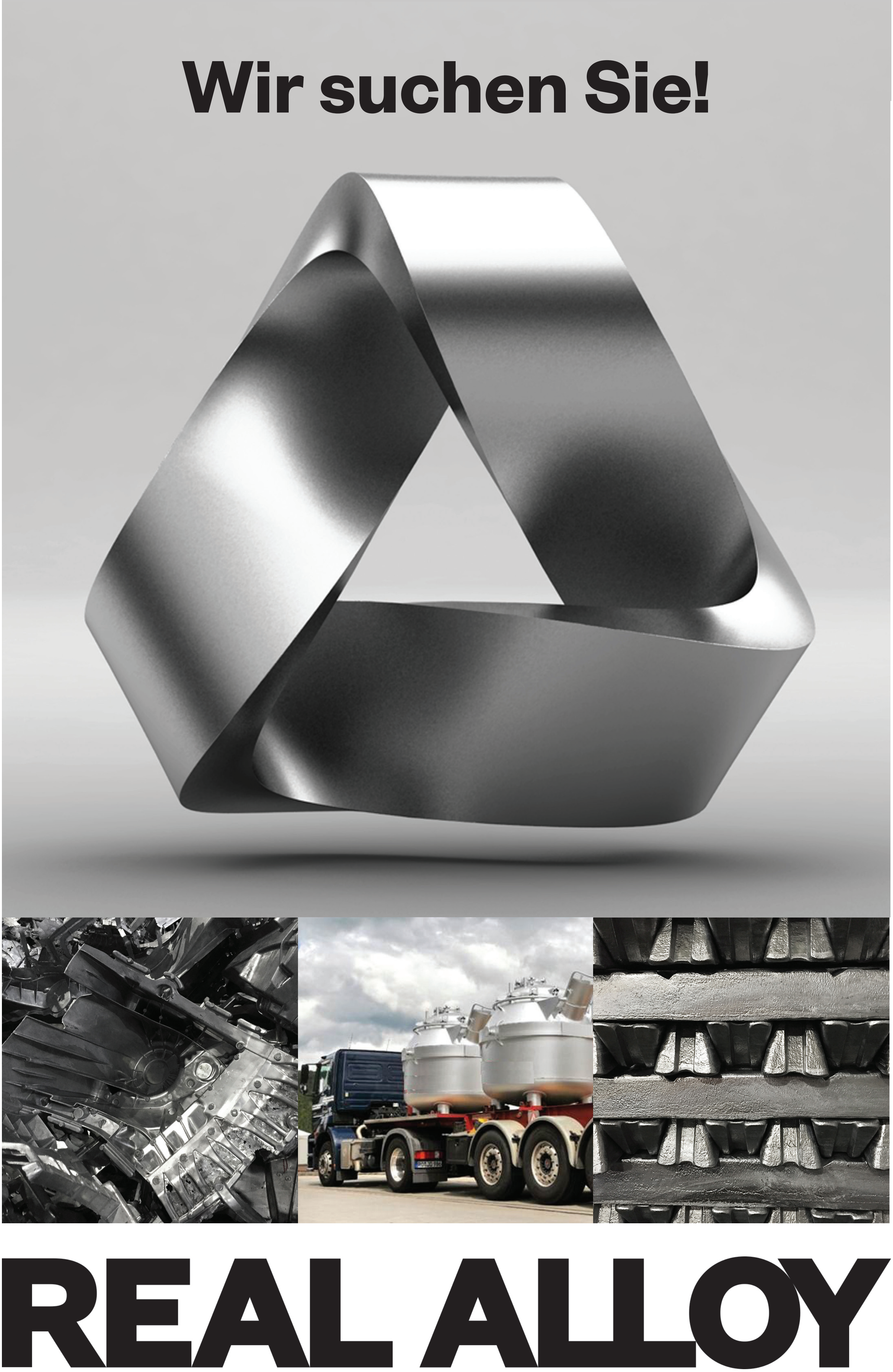
Wir suchen Sie!
REAL ALLOY

Hot blast stoves and non-premixed flame CFD modeling

Ing. Mario Machů; doc. Ing. Zuzana Klečková, Csc.
VŠB – Technical University of Ostrava
Faculty of Metallurgy and Thermal Engineering, Department of Thermal Engineering,
17. listopadu 15, 708 33 Ostrava - Poruba

Abstract

Burning processes involves many processes which are difficult to describe and to solve even more. Analytical solution of some equations describing the problem can be limited by extremely simplified boundary conditions, for example Navier-Stokes equations. Here comes the computational methods, in last decades represented mainly by CFD (Computer Fluid Dynamics) software (Ansys-Fluent, Ansys-CFX, Comsol Multiphysics, etc.) based on finite element method. Paper presents brief summary of used physics and results obtained for blast oven gas burned in hot blast stove.

Keywords: computer fluid dynamics, non- premixed flame, hot blast stove

1 Introduction

Increasing of energy consumption by mankind and hence related pollution led to concern about enviroment, which is represented by more or less strict law against pollution. As for air protection most relevant pollutants are dust, nitrogen oxides, carbon monoxide, volatile organic compounds, freons, etc.

Metallurgical enterprises very often works with „closed cycle" - from coke production and iron ore treatment through iron and steelmaking to products made by foundry or forging division. Waste/process gases from blast furnace and coke production can be utilised in powerplant boilers and replace coal or natural gas. More classic usage of those gases represents using them in technology itself for heating of hot blast air in stoves, re-heating slabs before forging operation in walking-beam furnaces, etc.

2 Hot blast stoves

Hot blast stoves (HBS, also known as cowpers, see Figure 1, Figure 2) are auxiliary installations in metallurgical plants being used to preheat the air for the blast furnace process. There are usually three or four (historically) of them designated to one blast furnace. Classic design represent those with internal or external combustion chamber. They consist of two shafts, one serves as combustion chamber, another one works as an regenerator and is filled by ceramic chequers. Modern design with one shaft – dome combustion hot blast stove – were developed for huge blast furnaces with high volume.

Process consists of two main periods separated by changeover periods. In the heating period the stoves are heated up by burning gases (until the dome reaches the desired process) temperature [1].

The dome temperature represents an important control parameter. It strongly influences the hot blast temperature. Increasing of hot blast temperature allows using less coke for reduction in blast oven and reduce the operational cost, similarly to injecting of oil ar blowing pulverized fuel as aditives. Those improvements of blast furnace operation leads to lower calorific values of blast oven gas, which sometimes has to be enriched, mostly by mixing with coke oven gas.

Increasing of the hot blast temperatures up to 1350°C, which becomes common in comparison with old generation of HBS operating with temperatures around 1050°C requires higher combustion temperatures. This can be obtained by using of enriched gas, decreasing of air excess ratio or by preheating of combustion air or even the gas itself in recuperator. Higher combustion temperatures requires using of high quality refractory materials and posiibly can lead to production of NO_x, which is unpleasant to environment.

The combustion starts in a ceramic burner at the bottom of the burning shaft. The flue gas streams upwards through the burning shaft and later through the dome into the regenerator shaft. The flue gas outlet is situated at the bottom of the regenerator shaft. The shaft interior contains refractory brickwork equipped with vertical gas channels. The refractories contact with the flue gas and store the gas heat which is used for the preheating of cold air in the blast period.

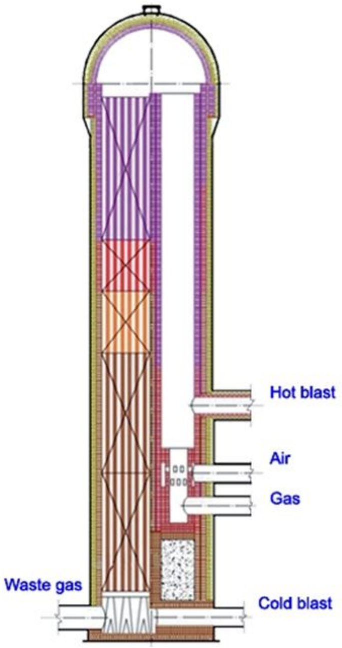

Figure 1: HBS with internal combustion chamber [2].

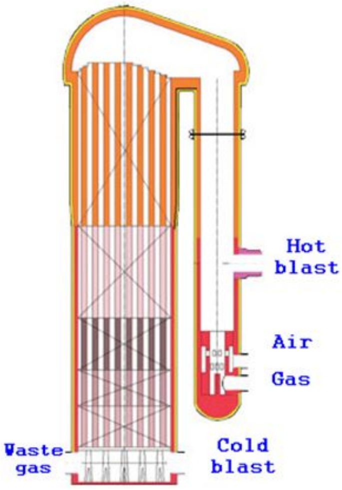

Figure 2: HBS with external combustion chamber [2].

Concern about NO_x production leads to improving burners configuration. Nitrogen oxides formation can be described by three mechanisms as thermal NO_x, fuel NO_x and prompt NO_x. Here in HBS we can expect vast majority of thermal NO_x, so cumputation model does not include equations for fuel a and prompt NO_x. Estimation of NO_x amount created during combustion is not easy, it depends on variables like temperature, concentration of reactants, residual time in reaction zone.

Modern software allows us to make some predictions which are more or less accurate. In fact more than accurate prediction they provide information about trends in dependance on changing conditions. In first step, it is recomended to make a model of combustion without pollutant creation which gives us temperature field and concentration of reactants in studied area and then step further and involve pollutant production [3].

3 Modelling of non-premixed flame

In non-premixed combustion, fuel and oxidizer enter the reaction zone in distinct streams. Non-premixed flames are used in industry very often due to safety reasons.

Governing laws for this case are laws of conservation: mass, energy and momentum conservation.

The equation for conservation of mass (continuity equation), can be written as follows:

$$\frac{\partial \rho}{\partial t} + \nabla \cdot (\rho \vec{v}) = S_m \tag{1}$$

where:
ρ – density ($\mathrm{kg\,m^{-3}}$),
t – time (s),
v – velocity ($\mathrm{m\,s^{-1}}$),
S_m – mass source ($\mathrm{kg\,m^{-3}\,s^{-1}}$).

Conservation of momentum (Navier-Stokes equation):

$$\frac{\partial}{\partial t}(\rho \vec{v}) + \nabla \cdot (\rho \vec{v} \vec{v}) = -\nabla p + \nabla \cdot \bar{\bar{\tau}} + \rho \vec{g} + \vec{F} \tag{2}$$

where:
p – pressure (Pa),
τ – stress tensor (Pa),
g – gravitational vector ($\mathrm{m^2\,s^{-1}}$),
F – external body force (N).

Conservation of energy:

$$\frac{\partial}{\partial t}(\rho E) + \nabla \cdot (\vec{v}(\rho E + p)) = \nabla \cdot \left(k_{eff} \nabla T - \sum_j h_j \vec{j}_j + \left(\bar{\bar{\tau}}_{eff} \cdot \vec{v} \right) \right) + S_h \tag{3}$$

where:
E – total energy (E),
k_{eff} – effective thermal conductivity ($\mathrm{W\,m^{-1}\,K^{-1}}$),

h – sensible enthalpy ($\mathrm{J\,kg^{-1}}$)
T – temperature (K)
S_h – volumetric heat source ($\mathrm{W\,m^{-3}}$).

For more equations describing turbulent flow, properties of gaseous mixture and reaction see [3, 4]. Proper choice of turbulent model should be considered as key issue. Various models gives different results and is obvious that correct solution in comply with the bahavior of real system is only one. Some are ceteris paribus are not usable at all because of diverging solution. More about turbulent flow models can be found in [5, 6]. As for introducing to practical approach into CFD one can use [7] and particularly for combustion modelling [8].

Model presented here is based on combustion chamber of HBS with capacity of 150 000 Nm3 of hot blast with temperature (1350 °C). For this the temperature in the dome need to be at least 100 °C higher. Various temperatures of combustion air were evaluated.

4 Results

Influence of air or gas preheating and air excess ratio on theoretical combustion temperature (t_t) which serves as an instrument to determine the practical combustion temperature is on Figure 3 and Figure 4.

In comparison with adiabatic flame temperature which is defined as the temperature that results from a complete combustion process that occurs without any heat transfer or changes in kinetic or potential energy. So no air or fuel preheating and stoichiometry is equal to one. Theoretical temperature is influenced by excess air ratio and temperatures of medias. Usual design excess air ratio for current hot blast stoves is 1.1.

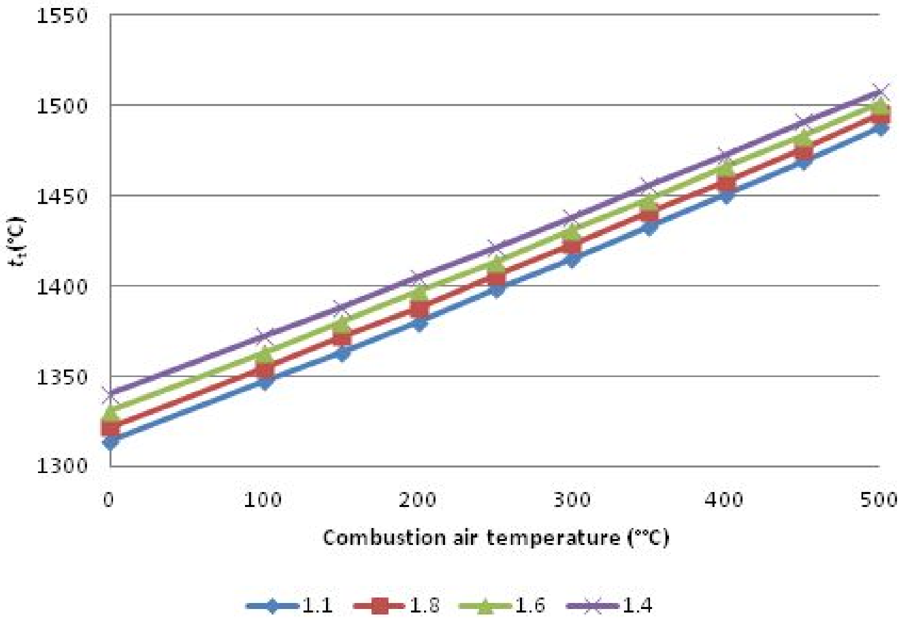

Figure 3: Theoretical combustion temperature as a function of excess air ratio and combustion air temperature (own).

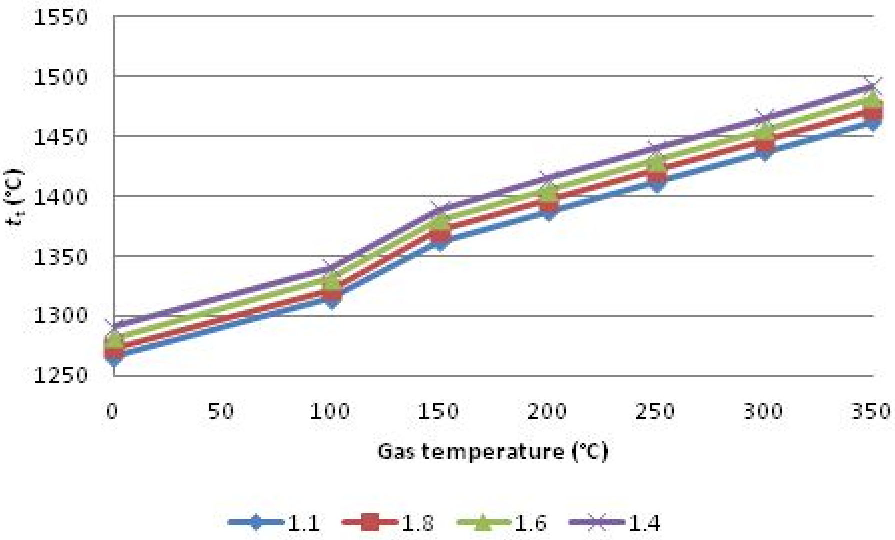

Figure 4: Theoretical combustion temperature as a function of excess air ratio and gas temperature (own).

Table 1: Composition and properties of blast oven gas.

compound	volume fraction (1)	mass fraction (1)
CO	0.23	0.222
CO_2	0.15	0.228
N_2	0.54	0.522
H_2	0.04	0.003
H_2O	0.04	0.025
Lower heating value		$3376.6\,\mathrm{kJ\,m^{-3}}$

Simplified it can be said that increasing of gas temperature by 100 °C leads to increase of t_t by 25 °C and incresing of air temperature has the effect of 35 °C. Effect of excess air ratio is like this: decrease by 0.01 leads to increase of t_t by 9°C ceteris paribus.

Three combustionair temperatures are evaluated – not-preheated (297 K) and preheated (373 and 473 K). Increasing temperature of reactants before combustion leads to higher temperature peak and shorter flame length due to higher reaction rate.

Table 1 shows the properties of blast oven gas, excess air ratio was set to 1.1. Table 2 comprises selected results like maximum temperture, temperature of flue gas entering the dome or NO_x. Visualisation of flow field and temperature field in the HBS from the burner to interface between combustion chamber and dome is on Figure 5 and Figure 6.

Table 2: Results.

Combustion air temperature (°C)	0	100	300	500
Maximum peak temperature (°C)	1366	1 397	1 458	1520
Mass-weighted average temperature entering the dome (°C)	1187	1209	1 254	1310
Mass-weighted average concentration of NO_x in waste gas (ppm)	0	0.03	0.1	0.2

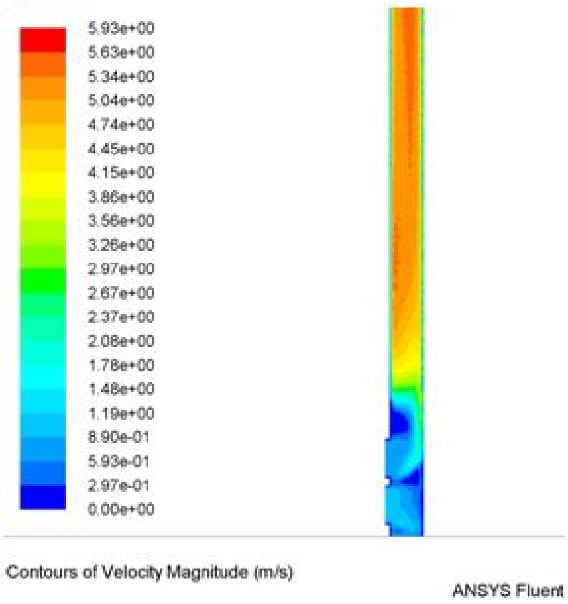

Figure 5: Velocity field (own).

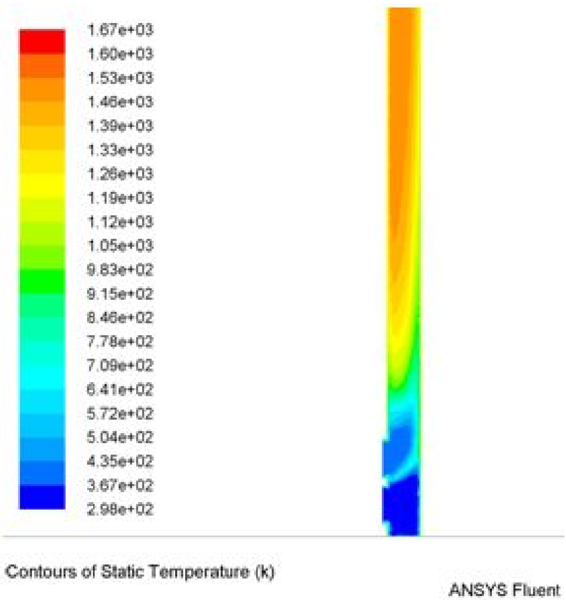

Figure 6: Temperature field (own).

5 Conclusion

CFD software represents powerful instrument which allows us evaluate processes with changing condition very quicly and quite comfortably in comparison with physical modelling either on model or on real system which is always time and money consuming. But it is recomended to compare gained results with those from measurement. As for first approach (e.g. in design) CFD gives sufficient base for prediction of real system behavior. Increasing expperience and growing base of solved engineering case with such instruments leads to more and more reliable results and it can be predicted that CFD software will be playing important role in future design of systems where mass, heat and moementum transfer occurs at the same time.

In design of hot blast stoves CFD tools like ANSYS Fluent can be used to find ideal design for required temperature and flow field through the cowper, or for designing better shapes of chequer bricks in order to achive higher heat transfer rates, lower presseure losses, etc.

Results for case with air preheated to 500 °C shows that NO_x for such a application should not be trouble in conditions of HBS - without high peak temperature which occurs. While the tt computed from energy balance equation rises by 35 °C with every increasing by 100 °C of air combustion temperature, CFD shows increase of 31 °C of average temperature entering the dome. It seems to be corelation between those two temperetaures, so in order to obtain requested temperature in the dome it can be made a estimation of air preheating degree.

Acknowledgement

This paper was created under the Project No. CV6005531 „Support and development of international relationship and mutual foreign activities of students and staff on FMMI“, funded by VŠB – Technical University of Ostrava, Czech Republic.

The work was supported by the specific university research of the Ministry of Education, Youth and Sports of the Czech Republic No. SP 2015/70 “Specific research in the metallurgical, materials and process engineering"

The work was supported by the specific university research of the Ministry of Education, Youth and Sports of the Czech Republic No. SP2015/86 “Reduction of the energy demands of the material production processes”

References

[1] Rieger, J., Weiss, C., and Rummer, B.: “Modelling and control of pollutant formation in blast stoves”. In: *Journal of Cleaner Production* 88.1 (2015), pages 254–261.

[2] Bernacký, D.: “Educational program for cowper control”. Master’s thesis. Technical University of Ostrava, 2014.

[3] *Ansys Fluent Theory Guide*. 14.5. ANSYS, inc.

[4] *Comsol Multiphysics Reference Manual*. 4.4. COMSOL AB. 2014.

[5] Bojko, M.: “Numerical computing of combustion processes”. In: *Mikrokogenerace - technický prostøedek decentralizace energetického hospodáøství*. Technical University of Ostrava. 2012, pages 22–25.

[6] Blejchaø, T.: *Turbulence - modelování proudìní - CFX*. Technical University of Ostrava, 2014.

[7] *Ansys Fluent User’s Guide*. 14.5. ANSYS INC. 2014.

[8] Kozubková, M.: *Modelování spalování paliv*. Technical University of Ostrava, 2013.

Untersuchung verschiedener Impfmittel für Gusseisen mit Kugelgraphit

Michael Kroker
TU Clausthal
Institut für Metallurgie, Abteilung für Gießereitechnik, Robert-Koch-Straße 42, 38678 Clausthal-Zellerfeld
michael.kroker@tu-clausthal.de

Abstract

Für die Herstellung von Gusseisen mit Kugelgraphit ist neben der Magnesiumbehandlung auch eine Impfung der Schmelze notwendig. Hierfür werden Ferrosiliziumvorlegierungen

verwendet, die verschiedenste weitere Elemente wie zum Beispiel Aluminium oder Calcium in geringen Mengen enthalten. Der genaue Mechanismus der Keimbildung durch Impfmittel ist bisher noch nicht verstanden. Darum wurde in der vorliegenden Arbeit ein experimenteller Weg geschaffen, um bis zu vier verschiedene Impfmittel direkt zu vergleichen. Hiermit wurden vier kommerziell verfügbare Impfmittel hinsichtlich ihrer Gefügeausbildung lichtmikroskopisch sowie im Rasterelektronenmikroskop untersucht.

1 Einleitung

Die Herstellung von Gusseisen mit Kugelgraphit birgt trotz seiner beinahe 70-jährigen Geschichte weiterhin großes Forschungspotential. Gusseisen ist ein kosteneffizienter Hochleistungswerkstoff: Es vereint die guten mechanischen Eigenschaften von Stahl mit den niedrigen Herstellungskosten des Gießprozesses.

Für die Herstellung von Gusseisen mit Kugelgraphit sind mehrere Verfahrensschritte notwendig. Nach dem Aufschmelzen und Legieren findet eine Magnesiumbehandlung statt; diese kann im Drahteinspul-, Sandwich-Cover- oder Konverterverfahren durchgeführt werden. Anschließend muss die Schmelze geimpft werden, um eine ausreichend hohe Anzahl an Fremdsubstraten in die Schmelze einzubringen. Diese Fremdsubstrate dienen der Graphitausscheidung durch heterogene Keimbildung und verringern die Unterkühlung während der eutektischen Erstarrung. Die Unterkühlung ist insofern von Bedeutung, als dass sie das Verhältnis von stabiler (Graphitausscheidung) und metastabiler Erstarrung (Zementitbildung) bestimmt. Auch für das Impfen werden verschiedene Verfahren angewandt. Hierbei sind das Einrühren des Impfmittels in die Schmelze, das Gießstrahlimpfen, die Impfung im Einguss-Tümpel und die Verwendung von Impflingen in der Form zu nennen. Die Impfung sollte immer möglichst kurz vor dem Abgießen und bei niedriger Temperatur erfolgen, da die Impfwirkung mit der Zeit abnimmt (das sogenannte Fading).

Zur Impfung von Gusseisen wurde in der Vergangenheit viel publiziert, dennoch herrschen verschiedene Lehrmeinungen zu ihrem Mechanismus vor. Eine gute Zusammenstellung der verschiedenen Theorien zur Bildung von kugeligem Graphit liefert Skaland [1]: Er nennt die Gasblasen-Theorie, die davon ausgeht, dass Kohlenmonoxid-Bläschen in der Schmelze vorliegen, in denen Graphit ausscheidet. Weiterhin beschreibt er die Graphittheorie, bei der angenommen wird, dass bereits in der Schmelze feste Graphitpartikel vorliegen, sowie die Siliziumkarbid (SiC)-Theorie, die sich vor allem auf die Wirksamkeit von SiC als Langzeit-Impfmittel stützt. Darüber hinaus erwähnt er die salzartige-Karbide-Theorie, die als Basis die Übereinstimmung der Gitterparameter von Graphit und möglichen Substraten verwendet. All diesen Theorien ist gemein, dass die von ihnen vorhergesagten Partikel oder Gasblasen kurz vor der Erstarrung in Abschreckversuchen nicht nachgewiesen werden konnten. Wesentlich interessanter sind hier die beiden sich relativ ähnlichen Sulfid/Oxid- und Silikat-Theorien. Beide gehen von der Bildung komplexer Oxide und Sulfide während der Magnesium- und Impfbehandlung aus. Während sich die Sulfid/Oxid-Theorie lediglich auf die Untersuchung vorhandener nicht metallischer Einschlüsse bezieht, wird dies in der Silikat-Theorie dahingehend erweitert, dass von einer mehrstufigen Bildung ausgegangen wird. Bereits während der Magnesiumbehandlung bilden sich MgO und MgS. Im zweiten Schritt keimen während der Impfung auf diesen Fremdsubstraten komplexe Silikate auf, die dann wiederum bei der Erstarrung dem Graphit als heterogener Keim dienen. Diese Silikate besitzen (anders als MgO bzw. MgS) in ihrer Gitterstruktur nur geringe Abweichungen zu den Gitterparametern von Graphit.

Der Vollständigkeit halber sei noch die vor allem im Japanischen Raum verbreitete Theorie genannt, die auf Grund der weitestgehenden Unlöslichkeit von Begleitelementen wie Aluminium und Calcium in Eisen davon ausgehen, dass diese im relevanten Temperaturbereich als flüssige Tropfen in der Eisenschmelze suspendiert sind und so als Keine dienen [2].

Viele der vorliegenden Untersuchungen zum Thema Impfen haben vor allem einen praxisnahen Charakter. So werden verschiedene Impfmittel, ihre Einsatzmengen, veränderbare Prozessparameter (z.B. Temperatur) und sogar verschiedene Impfverfahren über die mechanischen Kennwerte des hergestellten Gusseisens verglichen. Darüber hinaus wird an anderen Stellen lediglich der Einfluss der veränderten Impfstrategie und verschiedener Impfmittel auf die Abkühlkurven bei der Erstarrung untersucht. Der grundsätzliche Bildungsmechanismus des Kugelgraphits als solches konnte dabei jedoch nicht eindeutig nachgewiesen werden und bleibt somit weiterhin ungeklärt. Ein weiteres Problem bei den gesichteten Untersuchungen ist die mangelnde Vergleichbarkeit der Ergebnisse. In der Regel wurden unterschiedliche Schmelzen unter veränderten Bedingungen behandelt (Wahl des Impfmittels oder -verfahrens). Hierbei unterschied sich bereits die Zusammensetzung der Ausgangsschmelzen erheblich. Als Beispiel sei hier [2] genannt, in deren Arbeit acht verschiedene Impfmittel untersucht wurden, während sich der Siliziumanteil der Basisschmelze im Bereich von 1,96 % bis 2,31 % bewegte, was bereits deutlich unterschiedliche Eigenschaften des fertigen Gussteils erwarten lässt.

2 Experimentelles Vorgehen

Um dem vorgenannten Problem der Vergleichbarkeit zu begegnen, wurde ein experimenteller Aufbau gewählt, bei dem verschiedene Impfmittel aus einer Schmelze heraus verglichen werden können. Hierzu wurden genormte Y2-Porbekörper verwendet, die etwa 8 kg wogen. In Kombination mit dem an der TU Clausthal vorhandenen Induktionsofen (Inductotherm 125 CR Power Trax, mit frei stehendem Tiegel) mit einem Fassungsvermögen von 35 kg Eisenschmelze können somit vier verschiedene Impfmittel getestet werden.

Um die separate Impfung nach der gemeinsamen Behandlung zu ermöglichen, wurde das in Abbildung 1 gezeigte System aus Furan-Harz-gebundenen Sandformen entwickelt.

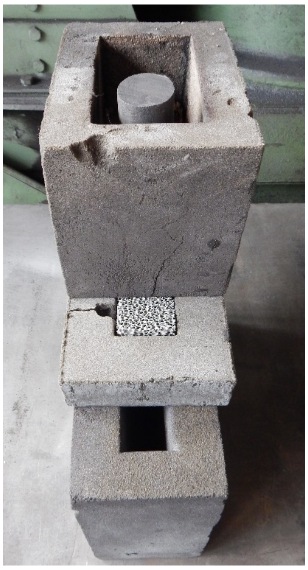

Abbildung 1: Impfbehälter und Y2 Form.

Abbildung 2: Tiegel zur Mg-Behandlung.

Der untere Teil stellt eine Y2-Form dar, der mittlere deckt diese ab und beinhaltet einen Filter (50 x 50 mm) und der obere Kasten stellt den Behandlungsbehälter für die Impfung dar. Dieser fasst maximal 10 kg Schmelze; der Abfluss am oberen Kasten wurde mit einer Graphitstange (Durchmesser 40 mm) verschlossen, die zusätzlich mit einem Feuerfeststein am Aufschwimmen gehindert wurde.

Die Magnesiumbehandlung wurde nach dem Überschüttverfahren durchgeführt, hierfür wurde der Schmelztiegel bei 1500 °C aus dem Induktionsofen entnommen und möglichst schnell in den auf 1100 °C vorgeheizten Behandlungstiegel (Abbildung 2) abgegossen. In diesem befand sich eine separate Tasche mit dem Behandlungsmittel, welches mit Elektrolyteisen abgedeckt war um die Reaktion zu verzögern. Die notwendige Menge des Behandlungsmittels wurde anhand des Schwefelgehalts der Schmelze bestimmt und lieferte gute Werte bei der Einstellung des Restmagnesiumgehalts.

Während des Schmelzvorgangs wurde die Temperatur mit Hilfe einer Temperaturmesslanze mit Einwegköpfen der Firma Heraeus, Typ Electro-Nite Positherm, und die chemische Zusammensetzung mit Hilfe eines Funkenspektrometers (Spectro MAXx LMM04) kontinuierlich überprüft.

Für den hier durchgeführten und beschrieben Versuch wurde eine Basisschmelze von 35 kg aus Roheisen und einem niedrig legierten Stahl im Verhältnis 2:1 hergestellt. Es mussten lediglich der Kohlenstoff- und Siliziumgehalt eingestellt werden, hierbei war zu beachten, dass durch das Aufheizen auf 1500 °C vor der Tiegelentnahme ein Kohlenstoffabbrand zu erwarten ist, während der Siliziumgehalt durch das Einbringen der Magnesiumvorlegierung noch deutlich ansteigt. Die durch das Impfmittel eingebrachte Siliziummenge wurde nicht betrachtet. Die chemische Zusammensetzung (Auswahl, alle anderen Elemente < 0,05 Gew.-%) der Basisschmelze vor der Behandlung gibt Tabelle 1 an (Angaben in Gew.-%)

Tabelle 1: Chemische Zusammensetzung der Basisschmelze (Angaben in Gew.-%).

C	**Si**	**Mn**	**P**	**S**	**Cr**
3,62	1,68	0,34	0,063	0,019	0,076

Die Magnesiumbehandlung wurde mit einem Ausbringen von 75 % wie oben beschrieben durchgeführt (Elmag der Firma ELKEM, Tabelle 2).

Tabelle 2: Chemische Zusammensetzung des Mg-Behandlungsmittels (Angaben in Gew.-%).

Bezeichnung	Al	Ba	Ca	Ce	La	Mg	Mn
Elmag	0,757	0,007	1,74	0,066	0,045	6,03	0,297
Bezeichnung	P	S	Si	Sr	Ti	Zr	
Elmag	0,010	0,005	44,8	0,004	0,045	0,008	

Folgende vier Impfmittel wurden verwendet: Reseed, Ultraseed, Superseed und Barinoc, alle sind kommerziell verfügbare Produkte der Firma ELKEM, ihre chemische Zusammensetzung zeigt Tabelle 3. Sie wurden mit 0,3 Gew.-% auf 8 kg Schmelze in die Impfbehälter gegeben, der Graphitstopfen wurde 20 s nach dem Befüllen mit der behandelten Schmelze gezogen, so dass diese in die Y2-Form fließen konnte.

Tabelle 3: Chemische Zusammensetzung der Impfmittel (Angaben in Gew.-%).

Bezeichnung	Al	Ba	Ca	Ce	La	Mg	Mn
Reseed	0,998	0,068	0,933	1,45	0,011	0,061	0,220
Ultraseed	1,25	0,093	2,10	0,023	0,007	0,030	0,163
Superseed	0,394	0,026	0,098	0,019	0,001	0,045	0,246
Barinoc	1,07	1,95	1,71	0,008	0,001	0,030	0,193
Bezeichnung	P	S	Si	Sr	Ti	Zr	
Reseed	0,009	0,005	73,7	0,015	0,063	0,065	
Superseed	0,012	0,034	70,2	0,023	0,072	1,73	
Ultraseed	0,008	0,005	72,9	1,03	0,074	1,25	
Barinoc	0,013	0,023	71,9	0,101	0,065	0,109	

Die Auswertung des Gefüges erfolgte lichtmikroskopisch mit Zeiss Axio.Imager M2m und der Software AMGuss der Firma GFaI zur Gefügeauswertung. Die Proben wurden geschliffen und abschließend mit Diamantsuspension (1 µm) poliert, zur Bestimmung des Perlit/Ferrit-Verhältnisses wurde mit Nital für wenige Sekunden geätzt. Die rasterelektronenmikroskopischen Untersuchungen wurden mit einem Rasterelektronenmikroskop (CamScan 44) mit angeschlossenem energiedispersiven Röntgenspektroskop (EDX) Eumex SphinX 133 CamScan durchgeführt.

Die chemische Analyse der abgegossenen Y2-Proben konnte aufgrund der Grauerstarrung nicht mehr mit dem Funkenspektrometer durchgeführt werden, hierfür wurde ein Glimmentladungsspektroskop (LECO GDS850A) für die allgemeine chemische Analyse und eine Verbrennungsanalyse (LECO CS230) zur Bestimmung von Kohlenstoff genutzt. Zur Bestimmung der chemischen Zusammensetzung des Behandlungs- sowie der Impfmittel wurde ein nasschemischer Aufschluss mit anschließender Analyse in einem optischen Emissionsspektrometer mit induktiv gekoppeltem Plasma (IRIS Intrepid II XDL, Thermo Scientific) verwendet.

3 Ergebnisse

Tabelle 4 zeigt die chemische Zusammensetzung der vier gegossenen Y2-Probekörper, alle Angaben in Gew.-%, für weitere interessante Elemente, wie Barium oder Calcium stehen keine Standards zur Kalibration des Glimmentladungsspektroskops zur Verfügung, diese Elemente konnten folglich nicht bestimmt werden.

Tabelle 4: Chemische Zusammensetzung der gegossenen Probekörper (Angaben in Gew.-%).

		C	Si	Mn	Mg	Al	Ce
1	Reseed	3,17	2,56	0,35	0,0265	0,0338	0,0268
2	Ultraseed	3,30	2,53	0,34	0,0299	0,0338	0,0256
3	Superseed	3,34	2,62	0,34	0,0304	0,0331	0,0290
4	Barinoc	3,33	2,62	0,34	0,0331	0,0342	0,0287

Aus Tabelle 4 geht hervor, dass die chemische Zusammensetzung trotz der unterschiedlichen Impfmittel über alle vier Proben relativ gleich ist. Bei den hier untersuchten Elementen sollte Probe 1 (Reseed) im Cer-Gehalt höher liegen, während zumindest zwischen Probe 2 (Ultraseed) und Probe 3 (Superseed) ein Unterschied im Aluminium-Gehalt sichtbar sein sollte. Allerdings sind die zugegebenen Mengen beider Elemente überaus gering; bei 0,3 Gew.-% Zugabe des Impfmittels, das einen Gehalt von angenommen 1 Gew.-% Al besitzt, ergibt sich theoretisch eine Erhöhung des Aluminiumgehaltes von 30 ppm, 0,003 Gew.-%.

Des Weiteren wurden die Gefüge der Proben untersucht, Abbildung 3 bis Abbildung 6 zeigen jeweils Übersichtsaufnahmen während in Tabelle 5 die mit der automatischen Gefügeauswertung erstellten Kenndaten zu finden sind.

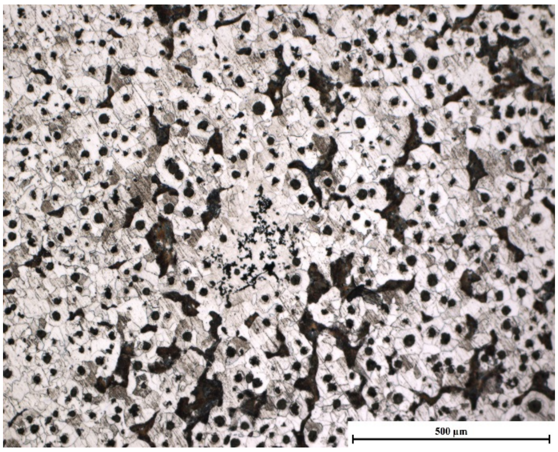

Abbildung 3: Probe 1 Reseed.

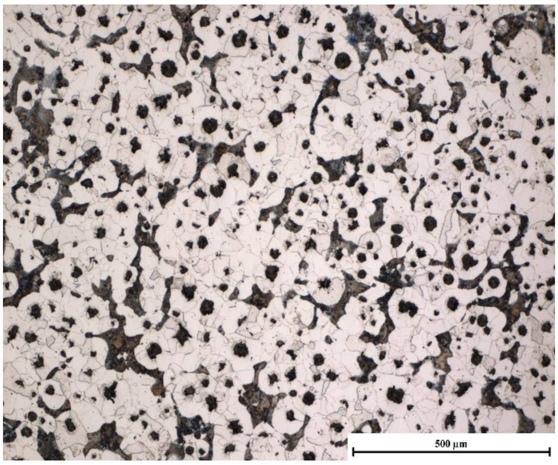

Abbildung 4: Probe 2 Ultraseed.

Tabelle 5: Gefüge-Kennzahlen der gegossenen Y2-Proben.

		Ferrit [%]	Perlit [%]	Graphit [%]	Graphitdichte [1/mm^2]	Nodularitätskennzahl [%]
1	Reseed	79,6	14,9	5,45	408	70,9
2	Ultraseed	79,9	14,2	5,89	389	72,0
3	Superseed	75,1	19,2	5,72	326	76,3
4	Barinoc	71,5	22,8	5,73	325	78,7

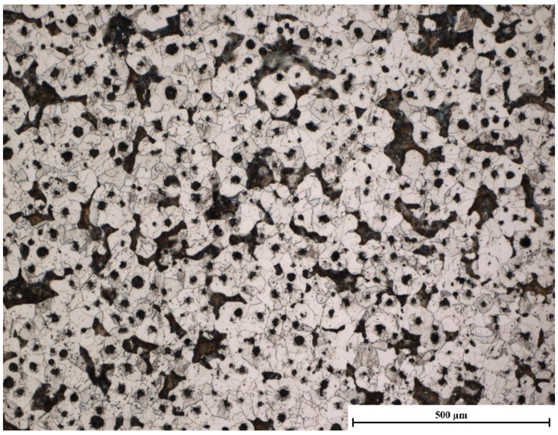

Abbildung 5: Probe 3 Superseed.

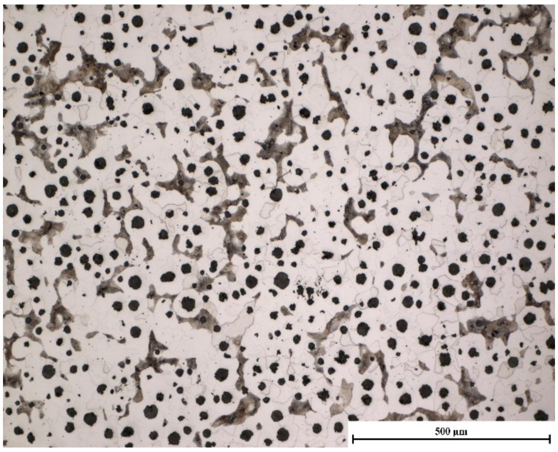

Abbildung 6: Probe 4 Barinoc.

Aus den in Tabelle 5 aufgeführten Gefüge-Kennzahlen lässt sich vor allem ein Schluss ziehen: Die Graphitausscheidungsdichte beeinflusst maßgeblich den Perlitanteil im Gefüge sowie die Nodularität (Rundheit) der Graphitkugeln. Insbesondere der Einfluss auf den Perlitgehalt lässt sich auch theoretisch leicht begründen: Mit steigender Graphitausscheidungsdichte werden die Diffusionslängen für den Kohlenstoff bei der eutektoiden Umwandlung kürzer, es wird sich hier also weniger Perlit bilden. Des Weiteren lassen diese Kennzahlen bereits eine Bewertung der verschiedenen Impfmittel zu: So zeigen Reseed und Ultraseed ein wesentlich besseres Verhalten als Superseed und Barinoc, da die Graphitdichte im Vergleich um 20 bis 25 % höher liegt. Allerdings führen die beiden letztgenannten zu einer besseren Ausbildung der Graphitkugeln.

Im Folgenden sind die REM-Bilder und EDX-Untersuchungen der einzelnen Proben dargestellt (jeweils unten rechts im Bild, alle Angaben in Gew.-%). Zusätzlich wurde für jedes Bild ein EDX-Mapping (Elementverteilungsbild) der relevanten Elemente erstellt. Die dargestellten Kugeln sind als repräsentativ anzusehen, Abbildung 7 bis Abbildung 14.

3.1 Probe 1 Reseed (Al, Ca, Ce)

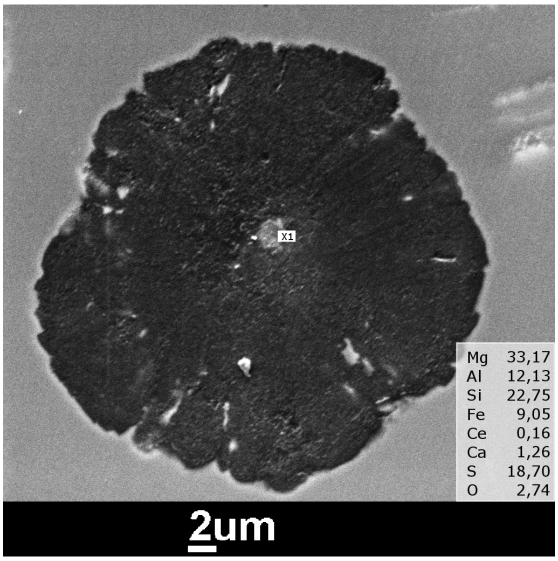

Abbildung 7: REM Aufnahme und EDX-Messung Probe 1 Reseed.

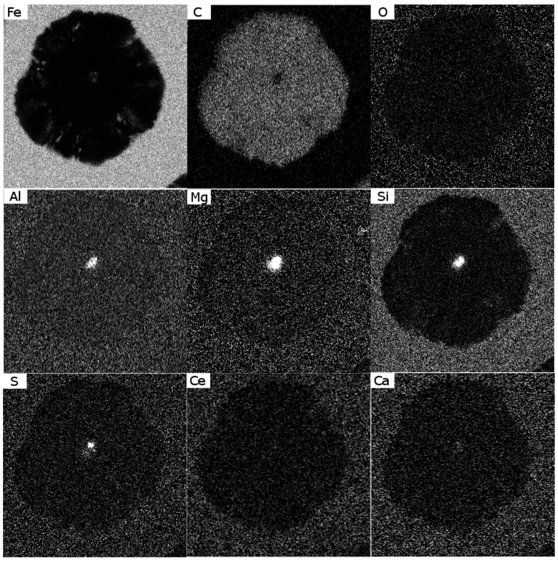

Abbildung 8: EDX-Mapping Probe 1 Reseed.

3.2 Probe 2 Ultraseed (Al, Ca, Zr)

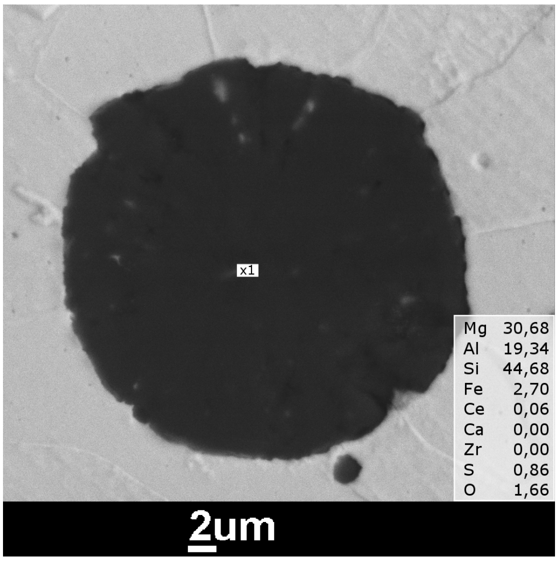

Abbildung 9: REM Aufnahme und EDX-Messung Probe 2 Ultraseed.

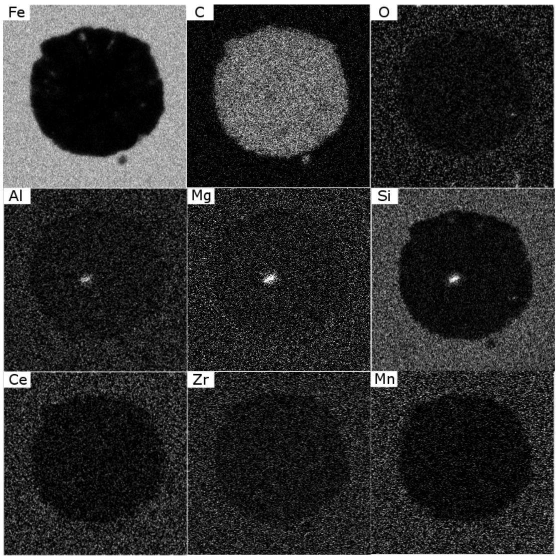

Abbildung 10: EDX-Mapping Probe 2 Ultraseed.

3.3 Probe 3 Superseed (Sr, Zr)

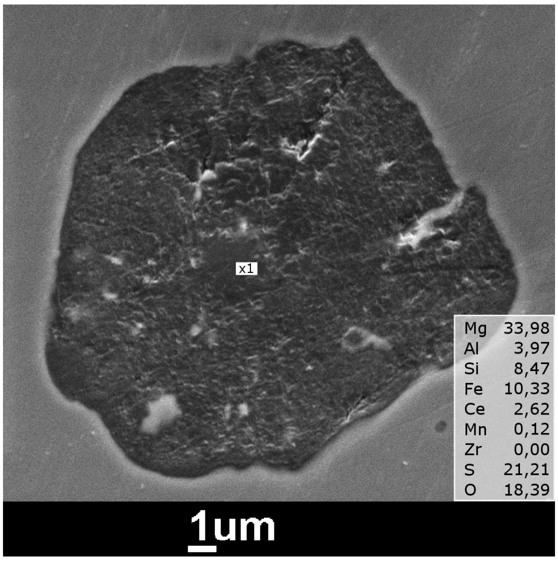

Abbildung 11: REM Aufnahme und EDX-Messung Probe 3 Superseed.

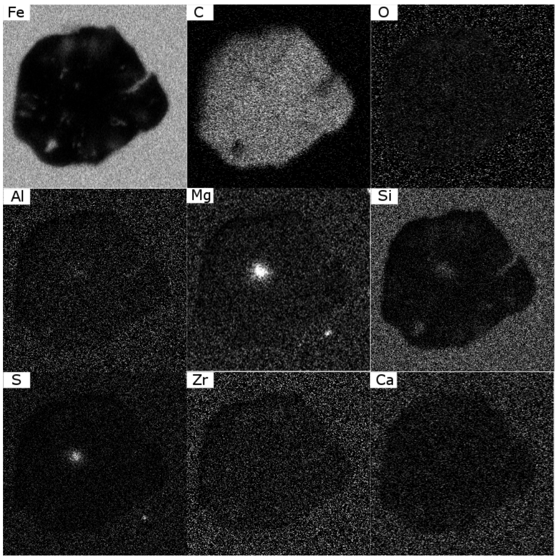

Abbildung 12: EDX-Mapping Probe 3 Superseed.

3.4 Probe 4 Barinoc (Al, Ba, Ca)

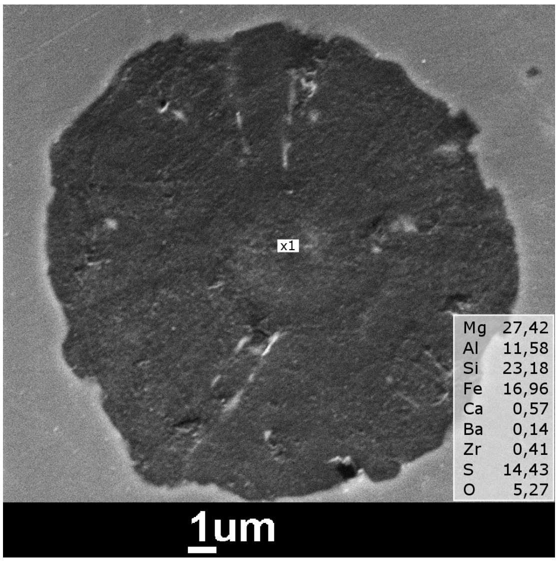

Abbildung 13: REM Aufnahme und EDX-Messung Probe 4 Barinoc.

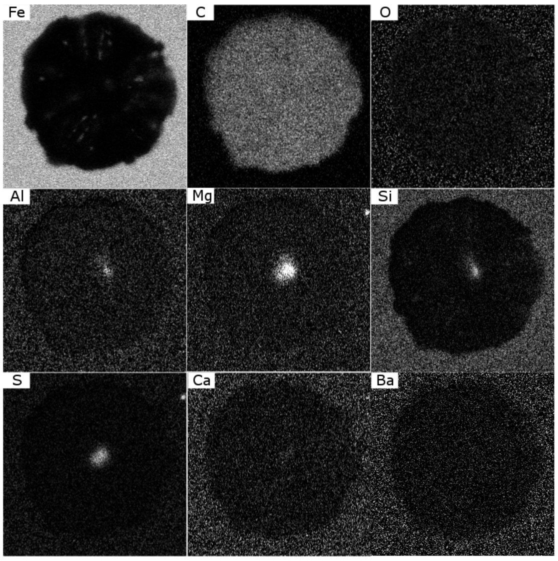

Abbildung 14: EDX-Mapping Probe 4 Barinoc.

3.5 Auswertung der REM- und EDX-Aufnahmen

Bei vielen Graphitkugeln konnte ein nichtmetallischer Einschluss in ihrem Zentrum identifiziert werden. Dass dies nicht bei allen gelang, liegt daran, dass die Spheroliten durch das Schleifen und Polieren nicht immer mittig angeschnitten wurden.

Diese nichtmetallischen Nuclei bestehen vorwiegend aus einer Mischung von Magnesium und Silizium, gebunden sind diese Elemente vorwiegend an Schwefel; Sauerstoff lässt sich nur in sehr geringen Gehalten detektieren. Die Begleitelemente der Impfmittel, die diese voneinander unterscheiden, konnten nur in sehr geringen Gehalten (Calcium, Cer, Barium) oder gar nicht (Strontium, Zirkonium) in den nichtmetallischen Keimen nachgewiesen werden. Eine Ausnahme stellt Aluminium dar, hier zeigen sich deutliche Unterschiede zwischen den mit Aluminium-haltigen Impfmitteln (Reseed, Ultraseed, Barinoc) behandelten Proben zu der mit Al-freiem Superseed geimpften Probe 3.

Im Allgemeinen lässt sich im Kern der nichtmetallischen Keime eine Magnesium-Schwefel Verbindung finden, die offensichtlich bei der Magnesiumbehandlung entstanden ist. Dazu abzugrenzen sind Silizium- und Aluminium-haltige Bereiche, die sich am Rand des Magnesium Einschlusses finden. Da beide Elemente nicht in ihrer elementaren Form vorliegen können, müsste sich hier auch Sauerstoff nachweisen lassen, dies war jedoch nicht der Fall und die Ursachen hierfür müssen geklärt werden.

Insgesamt lässt sich auch hier wieder sagen, dass sich die unterschiedliche chemische Zusammensetzung nicht in den gegossenen Proben wieder finden lässt, als einzige Ausnahme ist Aluminium zu nennen.

4 Zusammenfassung und Ausblick

Es wurden vier verschiedene Impfmittel der Firma ELKEM hinsichtlich ihrer Gefügeausbildung untersucht. Hierbei standen die nichtmetallischen Einschlüsse im Zentrum der Graphitkugeln im Fokus. Mit Ausnahme von Aluminium konnten keine Unterschiede in der chemischen Zusammensetzung der Keime gefunden werden, obwohl sich die Impfmittel hinsichtlich der Barium-, Calcium-, Cer-, Strontium- und Zirkonium-Gehalte in ähnlicher Weise wie beim Aluminium unterscheiden. Inwieweit diese Elemente tatsächlich an der Keimbildung teilnehmen beziehungsweise diese verändern ist fraglich. Auch in der Morphologie konnten keine Unterschiede der Nuclei festgestellt werden: In allen untersuchten Proben lag jeweils ein relativ großer Magnesium-Schwefel-haltiger Kern vor, an dessen äußeren Rändern sich Silizium und Aluminium fanden. Hiermit wird vor allem die zweistufige Silikat-Theorie zur Keimbildung unterstützt.

Das experimentelle Verfahren hat sich bewährt; eine Untersuchung verschiedener Impfmittel aus einer Schmelze heraus ist möglich. Im Weiteren wird nun eine zweiteilige Probenform konstruiert. Diese beinhaltet einen Y2- und einen Y4-Probekörper, der darüber hinaus zusätzlich thermisch-isoliert werden kann. Das Abgussgewicht dieser Form wird etwa 35 kg betragen, was in Kombination mit einem ebenfalls vorhandenen 150 kg Induktionsofen die Möglichkeit eröffnet, den Impfmitteleinfluss auch bei langen Erstarrungszeiten zu untersuchen.

Literaturverzeichnis

[1] Skaland, T.: "Nucleation Mechanisms in Ductile Iron". In: *Proceedings of the AFS Cast Iron Inoculation Conference*. Schaumburg, Illinois, 2005.

[2] Löblich H. und Hartmann, D.: "Optimierung der Verfahrensparameter zu Herstellung von kaltzähem ferritischem Gusseisen mit Kugelgraphit im Gusszustand". In: *Giessereiforschung* 21.3 (2003), Seiten 69–86.

Lead and Silver in the Copper Town

Tradition meets Innovation

Dr.-Ing. Urban Meurer
BERZELIUS STOLBERG GmbH
Binsfeldhammer 14, 52224 Stolberg

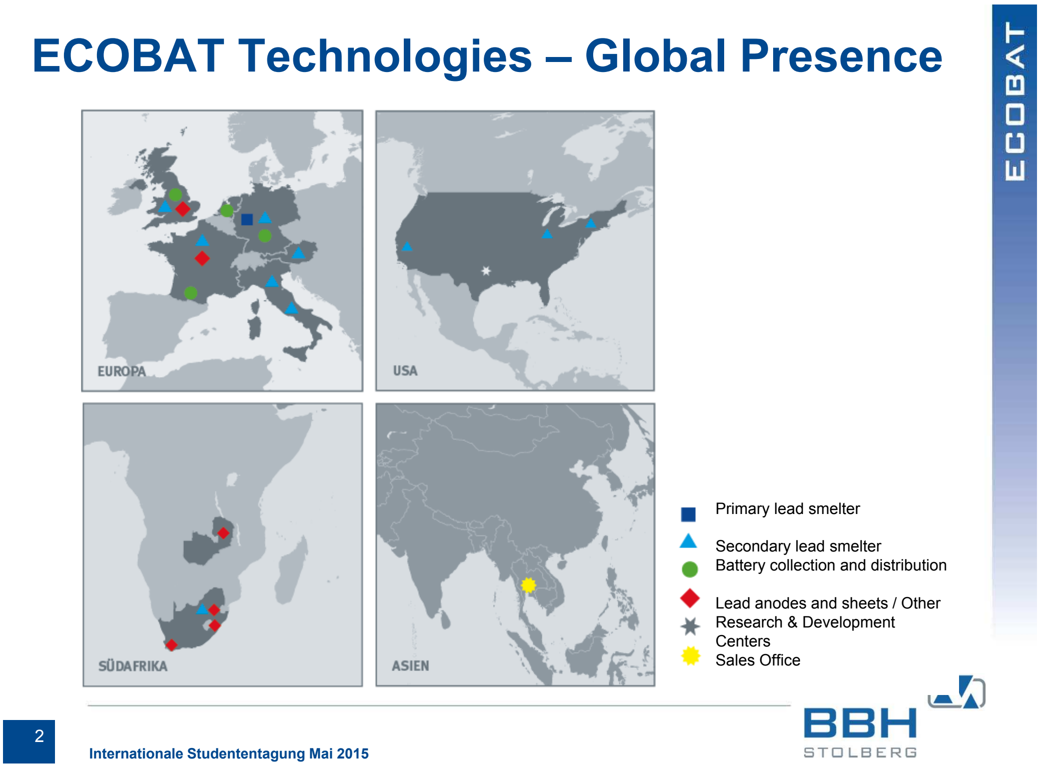

ECOBAT Technologies – Global Presence

- ■ Primary lead smelter
- ▲ Secondary lead smelter
- ● Battery collection and distribution
- ◆ Lead anodes and sheets / Other
- ✱ Research & Development Centers
- ✸ Sales Office

2

Internationale Studententagung Mai 2015

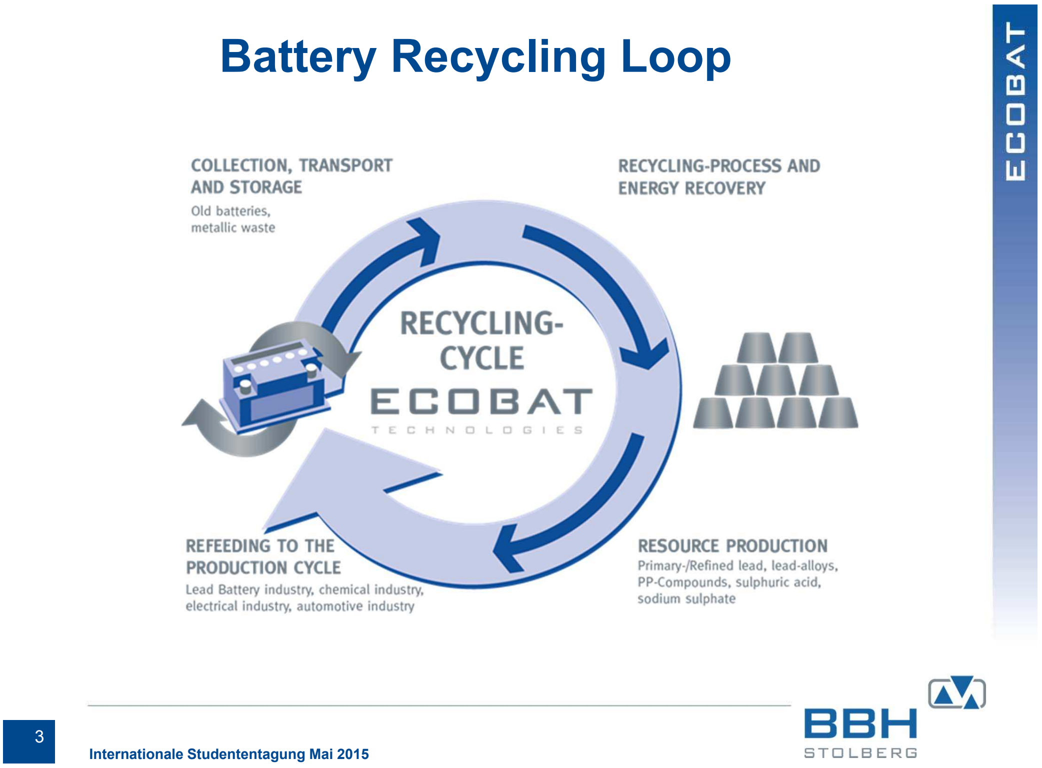

Battery Recycling Loop

COLLECTION, TRANSPORT AND STORAGE
Old batteries, metallic waste

RECYCLING-PROCESS AND ENERGY RECOVERY

RESOURCE PRODUCTION
Primary-/Refined lead, lead-alloys, PP-Compounds, sulphuric acid, sodium sulphate

REFEEDING TO THE PRODUCTION CYCLE
Lead Battery industry, chemical industry, electrical industry, automotive industry

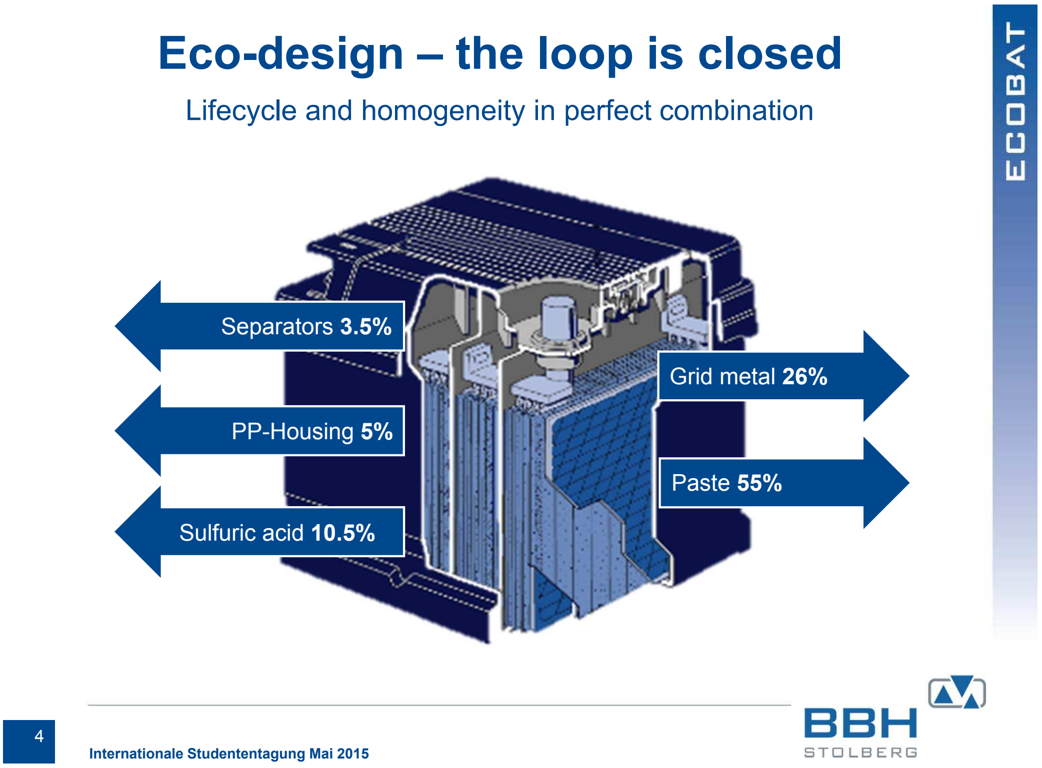

Eco-design – the loop is closed

Lifecycle and homogeneity in perfect combination

Separators **3.5%**

PP-Housing **5%**

Sulfuric acid **10.5%**

Grid metal **26%**

Paste **55%**

Lead-Acid Battery Recycling Process

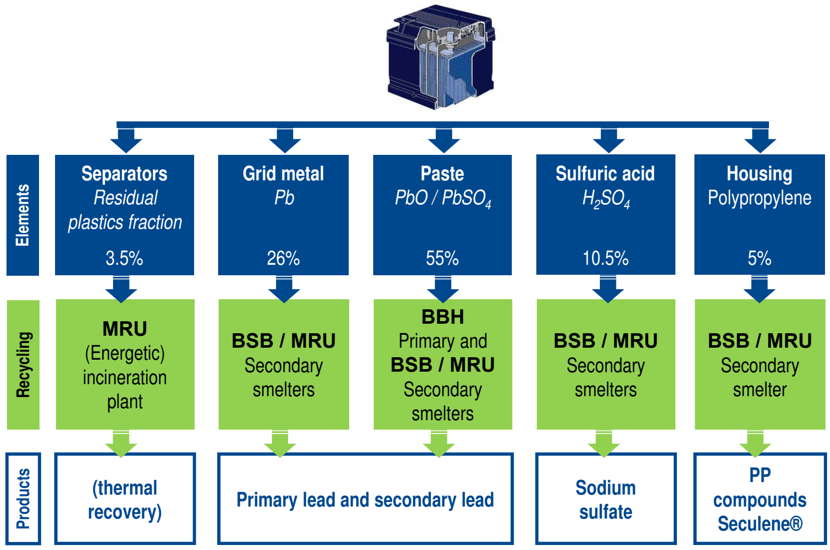

Elements	**Separators** *Residual plastics fraction* 3.5%	**Grid metal** *Pb* 26%	**Paste** *PbO / $PbSO_4$* 55%	**Sulfuric acid** *H_2SO_4* 10.5%	**Housing** Polypropylene 5%
Recycling	**MRU** (Energetic) incineration plant	**BSB / MRU** Secondary smelters	**BBH** Primary and **BSB / MRU** Secondary smelters	**BSB / MRU** Secondary smelters	**BSB / MRU** Secondary smelter
Products	**(thermal recovery)**	**Primary lead and secondary lead**		**Sodium sulfate**	**PP compounds Seculene®**

Lead in Products and Applications

Lead-acid battery reduces fuel consumption & CO_2 emissions

- In vehicles with start-stop technology, more efficient and larger lead-acid batteries enable fuel consumption to be reduced for the benefit of the environment and costs.
- Lead-acid batteries are completely recycled and thus constitute a sustainable mobility element.

- From the aspects of ecology and economy, lead-acid batteries are the best choice by far for the start-stop technology!

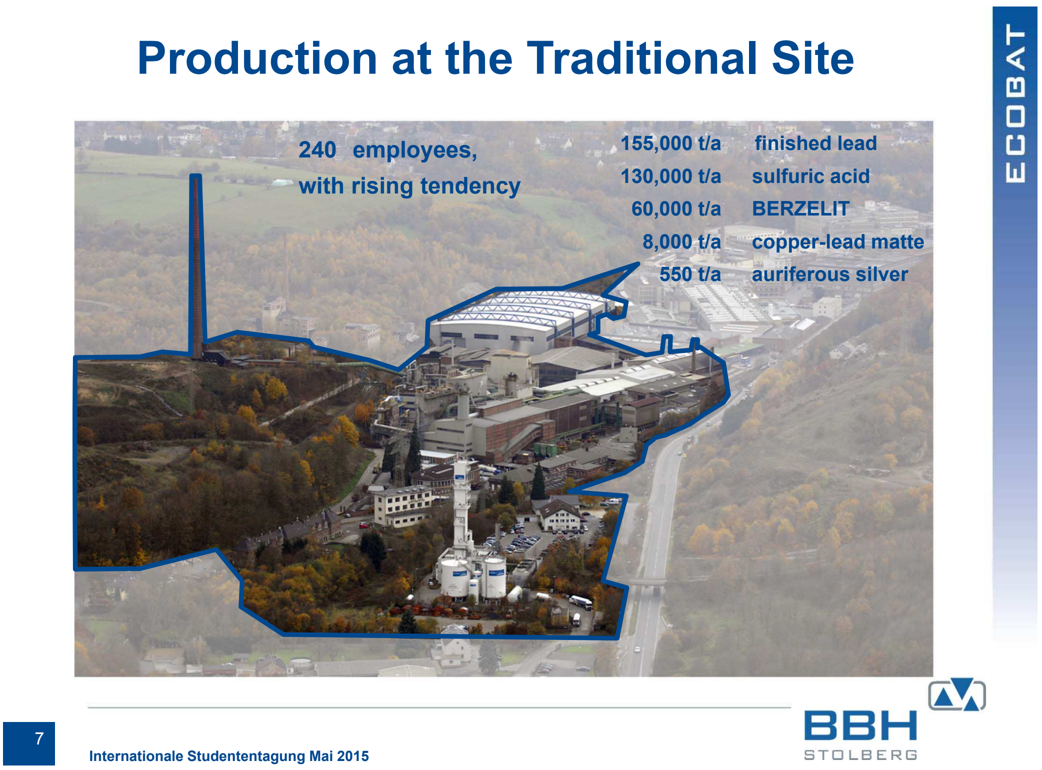

ECOBAT

Production at the Traditional Site

240 employees, with rising tendency

155,000 t/a	finished lead
130,000 t/a	sulfuric acid
60,000 t/a	BERZELIT
8,000 t/a	copper-lead matte
550 t/a	auriferous silver

BBH STOLBERG

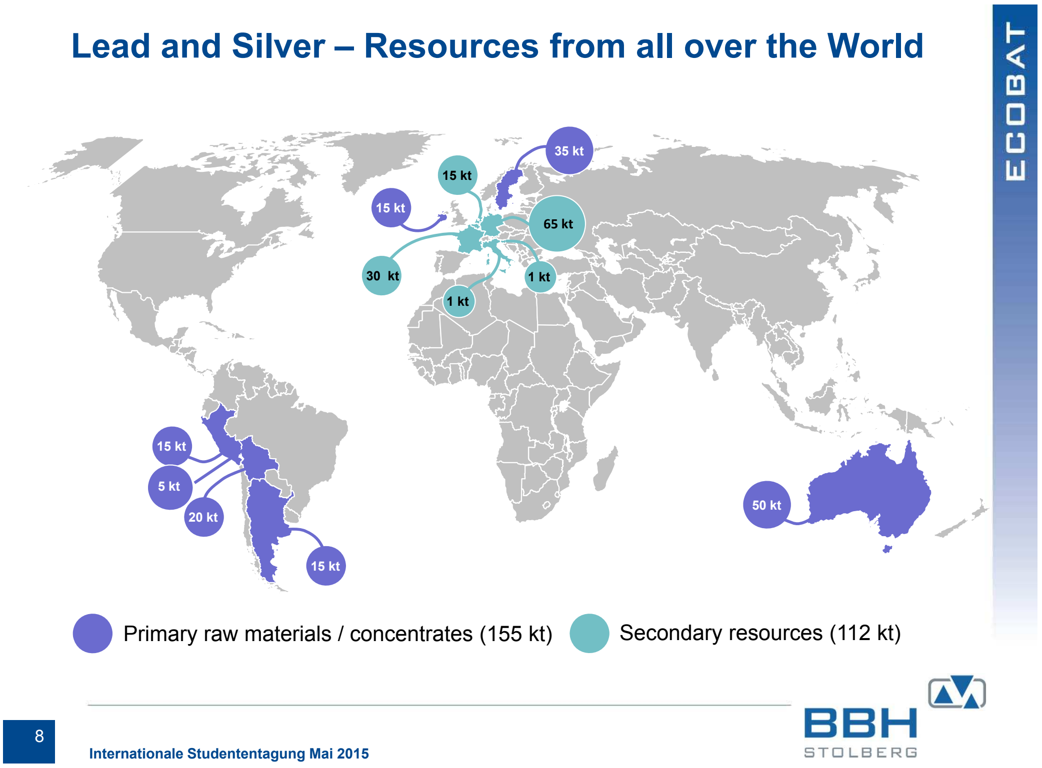

ECOBAT

Lead and Silver – Resources from all over the World

● Primary raw materials / concentrates (155 kt) ● Secondary resources (112 kt)

BBH STOLBERG

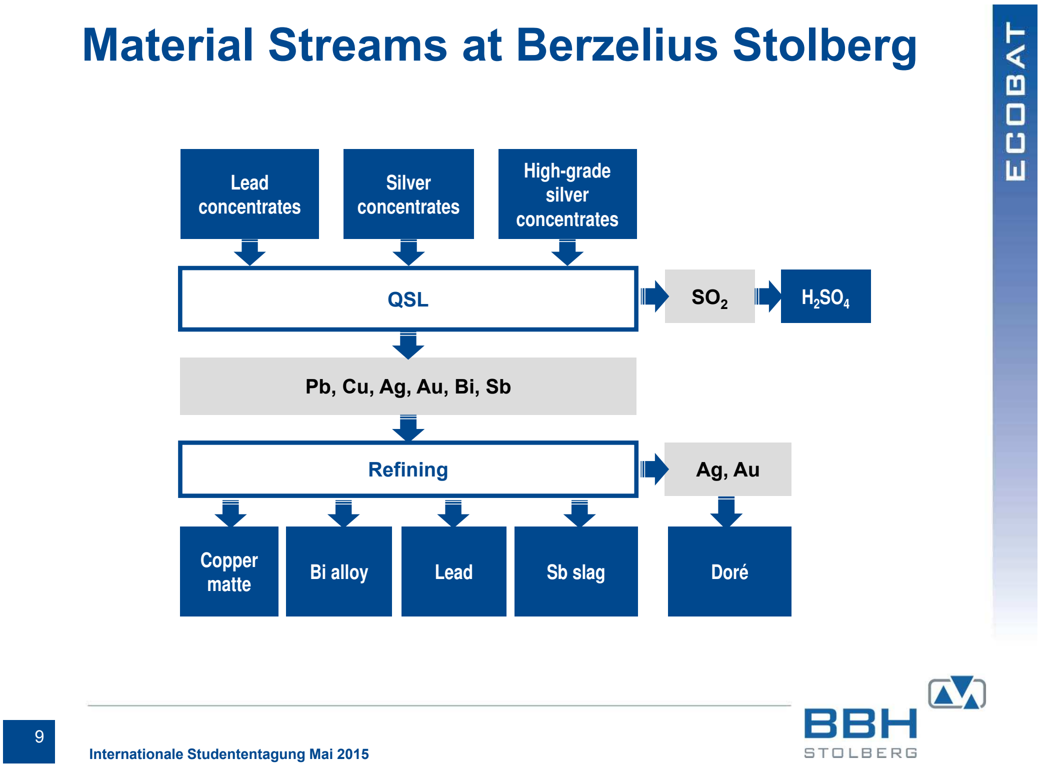

Material Streams at Berzelius Stolberg

Lead concentrates

Silver concentrates

High-grade silver concentrates

QSL

SO_2

H_2SO_4

Pb, Cu, Ag, Au, Bi, Sb

Refining

Ag, Au

Copper matte

Bi alloy

Lead

Sb slag

Doré

ECOBAT

BBH STOLBERG

9

Internationale Studententagung Mai 2015

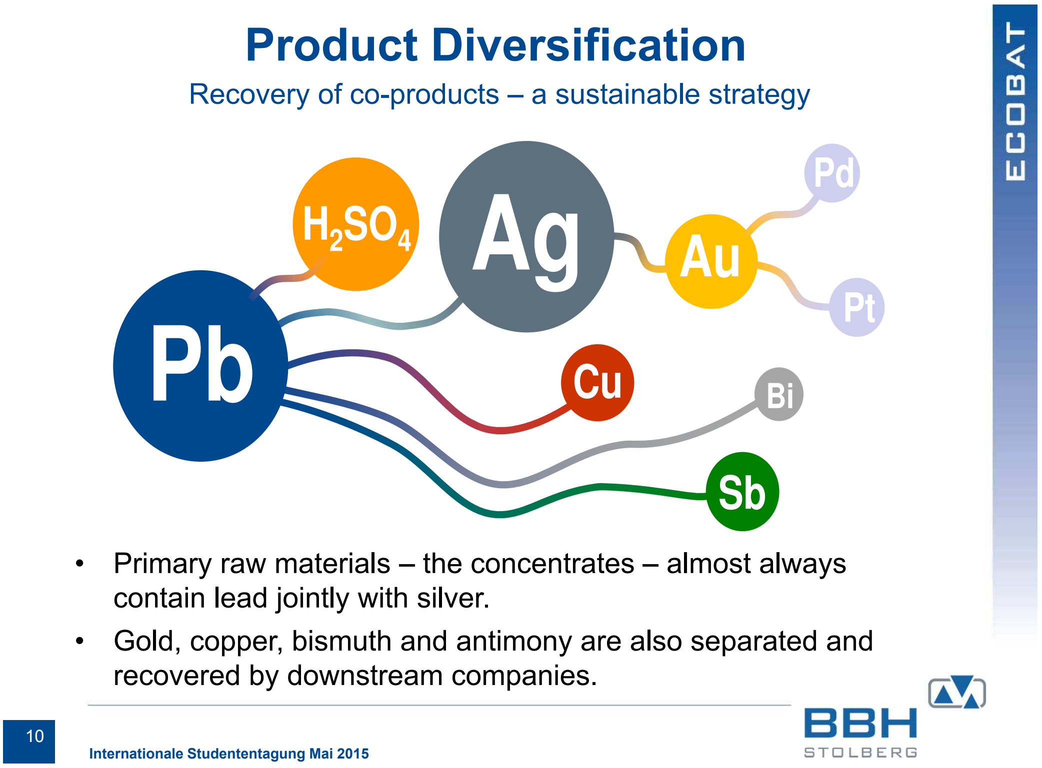

Product Diversification

Recovery of co-products – a sustainable strategy

- Primary raw materials – the concentrates – almost always contain lead jointly with silver.
- Gold, copper, bismuth and antimony are also separated and recovered by downstream companies.

ECOBAT

BBH STOLBERG

10

Internationale Studententagung Mai 2015

Open for Innovations …

Development and operation of the “Bayqik” for sulfuric acid production

ECOBAT

- The “Bayqik” process is a highly innovative development of Bayer Technologies and “Berzelius”.
- The “Bayqik” plant is the first of its kind, built at the Stolberg site, and allows offgas of high SO_2 content to be converted to sulfuric acid and the processing of feedstock of high sulfur content.

Open for innovations …

Development and operation of the “Bayqik” for sulfuric acid production

ECOBAT

- The new silver smelter at the Stolberg site has been equipped with the most advanced and energy-saving technology and is right now in the commissioning phase
- With this new construction, the auriferous-silver production capacity was doubled.
- Valuable reagents can be recovered so that substantial cost savings are achieved.

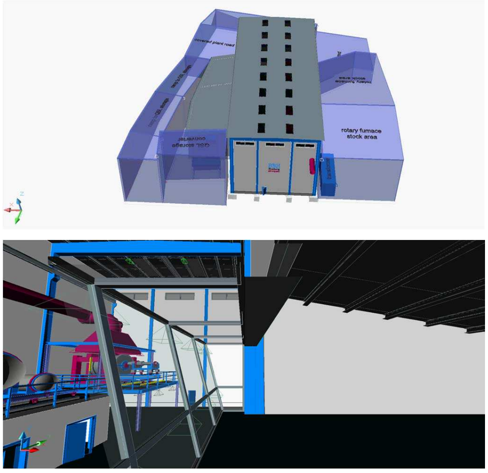

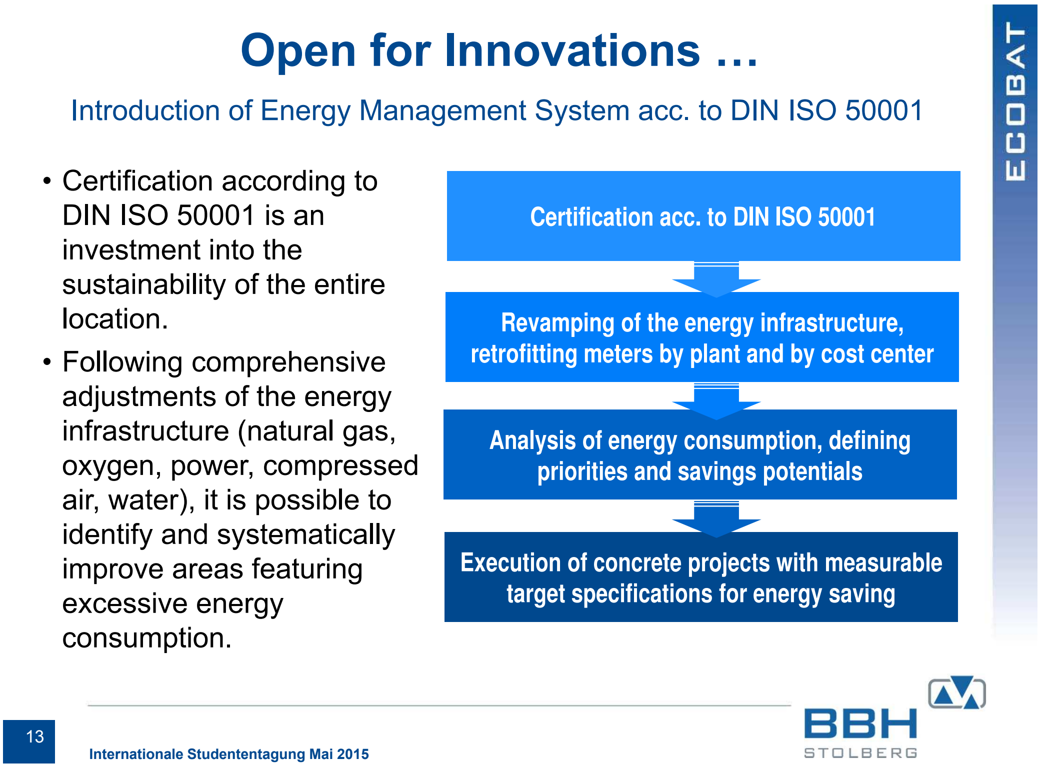

ECOBAT

Open for Innovations …

Introduction of Energy Management System acc. to DIN ISO 50001

- Certification according to DIN ISO 50001 is an investment into the sustainability of the entire location.
- Following comprehensive adjustments of the energy infrastructure (natural gas, oxygen, power, compressed air, water), it is possible to identify and systematically improve areas featuring excessive energy consumption.

Certification acc. to DIN ISO 50001

Revamping of the energy infrastructure, retrofitting meters by plant and by cost center

Analysis of energy consumption, defining priorities and savings potentials

Execution of concrete projects with measurable target specifications for energy saving

13

Internationale Studententagung Mai 2015

BBH STOLBERG

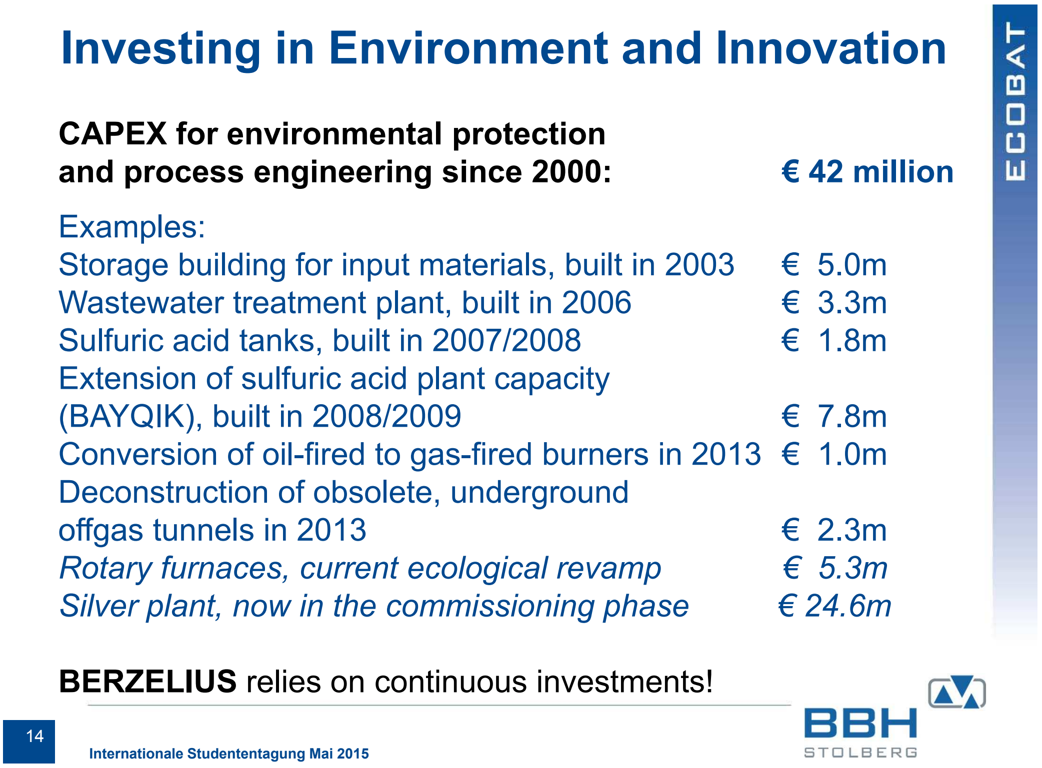

ECOBAT

Investing in Environment and Innovation

CAPEX for environmental protection and process engineering since 2000:	**€ 42 million**
Examples:	
Storage building for input materials, built in 2003	€ 5.0m
Wastewater treatment plant, built in 2006	€ 3.3m
Sulfuric acid tanks, built in 2007/2008	€ 1.8m
Extension of sulfuric acid plant capacity (BAYQIK), built in 2008/2009	€ 7.8m
Conversion of oil-fired to gas-fired burners in 2013	€ 1.0m
Deconstruction of obsolete, underground offgas tunnels in 2013	€ 2.3m
Rotary furnaces, current ecological revamp	*€ 5.3m*
Silver plant, now in the commissioning phase	*€ 24.6m*

BERZELIUS relies on continuous investments!

14

Internationale Studententagung Mai 2015

BBH STOLBERG

Regional Marketing

BERZELIUS STOLBERG – multiply committed and transparent

ERLEBEN SIE EINZIGARTIGE SPITZENTECHNOLOGIE!

PERSÖNLICHE EINLADUNG FÜR EINE EXKLUSIVE BETRIEBSBESICHTIGUNG

BLEI UND SILBER IN DER KUPFERSTADT

Die Blei- und Silberproduktion gehört zu Stolberg wie Burg und Kupfer. Seit mehr als anderthalb Jahrhunderten prägt **BERZELIUS** die Stolberger Wirtschaft.

Mit einem hochmodernen klimaschonenden Verfahren produzieren 230 Mitarbeiter jedes Jahr 155.000 Tonnen Blei und 350 Tonnen Silber. Das Blei ist zur Produktion von Autobatterien ökologisch und ökonomisch die allererste Wahl. **BERZELIUS** steht weltweit für Bleiproduktion und Batterierecycling auf höchstem Niveau; als einziges Unternehmen recycelt **BERZELIUS** ausgediente Bleibatterien komplett.

BERZELIUS in Stolberg trägt mit modernster Technik nachhaltige Verantwortung für Umwelt- und Arbeitsschutz und ist Ausbildungsbetrieb für kaufmännische und technische Berufe.

Die Bleimacher wünschen allen Besuchern ein tolles Stadtfest!

BERZELIUS Stolberg GmbH
Binsfeldhammer 14
52224 Stolberg
Telefon +49 2402 1206-0
Telefax +49 2402 1206-66
E-Mail bbh@berzelius.de
www.berzelius.de

STOLBERG

Thomas Schellhoff
Feierlicher Abschied mit humorvollen Einlagen ▶ Seite17

Seite 15 · Nummer 228 Dienstag, 1. Oktober 2013

Nachbarn aktiv für Natur- und Umweltschutz

Biologische Station und Bleihütte öffnen erstmals gemeinsam ihre Pforten. Rund 800 Besucher beim Tag der offenen Tür am Binsfeldhammer.

VON DIRK MÜLLER

„Wir betreiben aktiv Naturschutz und die Bleihütte mit ihrem modernen Verfahren Umweltschutz."
CONNY ZIMMERMANN, BIOLOGISCHE STATION

Urban Meurer, Geschäftsführer der BBH, Conny Zimmermann von der Biologischen Station, Künstlerin Annette Grösgen und Jörg Grösgen (v. r.) im Gespräch zwischen Biologischer Station und Bleihütte. Foto: D. Müller

Batteriepaste, Silber, Kupferstein und Co.

220 Arbeiter sind in der größten und modernsten Primärbleihütte Europas beschäftigt. Der Standort am Binsfeldhammer produziert jährlich rund 265 000 Tonnen Konzentrate und Batteriepaste, 155 000 Tonnen Fertigblei, 130 000 Tonnen Schwefelsäure.

Guten Morgen

Vogelsänger

KONTAKT
STOLBERGER NACHRICHTEN

ANZEIGE

NACHT der UNTERNEHMEN

Für Besucher · Für Aussteller · Aussteller 2014

Zurück zur Startseite

Teilnehmende Unternehmen 2013

Logos Teilnehmender Unternehmen | Teilnehmende Unternehmen von A-Z

- 4Jet Technologies GmbH
- Agentur für Arbeit Aachen
- AGIT mbH
- AixControl GmbH
- aixigo AG
- Ascom Deutschland GmbH
- Bauer+Kirch GmbH
- BERZELIUS STOLBERG GmbH
- car e.V. competence center automotive
- Carpus+Partner AG
- CASERIS GmbH
- Chemelot Campus
- ComConsult Beratung und Planung GmbH
- DASGIP GmbH - an Eppendorf Company
- DSA - Daten- und Systemtechnik GmbH

Kupferstadt Stolberg Städteregion Aachen

ART TOUR de Stolberg

KUNSTAUSFAHRT NR: 5
Sonntag 4. Mai 2014
Entdecken Sie die Galerie- und Ateliermeile in Stolberg

BERZELIUS Stolberg GmbH
„Blei und Silber in der Kupferstadt"
27. Oktober 2014, 18:30 Uhr

VON DER „HÜTTE" IN DIE MODERNE

„MISSIONAR FÜR METALLE"

PROGRAMM

Corporate Identity

BERZELIUS STOLBERG am Binsfeldhammer – a lively location

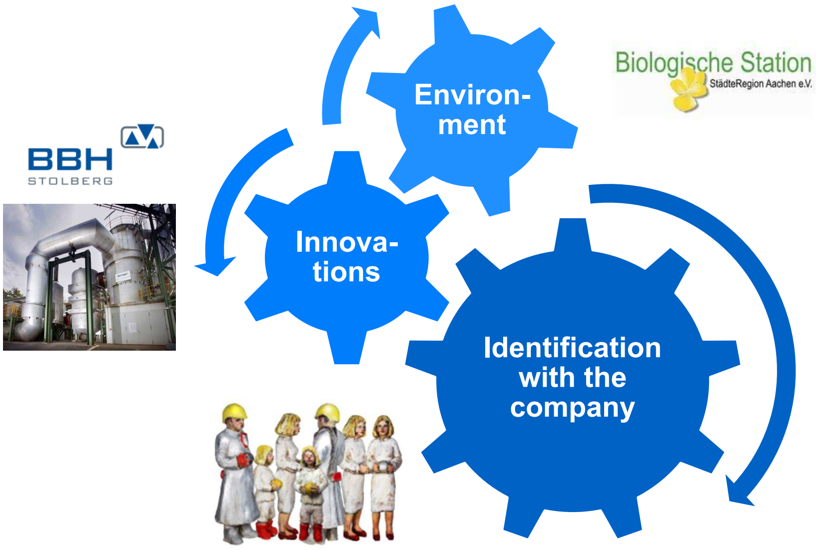

Preparation of the injection method four components iron – based alloys

Kamila Zdrodowska
Politechnika Częstochowska
Wydział Inżynierii Produkcji i Technologii Materiałów, Instytut Inżynierii Materiałowej
kzdrodowska@wip.pcz.pl

Abstract

The paper presents the results of the production of four components iron-based alloys by injection. Injection method is an innovative method for the preparation of amorphous and nanocrystalline alloys. Selected elements such as iron, cobalt, yttrium, and boron. All elements have been melted down repeatedly, so that the alloy was homogeneous. The alloy is divided in parts and is obtained by injection of an alloy with new properties. The paper shall exercise such studies as X-ray analysis, chemical composition analysis using a scanning electron microscope, pictures of structures in an optical microscope, Vickers microhardness test, surface roughness and abrasion. All tests were exercise both for the melted alloy as well as after the injection method. Iron-base alloys produced by injection are higher strength properties. In Figure 1 scheme of the device for injection. In Figure 2, is cast which is injecting alloy, and product plate.

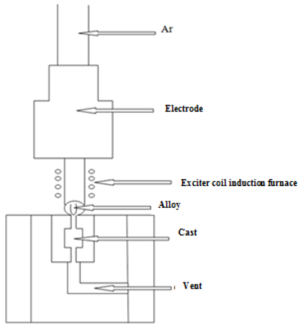

Figure 1: Scheme of the device for injection.

Figure 2: Cast which is injecting alloy, and product plate.

Acknowledgement

The project is financed by the European Union under the European Social Fund.

Magnesium Recycling

Stephanie Duwe
TU Clausthal
Institut für Metallurgie, Werkstoffumformung, Robert-Koch-Str. 42, 38678
Clausthal-Zellerfeld
Stephanie.Duwe@tu-clausthal.de

Abstract

Das Recycling von Magnesium ist aufgrund seiner Affinität zu vielen edleren Metallen nicht einfach, das Entfernen von korrosionsfördernden Verunreinigungen eine Herausforderung. Insbesondere für die Entfernung von Nickel aus der Magnesiumschmelze existiert noch keine wirtschaftliche Methode. In der hier zugrunde liegenden Arbeit ist es gelungen, den Nickelgehalt von verunreinigten Magnesium-Aluminium-Legierungen durch den kombinieren Einsatz von Aluminium und Zirkonium auf einen Massenanteil von 100 ppm zu senken. Dies entspricht zwar noch nicht dem höchsten geforderten Reinheitsgrad für Magnesium-Aluminium-Legierungen (10-50 ppm), ist aber ein großer Schritt hin zu einem effizienten Magnesium-Recycling.

1 Einleitung

Magnesium gehört zur Gruppe der Leichtmetalle. Mit einer Dichte von 1,74 g/m^3 [1] ist es um ein Drittel leichter als Aluminium (2,7 g/m^3 [1]) und viermal so leicht wie Stahl oder Gusseisen (Eisen: 7,9 g/cm^3 [1]). Es besitzt eine hohe spezifische Festigkeit und eignet sich demnach hervorragend für Leichtbaukonzepte. 80 % des Magnesiums werden in China produziert, 95 % davon im Pidgeon-Prozess, einem sehr energieintensiven, silicothermischen Reduktionsprozess.[2] Die so entstehende Abhängigkeit von Rohstoffimporten kann durch Recycling von Magnesiumschrotten gemindert werden. Unglücklicherweise besitzt Magnesium eine hohe Affinität zu Verunreinigungen, weshalb es eine Herausforderung darstellt, diese während des Recyclingprozesses aus eingeschmolzenen Magnesiumschrotten zu entfernen. Für ein hochwertiges Recycling und damit die Einsetzbarkeit des so entstehenden Sekundär-Magnesiums ist dies aber erforderlich. Eine Sauerstoffbehandlung ist hier unmöglich. Eine Reinigung der Schmelze ist aber unbedingt notwendig, da Störstoffe wie Kupfer, Eisen und Nickel die Korrosionsbeständigkeit des Magnesiums stark herabsetzen. Sie werden durch Fremdmaterialien wie Aluminiumlegierungen, Eisenanhaftungen oder beispielsweise Farbbeschichtungen eingetragen. Eisen und Kupfer lassen sich beispielsweise durch Zugabe von Mangan binden und ausfällen. Für Nickel hingegen existiert bisher keine solche Methode, die im industriellen Maßstab angewendet würde.

Elemente wie Aluminium und Zirkonium senken die Löslichkeit von Nickel in Magnesium deutlich – ein Verhalten, das neue Möglichkeiten zur Raffination eröffnet. Diesen Umstand vorausgesetzt und aufbauend auf einem Patent aus dem Jahr 1975 [3] wurde in dieser Arbeit eine Nickelentfernung aus Magnesium-Aluminium-Schmelzen durch den kombinieren Einsatz von Aluminium und Zirkonium erfolgreich durchgeführt.

2 Experimente

Mir reinem Magnesium (Magontech) und reinem Aluminium (Raffinal, Norsk Hydro) wurden Magnesium-Aluminium-Schmelzen mit unterschiedlichen Nickel-Verunreinigungsgraden (Massenanteil 0,001-2,5 %) in Al2O32-Tiegeln in einem widerstandsbeheizten Ofen hergestellt. Bei einer Temperatur von 720 °C wurde Zirkonium (Strem Chemicals) mit einem Massenanteil von 0,5 % zugegeben. Das für die Nickelentfernung nötige Aluminium wurde der Magnesium-Aluminium-Schmelze entzogen und muss folglich anschließend nachlegiert werden.

In den der Zugabe folgenden drei Stunden wurde die Schmelze in regelmäßigen Abständen gerührt. In dieser Zeit bildeten sich verschiedene hochschmelzende, in Magnesium unlösliche intermetallische Phasen aus Aluminium, Nickel und Zirkonium. Anschließend wurde ein bariumhaltiges Raffinationssalz (Massenanteile: 35 % $MgCl_2$, 10 % KCl, 40 % $BaCl_2$, 15 % MgF2) zugegeben. Dieses Salz lagert sich an die intermetallischen Phasen und Oxide an und begünstigt deren Sedimentation. Am Boden des Tiegels bildete sich so über die Raffinationszeit von vier Stunden nach und nach ein Schlamm aus. Abbildung 1 zeigt einen Querschnitt durch einen Tiegel(inhalt), der am Ende der Raffinationszeit bei Raumtemperatur erstarrte, anschließend geteilt und lichtmikroskopisch aufgenommen wurde.

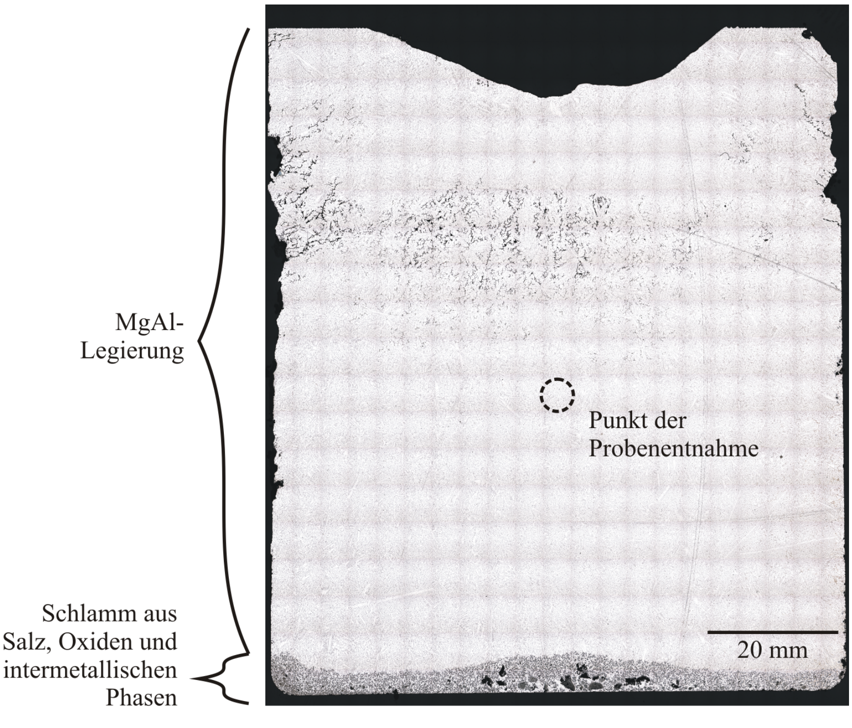

Abbildung 1: Schnitt durch einen Tiegel(inhalt), oben die Magnesium-Aluminium-Legierung, unten der Schlamm aus intermetallischen Phasen, Oxiden und Salz.

Im schmelzflüssigen Zustand wurde am Ende der Raffinationszeit bei jeder Versuchsschmelze eine Probe genommen (ohne Schlamm, siehe Abbildung 1) und nasschemisch in der optischen Emissionsspektroskopie mit induktiv gekoppelten Plasma (ICP-OES) auf die Massenanteile von Magnesium, Aluminium, Nickel und Zirkonium untersucht.

Die übrige Schmelze wurde danach in der Art abgegossen, dass der Schlamm im Tiegel zurückblieb. Dieser wurde im Rasterelektronenmikroskop (REM) untersucht, um die gebildeten intermetallischen Phasen zu identifizieren.

3 Ergebnisdarstellung

Die Resultate der nasschemischen Analyse lieferten ein Gleichgewichtsdiagramm von Nickel und Zirkonium bei 720 °C in Magnesium mit verschiedenen Aluminiumgehalten. Dieses Diagramm ist in Abbildung 2 dargestellt.

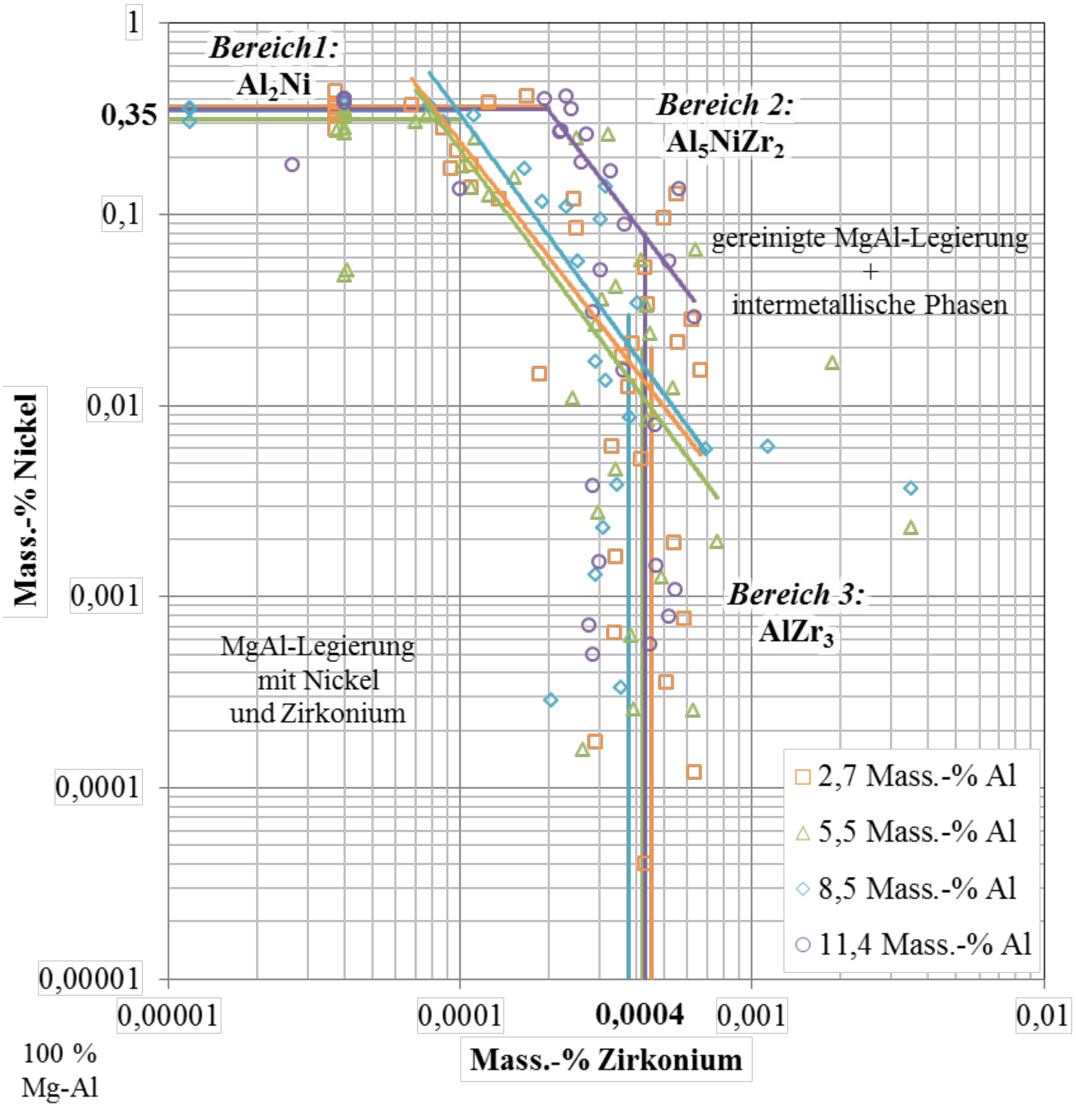

Abbildung 2: Gleichgewichtsdiagramm von Nickel und Zirkonium bei 720 °C in Magnesium mit verschiedenen Aluminiumgehalten.

Es zeichnen sich deutlich drei Bereiche ab, die im Gleichgewicht mit jeweils verschiedenen intermetallischen Phasen stehen: Bereich 1 mit konstanter Nickellöslichkeit unter Bildung von Al_3Ni/Al_3Ni_2, Bereich 2 mit voneinander abhängigen Nickel-und Zirkoniumgehalten unter Bildung von Al_5NiZr_2 und schließlich Bereich 3 mit konstanter Zirkoniumlöslichkeit unter Bildung von $AlZr_3$. Hierbei stellt der Schnittpunkt der Bereiche 2 und 3 den minimal erreichbaren Nickelgehalt von 100 ppm dar, da in Bereich 3 keine Phase mehr ausfällt, die noch Nickel enthält. Diese Phasen wurden außerdem mit energiedissipativer Röntgenspektroskopie (EDX) im REM in den Tiegelschlämmen identifiziert. Ein Beispiel zeigt Abbildung 3; die Aufnahme wurde zur Verdeutlichung eingefärbt.

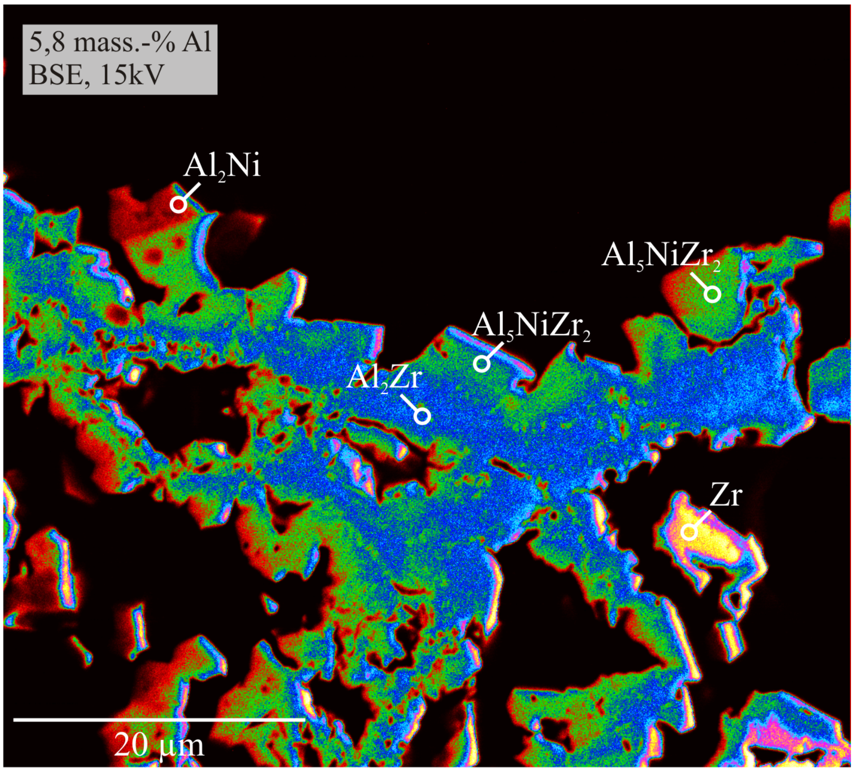

Abbildung 3: Intermetallische Phasen aus dem Schlamm einer Versuchslegierung mit einem Massenanteil von 5,6 % Aluminium (eingefärbte REM-Aufnahme).

Die Abbildung 3 ist insofern ungewöhnlich, als dass sowohl die nickel- als auch die zirkoniumhaltigen binären Phasen auftreten. Es handelt sich hier um einen lokalen Zirkonium-Überschuss, der allerdings trotzdem nur zur Bildung von Al_2Zr anstatt des $AlZr_3$ aus Bereich 3 (vgl. Abbildung 2) reicht.

4 Fazit und Ausblick

Die Resultate aus den Experimenten dieser Arbeit zeigen deutlich, dass eine Nickelentfernung aus Magnesium-Aluminium-Legierungen durch den kombinierten Einsatz von Aluminium und Zirkonium möglich ist. Durch die Bildung intermetallischer Phasen bei 720 °C wird das Nickel zuverlässig abgebunden und anschließend in einem Sedimentationsprozess aus der Schmelze entfernt. Hauptverantwortlich für die Nickelentfernung ist neben einem homogenen Gemisch aus Al_3Ni und Al_3Ni_2 die ternäre Phase Al_5NiZr_2. Diese Phasen (+ $AlZr_3$) konnten im REM identifiziert werden.

Auf diesem Weg konnte ein minimaler Massenanteil von 100 ppm Nickel in der Schmelze erreicht werden. Dies entspricht zwar noch nicht der geforderten High-Purity-Qualität für Magnesium-Aluminium-Legierungen – dieser liegt bei 10-50 ppm[4] – ist aber schon ein bedeutender Schritt in Richtung eines wirtschaftlichen und effizienten Magnesium-Recyclingverfahrens. Außerdem liegen die 100 ppm Nickel nach der Aluminium-Zirkonium-Behandlung nicht mehr im Magnesium gelöst vor, sondern ist in intermetallischen Phasen abgebunden. Dieser Umstand sollte die durch Nickel verursachte Korrosionsneigung des Magnesiums bereits deutlich hemmen.

In Zukunft muss versucht werden, die Nickelgehalte noch weiter zu senken. Weiterhin wird das verbleibende Korrosionsverhalten der gereinigten Magnesiumlegierungen untersucht.

Danksagung

Die Autorin dankt der DFG für die finanzielle Unterstützung des Projektes.

Literaturverzeichnis

[1] Lide, D. R.: *CRC handbook of chemistry and physics.* 85. ed. Boca Raton: CRC Press, 2005. ISBN: 0849304865.

[2] Zuliani, D. J. und Reeson, D.: "Making Magnesium a More Cost and Environmentally Competitive Option". In: *9th International Conference on Magnesium Alloys and Their Applications: Conference Proceedings.* Herausgegeben von W. J. Poole und Karl Ulrich Kainer. Band 9. Vancouver und Canada, 2012, Seiten 21–30.

[3] Foerster, G. S.: *Removal of nickel from molten magnesium metal.* George S. Foerster, 1975.

[4] Ditze, A. und Scharf, C.: *Recycling of Magnesium.* 1. Auflage. Clausthal-Zellerfeld: Papierflieger Verl., 2008. ISBN: 9783897209572.

Microstructure and mechanical properties of WE43 magnesium matrix composite with addition of 5% SiC particles

Adam Gryc[1], Michał Dudek[2], Tomasz Rzychoń[3]
Silesian University of Technology
ul. Krasińskiego 8, 40-019 Katowice, Poland
[1]gryadam@wp.pl, [2]mdudek215@gmail.com, [3]Tomasz.Rzychon@polsl.pl

Abstract

Metallic biomaterials are still most commonly materials used for medicinal purposes (for implants or medical devices construction). The combination of mechanical properties predeterminates them as a material for construction the most tough parts of implants, like joint replacements. These materials can be degradated by many mechanisms, like fatigue or corrosion. Especially corrosion properties are closely connected with the biocompatibility of these materials. This paper is basically focused on testing of corrosion properties of stainless steels and titanium alloys. Structures of tested materials were observed by light microscopy and pictures can be found in this paper. Also impact of surface treatment on corrosion properties of tested materials is discussed here. For tests the potentiodynamic polarization method was used. Characteristic corrosion potentials were measured and are mentioned in this paper too. Experiments were performed in artificial physiological and cerebrospinal solutions. These solutions can simulate different parts of human body environment. Corroded materials surfaces were studied by electron (SE and BSE) and light microscopy after tests. Bottoms of corrosion pits were checked for corrosion product and these products were analysed by EDS analysis.

Keywords: Biomaterials, Biocompatibility, Potentiodynamic polarization method, Pitting

1 Introduction

Biocompatibility of metallic materials is mostly determined by their corrosion behaviour. As the metal is corroded, there are metal ions released into surrounding hard or soft tissues. If these ions are toxic or react with body environment and create toxic substances, they can cause pathological changes of the surrounding tissues. In this case the corrosion damage of such a material has to be minimized and if not, this material is unusable in surgical medicine. On the other hand there are applications where corrosion damage is tolerated or even needed. This is case of bioactive metals used for temporary supports mostly inside of organisms. In this case the ions of corroded material are biogenic and they are processed by organism, which lead to slow dissolving of implant. Typical examples are temporary implants made from bioactive magnesium alloys. These implants have one really important advantage-there is no need for extraction. Extraction is a surgery procedure which is connected to another recovering of organism [1].

There are many types of bioinert metals used in implantology. Human body is highly aggressive corrosion environment so only metals with high corrosion resistance can be used for implants. Noble metals like gold or silver have been used in dentistry since 19th century. During 20th century stainless steels are widely used for temporary and even for long term implants. Austenitic stainless steels like 316, 316L or their modifications are still used in implantology especially for temporary implant construction. For long term implant metals like cobalt or titanium are used. Highly alloyed cobalt alloys are used mostly for casted application where higher mechanical properties (Young modulus and strength) are needed. On the other hand titanium implants are used for longest application. For better mechanical properties can be titanium alloyed by vanadium or aluminium. Ti6Al4V is a modern material with high corrosion resistance and Yield strength about 880 MPa [2].

Corrosion resistance of non-noble metallic materials is caused by thin oxidic layers on their surfaces. Even the base metals are very non-noble, the oxidic layer is distinctly noble. The non-conductive layer can protect the base material from external electric field and also makes a barrier against surrounding environment full of aggressive ions. In case of stainless steels the layer basically consists of CrO_2, resp. TiO_2 for titanium alloys. The stability of the layer determinate corrosion resistance of the material and can also be measured by potentiodynamic polarization method. Other electric properties of this layer can be measured by EIS (Electro Impedance Spectroscopy) method [2].

2 Experiment

There were five different alloys tested in this experiment. Their corrosion resistances were evaluated and surfaces after corrosion tests were studied by light and electron microscopy. Chemical composition of studied materials can be seen in Table 1.

Table 1: Chemical composition of tested alloys.

	Sample				
Element (wt. %)	M1	M2	M3	M4	M5
C	0,200	0,016	0,031	0,156	0,053
Si	0,301	0,370	0,018	0,510	0,037
Mn	0,800	1,810	0,026	1,560	0,240
P	0,028	0,033	-	0,106	0,009
S	0,022	0,011	-	0,039	0,026
Cr	14,420	16,010	0,040	17,230	>1,44
Ni	4,400	13,850	0,056	7,070	<64,11
Mo	0,139	2,450	0,087	0,376	0,062
Al	0,005	0,021	5,390	0,006	0,052
Cu	2,880	0,080	0,012	0,790	0,303
Co	0,060	0,066	-	0,101	<0,006
Ti	0,010	0,012	89,700	0,020	32,010
Nb	0,178	0,014	0,092	<0,004	0,040
V	0,100	0,070	3,360	0,090	0,009
Fe	76,500	64,990	0,013	<71,60	3,430

Structure of studied materials was observed and can be seen on Figure 1. There were made samples for electrochemical tests. Samples surfaces were grinded and polished on metallographic devices. Discs with different size of SiC particles were use for grinding and diamante suspension (1 µm) was used for polishing. There was made only 1 sample from each material for testing in isotonic solution. Samples of same size were made for testing in cerebrospinal solution, but another two samples were additionally made from material M2 and M5 was named M2P and M5P (there were 4 samples made from these materials for testing in cerebrospinal solution). The surfaces of samples M2P and M5P were passivated according ASTM F86 norm (35% HNO_3, 22 °C, 20 minutes) [3].

There were 2 different solutions made for potentiodynamic tests. The chemical composition of both solutions can be seen in Table 2.

During the potentiodynamic polarization measurement the characteristic potentials are measured. This measurement was preceded according ASTM F746 norm [4]. So tested material was connected to "working" electrode, and fixed in corrosion cell. After that reference calomel electrode was fixed into the cell. In the end the platinum countering electrode was fixed to create consistent electric field around working electrode. For the testing laboratory system VoltaLabTM21 and software Volta Master I was used. The

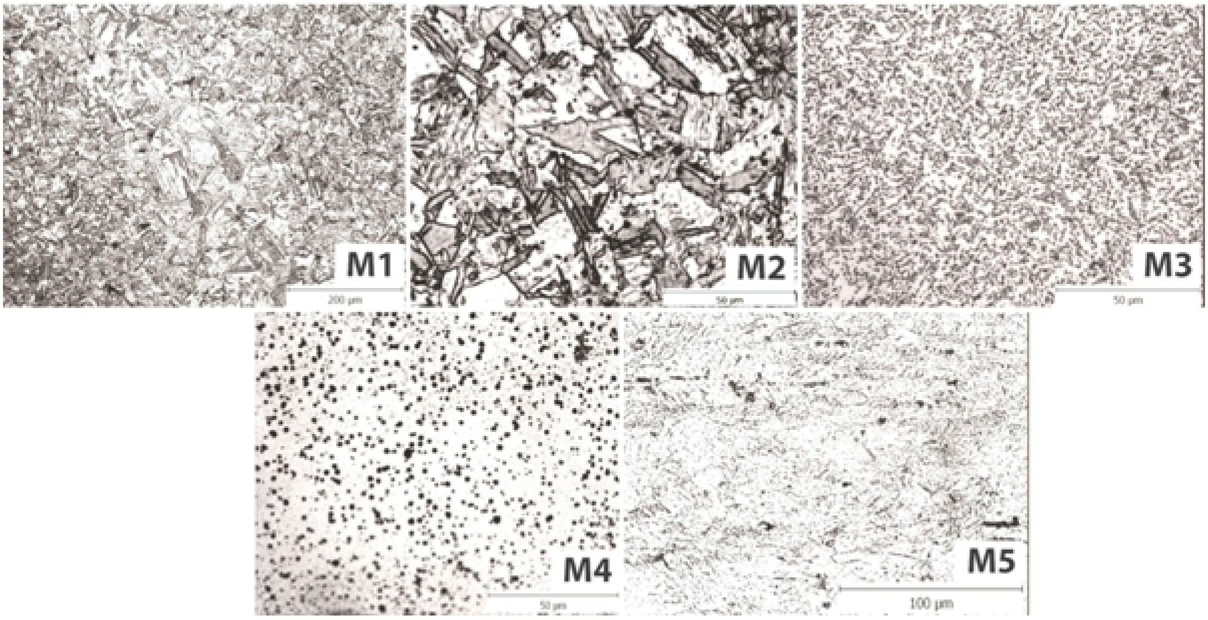

Figure 1: Microstructures of studied samples.

Table 2: Chemical composition of solution for corrosion testing.

Element	**Element concentration (g/litre destil H_2O)**	
	Physiological solut.	Cerebrospinal solut.
NaCl	9	8,66
KCl	-	0,224
$CaCl_2 .\ 2H_2O$	-	0,206
$MgCl_2 \cdot 6H_2O$	-	0,163
$Na_2HPO_4 \cdot 7H_2O$	-	0,214

samples were fixed and tested in Avesta corrosion cells, which were tempered to 37 °C. The free corrosion potential was measured before increasing the potential on working electrode. After that the potentials of depasivation and repasivation was measured. After the testing the surfaces of materials were checked for corrosion damage.

3 Results and Discussion

Polarization curves were measured for each material in each solution. Corrosion potentials were found out by Taffel method before other tests started. Also potentials of depasivation and repasivation were found out for each material. Results for this measurement can be seen in Table 3 and Table 4. There are polarization curves for measurement in cerebrospinal solution shown on Figure 2 [5].

Potentials of depasivation and repasivation couldn't be found out for M3 sample, because they are out of device measurement range. Testing of M2P and M5P demonstrates how corrosion properties of metals can be improved by correctly chosen surface treatment. The surface of M5 sample after the testing can be seen on Figure 3. There are corrosion pits and holes clearly visible on this picture, which was taken by electron microscopy. Some

Table 3: Potentials measured in cerebrospinal solution.

Sample	**Potentials [mV]**				
	E_{cor}	E_{dep}	$E_{dep\text{-}konv}$	E_{rep}	$E_{rep\text{-}konv}$
M1	-186	335	399	12	25
M2	-213	515	561	-50	56
M3	-450	—	—	—	—
M4	-145	485	527	-52	27
M5	-452	507	546	-36	139
M2P	404	1250	1280	1190	1215
M5P	-443	1364	1376	1026	1064

Table 4: Potentials measured in physiological solution.

Sample	**Potentials [mV]**				
	E_{cor}	E_{dep}	$E_{dep\text{-}konv}$	E_{rep}	$E_{rep\text{-}konv}$
M1	-197	64	66	-108	-120
M2	-164	277	295	-58	-2
M3	-292	≥1535	—	—	—
M4	-35	412	420	-25	-34
M5	-175	331	342	-178	-181

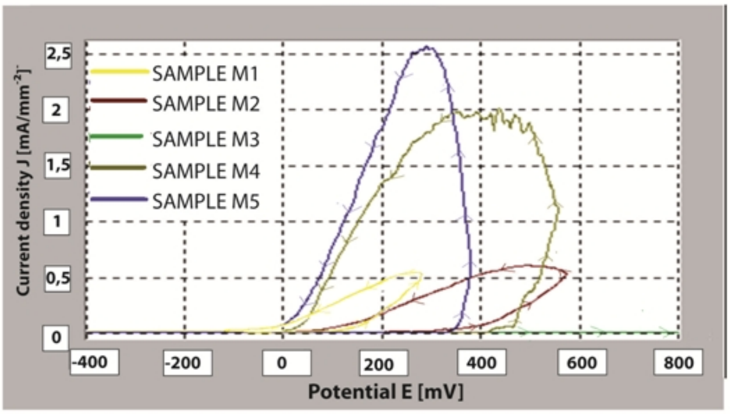

Figure 2: Polarization curves for materials tested in artificial cerebrospinal fluid.

of these pits also contain rest of corrosion products. Chemical composition of corrosion pits bottoms is shown in Table 5 and was found by EDS analysis of corrosion pit marked in Figure 3.

Table 5: Chemical composition of corrosion pit bottom from spot marked in Figure 3.

Chemical composition of corrosion pit bottom [wt. %]											
O	Na	Mg	Al	Si	S	Cl	K	Ca	Ti	Fe	Ni
38,58	5,75	1,00	0,90	2,87	0,74	5,92	1,19	1,96	14,82	11,47	14,80

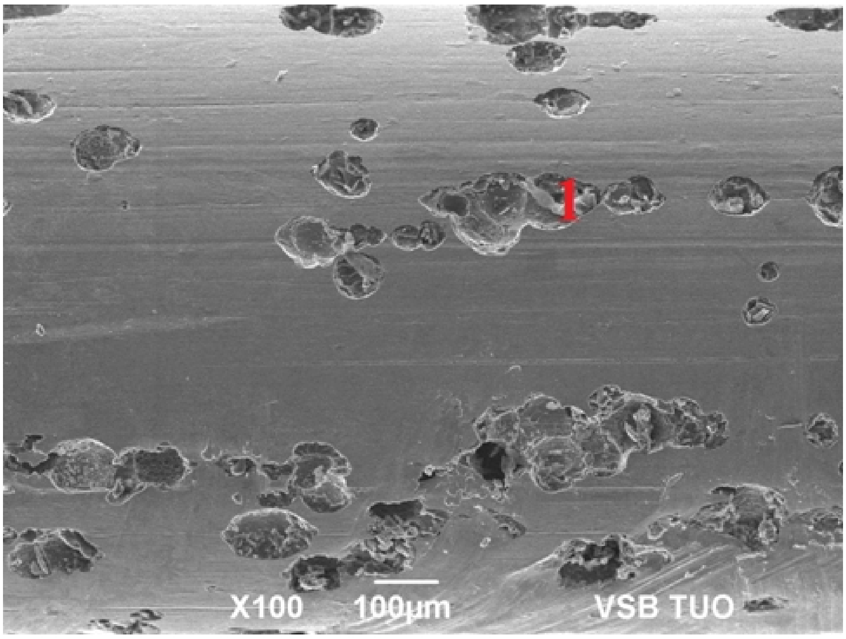

Figure 3: Surface of sample M5 after corrosion test, spot for EDS analysis is marked by red number 1.

4 Conclusion

These measurements helped to classify each material by its corrosion properties. Usability of biomaterials in implantology is determined by materials corrosion resistance in specific body environment. Any of tested materials can be advised for short-term implant construction, but Ti6Al4V alloy was found as most corrosion resistant tested material. There was also relationship between pasivation of surface and corrosion resistance of stainless steel and ninitol found. Pasivation highly increased corrosion resistance of tested materials. It is also very easy and cheap type of surface treatment. Results from in vivo test of these materials will be published later.

Acknowledgement

This paper was created under the Project No. CV6005531 „Support and development of international relationship and mutual foreign activities of students and staff on FMMI",and Project SP2015/102 „Rozvoj metodiky zkoušení korozních vlastností materiálů“ funded by VŠB – Technical University of Ostrava, Czech Republic

References

[1] Pruitt, L. A. and Chakravartula, A. M.: “Mechanics of biomaterials: Fundamental principles for implant design”. In: *MRS Bulletin* 37 (07 July 2012), pages 698–698. ISSN: 1938-1425. DOI: `10.1557/mrs.2012.165`. URL: `http://journals.cambridge.org/article_S0883769412001650`.

[2] *Capturing the Full Power of Biomaterials for Military Medicine: Report of a Workshop.* Washington, DC: The National Academies Press, 2004. ISBN: 978-0-309-09283-8. URL: `http://www.nap.edu/catalog/11063/capturing-the-full-power-of-biomaterials-for-military-medicine-report`.

[3] Lowenberg, B. et al.: “ASTM-F86 passivation increases trace element release from Ti6AI4V into culture medium”. In: *Journal of Materials Science: Materials in Medicine* 5.6-7 (1994), pages 467–472.

[4] Rondelli, G and Vicentini, B: “Localized corrosion behaviour in simulated human

body fluids of commercial Ni–Ti orthodontic wires". In: *Biomaterials* 20.8 (1999), pages 785–792.

[5] Hlinka, J.: "Zkoušení a hodnocení korozní odolnost vybranỳch kovovỳch biomateriálŭ". In: (2013).

ArcelorMittal

Aurubis
Our Copper for your Life

BSW

BENTELER

BBH
STOLBERG

BGH

CREMER
Thermoprozessanlagen GmbH

DEUTSCHE EDELSTAHLWERKE
Providing special steel solutions

GMH Gruppe
Georgsmarienhütte

STAHL.
DAS SIND WIR.
HKM

HYDRO
Infinite aluminium

LSW
Lech-Stahlwerke

The Bright World of Metals
GIFA METEC THERM PROCESS NEWCAST
Düsseldorf/Germany, 16 – 20 June 2015

PAUL WURTH
SMS group

SALZGITTER AG
Stahl und Technologie

ThyssenKrupp

vallourec

voestalpine
ONE STEP AHEAD.

Stahl

WS